A Rietveld-Approach for the Analysis of Neutron Time-Of-Flight Transmission Data

Dissertation
zur Erlangung des Doktorgrades
der Mathematisch-Naturwissenschaftlichen Fakultät
der Christian-Albrechts-Universität
zu Kiel
vorgelegt von

Sven Vogel
vogel@physics.lanl.gov

Kiel
2000

Referent:	Professor Dr. Hans-Georg Priesmeyer
Korreferent:	Professor Dr. Wulf Depmeier
Tag der mündlichen Prüfung:	2. Mai 2000
Zum Druck genehmigt:	Kiel, den

Der Dekan

Contents

Abstract

A novel technique to obtain crystallographic information on a sample with a temporal resolution in the order of ten seconds is presented. The crystallographic information is derived from neutron time-of-flight (TOF) transmission patterns utilising neutrons traveling through a sample without interaction. Neutron source, sample and detector are aligned on a single axis. The interaction of neutrons when penetrating a sample depends on the nuclear properties of the sample atoms and the spatial distribution of the atoms. For crystalline samples, neutron intensity is diffracted away from the direction of the incident beam, leaving a characteristic pattern in the transmitted signal from which structural information can be derived. Transmission geometry provides under certain circumstances several advantages over the conventional diffraction setup: The application of a pulsed neutron source provides Bragg-edge transmission patterns over a large wavelength range with sufficient statistics within seconds as the transmitted intensity is high compared to the neutron intensity diffracted into a certain solid angle and the neutron time-of-flight readily allows to determine the neutron wavelength. This allows to study kinetics of structural phase transitions in solids lasting for much less than one hour. As the 'reflections', the so-called Bragg-edges, result from backscattering (i.e. the Bragg angle ϑ is equal to 90°), there is no contribution of the scattering angle to the error of the d-spacing, making this technique an interesting alternative for neutron applications needing a high d-spacing resolution like strain measurements. Since no beam-path for diffracted intensity is necessary, equipment for special environments, e.g. temperature, atmosphere or pressure, can be designed much easier than for a diffraction experiment. Precise sample positioning, as is mandatory for a diffraction setup, is not required for transmission setup and further simplyfies experimentation.

The acquired patterns are naturally based on different laws than conventional powder diffraction data, thus, the available Rietveld software for the analysis of powder diffraction data cannot be used or even easily adapted for the analysis of transmission data. The large number of spectra acquired during the course of a phase transition, typically in the order of 1000, requires automated analysis. Consequently, a software package '**BETMAn**', (**B**ragg-**E**dge **T**ransmission **M**easurements **An**alysis) was developed. **BETMAn** allows for the first time to apply the Rietveld method to neutron transmission patterns.

BETMAn and its application for studying the mechanisms and kinetics of structural phase transitions and strain measurements is presented in this work. Application examples include tracking of the carbon content in the austenitic and ferritic phase during the temperature-induced isothermal decomposition of austenite to bainite in a Si-rich steel as well as a study of kinetics of nickeloxide reduction at temperatures above 1000°C. Calibration and benchmarking experiments are described also.

Chapter 1

Introduction

Neutron scattering is one of the most important techniques in many fields of modern science. In physics, materials science, structural chemistry and earth science neutrons play a vital rule in studying a variety of systems. Due to their in most cases very low absorption by solids, neutrons can penetrate a sample much deeper than x-rays, allowing to probe sample volumes deep inside a sample. Non-destructive characterisation and testing in engineering science is one application which benefits greatly from the penetration depths. Because of the neutrons' wave properties, neutrons are diffracted by crystalline solids. The diffraction of neutrons follows the same laws as the diffraction of x-rays, namely Bragg's law is applicable and quantities like d-spacing and structure-factor of a reflection are applied to describe neutron diffraction patterns. The former allows to measure the size and geometry of the unit-cell while the latter provides information on its content. Nevertheless, the fundamental interaction processes of neutrons with matter are different than in the case of x-rays: Neutrons are virtually only scattered by the nuclei of the atoms rather than the electronic shell as in the case of x-rays. Therefore, a form-factor is not necessary and the ability of a nucleus to scatter a neutron elastically (i.e. without changing its energy) and coherently (i.e. such that interference is possible) is described by a single quantity, the neutron scattering length b (see section 1.6.2). This scattering power of an atom, contrary to x-rays, does neither depend on the atomic number Z of the atom, but varies without a simple, continous functional dependence from isotope to isotope, nor does it depend on the scattering angle ϑ (see figure 1.1). The former allows to distinguish atoms with neutrons that are indistinguishable with x-rays because their atomic numbers are close to each other[1]. Other unique applications of neutron diffraction are localisation of hydrogen atoms, which are barely visible with x-rays, and studying the magnetic structure of solids.

In the following sections, neutron transmission[2] is introduced as well as the basics of neutron

[1] As also some elements are indistinguishable for neutrons because their scattering lengths are very similar, the combination of x-rays and neutrons is very powerful for solving structures. As an example, in the structure of the high-T_c superconductor $YBa_2Cu_3O_{7-x}$ the atoms of yttrium and copper are virtually identical for neutrons, hence it was not possible with neutron diffraction only to investigate whether these atoms order on their sites or not. However, the x-ray scattering factors are very different and Williams et al. (1988) could show by a joint refinement of the structure using both neutron and x-ray data that the atoms do not interchange on their sites. Additionally, anisotropic displacement factors for all atoms, estimates of the particle size and strain were determined. The software package used for this refinement was GSAS (Larson & Von Dreele, 1994).

[2] Occasionally, neutrons reaching a diffractometer detector by leaving the sample on the opposite surface of the one they entered are termed 'transmitted' (e.g. on a diffractometer with detectors at $\pm 90°$ and a plate-like sample with its plate normal under $+45°$ to the incident beam, neutrons reaching the $+90°$ detector would be termed transmitted). In the present work, by 'transmitted neutrons' such neutrons are meant which travel through the sample without any interaction.

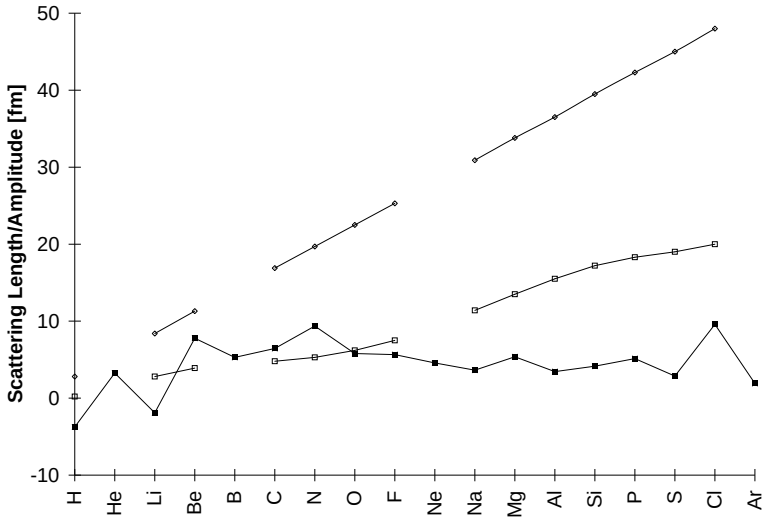

Figure 1.1: Scattering power of some elements for neutrons (full squares) and x-rays (open squares for $\sin\vartheta/\lambda = 0$ Å^{-1} and diamonds for $\sin\vartheta/\lambda = 0.5$ Å^{-1}). After Bacon (1955), table 2. The neutron scattering length of some elements is negative, see section 1.6.2.

generation, moderation and detection are described. The theoretical fundament of neutron scattering plus a brief history of the Bragg-edge transmission technique and a short introduction to the Rietveld method are presented. Where appropriate, it is refered to the experimental setup at flightpath 5 of the Los Alamos Neutron Science Center (LANSCE, Los Alamos, New Mexico, USA) where all experiments for the present work were performed.

1.1 Neutron Transmission

In general, to determine the crystal structure of a polycrystalline sample by neutron diffraction, a wavelength-dependent intensity spectrum is recorded under some angle to the direction of the incident neutron beam. At certain wavelengths strong intensity maxima are detected, so-called Bragg peaks. It is obvious that with this setup a large fraction of neutrons remains unused as usually only a small solid angle is covered with detectors but the neutrons are scattered over 4π. The yield is much higher when instead the transmitted intensity is used to determine the crystal structure. The experimental setup for such measurements is very simple as neutron source/moderator, sample and detector are placed on a single axis. Those neutrons are detected that travel without interaction through the sample while those that are scattered out of the direction of the incident beam, and which would be eventually detected in a diffraction experiment, leave a characteristic pattern in the incident intensity spectrum, so-called Bragg-edges. Figure 1.2 shows an example of a Bragg-edge transmission pattern of iron measured at LANSCE. In chapters 2 and 3 the advantages of the Bragg-edge transmission technique as well as the full model to describe Bragg-edge transmission patterns are presented. The motivation to utilize the Bragg-edge transmission technique at LANSCE was the possibility of real-time measurements: As the number of transmitted neutrons is typically much higher than the number of neutrons detected in a diffraction experiment, it is possible to collect a transmission pattern of sufficient statistics within a much shorter time than with a diffraction experiment. This allows for example to study kinetics of structural phase transitions (see chapter 7) lasting for less than one hour. In practice, the feasibility of Bragg-edge transmission experiments is limited by the fact that

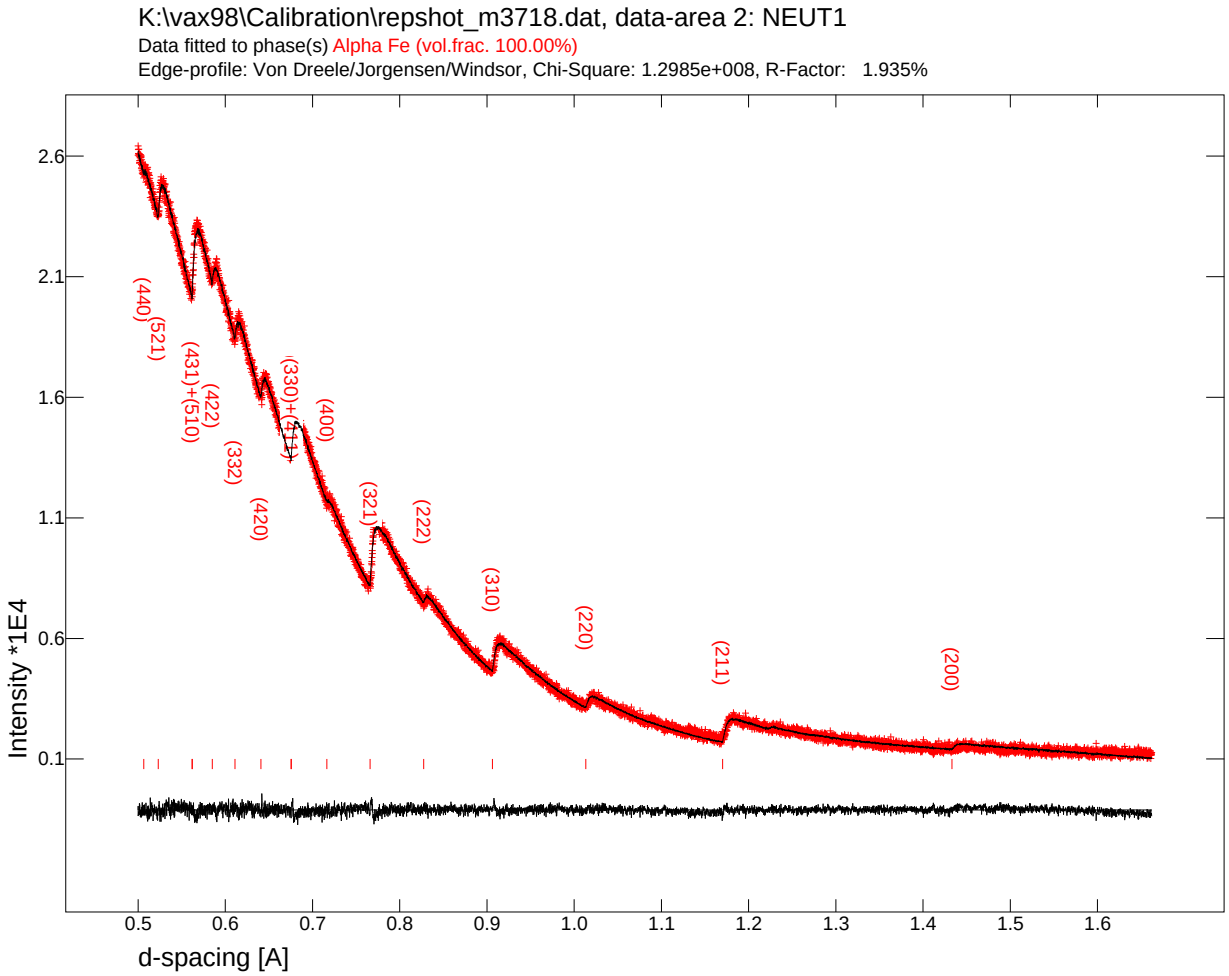

Figure 1.2: Fraction of the Bragg-edge transmission pattern of iron powder. The powder layer thickness is about 3 cm, the duration of the measurement was 3 minutes. The line through the measured data (crosses) is the **BETMAn** fit, tick-marks indicate calculated reflection positions. The edges are labeled with their Miller indices. The curve below the tick-marks is the difference curve between fit and measured data.

a small change (the intensity of a Bragg-edge) of a large signal (the transmitted intensity) has to be measured. This limits the application of Bragg-edge transmission measurements currently to systems of high symmetry (few, but intense reflections) consisting of good neutron scatterers.

With neutron transmission, sample volumes of several cubic centimeters are probed. Compared to techniques like TEM or conventional x-ray diffraction, surface effects can be neglected. As position, height and width of a Bragg-edge depend on the same laws as position, intensity and width of a diffraction peak, the same information as in a diffraction pattern is contained in a Bragg-edge transmission pattern. Naturally, the obtained parameter values (lattice parameters, volume fractions etc.) are averaged over the illuminated sample volume. As conventional diffraction setups are too slow to study the kinetics of phase transitions in real time, indirect methods (e.g. dilatometry, thermogravimetry) or interruptions of the phase transition are utilized for this purpose. In the latter case, the sample is quenched after a given time and then, under the assumption that the quenching froze the state of the sample, the sample is analyzed offline for example by x-ray diffraction or metallography. Both techniques probe only the sample surface and therefore care has to be taken to avoid differences

between bulk and surface properties. To obtain the desired kinetic information, the procedure is repeated several times with samples of the original state, introducing additional uncertainties. Contrary, indirect methods measure a quantity proportional to the volume fraction of one of the involved phases in real-time, for example changes of electric or magnetic resistivity, length or weight. Each of these techniques has to be calibrated and does not work if more than two phases are involved. Also no information on strain or texture evolution during the phase transition can be obtained. Neutron diffraction as well as transmission overcome these limitations and offer a possibility to monitor in-situ the changes of volume fractions, strain and texture. Bragg-edge transmission provides a way to obtain these parameters with a very good time resolution.

The goal of the present work was to develop a model describing the transmitted neutron intensity and a software capable of fitting parameters of the model to measured data. The fit parameters include the desired structural information on the sample.

1.2 Neutron Generation

The main natural source of free neutrons is secondary radiation of cosmic radiation (creation of particles by interactions of cosmic radiation particles with atoms of the earth atmosphere). The main source of artificially generated neutrons are nuclear reactors. Free neutrons have an average lifetime of about 888 seconds (e.g. Mampe et al., 1989a, Mampe et al., 1989b: 887.6 ± 3 seconds) and decay according to

$$n \rightarrow p + e + \tilde{\nu} \tag{1.1}$$

into a proton, an electron and an anti-neutrino. Hence, free neutrons must be produced shortly before their application. Besides reactors, where high energy neutrons from nuclear fission reactions partly induce further nuclear fissions (chain reaction) and partly emerge in a constant current from the reactor core and are available for experiments, neutrons for research may be generated in short bursts by a process called spallation[3].

For spallation, protons are accelerated to energies of typically 800 MeV (corresponding to about 84% of the speed of light) and directed to a heavy-metal target (e.g. uranium at ISIS or tungsten at LANSCE). Proton currents at the brightest spallation sources are 100 μA at LANSCE and 200 μA at ISIS. As the fast protons are generated in long pulses, they have to be accumulated and converted to short pulses (e.g. from $\sim$ 750 ms to 270 ns at LANSCE, Roberts, 1999) in storage rings or synchrotrons. Those rings release the protons 20 (LANSCE) or 50 (ISIS) times per second. When the target is hit by the protons, target nuclei are 'smashed' into many small particles (contrary to fission where basically two parts of roughly the same mass are generated), among them about 10 to 25 neutrons, depending on proton energy and target material (Windsor, 1981, section 2.2, for a specific description of the LANSCE target see Lisowski et al., 1990). The sources at ISIS and LANSCE[4] produce neutron fluxes in the order of 10^{16} neutrons per second and cm^2. Spallation neutron sources have, compared to reactor sources, the advantage that the proton current is virtually not limited and hence the neutron

[3] Another way to generate neutron bursts are pulsed reactors: Two neutron reflectors are rotated with fissable material inbetween such that a short chain reaction is induced when both reflectors are in appropriate orientation and a neutron pulse is generated. The research reactor IBR-2 at Dubna/Russia works after this principle and generates neutron pulses of 320 μs half-width (JINR, 1997).

[4] The projected spallation neutron source SNS (**S**pallation **N**eutron **S**ource) in the United States is designed for proton currents of 2 mA at 1 GeV proton energy on a mercury target, repetition rate 60 Hz, resulting in a peak neutron flux in the order of 10^{17} neutrons per second and cm^2 (Olsen et al., 1999). The ESS (**E**uropean **S**pallation **S**ource) in Europe will reach about $2 \cdot 10^{17}$ neutrons per cm^2 (ESS, 1999).

flux can be in principle increased without a physical limit. At reactor sources, this is not possible due to reactor safety. Spallation neutron sources are due to the time structure of the neutron flux ideal for time-of-flight (TOF) measurements (see section 1.3).

1.3 Neutron Moderation

Both at steady-state (reactor sources) and pulsed sources the generated neutrons initially have energies far too high as required for measuring properties relevant to solid state physics. Particle kinetic energy E and wavelength λ are related by de Broglie's law

$$E = \frac{p^2}{2m} = \frac{\hbar^2 k^2}{2m} = \frac{h^2}{2m\lambda^2} \tag{1.2}$$

where p is the particles's momentum, m its mass, $\hbar$ is Planck's constant over 2π and $k = 2\pi/\lambda$ the wave-vector of the particle. For measurements of the static distribution of the atoms in a solid (e.g. the crystal structure in crystalline or the average atomic distances in amorphous solids), the wavelength must be in the range of the atomic distances, equivalent to energies of several ten meV in the case of neutrons (for x-rays, this energy is in the range of several ten keV). Measuring the dynamic distribution of atoms (i.e. measurements involving phonons) requires neutron energies of the same order of magnitude[5]. Therefore, the neutron energy must be reduced from several ten or hundred MeV to several ten or hundred meV. The kinetic energy of neutrons can only be decreased by collisions as neutrons have no charge[6]. By guiding the neutron beam through appropriate materials like water or methane, the neutrons loose energy in collisions with atoms and molecules. This process is called moderation. In thermal equilibrium with the moderator medium, the neutron energies are in the order of thermal vibrations of moderator atoms and thus the neutrons may gain as well as loose energy. The most probable energy of a neutron after the moderation process is given by

$$E = \tfrac{3}{2} k_B T \tag{1.3}$$

(k_B is Boltzmann's constant, T the moderator temperature) resulting in a maximum at that energy of the so-called Maxwellian energy distribution of neutrons leaving the moderator (cf. section 3.8.2 and figure 6.1). Neutrons with energies corresponding to room temperature are called thermal neutrons, the moderation process in that case is frequently called thermalisation. As Bacon (1955, sect. 1.2) states, it is just a 'fortunate circumstance' that these wavelengths and energies are of just the energies desired for investigations of atomic arrangements and phonon energies in solids, making the moderation process relatively convenient. It is remarkable that a water layer of only 3 cm is sufficient to decrease the neutron energy by 10 orders of magnitude. Neutrons of energies above and below the thermal range are termed epithermal and cold neutrons, respectively. The velocities of thermal neutrons are in the order of 1000 m/s such that relativistic effects can be neglected. The moderation process introduces a broadening of the initially sharp neutron pulse ($\approx$ 270 ns initial neutron pulse width at LANSCE, determined by the pulse width of the proton pulse) which can be approximated for the

[5] Neutrons actually interact with the nuclei rather than the electron shell (neglecting spin-spin interactions with the shell electrons). The assumption that measured movements of the nucleus are also valid for the electron distribution, and hence for the movement of the complete atom, is known as the Born-Oppenheimer approximation.

[6] Under the assumption that the neutron charge must be equal to the difference of proton and electron charges (if such difference exists), King (1960) derived an upper limit of the neutron charge of $2 \cdot 10^{-22} e = 3.2 \cdot 10^{-41}$ coulombs from measurements of the electric charge of the SF_6 molecule. Baumann et al. (1988) found a neutron charge of $(-0.4 \pm 1.1) \cdot 10^{-21} e$ by measuring the deflection of cold neutrons traveling through a strong electric field of 9 meter in length.

water moderator used at flitghpath 5 of LANSCE (see below) by $\Delta t = 7.1/\sqrt{E} \approx 25 \cdot \lambda$ where Δt is in μs, λ in Å and E in eV (Hyer, 1990). Therefore, the pulse widths are for instance 7, 32 and 225 μs for neutron energies of 1 ($\lambda = 0.3$Å), 0.05 (1.3 Å) and 0.001 eV (9 Å), respectively. Converted to d-spacing resolution $\Delta d/d$, the above figures result in an instrumental contribution to reflection broadening from the moderator of $1.7 \cdot 10^{-3}$, cf. section 3.3.4, equation (5.1) and section 5.3.2.

The detector system at flightpath 5 at LANSCE views a high intensity moderator. With the water moderators of 33.63 mm as used at LANSCE, both high intensity and high resolution moderators can be built by placing a 0.38 mm thick gadolinium foil either 8 mm or 18 mm away from the spallation target within the water (Hyer, 1990, Windsor, 1981, sect. 3.4). The neutron pulse width is determined by the distance the already moderated neutrons travel in the moderator before leaving the moderator towards the experiment. Therefore, in the first case the relatively small amount of neutrons already moderated in the first 8 mm within the moderator is absorbed by the gadolinium while the unmoderated, fast neutrons pass the foil. This results in a relatively high flux at the cost of a relatively large instrumental contribution of the moderator to the width of Bragg-reflections (i.e. poor resolution).

1.4 Neutron Detection

To record neutron intensity spectra, neutrons must be converted to charged particles which in turn can be detected electronically. For thermal neutrons, typically scintillation counters or gas counters are employed. Scintillation counters consist of a scintillator and a photomultiplier. In the scintillator, the neutron absorption according to one of the exothermic reactions

$$^{6}\mathrm{Li} + \mathrm{n} \rightarrow \mathrm{T} + {}^{4}\mathrm{He} + 4.78\ \mathrm{MeV} \tag{1.4}$$

$$\begin{aligned} ^{10}\mathrm{B} + \mathrm{n} &\rightarrow {}^{7}\mathrm{Li} + {}^{4}\mathrm{He} + 2.79\ \mathrm{MeV} \quad (6\%) \\ ^{10}\mathrm{B} + \mathrm{n} &\rightarrow {}^{7}\mathrm{Li}^{*} + {}^{4}\mathrm{He} + 2.31\ \mathrm{MeV} \quad (94\%) \\ &\qquad \downarrow \\ &\qquad {}^{7}\mathrm{Li} + 480\ \mathrm{keV} \end{aligned} \tag{1.5}$$

is followed by the emission of an energetic charged particle which ionizes the working medium, causing fluorescent radiation[7]. The emitted light quanta partly reach the photocathode of the photomultiplier and initiate an electron avalanche which creates a measurable electric pulse at the anode. The pulses can be counted, resulting in the desired neutron intensity versus time patterns. As also energetic γ-radiation causes scintillation, neutron and γ-radiation have to be discriminated. This can be performed electronically based on the different pulse shapes of the radiation types.

In a gas counter, helium enriched with ^{3}He, or BF_3 enriched with ^{10}B is placed in a metal cylinder with a thin wire anode. Between anode and cylinder a high voltage is applied. Again the neutron is absorbed and according to the above reactions for boron or

$$^{3}\mathrm{He} + \mathrm{n} \rightarrow \mathrm{T} + \mathrm{p} + 0.765\ \mathrm{MeV} \tag{1.6}$$

fast charged particles are generated. The gas counter must not be run in the 'Geiger counter' mode, where the applied voltage is that high that the charge pulses created by a detected particle are

[7] The isotope ^{10}B has a natural abundance of about 20%, ^{6}Li of 7.5%.

independent of the energy of the particle, as this does not allow to discriminate against γ-rays. After discrimination, the pulses may be counted the same way as those of scintillation counters.

For Bragg-edge transmission experiments both at LANSCE (flightpath 5) and ISIS (ENGIN and also the planned ENGIN-X) scintillation counters are used. At ISIS arrays of 10 times 1 (ENGIN) or 10 times 10 (the new ENGIN-X instrument) pixelated detectors of 1 mm^2 active area are used. This allows spatially resolved measurements at the cost of measurement time. At LANSCE, only a single detector area of 43 cm in diameter is used, providing no spatial resolution but allowing very short accumulation times. In the past, for transmission measurements at LANSCE the so-called 'current-mode' was applied (Bowman et al. 1990): The applied photomultiplier voltage was high enough, that in combination with the high neutron intensity a current proportional to the neutron intensity was created. The current was converted to voltage which was recorded versus time with a transient digitizer. This method allows to readily measure very high neutron intensities and, contrary to counting mode, it is inherently not subject to dead time. Originally developed for high energy experiments, where the neutron intensity at a spallation source is much higher than in the thermal range, the resulting currents for thermal neutron intensites are much lower and subject to noise pickup (mostly 60Hz from the power supplies, see section 5.3.3). Despite the fact that counting statistics is not readily applicable to neutron intensities measured this way, for a full pattern analysis, this noise 'contamination' is a disadvantage. Since 1998 a new detector system is used at flightpath 5, allowing to count the transmitted neutron intensity up to a rate of 500 MHz (Yen et al., 1993, Knudson et al., 1996). It consists of a ^{10}B (8 wt. %) loaded hydrocarbon-based liquid scintillator (mineral oil) of 43 cm diameter which is divided into 55 honeycomb-shaped elements. Each element is viewed by a photomultiplier tube (see section 5.2 for further information on the detector and data acquisition system).

1.5 Neutron Wavelength

Neutron wavelengths can be determined by scattering the neutrons with a single crystal of known lattice spacing $d_{\vec{h}}$. Utilizing Bragg's law

$$\lambda = 2d_{\vec{h}} \sin \vartheta \tag{1.7}$$

the wavelength can be determined from the Bragg-angle ϑ. This process is used at reactor sources and requires many detectors and collimators or is time consuming as many different angles have to probed. The second method to determine neutron wavelengths is called time-of-flight-method (TOF) and assumes that the time t it takes for a neutron to travel a given distance L is known. This can be achieved by generating neutron pulses either by chopping a steady neutron current or generating the neutrons in pulses[8]. The latter is done at spallation sources and hence the TOF-method is the method of choice. From the de Broglie-relation $p = \hbar k$ the relation

$$\lambda = \frac{ht}{mL} \tag{1.8}$$

can be easily derived.

[8] A mixture between a constant current and pulses is the Fourier reverse time-of-flight (RTOF) method as utilized for example at the FSS instrument at the GKSS research center (e.g. Priesmeyer, 1992a, 1998).

1.6 Neutron Scattering

In this section, the fundamental quantities to describe neutron transmission patterns are introduced. The measured transmission at a given wavelength λ is the ratio of transmitted intensity $I(\lambda)$ and incident intensity $I_0(\lambda)$ and for a single phase described by

$$T(\lambda) = \frac{I(\lambda)}{I_0(\lambda)} = \frac{I_0(\lambda)\, e^{-n\sigma(\lambda)x}}{I_0(\lambda)} = e^{-n\sigma(\lambda)x} \tag{1.9}$$

where n is the number of scattering centers per unit volume and x is the sample thickness. The quantity $\sigma(\lambda)$ is the total cross-section per scattering center. Among others, it depends on the scattering lengths of the elements in the sample. Structural information can be derived from elastic coherent scattering (also known as Bragg-scattering). In the following sections the theoretical basis of the elastic scattering cross-section, the scattering length and the elastic coherent scattering by a crystal lattice is presented.

1.6.1 Nuclear Cross-Sections

For elastic scattering of a neutron by a nucleus, where 'elastic' means that the neutron energy before and after the scattering process are constant, the number of neutrons scattered into a solid angle $d\Omega = \sin\theta d\theta d\phi$ per unit time is given by (Lovesey, 1986, section 1.2)

$$N\left(\frac{d\sigma}{d\Omega}\right) d\Omega \tag{1.10}$$

where N is the number of incident neutrons per unit time and unit area. $d\sigma/d\Omega$ is termed differential cross-section. The cross-section σ has the dimension of an area and is measured in units of 1 barn= 10^{-28} m^2. Formally, scattering means the transition of an incident wave-vector $\vec{k}$ to a wave-vector $\vec{k}'$ after the scattering process. The probability per unit time for such a transition into a state of a continous spectrum is given by Fermi's Golden rule[9]

$$W_{\vec{k}\to\vec{k}'} = \frac{2\pi}{\hbar}\left|\int \Psi^*_{\vec{k}'}(\vec{r})\,\hat{V}(\vec{r})\,\Psi_{\vec{k}}(\vec{r})\,d\vec{r}\right|^2 \rho_{\vec{k}'}(E) \tag{1.11}$$

The functions $\Psi_{\vec{k}}(\vec{r}) = \frac{1}{a^{3/2}}\exp\left(i\vec{k}\vec{r}\right)$ are the normalized wave-functions of the neutron confined to a box of volume a^3 before $(\vec{k})$ and after $(\vec{k}')$ scattering. $V(\vec{r})$ is the interaction potential causing the scattering and $\rho_{\vec{k}'}(E)$ is the density of states (DOS) for the state $\vec{k}'$ per unit energy range. The latter is given by

$$\rho_{\vec{k}'}(E) = \left(\frac{a}{2\pi}\right)^3 \frac{mk}{\hbar^2} d\Omega \tag{1.12}$$

Determing the flux ϕ_N of the incident neutrons from their velocity v_N,

$$\phi_N = \frac{v_N}{a^3} = \frac{\hbar k}{ma^3} \tag{1.13}$$

the differential cross-section is given by

$$\frac{d\sigma}{d\Omega} = \frac{W_{\vec{k}\to\vec{k}'}}{\phi_N} = \left(\frac{a^3 m}{2\pi\hbar^2}\right)^2 \left|\int \Psi^*_{\vec{k}'}(\vec{r})\,\hat{V}(\vec{r})\,\Psi_{\vec{k}}(\vec{r})\;d\vec{r}\right|^2 = \left|\left\langle \vec{k}'\right|\hat{V}\left|\vec{k}\right\rangle\right|^2 \tag{1.14}$$

With this result the case of elastic neutron scattering can be described.

[9] The equation for the transition probability was derived by Pauli and termed 'Golden Rule' by Fermi due to its various applications (Schwabl, 1993, section 16.3.3).

Figure 1.3: Neutron trajectory in the vicinity of the nucleus. d is the shortest distance between neutron and nucleus. It can be shown, that d must be quantized and that only neutrons without angular momentum ($l = 0$) can interact with the nucleus.

1.6.2 Scattering Length

In this section, it is shown quasi-classically that scattering of neutrons is isotropic, i.e. no form factor depending on the scattering angle as in the case of x-ray scattering is necessary to describe the scattering. Furthermore, a single number is sufficient to describe the scattering power of a nucleus for neutrons. The angular momentum L of the neutron scattered by the nucleus (see figure 1.3) is given by

$$L = \left| m\vec{r} \times \dot{\vec{r}} \right| = p\ d = \hbar k\ d \tag{1.15}$$

where p is the momentum of the neutron and d is the shortest distance between neutron and scattering nucleus. With quantum mechanics it can be shown that the angular momentum is quantized as

$$L = \sqrt{l(l+1)}\hbar \qquad l = 0, 1, 2... \tag{1.16}$$

Hence, also d must be quantized and

$$d_l = \frac{L}{\hbar k} = \frac{\sqrt{l(l+1)}\hbar}{\hbar k} = \sqrt{l(l+1)}\frac{\lambda}{2\pi} \tag{1.17}$$

must hold. For $l = 1$, d would be approximately 0.2λ and for a wavelength of the order of 1 Å the neutron would not be reached by the strong interaction responsible for the scattering which reaches only a range in the order of the radius of the nucleus (approximately 10^{-14} m). Therefore, only neutrons with an angle independent wave-function, meaning $l = 0$ are scattered, which in turn means the scattering of neutrons by nuclei is isotropic.

Consequently, the potential V in (1.11) describing the scattering must be isotropic, too. This condition is fulfilled by Fermi's pseudo-potential of a nucleus located at $\vec{R}$

$$\hat{V}\left(\vec{r}\right) = \frac{2\pi\hbar^2}{m} b\delta\left(\vec{r} - \vec{R}\right) \tag{1.18}$$

The complex quantity b is the coherent scattering length for bound nuclei and is a measure for the amplitude of the scattered spherical wave[10]. The real part of b describes the cross-section for coherent scattering, the imaginary part that for absorption. The latter is for most isotopes much smaller than the former, resulting in the deep penetration of neutrons into most materials

[10] According to Huygens' principle the neutron outside the nucleus is described by a wave function

$$\Psi\left(\vec{r}\right) \quad = \quad e^{i\vec{k}\vec{r}} - \frac{b}{r}e^{ikr}$$

which is a plane wave before and a spherical wave after the scattering. The 'negative' definition of the scattering length makes b positive for most isotopes, meaning that most isotopes shift the phase of the wave describing the incident neutron by π (Dobrzynski & Blinowski, 1994, sect. 3.2).

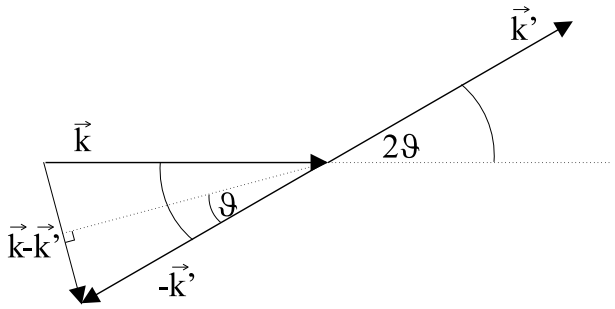

Figure 1.4: Wave vector $\vec{k}$ of the incident and $\vec{k}'$ of the neutron scattered under an angle of 2ϑ.

(Dobrzynski & Blinowski, 1994, sect. 3.3). Applying Fermi's pseudo-potential (1.18) to the differential cross-section (1.14) and transformation of the coordinate system such that the scattering nucleus is located at the origin, the relation

$$\frac{d\sigma}{d\Omega} = \left|\left\langle \vec{k}' \right| \hat{V} \left| \vec{k} \right\rangle\right|^2 = \left| \frac{a^3 m}{2\pi\hbar^2} \frac{2\pi\hbar^2}{m} b \frac{1}{a^3} \int e^{-i\vec{k}'\vec{r}} \delta\left(\vec{r}\right) e^{i\vec{k}\vec{r}} d\vec{r} \right|^2 = |b|^2 \tag{1.19}$$

is obtained. Integration over all solid angle elements $d\Omega$ yields the total cross-section for elastic scattering of a neutron by a single nucleus:

$$\sigma = 4\pi |b|^2 \tag{1.20}$$

It has the area of a sphere with radius $|b|$. The absolute value of the scattering length therefore is a measure for the target area of the nucleus for the neutron.

1.6.3 Interaction with Crystals

The differential coherent elastic scattering cross-section of a rigid crystal lattice (i.e. thermal motion of the nuclei is neglected for now) is given by (e.g. Lovesey, 1986, section 2.2)

$$\left(\frac{d\sigma}{d\Omega}\right)_{coh} = |\bar{b}|^2 \left| \sum_{\vec{l}} \exp\left(i\vec{\kappa}\cdot\vec{l}\right) \right|^2 \tag{1.21}$$

where $\bar{b}$ is the average scattering length of contributing nuclei and $\vec{\kappa} = \vec{k}' - \vec{k}$ is the momentum transfer of the incident to the scattered neutron (see figure 1.4). The sum runs over all lattice vectors $\vec{l} = l_1\vec{a}_1 + l_2\vec{a}_2 + l_3\vec{a}_3$, the $\vec{a}_i$ are the unit cell vectors. The large number of items results only in a non-negligible value when the items are added in phase. Because of the definition of reciprocal lattice vectors[11],

$$\vec{\tau}_3 = \frac{2\pi}{V_0}\vec{a}_1 \times \vec{a}_2 \qquad \text{and cyclical interchanged, where } V_0 = \vec{a}_1 \cdot (\vec{a}_2 \times \vec{a}_3) \tag{1.22}$$

this is non-trivially fulfilled when $\vec{\kappa}$ is equal to a reciprocal lattice vector

$$\vec{\kappa} = \vec{\tau} = \tau_1\vec{\tau}_1 + \tau_2\vec{\tau}_2 + \tau_3\vec{\tau}_3 \tag{1.23}$$

[11] In this work, $\vec{\tau}$ mean reciprocal lattice vectors as conventionally used in solid state physics, i.e. including a factor 2π, while $\vec{h}$ mean reciprocal lattice vectors as used in crystallography, i.e. without a factor 2π: $\vec{\tau} = 2\pi\vec{h}$.

If $\vec{\kappa} \neq \vec{\tau}$ the differential coherent scattering cross-sections falls to negligible values. With the representation of Dirac's δ-function (e.g. Schwabl, 1993, equation (A.20))

$$\delta(k) = \frac{1}{2\pi} \int_{-\infty}^{\infty} \exp(ikl)\, dl \tag{1.24}$$

the differential cross-section of a crystal of a very large number N of unit cells with one occupied site per unit cell becomes

$$\left(\frac{d\sigma}{d\Omega}\right)_{coh} = N \frac{(2\pi)^3}{V_0} |\bar{b}|^2 \sum_{\vec{\tau}} \delta(\vec{\kappa} - \vec{\tau}) \tag{1.25}$$

In the general case of more than one site per unit cell, the averaged scattering length b must be replaced by the structure factor

$$F(\vec{\tau}) = \sum_i b_i \exp(i\vec{\tau} \cdot \vec{x}_i) \tag{1.26}$$

which adds the fractions of the scattering amplitudes of all atoms in the unit cell to the contribution of one unit cell. $\vec{x}_i$ are the coordinates of the equilibrium position of nucleus i, expressed as fractions of the unit cell edges. If different isotopes of an element contribute, an average value weighted by their natural abundance of their scattering lengths must be used. The δ-function in equation (1.25) expresses that a significant scattered intensity can be only expected when $\vec{\kappa} = \vec{\tau}$. This condition allows to determine possible $\vec{\kappa}$ graphically with the so-called Ewald construction (see for example Kittel, 1996, chapter 2). From figure 1.4 it can be seen that under the assumption of elastic scattering (i.e. $|\vec{k}| = |\vec{k}'|$) for $\vec{\kappa}$

$$|\vec{\tau}| = |\vec{\kappa}| = \left|\vec{k} - \vec{k}'\right| = 2\left|\vec{k}\right| \sin\vartheta \tag{1.27}$$

must hold. With the relation

$$|\vec{\tau}| = \frac{2\pi}{d} \tag{1.28}$$

between a reciprocal lattice vector $\vec{\tau}$ and the lattice spacing d of the corresponding set of lattice planes (Lovesey, 1986, section 2.4) and the definition of the wave vector $\vec{k}$, the well-known Bragg equation

$$2d_{\vec{\tau}} \sin\vartheta = \lambda \tag{1.29}$$

may be derived.

1.7 The Rietveld Method

Crystallographic structure descriptions commonly consist of a unit cell of a certain geometry, the description of the content of the unit cell, consisting of atomic species and their position within the unit cell, and a space-group providing information on the symmetry of the crystal structure. The space-group also implies constraints on the unit cell geometry and the positions of the atoms. In a powder diffraction pattern, the dimensions of the unit cell determine the reflection positions according to equation (1.28), the content of the unit cell determines the (integrated) intensity ratios of the reflections as described by the structure factor (1.26). Because of symmetry constraints described by the space group certain reflections may be canceled. The goal of a structure refinement is to find a set of the above parameters that describe a measured pattern as good as possible. As there is still no direct experimental access to the accurate crystal structure, usually such a model of the crystal structure is refined by least-squares methods using Bragg intensity data as observations.

It is obvious that a large number of reflections and a good description of the peak profiles is necessary to obtain the required reflection positions and integrated intensities. Nevertheless, even the best description of a single peak will fail if severe overlap of peaks occurs due to the instrumental resolution or sample properties. Hence, the determination of position and intensity peak by peak independently of each other is not an appropriate approach in such cases. Rietveld (1967, 1969) proposed to fit parameters of a model function describing the whole measured pattern depending on crystallographic parameters of the sample, parameters describing the used instrument plus some numerical parameters against the measured data. With this approach, also the overlapping peaks contribute their information about the structure to the refinement. From some 'appropriate' starting values the fit minimizes the difference between a calculated curve and the measured data by adjusting the values of scaling factors, lattice parameters, atomic positions, atomic displacement factors etc.

This approach was first used for constant wavelength neutron data only until in 1977 the first codes for refinement of x-ray data were published; since then the method became generally accepted for both neutron and x-ray powder diffraction (Rietveld, 1993). A review of the method was published in 1982 by Albinati & Willis (1982). Decker et al. (1973), Worlton et al. (1976) and Von Dreele et al. (1982) applied the method to neutron time-of-flight diffraction data by developing appropriate models for the incident intensity, reflection profiles and descriptions of profile parameters depending on wavelength. Hill & Howard (1987) and Bish & Howard (1988) described quantitative phase analysis using the Rietveld method. The advantage in this particular field is that no calibration substance of known abundance has to be used as the volume or weight fractions of the contributing phases are determined from scale factors for each phase fitted during the refinement. Guéneau & Servant (1995) compared the quantitative phase determination for low volume fractions by Rietveld refinement of neutron data with other methods.

Sakata & Cooper (1979) carried out an analysis of the Rietveld method focussing on the estimated standard deviations (e.s.d.'s) of the refined parameters and systematic errors between structural parameters refined with the Rietveld and integrated intensity methods. Scott (1983) found, that misfits due to model errors result in an underestimation of e.s.d.'s of the structural parameters and suggested to scale the e.s.d.'s resulting from the fitting procedure with the goodness-of-fit to obtain parameter accuracy rather than parameter precision. Bérar & Lelann (1991) examined changes of e.s.d. values due to the influence of local or serial correlation, i.e. systematic differences between fit and oberved intensities with the differences having the same sign for adjacent data points. This might be, for example, due to inappropriate profile parameters or profile functions. Spagna & Camalli (1999) compared eighteen weighting schemes for structure refinement, suggesting that the *accepted model could be one which gives the 'best' estimates of the standard uncertainties rather than the lowest R-value.*

In recent years, the determination of texture (Von Dreele, 1997) and strain (Daymond et al., 1997, Balzar et al., 1998) became possible with the Rietveld method. Supported by publications like *Rietveld refinement guidelines* by McCusker et al. (1999) or the 'Rietveld book' (Young, 1993), the application of the Rietveld method has become common practice in many fields dealing with crystal structure determination. Refinement of a protein crystal structure containing as much as 1261 atoms by application of stereochemical restraints marks currently the upper limit for the complexity of refinable structures (Von Dreele, 1999).

Table 1.1 classifies several analysis methods for powder patterns. In **BETMAn**, the whole pattern is fitted to a function depending on structural parameters. Although a refinement of the actual structure, i.e. atomic positions, is not possible with **BETMAn**, it is classified as a Rietveld method after a definition of Young & Prince (1982) of the Rietveld method:

	Individual profile-fitting	Pawley	Rietveld
Aim of analysis	Pattern decomposition	Pattern decomposition and refinement of unit cell parameters	Structure refinement
Range of analysis	Partial patterns	*Whole pattern*	*Whole pattern*
Profile model:			
- Profile area	Independent parameters	Independent parameters	*Function of structural parameters*
- Peak position	Independent parameters	*Function of unit-cell parameters*	*Function of unit-cell parameters*
- Profile shape	Independent of angle in small 2ϑ range	*Angle-dependent*	*Angle-dependent*
A priori knowledge required to start the refinement	Null	Approximate unit-cell parameters	*Initial cell and structural parameters*

Table 1.1: Comparision of powder pattern analysis methods after Toraya (1993). For a description of the Pawley method, see Pawley (1981). The properties set in italics are applicable to **BETMAn**.

Whole-pattern-fitting of calculated to observed powder patterns through least-squares refinement of model(s) for the structure(s), diffraction optic effects, and instrumental factors. A key feature is the feedback, during refinement, between improving allocation of observed intensity to individual Bragg reflections.

1.8 A Brief History of Bragg-Edge Transmission

The neutron was predicted in 1920 by Rutherford and experimentally detected twelve years later by Chadwick at Cambridge. Elsasser prognosticated the wave properties of the neutron in 1936 which where experimentally proven in the same year by Halban and Preiswerk as well as by Mitchell and Powers (Bacon, 1975, sect. 1.1). Neutrons were accessible for investigations of nuclear properties of solids for the first time during the Manhattan Project for the development of the atomic bomb. Studied were for example nuclear cross-sections of the elements. For instance, Fermi et al. (1947) used neutron transmission to answer the question whether the scattering lengths of beryllium and oxygen have the same or opposite signs by comparing measured with calculated Bragg-edge transmission patterns based on structure factors for both cases. Winsberg et al. (1949) determined the scattering lengths of calcium, titanium and thallium also by measuring Bragg-edge transmission patterns. Both times the reactor source at Chicago was used and hence a time-consuming wavelength analysis using monochromator crystals was necessary. One of the first applications of Bragg-edge transmission for

engineering science was performed by Weiss et al. (1952) who studied the effect of cold rolling on brass at the Brookhaven reactor. The theoretical foundation for neutron transmission experiments was laid by the derivations of the total neutron scattering cross-section by Weinstock (1944) and Cassels (1950)[12]. In neutron filters, the transmitted intensity at wavelengths higher than twice the d-spacing of the lowest indexed Bragg-edge of a substance is utilized (e.g. Dobrzynski & Blinowski, 1994, sect. 2.5.2). From the same wavelength region, information on crystal defects can be derived (Mitchell & Stewart, 1967).

Parallel to the development of reactor technology for nuclear power plants, since the 1950s dedicated instruments for studying solids with neutrons were built. Since the 1970th, spallation sources became available (Carpenter et al., 1975), providing the ideal tool for fast Bragg-edge transmission measurements as no time consuming wavelength analysis is necessary. Johnson & Bowman (1982) proposed to measure lattice spacings with a very high resolution using Bragg-edges. In 1986, Windsor et al. (1986) prepared a draft titled '*Neutron Transmission Measurements on Bragg Edges and their Application to the Determination of Internal Strains*', where they described strain measurements in steel, but it was not published. It took until the 1990s before Bowman et al. (1991), Meggers (1994a, 1994b) at LANSCE and Wang & Edwards (1997) at ISIS utilized the Bragg-edge transmission technique to study the potential of single pulse measurements, kinetics of the decomposition of austenite to bainite and strain in steel plates, respectively. In 1990, following encouraging results from single pulse measurements (Priesmeyer et al., 1989, cf. figure 2.1), flightpath 5 at LANSCE was extended from 11 m to 60 m for improved resolution. Priesmeyer (1992b) reported also application of the Bragg-edge transmission technique at a reactor source. Since 1995, the technique was further developed both at LANSCE and ISIS and in 1998 a collaboration between both groups was established. While the application of the Bragg-edge transmission technique at ISIS focuses on strain measurements (the measurement of d_0 among others), at Los Alamos the main emphasis is on investigations of kinetics of structural phase transitions. Application of Bragg-edge transmission for structural studies at other places than ISIS and LANSCE are to the best of the author's knowledge not known.

[12] According to Placzek (1952), footnote 9, the statements in these works on the cross-sections at high energies are erroneous because of inconsistent approximations.

Chapter 2

Motivation

In the following sections the advantages of the Bragg-edge transmission technique are summarized and the decision to develop a new Rietveld refinement package is explained.

2.1 Short Integration-Times

Assuming an incident intensity of $2 \cdot 10^6$ neutrons per second and per cm^2 on a sample having an illuminated area of 1 cm^2 and a transmission $T = I/I_0 = 0.5$, the total number of neutrons at a transmission-detector is $1 \cdot 10^6$ per second. A typical number of channels for a diffraction or Bragg-edge transmission pattern is 10^4, thus, in average, 10^2 neutrons are counted per second into a single bin. Under these conditions, a statistical error of 1%, meaning a total number of

$$\frac{\sqrt{N}}{N} = 10^{-2} \Leftrightarrow N = 10^4 \tag{2.1}$$

neutrons, will be reached within a hundred seconds. Compared to conventional diffraction, this is a relatively short integration time. This estimation is empirically validated for example by the experience that the transmission pattern of an arbitrary sample system converges in a virtually smooth curve after approximately 5 minutes when an appropriate detector system is used.

Short intgegration times make it possible to use the Bragg-edge transmission technique for the observation of transient phenomena like irreversible structural phase transitions in solids[1] and make it comparable with other neutron[2] diffraction techniques of good time-resolution (Iizumi, 1986). So far, the shortest integration time used for studies of kinetics of structural phase transition with Bragg-edge transmission is 15 seconds. This is comparable or even better than time resolutions of 0.5 to 10 minutes achieved with instruments HRPD and POLARIS at ISIS (Wilson & Smith, 1997). The potential of the Bragg-edge transmission technique was shown by Bowman et al. (1991) who determined the (211) reflection position of steel from a single neutron pulse to an accuracy of $5 \cdot 10^{-3}$. Figure 2.1 shows such

[1] For reversible phase transitions, much better time resolutions with neutrons are achieved by repeating the transition many times, see for example Steigenberger et al. (1994), Eckold et al. (1997) who report time resolved studies on a millisecond time scale of a ferroelectric phase transition. Daymond & Withers (1996, 1997) achieved time scales in the order of 100 seconds by stroboscopic neutron diffraction with a sample under a cyclic load.

[2] With synchrotron radiation, due to the much higher available intensities, better time resolutions are possible. For example, Pennartz et al. (1992) report a study at HASYLAB of the kinetics of polymorphic phase transitions in sodium sulfate (Na_2SO_4) with a timescale of one second where a 2ϑ-range of 20° was used.

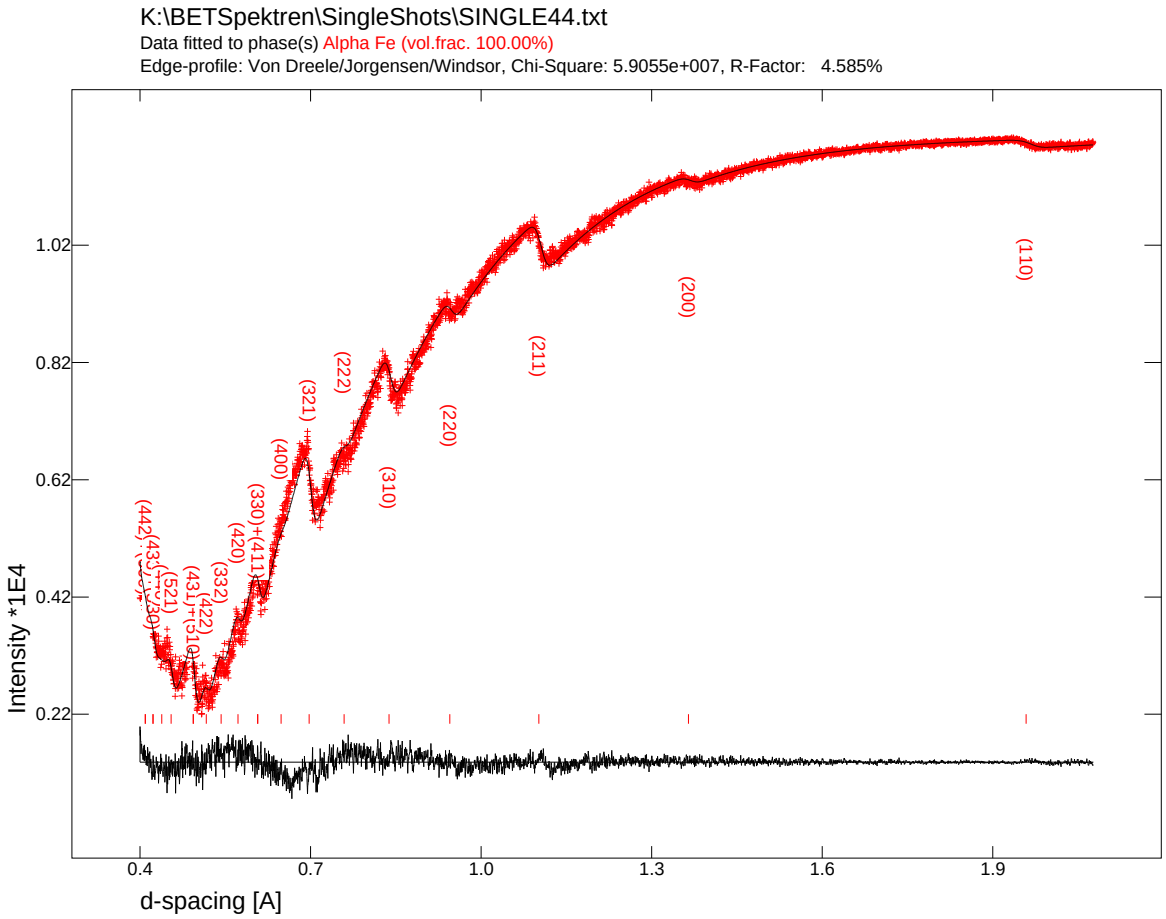

Figure 2.1: Bragg-edge transmission pattern of iron obtained from a single neutron pulse, i.e. within 50 ms (Priesmeyer et al., 1994). The 10 cm diameter ^{6}Li-glass detector was run in current mode. Due to the current-mode, neutron intensity is 'negative'. The line through the measured data (crosses) is the **BETMAn** fit, the tick marks indicate the calculated reflection positions, the reflections are labeled with their Miller indices. The curve at the bottom is the difference curve.

a single pulse pattern with the fit resulting from the **BETMAn** data analysis. The flightpath length was about 10.15 m (resulting from the fit). For full pattern analysis, single pulses are apparantly the ultimate time resolution, but in principle, if for example a lattice widening is probed by single reflections, the time resolution might be even lower than given by the repetition rate of the source. It is advantageous that the time resolution and contrast (i.e. edge heights) of a Bragg-edge transmission experiment can be optimized by increasing the illuminated area or the sample layer thickness in beam direction, respectively, without changing the d-spacing resolution (see next section). This is not possible in a diffraction experiment.

Structural details determined in 'real-time' reported in Young (1993), p. 19, used integration times of 3 minutes to collect a full-powder diffraction pattern on a conventional neutron diffractometer (D1B at ILL). The same source quoted on the refinement of 321 neutron powder diffraction patterns:

This example may be giving us a view into future problems with handling, storing, and doing refinements with great masses of different powder diffraction data sets. It is also giving us a view into a new world of relevant structural detail followed on a sufficiently small time or temperature (or both) grid to give us a totally new quality of insight into the dynamic changes in structural details which,

though small, have large effects on important material properties.

This statement is motivation to improve both the Bragg-edge transmission technique and the analysis of the resulting patterns using a Rietveld code. It stresses also the need of administrative tools to handle large numbers of datasets.

2.2 High Resolution

The error of the d-spacing is derived from Bragg's law (e.g. Buras & Holas, 1968)

$$d = \frac{\lambda}{2\sin\vartheta} \Rightarrow \frac{\Delta d}{d} = \left|\frac{\Delta\lambda}{\lambda}\right| + |\arctan\vartheta\Delta\vartheta| \tag{2.2}$$

Due to the knowledge of the precise edge-location at $\vartheta = 90°$ and therefore $\Delta\vartheta = 0$, the error of the d-spacing is given by

$$\frac{\Delta d}{d} = \left|\frac{\Delta\lambda}{\lambda}\right| \tag{2.3}$$

which is in principle smaller than any error achievable with conventional diffraction geometries as the other contributions in a transmission experiment are of the same order as in a diffraction setup. Windsor characterized the Bragg-edge transmission technique as follows (Windsor, 1981, p. 398):

The jumps are intrinsically very sharp, being determined only by the crystallite size and strain broadenings inherent in any Bragg peak width. The total cross-section measurement therefore gives a very quick and precise measurement of the d-spacings.

The resolution does not depend on the probed sample thickness, therefore the sample dimension can be optimized for optimal contrast. In diffraction, this is possible only at the cost of resolution.

2.3 Spatially Resolved Measurements

With appropriate collimation and detectors, it is possible to divide the incident neutron beam, which typically covers an area of several square centimeters, into several narrow beams and measure their transmission patterns. This allows to study, for example, strains in an engineering sample simultaneously at different locations and determine strain fields, which is hardly possible in diffraction geometry with a single measurement.

2.4 Relation to Sample Geometry

In a transmission measurement, always the ratio $T = I/I_0$ between incident and transmitted intensity is the result of the experiment. As this quantity does not depend on the integration time or any other numerical scaling, it corresponds directly to the number of scattering centers in the beam and thus the sample thickness in beam direction. With an accurate description of the underlying cross-sections, this allows to measure the sample thickness. A possible application could be tomography: The total thickness of certain phases can be retrieved by Rietveld analysis, while by rotation and shifting of the sample in the beam different paths through the sample can be measured. By means of the mathematics of tomography, from these different paths and the attenuation of the beam by different phases, the

spatial distribution of the phases can be re-constructed (Natterer, 1986). Combination with spatially resolved measurements described above allows to measure many paths simultaneously.

2.5 Temperature Measurement by Nuclear Resonances

Some isotopes show strong resonances in the transmission spectrum (see also section 5.3.1 and figure 5.3) when neutrons of certain energies are captured from the beam in the formation of excited states of the capturing nucleus according to

$$n + A \rightarrow (A + 1)^* \tag{2.4}$$

The capturing results in dips of the transmitted intensity, having a natural width of the order of 100 meV. Due to thermal motion of the nuclei, such resonances are Doppler-broadened, allowing to derive the sample temperature from the resonance lineshape (NRS = nuclear resonance spectroscopy). Resonances in the epithermal energy range between 1 and 100 eV are typically used for this purpose. As the cross-sections for these reactions are typically very high, very thin layers or low concentrations of these isotopes are sufficient to measure the resonances with negligible coherent scattering, i.e. without additional Bragg-edges from the resonant material (so-called resonant doping method). Hence, combination of Bragg-edge transmission and NRS allows to derive the average bulk sample temperature simultaneously with structural information from the same transmission patterns rather than measuring with thermocouples a temperature representing only the small volume around the thermocouple. The reported accuracy for such measurements range from 30 degree for an exploding sample or a sample subject to shockwaves measured during a single neutron pulse (Yuan et al., 1997) to one degree from static measurements (Mayers et al., 1989). The resonances do not appear in diffraction patterns and are therefore unique for the Bragg-edge transmission technique. It is also possible to derive phonon spectral parameters from these resonances (e.g. Lynn et al., 1998, Lynn, 1999), providing potential for further unique experiments in combination with the Bragg-edge transmission technique.

2.6 Simple Setup

For a transmission setup, only a single straight beam path from moderator to detector is necessary. Consequently, for example for sample heating, conventional tube furnaces may be used rather than designing and building special heating devices. Contrary to a diffraction setup, no precise alignment of the sample is required as long as the sample is not heavily tilted (resulting in a varying sample thickness) and fully covered by the beam. Detector setup is very simple compared to the alignment and calibration procedure of a diffraction experiment. Due to the low absoption of neutrons in materials like aluminum, for instance furnace endcaps allowing a controlled atmosphere in a tube furnace at high temperatures are easily made. Compared to the efforts necessary for example to provide such sample conditions at a synchrotron source, the Bragg-edge transmission technique is very cost effective. Especially for investigations of phase transition kinetics, the relatively large sample volumes required for Bragg-edge transmission are advantageous as surface effects can be neglected and many grains are probed.

2.7 Why yet another Rietveld Code?

As there are lots of fine working and well established Rietveld programs (see for example Young, (1993), section 1.6), it might be worth asking whether it is possible to use one of the existing packages for refinement of Bragg-edge transmission spectra. The model for conventional diffraction geometry (X-ray/synchrotron and both constant wavelength (CW) and time-of-flight (TOF) neutrons), is for a point S_i after Prince (1993, equation (3.7)) given by

$$M(S_i, \vec{x}) = b(S_i, \vec{x}_b) + \sum_{\vec{h},\varphi} I_{\vec{h},\varphi}(\vec{x}_s) h(S_i - S_{\vec{h},\varphi}, \vec{x}_p) \tag{2.5}$$

where b and h are functions for background and reflection profile, respectively, the latter depending on the difference between S_i and the calculated reflection position $S_{\vec{h},\varphi}$ and scaled with the reflection intensity $I_{\vec{h},\varphi}$. The reflections are summed over all reflections $\vec{h}$ of all phases φ contributing to the pattern. The functions depend on a parameter vector $\vec{x}$ consisting of background, structure and profile parameters $\vec{x}_b$, $\vec{x}_s$ and $\vec{x}_p$.

In the case of the transmission geometry, the (simplified) model becomes

$$M(S_i, \vec{x}) = I_0(S_i, \vec{x}_{I_0}) \left(e^{\sum_{\varphi} N_\varphi \left(\sigma_{abs,\varphi}(S_i) + \sigma^{tot}_{inc,\varphi}(S_i) + \sigma^{inel}_{coh,\varphi}(S_i) + \sum_{\vec{h}} I_{\vec{h},\varphi}(\vec{x}_s) k(S_i - S_{\vec{h},\varphi}, \vec{x}_p) \right)} + b(S_i, \vec{x}_b) \right) \tag{2.6}$$

where the additional terms and parameters are a function I_0 depending on a parameter vector $\vec{x}_{I_0}$ and describing the incident intensity, the number of scattering centers N_φ of a phase φ and the cross-sections for absorption $\sigma_{abs,\varphi}$, incoherent scattering $\sigma^{tot}_{inc,\varphi}$ and inelastic coherent scattering $\sigma^{inel}_{coh,\varphi}$ of each scattering center of a phase φ. k is a function varying between 1 and 0, describing the drop of the coherent scattering cross-section at the reflection position. It is obvious, that both models have fundamental differences additionally to the different functions to be used for the reflection profiles. Attempts to generate patterns similar to diffraction patterns by calculating the derivative with respect to wavelength of transmission patterns failed (Vogel, 1996). These fundamental differences would have made the efforts for changing an existing code, the Los Alamos code GSAS by Larson & Von Dreele (1994) in this particular case, nearly as high as writing a completely new code. Taking into consideration the need to analyze and administrate large volumina of data, for which most available Rietveld packages were not designed, it was chosen to do the latter.

Chapter 3

Neutron Transmission

In this chapter the model used to describe and fit a measured Bragg-edge transmission pattern is introduced.

3.1 Transmitted Intensity

The wavelength-dependent intensity detected by a detector system positioned in transmission geometry with a sample system consisting of phases φ in the beam is given by

$$I(t) = A\left(I_0(t)\left(b(t) + (1-p)\, e^{-\sum_{\varphi} N_\varphi \sigma_{tot,\varphi}(\lambda(t))} + p\right) + b_{dec}(t) + OFF\right) \tag{3.1}$$

where A is an overall scale factor, $I_0(t)$ describes the incident intensity, $b(t)$ is a background function, p is the fraction of neutrons passing the sample rather than going through the sample, OFF is an offset (see section 3.9.1), b_{dec} models a decaying background (see section 3.9.2), N_φ and $\sigma_{tot,\varphi}$ are the number of scattering centers per unit area and the total cross-section per scattering center of phase φ, respectively. In **BETMAn**, a scattering center is equivalent to a unit cell, hence the cross-sections are calculated per unit cell in the following sections. All parameters and functions are refinable or contain refinable parameters. A measured intensity needs to be corrected for deadtime before fitting these parameters, else deviations between fit and measured data which are largest in the region of highest intensity will occur. If a background is fitted, this deviation will be compensated by an non-realistic background.

3.2 Scattering Cross-Sections

The total[1] cross-section for the interaction of neutrons with matter is given by

$$\sigma_{tot}(\lambda) = \bar{\sigma}_{coh}\left(S^{el}_{coh}(\lambda) + S^{inel}_{coh}(\lambda)\right) + \bar{\sigma}_{inc}\left(S^{el}_{inc}(\lambda) + S^{inel}_{inc}(\lambda)\right) + \sigma_{abs}(\lambda) \tag{3.2}$$

where the contributions describe the elastic and inelastic coherent and incoherent scattering and the absorption of neutrons, respectively. For a Rietveld refinement, it is convenient to describe σ_{tot} per

[1] Magnetic scattering is currently not included.

unit cell which defines a scattering center. $\bar{\sigma}_{coh}$ and $\bar{\sigma}_{inc}$ are the average coherent and incoherent scattering cross-sections per nucleus for bound nuclei in the high energy limit (i.e. ignoring effects of the spatial arrangement of the nuclei described by the functions S) and are calculated from the scattering lengths b_n and the nuclear constants $\sigma_{inc,n}$ (given in tables of nuclear constants, e.g. NIST, 1999) of the participating nuclei. They are given by (e.g. Granada, 1984)

$$\bar{\sigma}_{coh} = 4\pi \langle b \rangle^2 = 4\pi \left(\sum_n c_n b_n \right)^2 \tag{3.3}$$

$$\begin{aligned} \bar{\sigma}_{inc} &= 4\pi \left(\left\langle b^2 \right\rangle - \langle b \rangle^2 \right) + \sum_n c_n \sigma_{inc,n} \\ &= 4\pi \left(\left(\sum_n c_n b_n^2 \right) - \left(\sum_n c_n b_n \right)^2 \right) + \sum_n c_n \sigma_{inc,n} \end{aligned} \tag{3.4}$$

The sums run over all atoms contributing to a unit cell. c_n is the concentration of the n-th atom in the unit cell and calculated by dividing the site occupation factor of the atom by the total number of occupied sites per cell. The first part of the incoherent scattering cross-section accounts for the incoherence introduced by mixing two atomic species, the third sum accounts for the contribution of the elements to the incoherence (spin and isotope incoherence). As all desired structural parameters are contained in the elastic coherent scattering cross-section S_{coh}^{el}, it is sufficient to approximate all other cross-sections. As the cross-sections are described by smooth, continuous functions, any deviations from these approximations will be compensated by the background and variable parameters of the cross-sections fitted simultaneously during the data analysis.

3.2.1 Elastic Coherent Scattering Cross-Section

The elastic coherent scattering cross-section for a neutron of energy E for the case of a simple primitive cell (a non-centered unit cell with a base consisting of one atom only) is given by Granada (1984) as

$$\bar{\sigma}_{coh} S_{coh}^{el}(E) = \underbrace{4\pi b^2}_{\bar{\sigma}_{coh}} \frac{\pi^2 \hbar^2}{2mEV_0} \sum_{\tau \neq 0}^{\tau < 2k} \frac{\omega(\tau)}{\tau} \exp\left(-\frac{3\hbar^2 \varphi_1(\Theta)}{2Mk_B\Theta_D} \tau^2 \right) \tag{3.5}$$

with m the neutron mass, h Planck's constant, V_0 the unit cell volume, $\omega(\tau)$ the multiplicity of the reciprocal lattice vector of modulus τ, $\varphi_1(\Theta)$ is given by

$$\varphi_1(\Theta) = \int_{-1}^{1} \frac{\varepsilon}{\exp(\varepsilon/\Theta) - 1} d\varepsilon \tag{3.6}$$

and evaluated for the argument $\Theta = \frac{T}{\Theta_D}$ (see appendix A for further information on the evaluation of this function), M the mass of the scattering nucleus and Θ_D the Debye temperature of the scattering element. Substituting the following equivalences

$$\tau = \frac{2\pi}{d}, \; E = \frac{p^2}{2m} = \frac{\hbar^2 k^2}{2m} = \frac{h^2}{2m\lambda^2} \tag{3.7}$$

and inserting the omitted contribution of the structure factor $F_{\vec{h}}$ (which is of course unity for a simple primitive cell)

$$F_{\vec{h}} = w\left(\vec{h}\right) \sum_n o_n b_n \exp\left(2\pi i \vec{h} \cdot \vec{x}_n\right) \exp\left(-\frac{3h^2 \varphi_1(\Theta_n)}{4M_n k_B \Theta_{D,n} d_{\vec{h}}^2} \right) \tag{3.8}$$

($\vec{x}_n$ is the position of the n-th atom within the unit cell in fractional coordinates, o_n site occupation factor of n-th atom) this description becomes for any type of structure (see also Windsor, 1981, equation (1.18), Lovesey, 1986, equation (2.42))

$$\bar{\sigma}_{coh} S^{el}_{coh}(\lambda) = \frac{\lambda^2}{2V_0} \sum_{d_{\vec{h}}=0}^{2d_{\vec{h}}<\lambda} \left|F_{\vec{h}}\right|^2 d_{\vec{h}} \tag{3.9}$$

The summation over all sets of lattice planes with a d-spacing smaller than $\lambda/2$ describes the discontinuities in σ^{el}_{coh} that result in the Bragg edges in the transmission pattern. The second exponential term in (3.8) takes into account that an atom in a crystal is never in rest but deviates from its average position due to thermal motion. As for the case of the average position $\vec{x}_n$ of an atom, the Born-Oppenheimer approximation applies for the case of the displacements (instantaneous electronic-nuclear coupling, Kuhs, 1992) and it is necessary to model the attenuation of the coherent elastic scattering by this factor. It is also known as the Debye-Waller factor[2] and a description more suitable for Rietveld refinement is given for the isotropic case by

$$\exp\left(-8\pi u^2 (\sin\vartheta/\lambda)^2\right) = \exp\left(-B_{iso}\Big/4d^2_{\vec{h}}\right) \tag{3.10}$$

(u is the root mean square displacement in all directions). Although many cases of vibrational anharmonicity and therefore anisotropic atomic displacement are known (e.g. experimental results by Cooper et al., 1968, Williams et al., 1988, or a review of the topic by Kuhs, 1992), **BETMAn** is currently restricted to the isotropic case which is a good approximation for metals and alloys. Consequently, there is one refinable factor $B_{iso,n}$ for each site in the asymmetric unit[3] of a structure and by equating (3.10) r.h.s. and the second exponential expression in (3.8), from

$$\frac{3h^2\varphi_1(\Theta)}{4Mk_B\Theta_D d^2_{\vec{h}}} = \frac{B_{iso}}{4d^2_{\vec{h}}} \tag{3.11}$$

the equivalence

$$B_{iso} = \frac{3h^2\varphi_1(\Theta)}{Mk_B\Theta_D} \tag{3.12}$$

is found. The structure factor depending on $B_{iso,n}$ (also known as isotropic atomic displacement factor, ADF) is then given by

$$F_{\vec{h}} = w\left(\vec{h}\right) \sum_n o_n b_n \exp\left(-\frac{B_{iso,n}}{4d^2_{\vec{h}}}\right) \exp\left(2\pi i \vec{h}\cdot\vec{x}_n\right) \tag{3.13}$$

3.2.2 Elastic Incoherent Scattering Cross-Section

The attenuation of the elastic coherent scattering cross-section due to neutrons that are scattered elastically incoherently because of the thermal motion of the nuclei is, according to Granada (1984),

[2] Castellano & Main (1985) pointed out that the correct derivation of the Debye-Waller factor is a space average over a large number of oscillators with a Boltzmann energy distribution rather than a time average over a single oscillator as given in some textbooks.

[3] According to Prince (1994, p. 152) the relation between space group and asymmetric unit is as follows: *In a symmetric space group each point in the unit cell is related by symmetry to a set of other points at which the scattering density is equal. Each such set is called an orbit, and an asymmetric unit is a region of the unit cell that contains exactly one member of each distinct orbit.* For example, in α (bcc) iron, the atom at $(1/2, 1/2, 1/2)$ is symmetry equivalent to the one at $(0, 0, 0)$, i.e. they belong to the same orbit and each of them is contained in one of the possible asymmetric units. Because of the symmetry equivalence, both must have the same properties, in the present case this means during refinement $B_{iso,n}$ must be the same for both atoms which is achieved by refining only the parameters of the atoms of one of the asymmetric units.

again for the case of a simple primitive unit cell, described by

$$S_{inc}^{el}(E) = \frac{1}{12}\left(\frac{M}{m}\right)\frac{k_B\Theta_D}{E\varphi_1(\Theta)}\left(1-\exp\left(-12\left(\frac{m}{M}\right)\frac{E\varphi_1(\Theta)}{k_B\Theta_D}\right)\right) \tag{3.14}$$

With the equivalences (3.7), this can be transformed to a wavelength dependent elastic incoherent scattering cross-section of a single nucleus:

$$S_{inc}^{el}(\lambda) = \frac{Mk_B\Theta_D\lambda^2}{6h^2\varphi_1(\Theta)}\left(1-\exp\left(-\frac{6h^2\varphi_1(\Theta)}{Mk_B\Theta_D\lambda^2}\right)\right) \tag{3.15}$$

Applying the definition of the isotropic displacement factor B_{iso} (3.12), this becomes

$$S_{inc}^{el}(\lambda) = \frac{\lambda^2}{2B_{iso}}\left(1-\exp\left(-\frac{2B_{iso}}{\lambda^2}\right)\right) \tag{3.16}$$

As σ_{inc}^{el} in a first order approximation does not depend on the spatial arrangement of the nuclei, i.e. it does not depend on the crystal structure, the contributions of each atom of an arbitrary unit cell simply are added to calculate the elastic incoherent scattering cross-section per unit cell:

$$\sigma_{inc}^{el}(\lambda) = \bar{\sigma}_{inc}\sum_n \frac{\lambda^2}{2B_{iso,n}}\left(1-\exp\left(-\frac{2B_{iso,n}}{\lambda^2}\right)\right) \tag{3.17}$$

3.2.3 Elastic Scattering in the Epithermal Range

As can be seen from (3.9) and (3.17), for $E \to \infty$ ($\lambda \to 0$) the cross-section for elastic scattering vanishes. In the epithermal energy region, the discontinuities in the elastic coherent scattering cross-section, forming the Bragg-edges in the transmission pattern, are getting weaker with decreasing wavelength. The infinite sum (3.9) therefore can be approximated by a continuous function. The two components derived above of the total elastic scattering cross-section may be written as

$$\begin{aligned}
\sigma_{tot}^{el}(\lambda) &= \sigma_{coh}^{el}(\lambda) + \sigma_{inc}^{el}(\lambda) \\
&= 4\pi\langle b\rangle^2 S_{coh}^{el}(\lambda) + 4\pi\left(\left\langle b^2\right\rangle - \langle b\rangle^2\right)S_{inc}^{el}(\lambda) \\
&= 4\pi\left\langle b^2\right\rangle S_{inc}^{el}(\lambda) + 4\pi\langle b\rangle^2\left(S_{coh}^{el}(\lambda) - S_{inc}^{el}(\lambda)\right) \\
&= 4\pi\left\langle b^2\right\rangle S_{inc}^{el}(\lambda) + 4\pi\langle b\rangle^2\,\delta S(\lambda)
\end{aligned} \tag{3.18}$$

Setting $\delta S(\lambda)$ to zero, the total elastic scattering cross-section is approximated by the elastic incoherent scattering cross-section as given in (3.17). Placzek et al. (1951) have shown that a much better description of $\delta S(\lambda)$ is given by

$$S_{coh}^{el}(\lambda) - S_{inc}^{el}(\lambda) = \delta S(\lambda) = -\frac{\lambda^2\rho^{2/3}}{8\pi}I \tag{3.19}$$

where ρ is the number of particles per unit volume and I a coefficient depending on the crystal lattice (Placzek et al., 1951, Placzek & Van Hove, 1955). Some values for I are given in table 3.1. Placzek et al. (1951) showed also that $I < 3$ must hold. According to Placzek & Van Hove (1955), the approximation is valid for $\lambda < 2\pi u$, where u is the root mean square nuclear displacement in any direction (cf. (3.10)). With u being of the order of 0.1 Å, the approximation is valid for wavelengths up to about 0.6 Å. Binder (1970) compared the calculated correct values with the approximation of the elastic coherent scattering cross-section for bismuth and aluminum and found very good agreement.

For steel, the correction factor evaluates for the minimum wavelength used for Bragg-edge transmission experiments at flightpath 5 at LANSCE ($\lambda = 0.5$ Å) to $\delta S = 5.55 \cdot 10^{-3}$. This is less than 1% of S_{inc}^{el} for this wavelength calculated with (3.16) ($B_{iso,n}$ calculated as $8\pi u^2$ with $u = 0.1$ Å). Taking into account that for the present purpose the experimental data always will be subject to noise, the approximation can be treated as sufficient. The quality of the approximation for structures consisting of more than one atomic species is currently unkown, but expected to be smooth and hence deviations should be correctable by a background function. For the simple systems studied so far, the precise expression for (3.9) was evaluated up to a variable minimum reflection d-spacing. For future applications, involving more complicated structures with much more weak reflections in the epithermal range, the approximation may save calculation time.

3.2.4 Total Inelastic Scattering Cross-Section

The inelastic scattering cross-sections describe probabilities for neutron interactions with the crystal lattice of the sample involving the creation and annihilation of phonons during which the neutron looses or gains energy[4]. As was the case for the total elastic scattering cross-section in the epithermal range, Placzek & van Hove (1955) showed that the inelastic coherent scattering cross-section is very good approximated by the inelastic incoherent scattering cross-section. Binder (1970) found that in this case the approximation is sufficient also for the range of the thermal neutrons. Hence, both inelastic contributions are described by

$$\sigma_{tot}^{inel}(\lambda) = \sigma_{coh}^{inel}(\lambda) + \sigma_{inc}^{inel}(\lambda) = (\bar{\sigma}_{coh} + \bar{\sigma}_{inc})\, S_{inc}^{inel}(\lambda) \tag{3.20}$$

Calculation of the inelastic incoherent scattering cross-section is complicated, but the total incoherent scattering cross-section can be evaluated and with the elastic incoherent scattering cross-section (3.16), the inelastic incoherent scattering cross-section can be evaluated from

$$S_{inc}^{inel}(\lambda) = S_{inc}^{tot}(\lambda) - S_{inc}^{el}(\lambda) \tag{3.21}$$

as the difference between the equation (3.22) following below and (3.16). The total incoherent scattering cross-section is given by (Placzek, 1954, Granada, 1984)

$$S_{inc}^{tot}(\lambda) = \sum_{n=0}^{\infty} \left(\frac{1}{A}\right)^n A_n(\lambda, \Theta) \tag{3.22}$$

[4] Same as the approximation for the elastic coherent scattering cross-section in the epithermal range, implementation of a model for inelastic scattering cross-sections into **BETMAn** is still under development. As all structural information is derived from the correctly implemented elastic coherent scattering cross-section and all other cross-sections are continuous functions, the influence of the incomplete model on fitted structural parameters is negligible. Deviations between model and measured data are compensated by a simultaneously fitted background.

Lattice	I
Cubic face-centered	2.888462
Hexag. close-packed	2.888377
Cubic body-centered	2.888282
Mercury type (rhomb.)	2.872771
Diamond	2.693400

Table 3.1: The coefficient I for various lattices-types (after Placzek et al., 1951, table 1).

where $A = M/m$,

$$A_n(\lambda,\Theta) = \frac{1}{4x^2}\cdot\frac{3^n}{n+1}\sum_{l=0}^{n} a_l^{(n)}; \qquad A_0(\lambda,\Theta) = 1 \tag{3.23}$$

and

$$a_l^{(n)} = \frac{(-\phi_1(\Theta))^{n-1}}{l!\,(n-l)!}\prod_{j=1}^{l}\int_{-1}^{1}\frac{\varepsilon_j}{e^{\varepsilon_j/\Theta}-1}\left\{(x+x')^{2n+2}-(x-x')^{2n+2}\right\}d\varepsilon_j \tag{3.24}$$

The definition of the dimensionless parameters x and x' is as follows:

$$x^2 = \frac{h^2}{2k_B\Theta_D m\lambda^2} = \frac{AB_{iso,n}}{6\phi_1(\Theta)\lambda^2}; \qquad x' = \begin{cases} \sqrt{x^2+\sum_{j=1}^{l}\varepsilon_j} & \text{if} \quad \sum_{j=1}^{l}\varepsilon_j > -x^2 \\ 0 & \text{otherwise} \end{cases} \tag{3.25}$$

Although Granada (1984) states that this so-called mass expansion converges rapidly, the numerical integration would slow down the refinement process very much and hence approximations for the thermal energy range are highly desired. Additionally, the quality of this description for other than monoatomic systems is unknown. According to Granada (1984), only for the epithermal and cold neutron range good approximations are known, but none for the region of interest in a Bragg-edge transmission experiment, the thermal neutrons. Cold neutrons, i.e. neutrons of wavelength above ≈5 Å, are currently not accessible in Bragg-edge transmission experiments at LANSCE or ISIS and shall be ignored for now. In the epithermal region, according to Granada (1984), a good approximation of the total incoherent scattering cross-section is for the case

$$x^2 \gg 1 \quad\Leftrightarrow\quad \lambda \ll \frac{h}{\sqrt{2mk_B\Theta_D}} \tag{3.26}$$

for a monoatomic structure given by

$$S_{inc}^{tot}(E) = \left(\frac{A}{A+1}\right)^2\left(1+\frac{3m^2\varphi_3(\Theta)k_B\Theta_D\lambda^2}{2Mh^2}\right) = \left(\frac{A}{A+1}\right)^2\left(1+\frac{9\varphi_3(\Theta)\varphi_1(\Theta)\lambda^2}{2A^2B_{iso}}\right) \tag{3.27}$$

where $\varphi_3(\Theta)$ is given by

$$\varphi_3(\theta) = \int_{-1}^{1}\frac{\varepsilon^3}{e^{e/\theta}-1}d\varepsilon \tag{3.28}$$

(see appendix A for further information on the evaluation of this function). The inelastic incoherent scattering cross-section is therefore described in the epithermal energy range by

$$\begin{aligned} S_{inc}^{inel}(\lambda) &= S_{inc}^{tot}(\lambda) - S_{inc}^{el}(\lambda) \\ &= \left(\frac{A}{A+1}\right)^2\left(1+\frac{9\varphi_3(\Theta)\varphi_1(\Theta)\lambda^2}{2A^2B_{iso}}\right) - \frac{\lambda^2}{2B_{iso}}\left(1-\exp\left(-\frac{2B_{iso}}{\lambda^2}\right)\right) \end{aligned} \tag{3.29}$$

The range of validity of the approximation as given by (3.26) is for example in the case of iron

$$\lambda \ll \frac{6.626\cdot10^{-34}Js}{\sqrt{2\cdot1.675\cdot10^{-27}kg\cdot1.381\cdot10^{-23}\frac{J}{K}\cdot456K}} = 1.446\text{Å} \tag{3.30}$$

and hence not valid for the thermal energy range. Lacking a better model, currently the inelastic scattering is described using this function. $B = \varphi_3(\Theta)\varphi_1(\Theta)$ is a refinable parameter for each contributing atom.

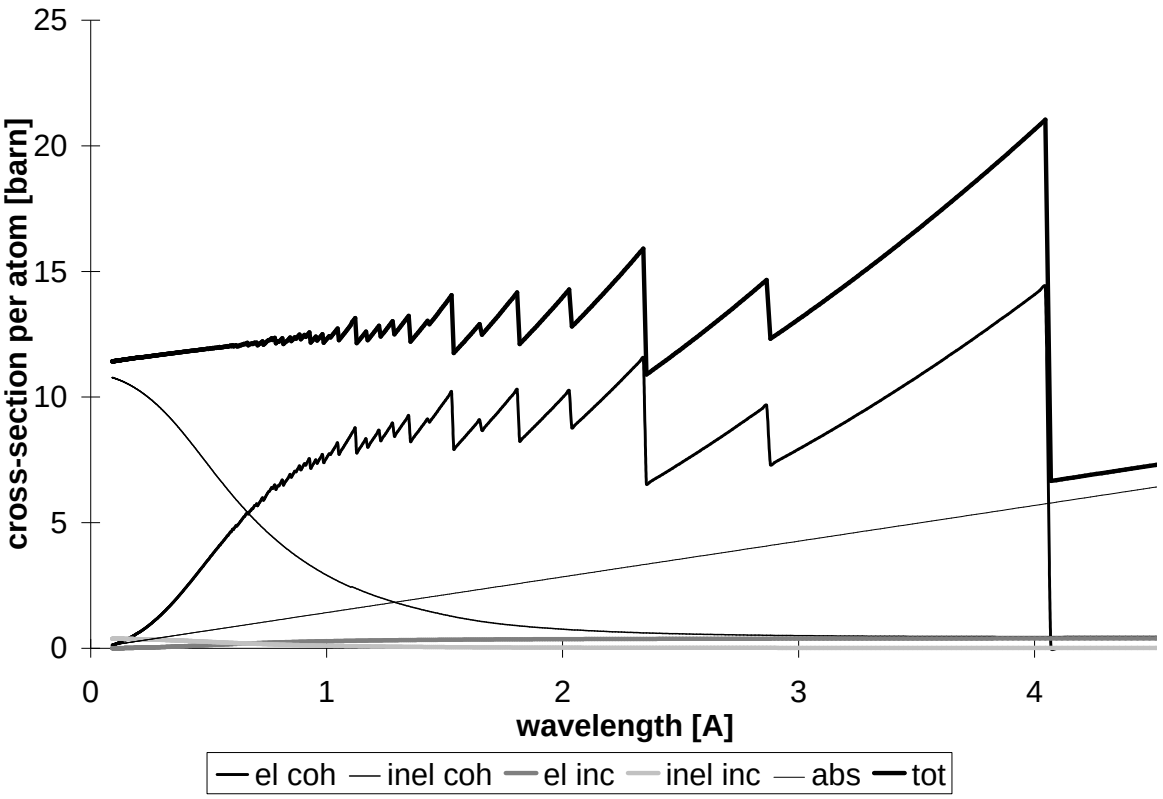

Figure 3.1: Cross-sections of α-iron per atom calculated with BETMAn.

3.2.5 Total Scattering Cross-Section

With this, expressions for all scattering cross-sections are available and the approximate total scattering cross-section of an arbitrary sample system in the range of thermal energies is given by

$$\begin{aligned}\sigma_{tot}(\lambda) &= \underbrace{\frac{\lambda^2}{2V_0}\sum_{d_{\vec{h}}=0}^{2d_{\vec{h}}<\lambda}\left|F_{\vec{h}}\right|^2 d_{\vec{h}}}_{\sigma_{coh}^{el}} + \underbrace{\bar{\sigma}_{inc}\sum_n o_n \frac{\lambda^2}{2B_{iso,n}}\left(1-\mathrm{e}^{-\frac{2B_{iso,n}}{\lambda^2}}\right)}_{\sigma_{inc}^{el}} \\ &\quad \underbrace{+(\bar{\sigma}_{coh}+\bar{\sigma}_{inc})\left(\sum_n o_n\left\{\underbrace{\left(\frac{A}{A+1}\right)^2\left(1+\frac{9B_n\lambda^2}{2A^2B_{iso,n}}\right)}_{S_{inc}^{tot}(\lambda)} - \underbrace{\frac{\lambda^2}{2B_{iso,n}}\left(1-\exp\left(-\frac{2B_{iso,n}}{\lambda^2}\right)\right)}_{S_{inc}^{el}(\lambda)}\right\}\right)}_{\sigma_{tot}^{inel}}\end{aligned} \tag{3.31}$$

where n runs again over all nuclei contributing to a unit cell.

The correct descriptions of the cross-sections of monoatomic crystals for epithermal to cold neutrons are incorporated in the CRIPO code of Kropff & Granada (1977). This code was used to validate the **BETMAn** results. Rather than combining the functions describing the vibrational properties of the atoms with refinable factors, as done for the approximations in **BETMAn**, the appropriate functions are evaluated in CRIPO for the given material with the corresponding Debye temperature Θ_D. For pure elements, this provides the precise cross-sections. This approach was not possible in **BET-**

MAn, as the assumptions for the models used to describe the vibrational properties are valid only for pure elements. Refining those parameters allows to account for changes of the vibrational properties in compounds. Generally, the appropriate description of the cross-section of compounds is problematic as simplifications, like the Debye model as used in the approximation above, may lead to larger deviations than in the case of mono-atomic structures. Even the Debye-temperature of pure elements is reported by Binder (1970) for instance in the case of aluminum as $\Theta_D = 358$, 372 or 418 K, depending on the method employed in deriving at it.

In figure 3.1, the cross-sections for α-iron as calculated with **BETMAn** are presented. The refinable parameters $B_{iso,n}$ and B_n used for the **BETMAn** calculation are derived from the Debye temperature of iron (which is stored together with the atomic mass and nuclear constants for each element in **BETMAn**'s database). Those values are also used as starting values for the refinement. As the cross-section of a pure element is shown, the CRIPO and **BETMAn** results are identical. Nevertheless, an approximation of the total incoherent scattering cross-section for the thermal energy range and, generally, approximations for all cross-sections except the elastic coherent valid for arbitrary systems and their experimental verification have not been found in literature yet and are missing in the model function.

3.3 Edge-Profile Functions

In (3.9), the contribution of a single set of lattice planes to the coherent elastic scattering cross-section drops to zero as a step function at $\lambda = 2d_{\vec{h}}$. Hence, the contribution of a single set of lattice planes to (3.9) can be written as

$$\sigma_{\vec{h}}(\lambda) = \frac{\lambda^2 \left|F_{\vec{h}}\right|^2 d_{\vec{h}}}{2V_0} \left(1 - \Theta \underbrace{\left(\lambda - 2d_{\vec{h}}\right)}_{\Delta}\right) \tag{3.32}$$

where $\Theta(x)$ is Heaviside's step-function, modeling the drop of the coherent elastic scattering cross-section. The elastic coherent cross-section is now an infinite sum over all reflections $\vec{h}$ without any condition in the upper limit of the summation. In order to describe a measurement, the step function needs to be convoluted with a profile $h(\Delta)$, describing the distribution of neutrons of a given wavelength depending on time-of-flight or wavelength. This profile is the same profile used to describe a peak in a diffraction measurement. Therefore, the edge profile is given by

$$k(\Delta) = h(\Delta) * (1 - \Theta(\Delta)) = \int_{-\infty}^{\infty} h(x)\,(1 - \Theta(\Delta - x))\,dx \tag{3.33}$$

Since peak profile functions suitable for a Rietveld fit must be normalized, i.e.

$$\int_{-\infty}^{\infty} h(x)\,dx = 1 \tag{3.34}$$

must hold, this becomes

$$k(\Delta) = 1 - \int_{-\infty}^{\Delta} h(x)\,dx \tag{3.35}$$

Thus, the requirement of a diffraction profile function to have a total area of 1 becomes the requirement for an edge profile function to vary between 1 and zero for Δ varying between $-\infty$ and ∞. Any

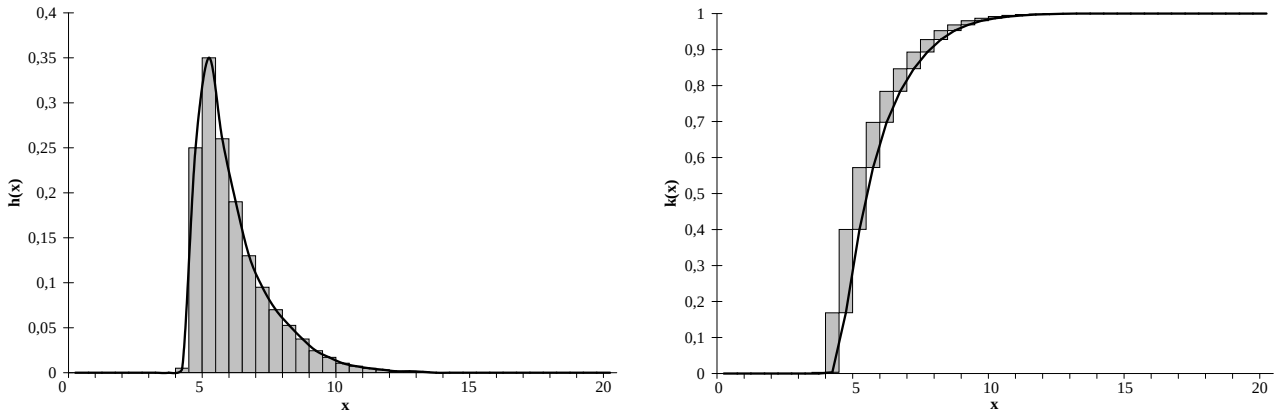

Figure 3.2: Relation between diffraction peak profile (left) and transmission edge profile (right). An edge profile can be derived from a peak profile by integration. In both cases, the profiles after Jorgensen et al. (1978) were calculated for a reflection position at $x = 5$.

diffraction peak profile function used for refinement of diffraction data may be used for refining transmission data of the same instrument (the peak profile function is governed by the source/moderator behaviour) by applying it to (3.35). Figure 3.2 shows the relationship between diffraction peak and corresponding transmission edge for the case of a diffraction profile proposed by Jorgensen et al. (1978) (displayed is the equivalent intensity profile $1 - k(\Delta)$). Applying equation (3.35) to diffraction peak profiles, three Bragg-edge profiles with increasing amount of detail will be derived in the next sections. All three models are implemented in **BETMAn**. To test the models presented here, they are fitted to the (321) reflection of α-iron and the agreement with the data is compared. The raw data used for all models were taken using a cylindrical steel sample of 20 mm thickness in beam direction and 50 mm in diameter. The total flightpath length at LANSCE was about 58.15 meters. Flightpath length L and time offset t_0 depend slightly on the profile used[5] and hence need to be calibrated for each profile. The neutron intensity was sufficiently high to run the detectors in current mode instead of counting mode, thus, the intensity is a digitized voltage rather than a count rate (see Bowman et al., 1990, for a description of this technique and the general setup used). The fit was limited to the part of the whole pattern displayed in figures 3.3 to 3.5, but the full model was used. Fitted were five parameters for the incident intensity (see section 3.8) plus the flightpath length (section 3.7), and the number of scattering centers per unit area of the α-iron. Additional profile parameters were fitted depending on the profile type.

3.3.1 Heaviside's Step-Function

The simplest way to describe a reflection in a diffraction measurement is a δ-function, scaled to an appropriate height. The only degree of freedom is the reflection position. Application of equation (3.35) results in a Bragg-edge described by a step function:

$$k(\Delta) = 1 - \int_{-\infty}^{\Delta} \delta(x)\, dx = 1 - \Theta(\Delta) \tag{3.36}$$

The resulting fit is shown in figure 3.3 and yields strong deviations between data and fit around the

[5] In this context, L and t_0 are calibration constants of the instrument, their physical values are of course independent of the profile used for the analysis.

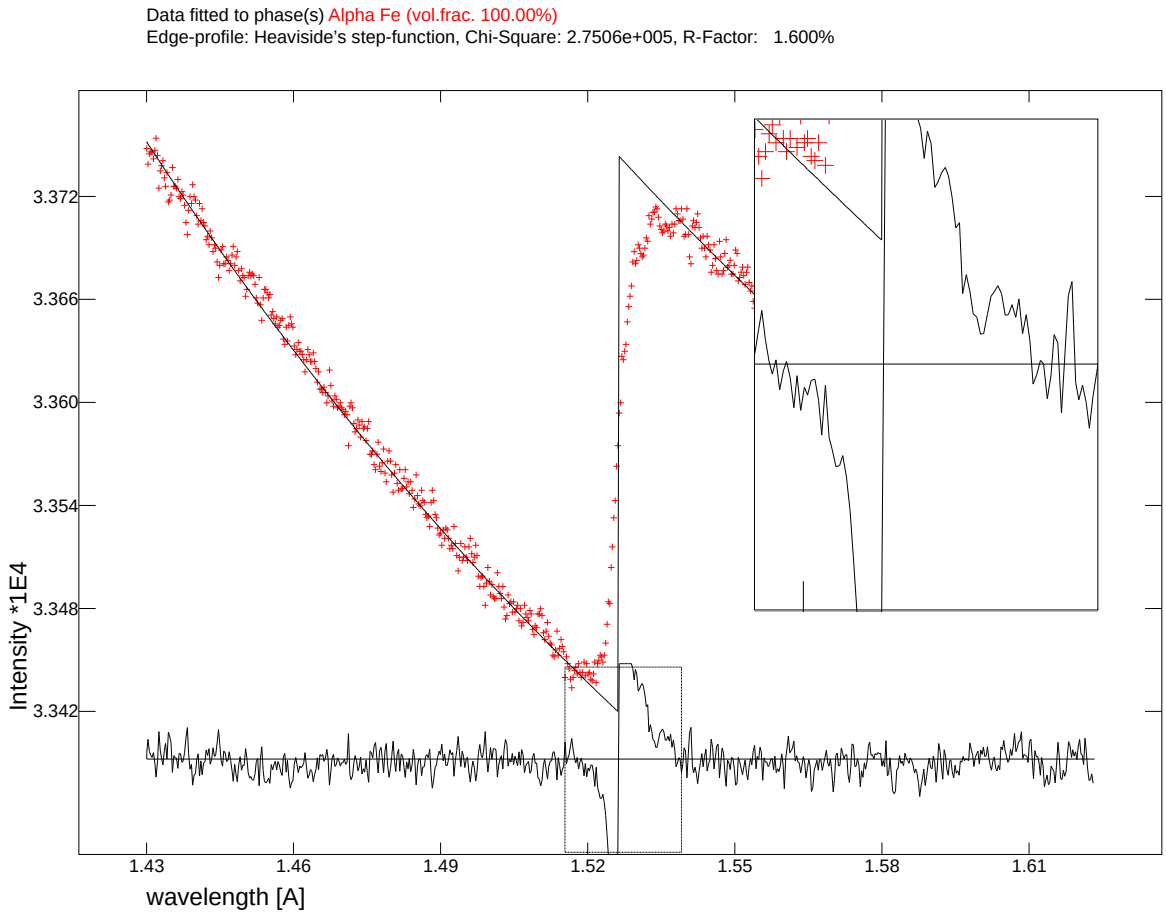

Figure 3.3: Iron (321)-reflection fitted with Heavisides step function. The merit function of the fit is given by $\chi^2 = \sum_i \left(\left(y_{i,obs} - y_{i,calc} \right) / \sigma_i \right)^2$ (sum over all datapoints of the difference between observed and calculated values weighted by the e.s.d. of the corresponding observed value) and evaluates in the present case to $\chi^2 = 27.5 \cdot 10^4$. The inset shows the marked region of the difference curve.

reflection position. Clearly, the asymmetry of the measured edge-profile is visible in the difference curve. Despite its simplicity, this crude approximation is useful for determination of phase fractions from transmission measurements: As can be seen from (3.9), in transmission data the reflection intensity, and therefore the structure factor, is 'visible' not only at the reflection position itself, i.e. at the edge position, but also at wavelengths smaller than the edge-wavelength. Therefore, for the derivation of the number of scattering centers and thus the volume fraction of a phase, the particular model chosen for the reflection is not that crucial as for diffraction data. In other words, in transmission data also the areas between the reflections contain valuable information as they provide information about the jump at the edge position itself. In contrast, considering diffraction data, the area between reflections is basically determined by background and therefore more or less worthless for determination of structure or volume fractions. It should be mentioned here that this point is a principle difference between transmission and diffraction data, preventing an 'easy' modification of existing Rietveld codes for the analysis of transmission data.

Basically, the approach of a simple step in the transmitted intensity at the edge position was used in previous works by Meggers et al. (1994a, 1994b), Stalder et al. (2000) on the application of the Bragg-edge transmission technique to study the kinetics of structural phase transitions in steels: Two

lines were fitted to a small region before and after the edge, from the difference of those lines at the reflection position the volume fractions were derived. Nevertheless, for applications involving precise determination of the lattice parameters, an accurate description of the edge profile is of paramount interest.

3.3.2 Complementary Error-Function

The most general model for a reflection obtained in diffraction geometry is the description by a Gaussian, which increases the number of degrees of freedom compared to the δ-function by one by providing a peak-width σ:

$$h(\Delta, \sigma) = \frac{1}{\sqrt{2\pi}\sigma} e^{-\frac{\Delta^2}{2\sigma^2}} \tag{3.37}$$

From equation (3.35) follows by substitution

$$k(\Delta, \sigma) = 1 - \frac{1}{\sqrt{\pi}} \int_{-\infty}^{\frac{\Delta}{\sqrt{2}\sigma}} e^{-x^2} dx \tag{3.38}$$

Splitting the integral and application of the definition of the complementary error function[6] yields

$$k(\Delta, \sigma) = \frac{1}{2} \mathrm{erfc}\left(\frac{\Delta}{\sqrt{2}\sigma}\right) \tag{3.39}$$

Thus, the peak description by a Gaussian corresponds to an edge description by the complementary error function. As for diffraction data, the data is described well by this model and the residual is reduced significantly compared to the first model (figure 3.4). As the resolution function of a spallation source is not symmetric, some misfits appear at the tail of the edge. Again, for the determination of volume fractions of phases, this is not too crucial. The choice of this symmetric profile results in an edge-intensity dependent shift of the edge position as the misfit increases with the edge-height and the residual is minimized by shifting the edge-position. For a reliable determination of the edge-position, for example to be able to study strain, this effect must be minimized by a more sophisticated edge-model.

3.3.3 Jorgensen et al. Profile Function

A successful model for diffraction peak profiles at spallation neutron sources is a function proposed by Jorgensen et al. (Jorgensen et al. (1978), Carpenter et al. (1975))

$$h(\Delta, \sigma, \alpha, \beta) = \frac{\alpha\beta}{2(\alpha + \beta)} \left(\exp(u)\,\mathrm{erfc}(y) + \exp(v)\,\mathrm{erfc}(z)\right) \tag{3.40}$$

[6] The error function erf and the complementary error function erfc are defined as (e.g. Press et al., 1992, p. 220)

$$\mathrm{erf}(x) = \frac{2}{\sqrt{\pi}} \int_0^x e^{-t^2} dt \qquad \mathrm{erfc}(x) = 1 - \mathrm{erf}(x) = \frac{2}{\sqrt{\pi}} \int_x^\infty e^{-t^2} dt$$

The functions have the following properties

$$\begin{array}{lll} \mathrm{erf}(0) = 0 & \mathrm{erf}(\infty) = 1 & \mathrm{erf}(-x) = -\mathrm{erf}(x) \\ \mathrm{erfc}(0) = 1 & \mathrm{erfc}(\infty) = 0 & \mathrm{erfc}(-x) = 2 - \mathrm{erfc}(x) \end{array}$$

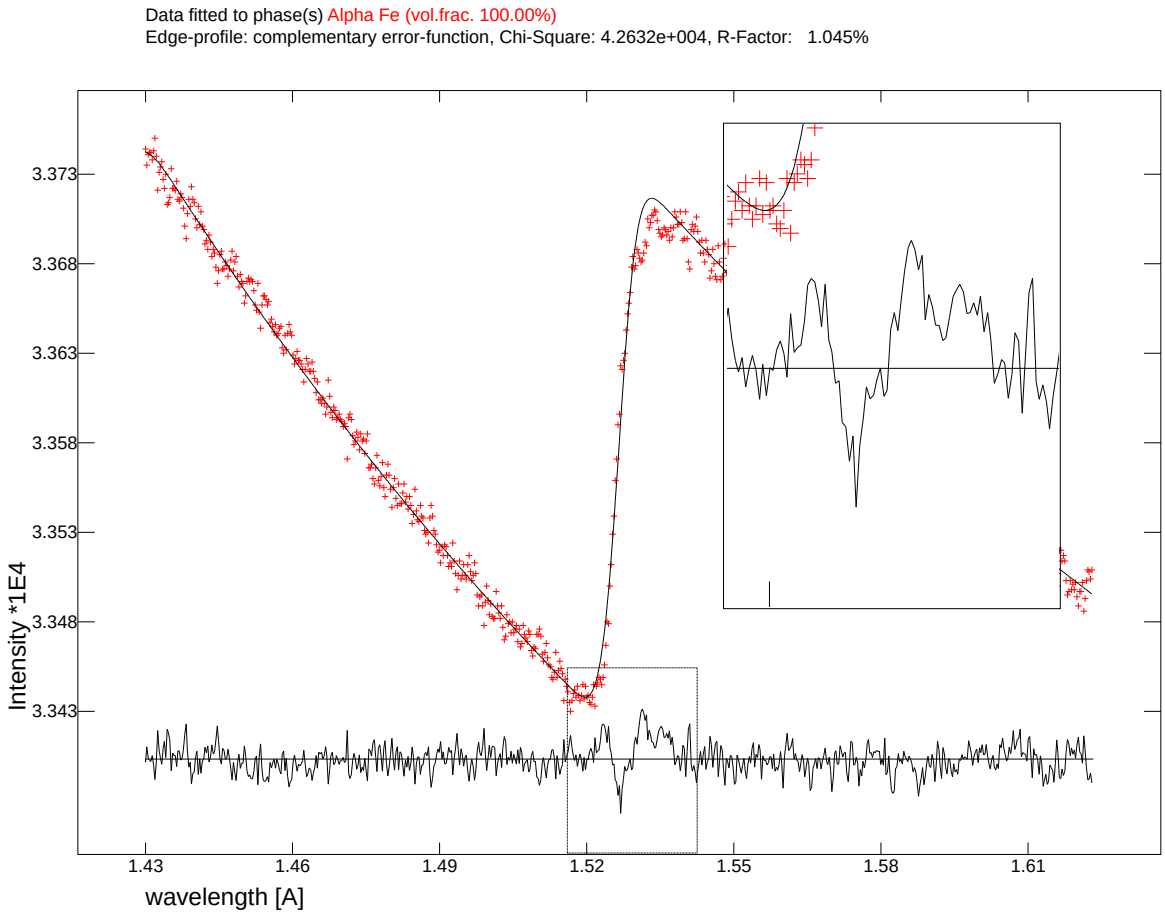

Figure 3.4: Iron (321)-reflection fitted with complementary error function. $\chi^2 = 4.3 \cdot 10^4$. The inset shows the marked region of the difference curve.

where erfc is again the complementary error function. The arguments of the exponentials are

$$u = \frac{\alpha}{2}\left(\alpha\sigma^2 + 2\Delta\right), \qquad v = \frac{\beta}{2}\left(\beta\sigma^2 - 2\Delta\right) \tag{3.41}$$

while the arguments of the complementary error function are given by

$$y = \frac{\alpha\sigma^2 + \Delta}{\sqrt{2}\sigma}, \qquad z = \frac{\beta\sigma^2 - \Delta}{\sqrt{2}\sigma} \tag{3.42}$$

This function results from convoluting a Gaussian with 'back-to-back' exponentials with different rise (α) and decay (β) constants (see equation (3.52)) and is for example implemented for neutron time-of-flight data in the widely used Rietveld code GSAS (Larson & Von Dreele, 1986). Again, equation (3.35) needs to be applied to derive a Bragg-edge profile from this function. The algebra can be found in appendix B, the resulting edge description is

$$k\left(\Delta, \sigma, \alpha, \beta\right) = \frac{1}{2}\mathrm{erfc}\left(w\right) - \frac{\beta \exp\left(u\right)\mathrm{erfc}\left(y\right) - \alpha \exp\left(v\right)\mathrm{erfc}\left(z\right)}{2\left(\alpha + \beta\right)} \tag{3.43}$$

with the additional factor

$$w = \frac{\Delta}{\sqrt{2}\sigma} \tag{3.44}$$

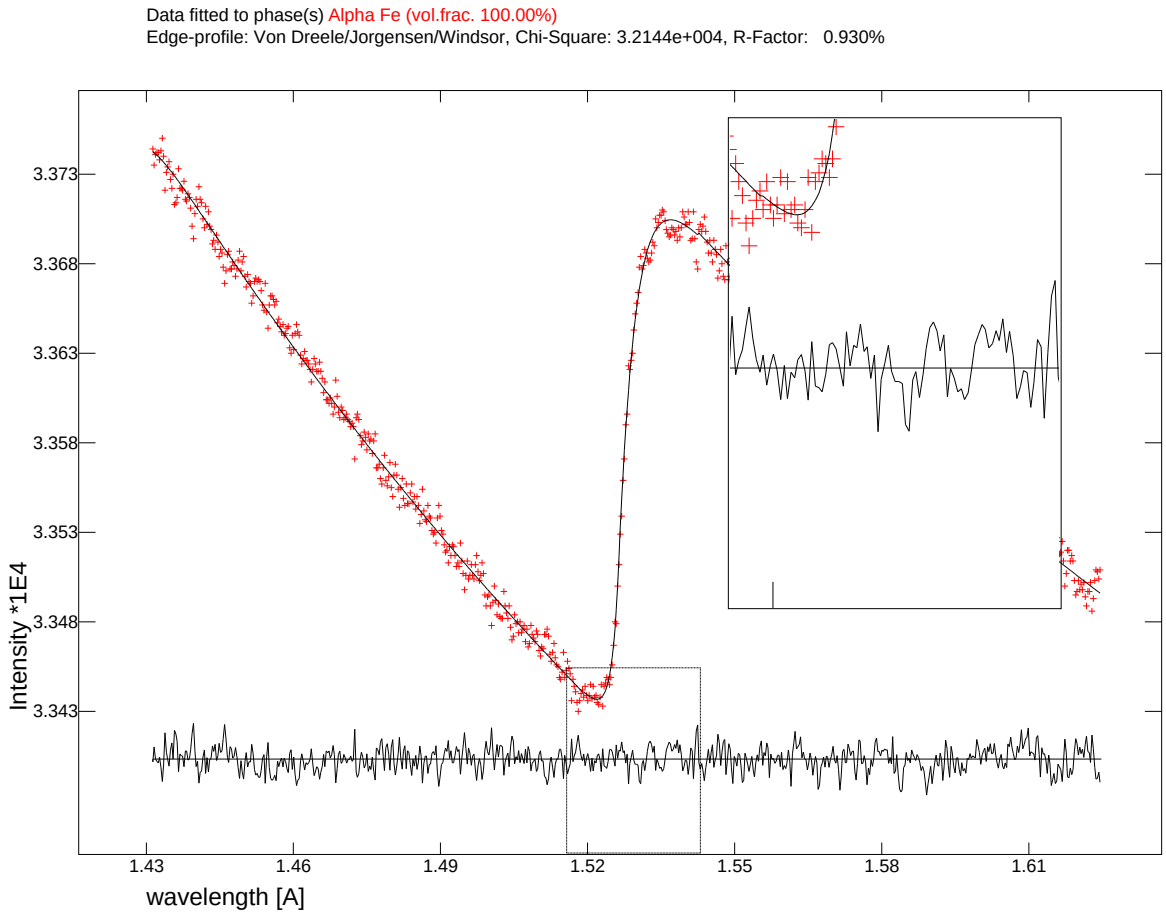

Figure 3.5: Iron (321)-reflection fitted with non-symmetric edge-profile-function derived from neutron time-of-flight diffraction peak profile-function proposed by Jorgensen et al. (1978). $\chi^2 = 3.2 \cdot 10^4$. The inset shows the marked region of the difference curve.

The edge is described in this model by a complementary error function as presented in the previous section plus contributions of the terms of the non-symmetric diffraction peak profile of (3.40). As can be seen from figure 3.5, the model describes the measured data very well. Contrary to the models presented above, it is not possible to determine the reflection position from the difference curve. Due to the tight relation between edge and peak profile, the limits defining the range where the edge profile needs to be evaluated can be applied as given by Von Dreele et al. (1982). Also the application of models for the d-spacing dependence of the profile parameters α and β developed by Von Dreele et al. (1982) is possible (see next section).

3.3.4 Profile Parameters

For both the complementary error function and the Jorgensen et al. edge profiles the edge width σ is modeled in **BETMAn** by the same function as used in GSAS for the case of isotropic broadening:

$$\sigma_{\vec{h}}^2 = \sigma_0^2 + \sigma_1^2 d_{\vec{h}}^2 + \sigma_2^2 d_{\vec{h}}^4 \tag{3.45}$$

The constant σ_0 accounts for the finite width of the neutron pulse but is negligible and usually set to zero. σ_1 describes both the broadening due to the instrument and the sample (microstrain). σ_2

Figure 3.6: Effect of strain (left) and particle size (right) broadening on reciprocal lattice points (after Von Dreele, 1989).

describes broadening due to particle size and stacking fault effects, usually also negligible and set to zero. Hence, from the latter two parameters information on the microstructure of the sample may be derived. The explanation of the assignments between the broadening parameters and the two effects is as follows (Von Dreele, 1989, p. 355-357):

- In a non-ideal crystal, the dimensions of the unit cells are not constant but vary due to defects around an average value. The latter is probed by the fitted lattice parameter. In a first approximation, the distribution of the lattice parameters around the mean value can be approximated by a Gaussian (Todd et al., 1995). In the reciprocal space, this is represented by also poor defined reciprocal lattice parameters. Hence, a reflection in the direction of the reciprocal lattice vector $\vec{h} = ha^* + kb^* + lc^*$ is only half as broad as $2\vec{h} = 2ha^* + 2kb^* + 2lc^*$, i.e. the broadening is proportional to the distance of the reciprocal lattice point from the origin (figure 3.6, left):

$$\Delta d^* = \text{const} \cdot d^* \tag{3.46}$$

To convert this relation to real space, $d^* = 1/d$ and its differential form $\Delta d^* = \Delta d/d^2$ must be applied which yields

$$\Delta d = \text{const} \cdot d \tag{3.47}$$

From the moderation process, beam divergence, path length in the detector before detection and from the binning in the data acquisition, uncertainties in the time-of-flight and the flight path are introduced. This instrumental contribution to the broadening is also proportional to the d-spacing as can be seen from the relative error of the d-spacing and time-of-flight:

$$\frac{\Delta d}{d} = \sqrt{\left(\frac{\Delta t}{t}\right)^2 + \left(\frac{\Delta L}{L}\right)^2 + (\Delta\vartheta \cot\vartheta)^2} = \frac{\sigma_{1,instr}}{d} \tag{3.48}$$

where the contribution of the Bragg angle ϑ is zero in a transmission measurement as the edges are located at precisely $\vartheta = 90°$. As both instrumental and sample contribution may be expressed as variances of a Gaussian contribution to the peak shape, the instrumental contribution $\sigma_{1,instr}$ may be subtracted from the fitted value of σ_1 to obtain the pure strain broadening. With the following equation, a dimensionless strain value S ('percent strain', 'fractional strain') may be computed (after Von Dreele, 1989, equation (59), Larson & Von Dreele, 1994, p. 132)[7]:

$$S = \sqrt{\left(\sigma_1^2 - \sigma_{1,instr}^2\right) \cdot 8\ln 2} \cdot 100\% \tag{3.49}$$

[7] In GSAS, the equation is given as $S = \sqrt{8ln2(\sigma_1^2 - \sigma_{1,instr}^2} \cdot 100\%/DIFC$ where $DIFC$ is the diffractometer constant relating d-spacing to time-of-flight (unit μs/Å, σ_1 has the same unit in GSAS). In **BETMAn**, σ_1 is already dimensionless and hence division by DIFC not necessary.

The observed values for σ_1 range from about $2.5 \cdot 10^{-3}$ (compressed and sintered NiO powder) to $50 \cdot 10^{-3}$ (austenitic steel with a broad range of local carbon concentrations). Assuming the instrumental resolution of $0.6 \cdot 10^{-3}$ (see equation (5.1)) as instrumental contribution $\sigma_{1,instr}$, this results in fractional strain values of 0.7 to 11.8%.

- The explanation for the contribution of particle size broadening being proportional to the square of the d-spacing can be given again with the reciprocal lattice: As small particles significantly violate the assumption of an infinite lattice (see section 1.6.3), the reciprocal lattice points are no more described by δ-functions but occupy a finite volume in reciprocal space. This finite volume is the same for any lattice point and depends on the actual particle size (see figure 3.6, right). Hence

$$\Delta d^* = \text{const} \tag{3.50}$$

holds. Applying again the differential form of the relation between d and d^* results in

$$\Delta d = \text{const} \cdot d^2 \tag{3.51}$$

The edge profile derived from the Jorgensen et al. (1978) peak profile requires parameters α and β describing the rise and decay of the emission time distribution assumed to be of the form

$$\phi(t) = \frac{A}{\frac{1}{\alpha} + \frac{1}{\beta}} \begin{cases} e^{\alpha t} & t < 0 \\ e^{-\beta t} & t \geq 0 \end{cases} \tag{3.52}$$

This describes the asymmetry of the peak/edge-profile. The wavelength dependence of these parameters is described by Von Dreele et al. (1982) as

$$\alpha = \alpha_0 + \frac{\alpha_1}{d} \qquad \beta = \beta_0 + \frac{\beta_1}{d^4} \tag{3.53}$$

All four parameters are refinable but, as the emission spectrum is assumed to be constant, parameters should be gathered during a calibration run and remain constant afterwards. For α, it is sufficient to vary only α_0 and set α_1 to zero.

3.3.5 Discussion of Edge-Profiles

The edge model derived from the diffraction peak function proposed by Jorgensen et al. (1978) provides a very good fit to data measured at LANSCE. It is believed, that this is the first adequate description of a Bragg-edge profile and will allow further applications of this method, both by means of single edge and full pattern fits. If the Bragg-edge transmission method is to be applied at other neutron sources using different profiles for their diffraction peaks (for example the profile type used at ISIS, Cole & Windsor, 1980 or the Ikeda-Carpenter (1985) function, describing moderator pulse shapes of polyethylene moderators), e. g. due to different moderator types, corresponding edge profiles can be derived readily using equation (3.35). As the method allows to derive analytical expressions like the presented edge profiles, computing time can be reduced compared to numerical integration.

3.4 Absorption Cross-Section

The absorption cross-section (Windsor, 1981, p.406) is assumed to be proportional to the reciprocal of the neutron velocity, i.e. possible resonances (see section 5.3.1) of some isotopes are neglected. This

is by

$$E = \frac{p^2}{2m} = \frac{h^2}{2m\lambda^2} = \frac{mv^2}{2} \Rightarrow v = \frac{h}{m\lambda} \tag{3.54}$$

changed to an appropriate wavelength dependence:

$$\sigma_{abs}(\lambda) = B \cdot \frac{1}{v} = B \cdot \frac{m}{h}\lambda \tag{3.55}$$

where B is an appropriate proportionality factor for absorption. In tables of neutron data (e.g. Windsor, 1981, p. 407), the absorption cross-section σ_{abs} in most cases is given for neutrons of a standard velocity $v_0 = 2200$m/s ($\lambda_0 = 1.8$Å, $E_0 = 25.3$meV). From this value, the constant B can be calculated

$$\sigma_{abs}(v = 2200m/s) = B \cdot \frac{1}{2200\,m/s} \Leftrightarrow B = 2200\,m/s \cdot \sigma_{abs}(v = 2200m/s) \tag{3.56}$$

For the absorption cross-section of a unit cell, the absorption cross-sections of the atoms contained in the unit cell are added as the absorption does not depend on the crystal structure. To avoid a multiplication with m/h each time the absorption cross-section is needed, in the code the dependence between the literature value of the absorption cross-section and the proportionality factor is

$$B = 2200\,m/s \cdot \sigma_{abs}(v = 2200m/s) \cdot \frac{m}{h} \tag{3.57}$$

3.5 Structural Parameters

The part of the cross-section providing the desired information on the crystal structure of the sample is the elastic coherent scattering cross-section $\sigma_{coh}^{el}(\lambda)$ as given by equation (3.9). The geometry of the unit cell determines the reflection, or, in the case of a transmission experiment, the edge position (the 'd-spacing') while the content of the unit cell determines the ratios of the reflection intensities. The edge intensities are scaled by the number of unit cells per unit area N_φ and determine the volume fraction or 'layer thickness' of a phase (see equation (3.1)). The content of the unit cell is fixed in **BETMAn**, i.e. atomic positions or site occupation factors are not refinable. Due to the poor signal to noise ratio of a Bragg-edge transmission pattern (i.e. the ratio of edge height to the transmitted intensity), it is doubtful whether a refinement of such parameters makes sense for transmission data. Hence, the only refinable quantity contributing to the structure factor $F_{\vec{h}}$ is the isotropic displacement parameter $B_{iso,n}$ for each atom in the asymmetric unit of the structure.

The parameters V_0 and d in (3.9) reflect the dependence of the elastic coherent scattering cross-section on the unit cell geometry. The unit cell volume V_0 is in the general case of a triclinic lattice given by

$$V_0 = abc\sqrt{1 - \cos^2\alpha - \cos^2\beta - \cos^2\gamma + 2\cos\alpha\cos\beta\cos\gamma} \tag{3.58}$$

where a, b and c are the lattice constants while α, β and γ are the lattice angles. The lattice spacing $d_{\vec{h}}$ of a set of lattice planes $\{hkl\}$ is given by

$$d_{\vec{h}} = \frac{1}{\left|\vec{h}\right|} \quad \text{with the reciprocal lattice vector } \vec{h} = h\vec{a}^* + k\vec{b}^* + l\vec{c}^* \tag{3.59}$$

Applying the definition of the reciprocal lattice vectors a^*, b^*, c^*, for the general case of a triclinic system this becomes

$$d_{\vec{h}} = \frac{abc\sqrt{1 - \mathrm{c}_\alpha^2 - \mathrm{c}_\beta^2 - \mathrm{c}_\gamma^2 + 2\mathrm{c}_\alpha\mathrm{c}_\beta\mathrm{c}_\gamma}}{\sqrt{h^2b^2c^2\mathrm{s}_\alpha^2 + a^2k^2c^2\mathrm{s}_\beta^2 + a^2b^2l^2\mathrm{s}_\gamma^2 + 2abc\left\{hkc\left(c_\alpha c_\beta - c_\gamma\right) + hbl\left(c_\alpha c_\gamma - c_\beta\right) + akl\left(c_\beta c_\gamma - c_\alpha\right)\right\}}} \tag{3.60}$$

where the sines and cosines of the lattice angles were for brevity replaced by s_i and c_i, respectively. Depending on the crystal system, **BETMAn** uses optimized formulas listed in appendix C.

3.6 Texture

In many sample systems, the distribution of grain orientations is not random but a certain crystallographic plane, described by its normal vector $\vec{H}$ (also called the 'pole') of each grain exhibits a certain orientation distribution around a sample direction $\vec{S}$ (e.g. Wenk, 1985). In case of a rolled plate (rolling texture), $\vec{S}$ might be the rolling direction, or, in case of a fibre texture of a cylindrical sample, the fibre axis. The diffracted intensity (3.9) is calculated for the case of a random distribution, hence a correction of the elastic coherent scattering cross-section has to be introduced for the case of a textured sample. After the March-Dollase model (March, 1932, Dollase, 1986), the probability of a grain oriented such that $\vec{H}$ is found under a certain angle α to $\vec{S}$ is assumed to have cylindrical symmetry, i.e. depends only on the azimuth angle $\alpha_{\vec{H}}$. Table 3.2 provides a list of symbols used throughout the following sections.

Symbol	Meaning
$\vec{S}$	Preferred orientation axis. The macroscopic direction around which grains exhibit a preferred orientation. Examples: Rolling direction of a rolled plate or the normal of a plate-shaped sample.
$\vec{H}$	Preferred orientation direction. Unit vector normal to a specific set of lattice planes that exhibits a preferred orientation around $\vec{S}$.
$\alpha_{\vec{H}}$	Angle between $\vec{S}$ and $\vec{H}$.
$\vec{h}$	Unit vector normal to an arbitrary set of diffracting lattice planes.
$\alpha_{\vec{h}}$	Angle between $\vec{S}$ and $\vec{h}$.
β	Angle between $\vec{h}$ and $\vec{H}$.
$P_{\vec{h}}(\vec{\kappa})$	Probability of finding $\vec{h}$ parallel to the macroscopic direction $\vec{\kappa}$, the scattering vector.
$P_{\vec{H}}\left(\alpha_{\vec{H}}\right)$	Probability of finding $\vec{H}$ under an angle $\alpha_{\vec{H}}$ to $\vec{S}$.
$\{hkl\}$	Set of symmetry equivalent lattice planes.
$M_{\vec{h}}$	Number of symmetry equivalent lattice planes to $\vec{h}$ ($\lvert\{hkl\}\rvert$).
$\{\beta\}$	Set of angles between $\vec{h} \in \{hkl\}$ and $\vec{H}$.
m_β	Number of occurences of an angle β in $\{\beta\}$.

Table 3.2: Symbols used in the texture model.

The texture correction for the case of Bragg-edge transmission is adapted from the treatment in diffraction geometry[8]. Consequently, the case of texture correction after the March-Dollase model in diffraction geometry is briefly described first.

[8] The results presented in this section were achieved in collaboration with Dr. Giovanni Bruno, at that time Open

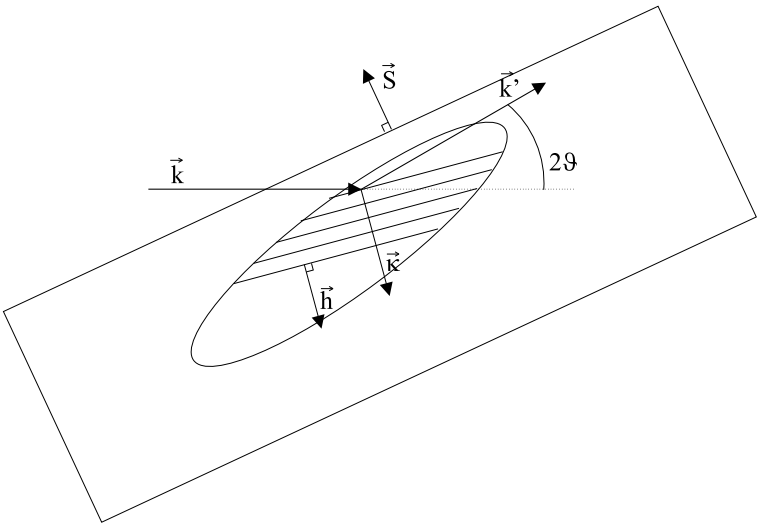

Figure 3.7: Schematic of the geometry used for texture correction in diffraction. Displayed is a plate with the plate normal $\vec{S}$ and a grain oriented such that $\vec{h}$ scatters (i.e. is parallel to $\vec{\kappa}$).

3.6.1 Diffraction

Let $\vec{H}$ be the preferred orientation plane exhibiting preferred orientation around the normal $\vec{S}$ of a plate and $\vec{h}$ the normal of an arbitrary lattice plane oriented such that it scatters, i.e. $\vec{h} \parallel \vec{\kappa} = \vec{k} - \vec{k}_0$ (see figure 3.7 for a schematic of the geometry). The plate normal $\vec{S}$ is also assumed to be parallel to the scattering vector $\vec{\kappa}$. Let β be the angle between $\vec{h}$ and $\vec{H}$. Because of $\vec{h} \parallel \vec{\kappa} \parallel \vec{S}$ and due to the cylindrical symmetry of the orientation distribution, all $\vec{H}$ with the same probability lie on a cone with opening angle 2β around $\vec{h}$. The probability $P_{\vec{h}}(\vec{\kappa})$ of finding $\vec{h}$ in this particular orientation is the same as the probability for finding $\vec{H}$ at an azimuthal angle $\alpha_{\vec{H}}$ to $\vec{S} \parallel \vec{\kappa}$ which is equivalent to β in this case. This is expressed by the so-called 'reciprocity relation'

$$P_{\vec{h}}(\vec{\kappa}) = P_{\vec{H}}(\beta = \alpha_H) \tag{3.61}$$

By probing the normalised intensities (i.e. measured intensities divided by the structure factor, multiplicity and other correction factors) of reflections $\vec{h}$, the function $P_{\vec{h}}(\vec{\kappa})$ is sampled for different $\vec{h}$ and therefore points of the function $P_{\vec{H}}\left(\alpha_{\vec{H}}\right)$ are obtained at different angles $\alpha_{\vec{H}}$. This allows to fit a function between those points and describe the sample texture. The procedure is depicted in figure 3.8.

3.6.2 Transmission

In transmission geometry, the preferred orientation plane $\vec{H}$ is assumed to exhibit a preferred orientation in the direction $\vec{S}$ parallel to the incident beam. A preferred orientation direction perpendicular

University, Milton Keynes, UK, now Hahn-Meitner-Institut, Berlin, Germany within the collaboration between the Bragg-edge transmission groups at ISIS and Kiel. It was thought to be able to correct for a bump in the difference curve appearing in some patterns obtained at ISIS, which was assumed to be due to a missing description of sample texture in the fit function. As it turned out later, the bump was explained by the at that time missing inelastic contributions to the total scattering cross-section in the model of **BETMAn**. Hence, an experimental validation of the developed texture model is still missing.

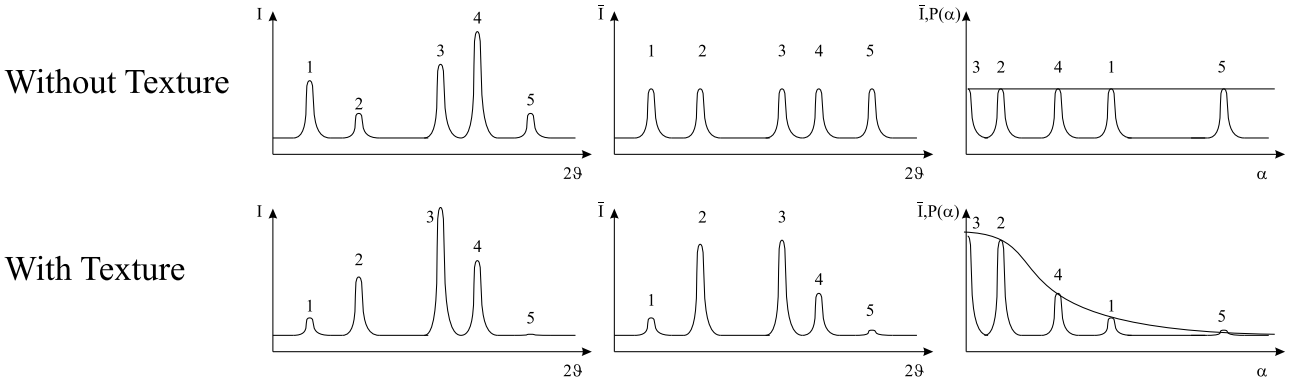

Figure 3.8: Schematic of the texture correction after March-Dollase. From left to right the measured intensity I versus scattering angle, the normalized intensity $\bar{I}$ versus scattering angle and the normalized intensity versus the angle between the normals of the scattering lattice plane and the preferred orientation plane (reflection number 3) are displayed. In the top row, the case of a random orientation distribution (no texture) is displayed, in the bottom row that of a textured sample. See figure 3.9 for an example of $P(\alpha)$.

to the incident beam is possible also, but in this case the Bragg-edge transmission pattern contains no information around which direction (e.g. upward, downward, left etc.) the grains are oriented. This is because a single scattering vector $\vec{\kappa}$ as in the case of diffraction is only defined for the case of backscattering, i.e. for neutrons of the wavelength $\lambda = 2d_{\vec{h}}$. For any other scattering angle 2ϑ, changes in the diffracted intensity may become visible in the Bragg-edge transmission pattern but no information about the distribution of the directions of the corresponding scattering vectors on the Debye-Scherrer cone is contained in the pattern. The same restriction to two cases applies to the model of Dollase (1986). The two cases hold for example for acicular (needle-shaped) crystallites oriented with their axis along or perpendicular to the incident beam direction.

The procedure in texture correction for the case of Bragg-edge transmission patterns is to define a 'master' correction function $P_{\vec{H}}(\alpha_{\vec{H}})$ for reflections $\vec{H}$ from which the dependent corrections functions $P_{\vec{h}}(\alpha_{\vec{h}}(\lambda))$ for all other reflections $\vec{h}$ are derived. These correction functions are multiplied to the elastic coherent scattering cross-section of the particular reflection, making σ^{el}_{coh} dependent on the parameters of $P_{\vec{H}}(\alpha_{\vec{H}})$:

$$\sigma^{el}_{coh}(\lambda) = \sum_{\vec{h}} \sigma^{el}_{coh,\vec{h}}(\lambda) P_{\vec{h}}\left(\alpha_{\vec{h}}(\lambda)\right) \tag{3.62}$$

A measured Bragg-edge transmission pattern can then be fitted to the coefficients of the 'master' function based on the observed changes of the diffracted intensity for all observed reflections at all observed wavelengths. It is a fundamental difference between diffraction and transmission data that in transmission all possible scattering vectors contribute to the measured signal, although only the opening angle of the corresponding Debye-Scherrer cone is determined. Hence, the elastic coherent scattering cross-section of an individual set of lattice planes contains all information on the texture *correction* for the whole pattern. It does *not* contain the necessary information to reconstruct the orientation distribution function (ODF) as the information is lost into which direction neutron intensity missing in the Bragg-edge transmission pattern was scattered.

The angle $\vartheta_{\vec{h}}$ between the preferred orientation axis (the direction of the incident beam in this

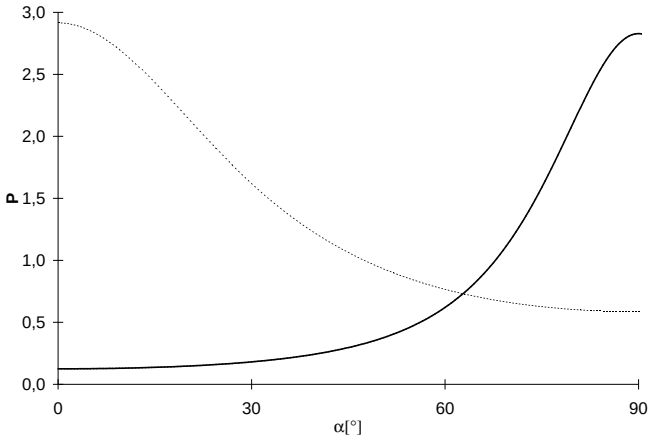

Figure 3.9: Probability distribution according to (3.66) for finding $\vec{H}$ under an angle α to the preferred orientation direction for the case of $r = 2.0$ (solid line) and $r = 0.7$ (dotted line). r is a parameter describing the degree of texture of the sample.

case) and a diffracting lattice plane $\vec{h}$ is the Bragg angle and hence related to the wavelength λ via Bragg's law:

$$\vartheta_{\vec{h}}(\lambda) = \arcsin\left(\frac{\lambda}{2d_{\vec{h}}}\right) \tag{3.63}$$

The necessary angle between the preferred orientation axis $\vec{S}$ and the the normal $\vec{h}$ of the diffracting lattice plane is then

$$\alpha_{\vec{h}}(\lambda) = \tfrac{\pi}{2} - \arcsin\left(\frac{\lambda}{2d_{\vec{h}}}\right) \tag{3.64}$$

As $\vec{H}$ of the same grain can appear in any direction with angle β to $\vec{h}$ (but with different probability, governed by $P_{\vec{H}}$), the probability for a grain to be found in an orientation such that $\vec{h}$ actually contributes to the elastic coherent scattering cross-section at a given λ is determined by the average probability of the possible directions of $\vec{H}$ around $\vec{h}$. Furthermore, as each symmetry-equivalent member of the set of lattice planes $\{hkl\}$ has a different angle to $\vec{H}$, the averaging must be performed over all symmetry equivalent directions $\vec{h}$ and normalized by the multiplicity $M_{\vec{h}}$ of the reflection $\vec{h}$:

$$P_{\vec{h}}\left(\alpha_{\vec{h}}(\lambda)\right) = \frac{1}{M_{hkl}} \sum_{\vec{h}\in\{hkl\}} \bar{P}_{\vec{H}}\left(\alpha_{\vec{H}}\left(\alpha_{\vec{h}}(\lambda), \beta\right)\right) = \frac{1}{2\pi M_{hkl}} \sum_{\vec{h}\in\{hkl\}} \int_0^{2\pi} P_{\vec{H}}\left(\alpha_{\vec{H}}\left(\alpha_{\vec{h}}(\lambda), \beta, \phi\right)\right) d\phi \tag{3.65}$$

where ϕ is a variable parameterising a path of $\vec{H}$ around $\vec{h}$. In principle, the sum has to run also over all members of $\{HKL\}$ and normalized by M_{HKL}, but for each term, the angles $\beta_{\vec{h}}$ would only be permuted and thus each term of this sum would have the same value. Consequently, it is sufficient to calculate (3.65) for one member $\vec{H} \in \{HKL\}$ only. The problem is then reduced to find the parameterisation of the path of $\vec{H}$ around $\vec{h}$, calculate the angle $\alpha_{\vec{H}}(\varphi)$ between $\vec{H}$ and the direction of the incident intensity at each point of this path and solve the integral. The parameterisation of the path around $\vec{h}$ is described in appendix D. Applying the March-Dollase model (see figure 3.9 for examples of this function)

$$P_{\vec{H}}\left(\alpha_{\vec{H}}\right) = \left(r^2 \cos^2 \alpha_{\vec{H}} + \tfrac{1}{r} \sin^2 \alpha_{\vec{H}}\right)^{-\frac{3}{2}} \tag{3.66}$$

where r is a refinable parameter describing the degree of texture, the integral becomes

$$\begin{aligned} P_{\vec{h}}\left(\alpha_{\vec{h}}(\lambda)\right) &= \frac{1}{2\pi M_{\vec{h}}} \sum_{\vec{h}\in\{hkl\}} \int_0^{2\pi} \left(r^2 \cos^2 \alpha_{\vec{H}}\left(\alpha_{\vec{h}}(\lambda),\beta,\phi\right) + \tfrac{1}{r}\sin^2 \alpha_{\vec{H}}\left(\alpha_{\vec{h}}(\lambda),\beta,\phi\right)\right)^{-\frac{3}{2}} d\phi \\ &= \frac{1}{\pi M_{\vec{h}}} \sum_{\vec{h}\in\{hkl\}} \int_{-\frac{\pi}{2}}^{\frac{\pi}{2}} \left(\left(r^2-\tfrac{1}{r}\right)\cos^2 \alpha_{\vec{H}}\left(\alpha_{\vec{h}}(\lambda),\beta,\phi\right) + \tfrac{1}{r}\right)^{-\frac{3}{2}} d\phi \end{aligned} \tag{3.67}$$

With the result derived in appendix D, this becomes

$$P\left(\alpha_{\vec{h}}(\lambda)\right) = \frac{1}{\pi M_{\vec{h}}} \sum_{\vec{h}\in\{hkl\}} \int_{-\frac{\pi}{2}}^{\frac{\pi}{2}} \left(\left(r^2-\tfrac{1}{r}\right)\cdot\left(\cos\alpha_{\vec{h}}(\lambda)\cos\beta - \sin\alpha_{\vec{h}}(\lambda)\sin\beta\sin\phi\right)^2 + \tfrac{1}{r}\right)^{-\frac{3}{2}} d\phi \tag{3.68}$$

where every member of $\{hkl\}$ has got the same angle $\alpha_{\vec{h}}(\lambda)$ (because they all diffract at the same angle 2ϑ) and hence $\alpha_{\vec{h}}(\lambda)$ is constant during summation. The integral may be reduced to the form

$$\int_{-\frac{\pi}{2}}^{\frac{\pi}{2}} \left(a\sin^2\phi + b\sin\phi + c\right)^{-\frac{3}{2}} d\phi = \int_{-1}^{1} \frac{dx}{\sqrt{(ax^2+bx+c)^3\,(1-x^2)}} \tag{3.69}$$

3.6.3 Implementation

So far, no analytical solution of this integral was found (for a similar integral, Dollase uses also a numerical solution). The numerical solution for the average probability of finding $\vec{H}$ around $\vec{h}$ based on $P_{\vec{H}}(\alpha_{\vec{H}})$ is implemented as follows into **BETMAn**:

- To avoid multiple evaluation,
  - for each symmetry equivalent plane of a reflection, $\cos\beta$ and $\sin\beta$ are calculated once and stored. At this point, also symmetry equivalent $\vec{h}$ with the same β are found and a 'multiplicity' factor m_β is assigned, further reducing the amount of necessary calculations.
  - the interval $[-\pi/2;\pi/2]$ is split into N equidistant points and values of $\sin\beta\sin\phi$ are calculated and stored for each point in a lookup table. Because of symmetry, only one half of the circumference of the circle of $\vec{H}$ around $\vec{h}$ needs to be considered.
  - a lookup table for M values of $P_{\vec{H}}(\alpha_{\vec{H}})/(N+1)$ with constant steps in $\cos\alpha_{\vec{H}}$ is created. Normalisation with $N+1$ is performed to avoid divisions in the subsequent numerical integration.
- All other terms depend on the wavelength and cannot be pre-calculated:
  - For each visible $\{hkl\}$, calculate sine and cosine of $\alpha_{\vec{h}}(\lambda)$ as given in (3.64).
  - Calculate N values for $\cos\alpha_{\vec{H}}$ as given in (D.5) with these values and the lookup table for $\sin\beta\sin\phi$.

– Use the lookup table for $P_{\vec{H}}(\alpha_{\vec{H}})/N+1$ and execute the summation

$$\begin{aligned} P_{\vec{h}}\left(\alpha_{\vec{h}}\right) &= \frac{1}{M_{\vec{h}}} \sum_{\vec{h}\in\{hkl\}} \bar{P}_{\vec{H}}\left(\alpha_{\vec{H}}\left(\alpha_{\vec{h}}\left(\lambda\right),\beta\right)\right) \\ &= \frac{1}{M_{\vec{h}}} \sum_{\beta\in\{\beta\}} m_\beta \frac{1}{2\pi} \int_0^{2\pi} P_{\vec{H}}\left(\alpha_{\vec{H}}\left(\alpha_{\vec{h}}\left(\lambda\right),\beta,\phi\right)\right) d\phi \\ &\approx \frac{1}{M_{\vec{h}}} \sum_{\beta\in\{\beta\}} m_\beta \sum_{i=0}^{N} \left(\tfrac{1}{N+1} P\left(\cos\alpha_{\vec{H},\beta,i}\right)\right) \end{aligned} \tag{3.70}$$

Using this algorithm, for each set of lattice planes and each wavelength a correction factor for the elastic coherent scattering cross-section can be calulcated with a minimum number of calls to the time-consuming functions sine, cosine and sqrt (necessary for the calculation of $x^{-3/2}$). The parameter r of the one-dimensional probability distribution function can be fitted, affecting the elastic coherent scattering cross-section of all reflections. For wavelength slightly larger than $2d_{\vec{h}}$, where the elastic coherent scattering cross-section should be zero but is still finite due to the width of the edge profile, the value at $\lambda = 2d_{\vec{h}}$ is used.

The treatment was extended to the case of multiple textures with preferred orientation planes $\vec{H}_i$, each with refinable parameters r_i and f_i. The latter describes the fraction of grains exhibiting preferred orientation of $\vec{h}$ along $\vec{H}_i$.

3.6.4 Texture Perpendicular to I_0

Similar to the treatment of Dollase (1986), for the case of a preferred orientation direction perpendicular to the one treated above an integration has to be performed to convert the probability distribution $P_{\vec{H}}$ from the case of a preferred orientation around I_0. After this, the treatment is the same as above. For a preferred orientation direction perpendicular to the incident beam direction, the angles $\vartheta_{\vec{H}}$ between incident beam direction and $\vec{H}$ and $\alpha_{\vec{H}}$, the parameter of the probability distribution function, are no more equivalent. By averaging the new probability function around a circle where the probability function for the case of a preferred orientation around the incident beam was constant (i.e. a circle around $\vec{I}_0$), a function is generated that can be used with the procedure outlined above but describes a preferred orientation around an axis perpendicular to $\vec{I}_0$.

Some examples of the correction factors versus wavelength for several sets of lattice planes are presented in figure 3.10. As can be seen from these plots, the correction factors are, unlike the March-Dollase function (3.66) (figure 3.9), not monotonic and in many cases the biggest corrections are at the edge-positions. Although experimental validation for the texture model described is still missing, these plots provide an idea on how the transmission pattern of a textured sample will look.

3.6.5 Discussion

Though the March-Dollase model was reported to be successful in some cases (e.g. Williams et al., 1988), more powerful but also more complex models for preferred orientation correction and even for quantitative texture analysis are available. If it turns out that the appropriate correction of texture becomes a major problem in Bragg-edge transmission, more sophisticated models involving

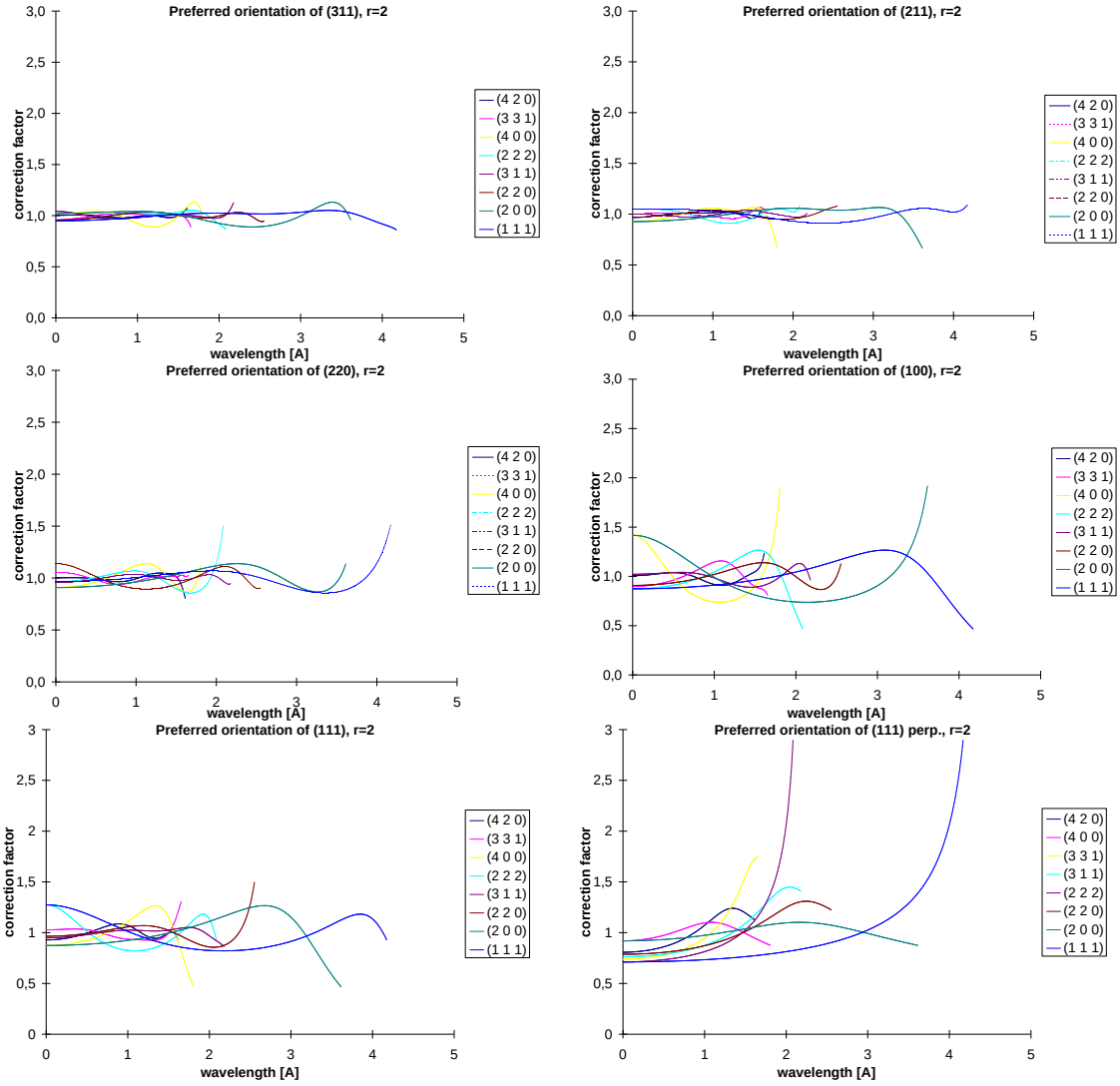

Figure 3.10: Examples of preferred orientation correction factors for several preferred orientation planes. Except for bottom right, the preferred orientation direction is parallel to the incident beam direction.

the description of the sample texture by spherical harmonics (Dahms & Bunge, 1989, Dahms, 1992, Popa, 1992, Von Dreele, 1997) or the WIMV model (reviewed for example in Matthies et al., 1988) may be incorporated. In Bragg-edge transmission, only the information that some intensity was diffracted under an angle 2ϑ to the incident beam is available, but it is not known into which particular direction in the sample coordinate system this intensity was diffracted. Furthermore, it is not possible to define a gauge volume in the sample by collimation, like in diffraction, and rotate the sample to obtain the texture information for that gauge volume only in different sample orientations. Therefore, only a correction with respect to texture rather than a measurement of the sample texture is possible in all cases other than a fibre texture with the fibre axis parallel to the incident beam direction.

3.7 Instrumental Parameters

At least at the beginning of a beam cycle, the setup consisting of flight path, moderator, detector system and electronics has to be calibrated. To establish the relation between the metrics of the instrument and the sample, a pattern of a substance of well known crystal structure is fitted with instrumental rather than crystallographic parameters. These parameters are held constant afterwards. The relation between wavelength and time-of-flight is given by

$$\lambda\left(t_i\right) = \frac{h}{mL}\left(t_0 + t_i\right) \tag{3.71}$$

where t_i is the time-of-flight of channel i of the data acquisition, t_0 a time offset between the spallation pulse and the start of a sweep at channel 0 of the data acquisition and L is the flight path length[9]. Both L and t_0 are fitted[10]. L scales the pattern on the wavelength or d-spacing axis while t_0 shifts the whole pattern.

3.8 Incident intensity

Two options are currently implemented in **BETMAn** to model the incident intensity: Providing a measured open-beam spectrum or use of a function with refinable parameters. In both cases the incident intensity is scaled by the overall scale factor A (see the overall model (3.1)).

3.8.1 Measured Pattern

Using a scaled measured open beam pattern as incident intensity clearly has the advantage of including any contamination like from the aluminum covers of the beam tube. Of course this assumes that the whole profile remains constant with time, source/moderator temperature and beam intensity variations. This has not been proven yet, but seems to be a reasonable assumption. If it would be not the case, the differences are most likely smooth curves and deviations between measurement and applied model would be compensated by the simultaneously fitted background. The option is also beneficial when additional contamination is introduced, for example by a controlled atmosphere setup of a tube furnace (cf. section 7.2). Here, the furnace endcaps add an additional layer of approximately 2 cm aluminum to the patterns. To obtain a suitable open beam pattern in that case, the furnace needs to be heated to the desired temperature before taking such a pattern as the endcaps are subject to a slight thermal expansion (which is of course not the case for the beam tube endcaps measured at the same time - modeling this effect with two aluminum phases against weak edges due to the small σ_{coh} of aluminum is clearly a task one should avoid). In any case, an accumulation time in the order of an hour is sufficient to obtain a pattern that is smooth enough to neglect its contribution to the statistical error of the parameters fitted from short term patterns. To avoid a saturation of the

[9] The given relation, derived from the de Broglie equation, is a very good approximation. For very precise measurements a relation of the type

$$t_i = \frac{mL}{h}\lambda + const \cdot \lambda^2 + t_0 \tag{3.72}$$

as for example used in GSAS (Larson & Von Dreele, 1994, p. 126) might be used in the future.

[10] In a calibration experiment, additionally the instrumental contribution $\sigma_{1,instr}$ to the reflection broadening and the coeffcients for the descritpion of the rise and decay constants α and β must be determined (see section 3.3.4). This requires a sample with a well known lattice parameter, exhibiting as few variation of its lattice dimensions as possible. Magnesiumoxide might be an appropriate candidate besides (annealed) iron, nickel or calciumflouride powder.

detector system, in counting mode a collimation is necessary to reduce the number of neutrons per pulse when measuring the open beam pattern.

3.8.2 Model Function

The second option uses a model function and parameters are fitted to describe the incident intensity. Any contamination (i.e. Bragg-edges of phases other than those of the sample) has to be introduced as an additional phase, usually only aluminum. Else, the structural parameters describing the sample would be 'abused' to partly compensate for the contamination and, in case of small volume fractions of the phases under investigation, most likely a divergence or senseless parameters would be the result of the fit. Nevertheless, this approach has turned out to be useful to compensate non-linearities with the current-mode setup at flight path 5 and to analyse the open beam spectrum itself (e.g. estimate the aluminum layer and the moderator temperature, see section 6.1). The model was taken from the GSAS technical manual (Larson & Von Dreele, 1994, p. 118, see also Worlton et al., 1976). The type 2 function with the maximum of eleven coefficients has been chosen to be able to estimate the moderator temperature from the Maxwellian term. The incident intensity depending on time-of-flight is given in this model by

$$I_0(t) = P_1 + P_2 \frac{e^{-P_3/t^2}}{t^5} + P_4 e^{-P_5 t^2} + P_6 e^{-P_7 t^3} + P_8 e^{-P_9 t^4} + P_{10} e^{-P_{11} t^5} \tag{3.73}$$

The second term describes the Maxwellian energy distribution of the moderated neutrons and allows the calculation of an approximate moderator temperature (see Larson & Von Dreele, 1994, p. 118 and Von Dreele, 1989, p. 335). This function is fitted once to an open-beam spectrum to obtain starting values for its parameters. To derive starting values for P_2 and P_3 or the moderator temperature from the fitted parameters, the Maxwell-Boltzmann distribution is used (Von Dreele, 1989, p.335):

$$\frac{dN}{N} = \frac{2}{\lambda}\left(\frac{E}{kT}\right)^2 e^{-\frac{E}{kT}} d\lambda \tag{3.74}$$

As the function is defined dependent on time-of-flight, the wavelength dependence of the Maxwell-Boltzmann distribution must be transformed to a time dependence: Using

$$E = \frac{1}{2}mv^2 = \frac{mL^2}{2t^2}, \quad \lambda = \frac{h}{p} = \frac{ht}{mL} \tag{3.75}$$

the Maxwell-Boltzmann distribution becomes

$$\frac{dN}{N} = \frac{2mL}{ht}\left(\frac{mL^2}{2kTt^2}\right)^2 e^{-\frac{mL^2}{2kTt^2}} \frac{h}{mL} dt = \frac{1}{2t^5}\left(\frac{mL^2}{kT}\right)^2 e^{-\frac{mL^2}{2kTt^2}} dt \tag{3.76}$$

and the relations between the paramters and 'the real world' are

$$P_2 = \frac{m^2L^4}{2k^2T^2}, \quad P_3 = \frac{mL^2}{2kT} \tag{3.77}$$

The second equation allows to estimate the moderator temperature independently of any scaling when the flight path length is known. As a consistency check, this temperature is provided by **BETMAn** on the incident intensity page of the fit control dialog when this function is used to describe the incident intensity. Application of this function to the open beam pattern used for the refinement of the patterns taken in the 1998 beam cycle is described in section 6.1.

Assuming that no time-dependent decaying background is described by the parameters, the parameters can be converted between different flightpath lengths: A neutron arriving at time t with a flightpath of L will arrive at a time t' when the flightpath is changed to L'. As the wavelength is constant, the relation between the two times is given by

$$\lambda = \frac{ht}{mL} = \frac{ht'}{mL'} \quad \Leftrightarrow \quad t = t'\frac{L}{L'} \tag{3.78}$$

To convert the parameters obtained for the setup with L to the setup with L', for example the third term of the incident intensity must be modified as follows:

$$P_4 e^{-P_5 t^2} = P_4 e^{-P_5\left(\frac{L}{L'}t'\right)^2} = P_4 e^{-P'_5 (t')^2} \tag{3.79}$$

with the converted parameter

$$P'_5 = \left(\frac{L}{L'}\right)^2 P_5 \tag{3.80}$$

Applying this to all parameters of the incident intensity, a conversion scheme as displayed in table 3.3 results.

$P_i(L)$	$P'_i(L')$
P_1	P_1
P_2	P_2/x^5
P_3	P_3/x^2
P_4	P_4
P_5	$x^2 \cdot P_5$
P_6	P_6
P_7	$x^3 \cdot P_7$
P_8	P_8
P_9	$x^4 \cdot P_9$
P_{10}	P_{10}
P_{11}	$x^5 \cdot P_{11}$

Table 3.3: Conversion of incident intensity parameters between different flightpath length L and L' ($x = L/L'$).

3.9 Background

This section describes background models currently implemented in **BETMAn**. The constant background OFF is unique to the transmission geometry, the other models are also used for the analysis of powder diffraction data (e.g. Richardson, 1993).

3.9.1 Offset

The most trivial background is simply a constant added to the measured intensity as given by OFF in equation (3.1). Until 1998, at flightpath 5 at LANSCE Bragg-edge transmission patterns were acquired in current-mode, where a certain reference voltage was measured when no neutrons were

detected. This voltage was decreased proportional to the number of detected neutrons when the electron avalanche reached the anode in the photomultiplier tubes. Therefore, compared to counting mode, current mode patterns are mirrored by the abscissa when the reference voltage was adjusted to zero. The reference value could be set to an arbitrary value which needs to be modeled during a refinement, which is the purpose of this parameter.

3.9.2 Exponential Decay

At the 60 m station at flightpath 5, a background exhibiting an exponential decay was observed (see section 5.3.1). Although it was observed that this background vanished before the region where Bragg edges are usually analysed, a correction function is implemented to be able to model this background in case it lasts longer due to a shorter flightpath L or a higher incident intensity I_0:

$$b_{dec}(t) = b_{dec,1} e^{-b_{dec,2} t} \tag{3.81}$$

Same as the intensity offset, this background is added to the transmitted intensity given by equation (3.1). The two refinable parameters are the scale $b_{dec,1}$ of this background and the decay time constant $b_{dec,2}$.

3.9.3 Oscillating Background

To fit a neutron background similar to a background observed in a powder diffraction experiment, two functions were chosen from the GSAS library of background functions, which can be selected alternatively for refinement. The number of variable parameters can be adjusted by the user. This type of background is also assumed to compensate for any systematic difference between the model implemented in **BETMAn** and the measured data. Both background functions are scaled by the incident intensity as shown for the function $b(\lambda)$ in equation (3.1).

Fourier Series

The GSAS background type 2 (Larson & Von Dreele, 1994, p. 120) is a cosine Fourier series. The function is given by

$$b(t) = b_0 + \sum_{j=1}^{30} b_j \cos\left(\frac{t}{t_{\max}} \pi j\right) \tag{3.82}$$

t_{max} is the maximum time-of-flight at which the incident intensity may be higher than zero. This is set to the period between subsequent neutron pulses and consequently choosable by the user depending on the source frequency (20 Hz at LANSCE, 50 Hz at ISIS). All parameters b_i are refinable. This model is used in virtually all refinements performed so far.

Amorphous Phase

This function may be used to model diffuse background from an amorphous phase. It is derived from GSAS background type 3 (Larson & Von Dreele, 1994, p. 120), given by

$$b(\lambda) = b_0 + b_1\lambda + \sum_{j=1}^{15} \frac{b_{2j} \sin(\kappa b_{2j+1})}{\kappa b_{2j+1}} = b_0 + b_1\lambda + \frac{\lambda}{4\pi} \sum_{j=1}^{15} \frac{b_{2j} \sin\left(\frac{4\pi b_{2j+1}}{\lambda}\right)}{b_{2j+1}} \tag{3.83}$$

where the absolute value $2\pi/d = 4\pi/\lambda$ of the scattering vector $\vec{\kappa}$ has been applied. The maxima of the correlation function $d(r)$ are given at b_{2j+1} with intensities of b_{2j} (Richardson, 1993, p. 107). The positions of the maxima correspond to distances r from an atom at which the probability to find another atom has a local maximum. The scattering from amorphous solids, liquids or gases is isotropic. Experimental validation of this function in transmission geometry using a characterized amorphous sample is lacking.

3.10 Volume Fractions

From the fitted numbers of scattering centers per unit area and unit cell volumes of contributing phases, according to

$$x_\varphi = \frac{N_\varphi V_{o,\varphi}}{\sum\limits_{\varphi} N_\varphi V_{o,\varphi}} \tag{3.84}$$

the volume fractions are calculated. This figure is given in the main window during manual refinement (see 4.4) or may be output in the result file during an automated refinement (see appendix G.1).

Chapter 4

Implementation

This chapter describes some aspects of the implementation of the program **BETMAn**. The number of lines of the source code provides a rough measure of the complexity of the software: The source code of **BETMAn** currently consists of 34100 lines (not including empty lines for formatting purpose), 6500 of which contain partly or only comments. The platform-independent core classes consist of 12200 lines of code with comments in about 2300 lines, the remainder of 21900 lines provides the graphical user interface and the batch processing.

In the following, the object oriented programming approach and the core classes of the program are briefly outlined in section 4.1. The library `SgInfo` used for the calculation of symmetry related atoms is described as well as the processing of phase descriptions in section 4.2. For the fitting, the Levenberg-Marquardt algorithm was employed, section 4.3 describes this algorithm and adaptions for **BETMAn**'s fit-class. As graphical user interface, Microsoft Windows 95/98/NT is used and **BETMAn**'s user interface is briefly explained in section 4.4. The input of phase descriptions and automated batch processing of Bragg-edge transmission patterns is documented in sections 4.5 and 4.6, respectively. Finally, section 4.7 describes the database interface of **BETMAn** and the database used for nuclear data and measurement files.

4.1 Object-Oriented Approach

BETMAn is written in C++ using the implementation of the Microsoft Visual C++ development environment. As in any object oriented language, in C++ variables (attributes) and the functions to process these variables (methods) are joined in classes. This allows to encapsulate data in objects, allowing access and modification only via defined interfaces. Classes may be derived from other classes (inheritance), allowing to re-use code and add only those features needed for the specific application. The need of a clearly defined interface by the programming language inherently forces readability and re-usability of the code (e.g. Stroustrup, 1992, or Van Der Linden, 1995, chapter 11). The classes of **BETMAn** are separated in platform independent core-classes for managing measured data (e.g. loading, saving, conversion), phases (e.g. loading of `pha` and `CIF`-files, calculation of symmetry equivalent sites, cross-section calculations), fitting (e.g. initialisation of parameters, generation of files containing the correlation matrix, actual fitting) and, on the other hand, classes derived from classes provided by the Microsoft Foundation Classes (MFC). The latter provide access to the graphical user interface (see section 4.4) and other Windows functions (printing, clipboard etc.) and are extended

for the special needs of **BETMAn**. The object oriented approach in conjunction with a so-called application framework like the MFC hereby simplifies the development of windows oriented software: By providing the core framework of an application, the development of new programs does not have to start from scratch, but the framework is extended with the specific functionality by adding new attributes and methods to existing classes. For example to add a dialog, a new dialog class is derived from the MFC base class `CDialog`, providing the basic functionality of a dialog, and the desired fields and their validation are added as new attributes and methods. As those portions of the code provided by the application framework are used in a huge number of programs, especially in the case of the MFC, it is virtually bug-free. A very convenient feature of the MFC in particular is the ability to detect memory leaks and access violations during the development, decreasing the risk of instabilities of the final product. In **BETMAn**, only dynamic memory allocation is used, i.e. there are no arrays of pre-defined size for atoms, phases, reflections etc.

Another important feature of C++ widely used in **BETMAn** are so-called exceptions, simplifying the error-handling: Any function called within a `TRY` block may `THROW` an exception in case of an error, specifying error-cause and location. In a `CATCH` block following the `TRY` block, those exceptions are handled in a single error-handler.

4.2 Crystallography

As each phase of a refinement has its own crystallographic description, the corresponding variables and functions are part of the phase class. For optimisation purpose, quantities like unit cell volume V_0, reflection d-spacings etc. are calculated once and stored. If during fitting the lattice parameters change, a call to the method `phase::recalc()` for each involved phase updates all information. For calculation of symmetry-related atomic positions during initialisation of a phase and general handling of space-groups, the library `SgInfo` by Grosse-Kunstleve (1999) is used. `SgInfo` provides ANSI C routines for the generation of symmetry matrices from a given space group symbol. The also available command-line utility provides access to many features useful for example for single crystal data analysis which are not used in **BETMAn**. After the space group symbol is read from a phase description file (see section 4.5), it is validated and for a valid space group symbol the matrices are generated. For each atom read from the phase description file, all possible symmetry equivalent atoms are derived from these matrices and when a previously unoccupied position is found, a new unit-cell atom is generated. During the whole process, messages are reported to the protocol output. With the content of the unit cell, the structure factor of any reflection of arbitrary structures may be calculated. Although currently not all structures are refinable (no triclinic and monoclinic systems, other than cubic implemented but not yet tested), for all structures the cross-section and simulated Bragg-edge transmission patterns may be calculated (see section 6.2). Reflection d-spacings are calculated by scanning all reflections between (HKL) and $(\bar{H}\bar{K}\bar{L})$ where (HKL) are adjustable maximum values for the Miller indices (`File - Settings`). If the d-spacing is above an also changable limit, the reflection is initialised and structure factor etc. are calculated. If the smallest d-spacing found by this procedure is more than 1% above the limit, a warning for the user is generated as (HKL) may be chosen inappropriately. The d-spacing limit is typically set to the minimal d-spacing of the instrument, at LANSCE this is about 0.25 Å. For example, for α-iron reflections (18 11 9) or (22 6 2) lie in this range, hence the edges are already very weak.

4.3 Fitting Algorithm

The fitting is implemented by the Levenberg-Marquardt algorithm as described by Press et al. (1992, section 15.5). This algorithm provides a combination of the steepest descent and inverse-Hessian methods and varies between the two extreme cases depending on the success of the trial values. It requires the first derivatives of the model function with respect to all fitted parameters (comments on this may be found in appendix E). The algorithm is reported to be robust and stable for the purpose of Rietveld refinements (Izumi, 1993). The routines provided by Press et al. (1992) are extended to use C++ exceptions, avoiding termination of the program in case of errors or divergence. The calling interfaces are changed to allow access to the data of phases, avoiding time-consuming re-calculation of frequently used quantities like unit cell volume or reflection d-spacings. The fit class also allows to name parameters, simplyfing generation of error messages (e.g. in the case of a zero derivative or too high parameter correlations) and intermediate result files. Routines to compare the derivatives calculated by the implementation of the fit-function and a numerical evaluation using Ridder's method (Press et al. (1992, section 5.7) are included. The fit function implementing the developed model for Bragg-edge transmission patterns is designed to handle further extensions, e.g. additional models for incident intensity, background or edge profiles. From the fit class, a class is derived adding features specific to fitting Bragg-edge transmission patterns (e.g. using measured data as incident intensity rather than modeling it, actual naming of the parameters, saving and loading of intermediate result files, loading of a setup-file `.set` providing starting values for instrument dependent parameters). The original fit class is much more general and was for example used to create a fit program for fitting kinetic data to the Johnson-Mehl-Avrami equation (Avrami, 1939-41, Johnson & Mehl, 1939) with just a few lines of source code. The listing can be found in appendix F.1.

The fitting of a Bragg-edge transmission pattern is terminated when for a given number of successive iterations no reduction of the residual is achieved. This was necessary as it was found in some cases that the fit remained for several iterations at a constant residual and then kept decreasing the residual significantly. For the fitting of Bragg-edge transmission patterns, after each refinement step (defined by the termination of the fitting algorithm) an ASCII-file containing the parameter values at that stage, their e.s.d. (estimated standard deviation) as provided by the Levenberg-Marquardt algorithm, the relative e.s.d. and the refinement flag indicating whether a parameter was variable during that refinement step is created. The extension of this file is `.irXXX` (**I**ntermediate **R**esult), where `XXX` is a number starting from zero and increased by one after each step. If a refinement is resumed, even in another session, the latest intermediate result file is automatically loaded. This allows to go back several steps simply by deleting the unwanted `.irXXX`-files. In appendix F.2, an example of an `.irXXX`-file of the refinement displayed in figure 2.1 of a single pulse Bragg-edge transmission pattern of an α-iron sample is listed.

The same type of files is used to provide starting values and variation schemes for the automated refinement (see section 4.6). In the latter case, the variation flags in the fourth column may be changed using any text-editor. No other changes should be performed.

4.4 User Interface

In order to simplify the application of **BETMAn**, a graphical user interface (GUI) was developed. As a platform-independent approach (Java, Tcl, WxWindows were examined for this purpose) at least at the time when the development started would have implied restrictions (stability, hardware resources,

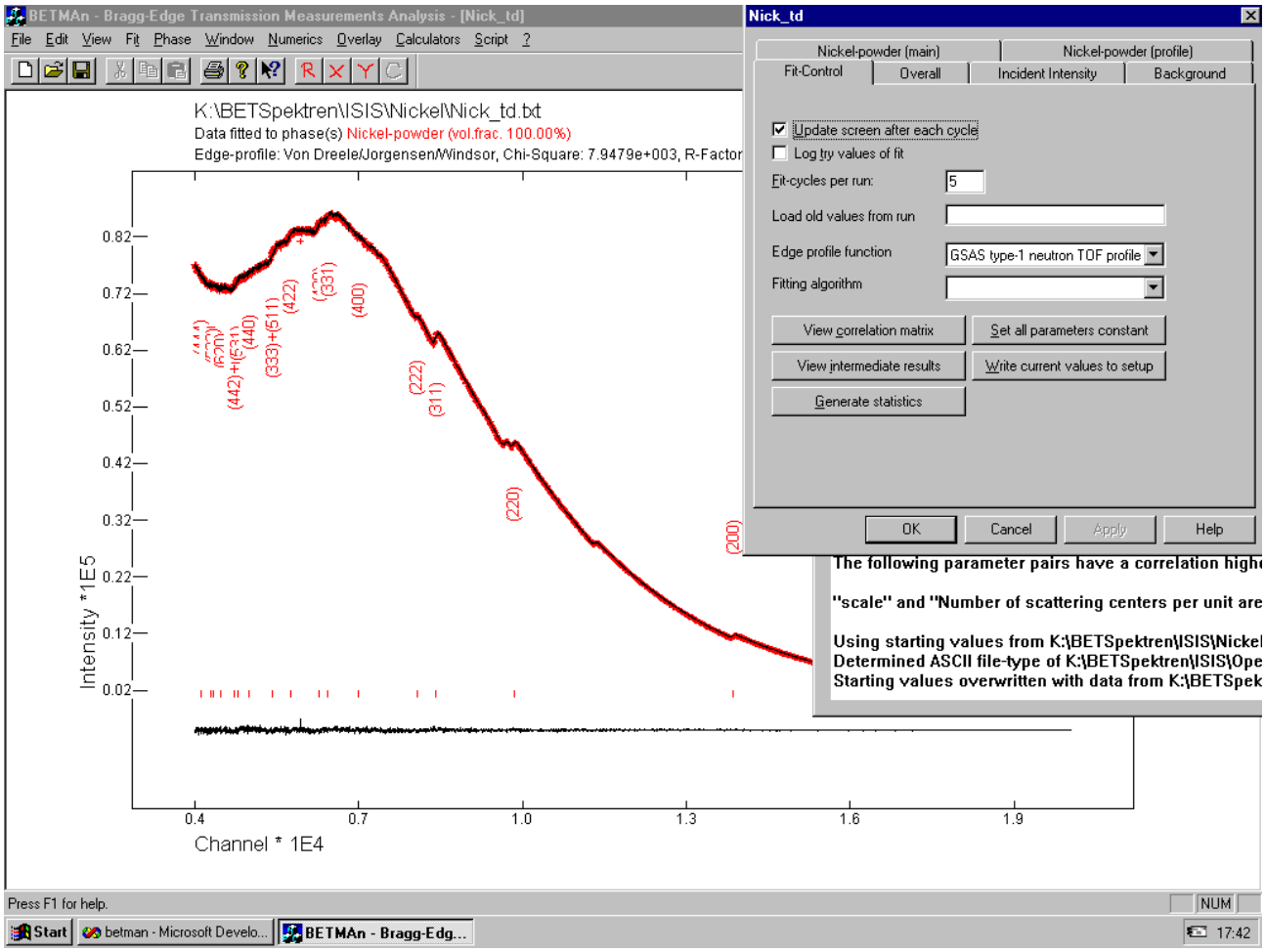

Figure 4.1: Screenshot of **BETMAn**'s user interface. Visible is the currently refined pattern, the menu structure (top) with the toolbar below, the fit control dialog (top right) and the protocol window (bottom right).

documentation, performance to mention some), Microsoft Windows was chosen as a platform and the Microsoft Foundation Classes (MFC) as an application framework. **BETMAn**'s user interface allows to access all functions via menus (see figure 4.1). Some frequently used program functions are also accessible via toolbars and keyboard shortcuts. The pattern currently under examination is shown together with the fit and the difference curve. Optionally, reflection tick marks and Miller indices, the background, the zero-line and the incident intensity as used by the fit may be displayed. Overlay of other patterns, for example to show the progress of a phase transition is also possible (see figure 7.3). Zooming is possible by choosing a smaller abscissa range. Multiple patterns may be loaded at the same time in their own windows (multiple document interface (MDI) as in Microsoft Word or Excel). Via the printing interface of Windows, any printer supported by Windows is accessible, including the generation of PostScript (`.ps`) files by spooling the output of a PostScript printer to a file. Such files may be converted for inclusion into text processors to encapsulated PostScript (`.eps`), Windows Bitmap (`.bmp`) or tagged image file format (`.tif`) files using the freely available software GhostScript. Direct export of cross-sections or measured patterns including fit, difference curve and any overlayed pattern to ASCII-files for processing in graphics software is also possible. For presentation purpose, the

abscissa can be converted from the default channel-format to energy, d-spacing, wavelength or time-of-flight. **BETMAn** can directly read the XSYS binary data format (`.dat`-files, used at LANSCE), the ISIS binary data format (`.raw`-files) and several ASCII formats (e.g. the one created by the ISIS software GENIE).

The fit is controlled by a dialog, divided into several functional pages (see figure 4.1). The 'fit-control' page allows to change the number of consecutive fit cycles without change of the residual before the refinement stops, the choice between the implemented edge-profile functions and several controls of the fitting algorithm (output of guess values, numerical calculation of derivatives). This page also provides access to the correlation matrix and the last result `irXXX-file`. All other pages contain fit parameters: Overall fit parameters (flightpath length, time offset, overall scale factor etc.), incident intensity (measured or function, file of the pattern used for measured incident intensity or access to the model parameters), background (type of background model, source frequency, background parameters) and two pages for each phase where phase dependent parameters (number of scattering centers per unit area, lattice parameters, atomic parameters, profile parameters) are accesible. For each fit parameter the current value and the flag indicating whether the parameter is actually refinable is displayed and may be modified. For application examples see the tutorial in appendix H.

4.5 Phase Description

BETMAn currently provides two possibilities to input a phase description: Its own `pha` format and the well-established CIF (**C**rystallographic **I**nformation **F**ile) format.

4.5.1 `pha`-file

Based on `pha`-files describing cell-geometry and -content, cross-sections of samples can be calculated and starting values for lattice parameters are provided. A `pha`-file looks like

```
#phase Ortho-Enstatit

#space P b c a

#a   18.21
#b   8.812
#c   5.178

#atom         Mg   0.3760   0.6544   0.8663
#atom         Mg   0.3769   0.4854   0.3609
#atom         Si   0.2716   0.3411   0.0494
#atom         Si   0.4740   0.3373   0.7988
#atom         O    0.1832   0.3386   0.0349
#atom         O    0.3118   0.5022   0.0430
#atom         O    0.3036   0.2252  -0.1698
#atom         O    0.5628   0.3382   0.8009
#atom         O    0.4337   0.4841   0.6880
#atom         O    0.4470   0.1961   0.6004
```

This file describes the structure of ortho-enstatite, an orthorhombic modification of the single chain ('Zweier-Einfachkette' after Liebau, 1962) silicate enstatite $Mg_2Si_2O_6$ (orthopyroxene group, e.g. Putnis, 1992, sect. 6.4.1). The first keyword, `#phase`, provides simply a phase name. `#space` provides the space-group of the phase in the common way ('international' or 'Hermann-Mauguin' symbols, no

Schönflies symbols). `#a`, `#b` and `#c` define the corresponding lattice constants, in monoclinic and triclinic systems the keywords `#alpha`, `#beta` and `#gamma` are used for input of lattice angles (for trigonal and hexagonal symbols the angle γ can be omitted as **BETMAn** deduces it from the space-group). Each `#atom` line contains the type and fractional coordinates of an atom of the asymmetric unit. The total number of 80 symmetry related atoms in the unit cell of ortho-enstatite is calculated using the space-group routines (see 4.2). If a fourth number is provided, it is interpreted as a site occupation factor (sof) which allows for example to describe alloys with significant amounts of substitutional elements. If nothing is given, an occupation of 1.0 is assumed. Fifth to seventh numbers are treated as scattering length (given in fm), incoherent scattering cross-section (given in barn) and absorption cross-section (given in barn). These numbers are usually not necessary as the nuclear data of the atoms is taken from a database if this input is missing. The input file is format free, e.g. the entries may be separated by any number of spaces or tabs. Any line not beginning with `#` is treated as comment. The input is not case-sensitive.

4.5.2 CIF-file

The Crystallographic Information File (CIF) format is described by Hall et al. (1991). It is basically an ASCII file format consisting of several fields. The format is for example generated by the Inorganic Crystal Structure Database (ICSD) and was added as input format for **BETMAn** to be able to directly read such files. In appendix F.3, an example of a CIF-file, describing the same structure ortho-enstatite as above is presented. **BETMAn** extracts the same information as is the case for the `pha`-format and ignores any further information.

4.6 Batch Processing

The need to process hundreds or even thousands of Bragg-edge transmission patterns to study a phase transition definitely requires automated refinements. For this purpose a batch mode was implemented. The commands are described in appendix G, an application example is given in appendix F.4. See also sections 7.1.4 and 7.2.4 for further information. Starting values for the first pattern of a sequence of Rietveld refinements have to be provided by the user. The resulting parameter values of the fit of the first pattern are used as starting values for the second pattern and so on, resulting in a long chain of Rietveld refinements. To avoid divergence because of fitting structural parameters of phases with a too low volume fraction or fits of patterns with too few counts due to beam failure, conditional refinements are possible.

4.7 Database

BETMAn uses a database consisting of a number of tables. In the database, nuclear data as well as atomic mass and Debye-temperature of isotopes and elements are stored. The parameters describing a measurement file, namely flightpath length, time-offset and channel width and a comment describing the measurement file are stored together with the fit-setup file and the phases used for the refinement. The data is accessed via ODBC (Open DataBase Connectivity), a programming API (Application Programming Interface) allowing to access data independently of the used database and -format via SQL (Structured Query Language) and a driver (e.g. Geiger, 1995). This allows to use any database

software providing an ODBC driver for storing the data and therefore allows to scale the database without changing the source code. Currently, the format is dBASE using a DBF-ODBC driver as this appears to be the easiest way to distribute **BETMAn**.

The nuclear data is also accesible via a DOS-program `SCATTL.EXE`, allowing to search and view the records of each isotope or element. `SCATTL.EXE` is installed together with **BETMAn**. The nuclear data (scattering length, incoherent scattering and absorption cross-section) are once directly read from a HTML page generated by NIST (1999) into the database. The Debye-temperatures were obtained from Kittel (1996), the atomic mass data from a standard periodic table of the elements.

Chapter 5

Experimental Setup at LANSCE

This chapter describes the setup of flightpath 5 at LANSCE where all Bragg-edge transmission experiments at LANSCE were executed. The current state of the data acquisition system is outlined as well as experiments for the background determination and flightpath length calibration. The problem of the 60 Hz noise in the current mode is briefly explained.

5.1 General Setup

The generation and moderation of neutrons at LANSCE was already described in sections 1.2 and 1.3. The used flightpath consists of an evacuated beam tube between moderator and the shielded experimental room, the 'cave', followed by a second evacuated beam tube leading to the detector station. A beam dump is located behind the detector system (see figure 5.1). The first beam tube starts close to the high-flux water moderator and has a length of 6.73 m. In direction of the neutron beam, a changable collimator made of polyethylene (CH_2) and steel with holes of converging diameter is installed in the tube. Steel slows and scatters high energy neutrons away from the incident beam direction, polyethylene does the same for low energy neutrons. Currently, collimators of 19.8 and 42.8 mm exit diameter are available. It is possible to position a detector directly in the cave for experiments demanding a very high neutron flux. The single pulse experiments reported by Bowman et al. (1991) were taken with a detector run in current mode at this position.

The second beam tube has a diameter of 74.3 cm and runs over a length of 45.7 m through volcanic rocks to the detector station. Both tubes are made of steel and covered at both ends with aluminum plates. Holes covered with thinner aluminum sheets are drilled into the plates where the highest neutron intensity is expected (so-called 'neutron windows'). Aluminum is used as it has low coherent and absorption cross-sections and virtually no incoherent scattering cross-section. The spots of maximum intensity are marked and used to align samples with a laser setup such that both points on the end-plate of the first tube and the entry-plate of the second are hit by the laser beam. The evacuation of both tubes (less than 50 Pa, equivalent to less than 0.1 % of local atmospheric pressure) prevents the severe intensity losses of approximately 5% per meter in air (Windsor, 1981, p. 204). In a distance of approximately 20 cm from the exit of the second beam tube, the detector system is located (see next section and section 1.4). In the detector station, on the opposite side of the beam tube a short tube is drilled into the rock where neutrons not captured in the detector decay according to (1.1). A schematic of the setup is given in figure 5.1. According to Windsor (1981, equation (10.9)),

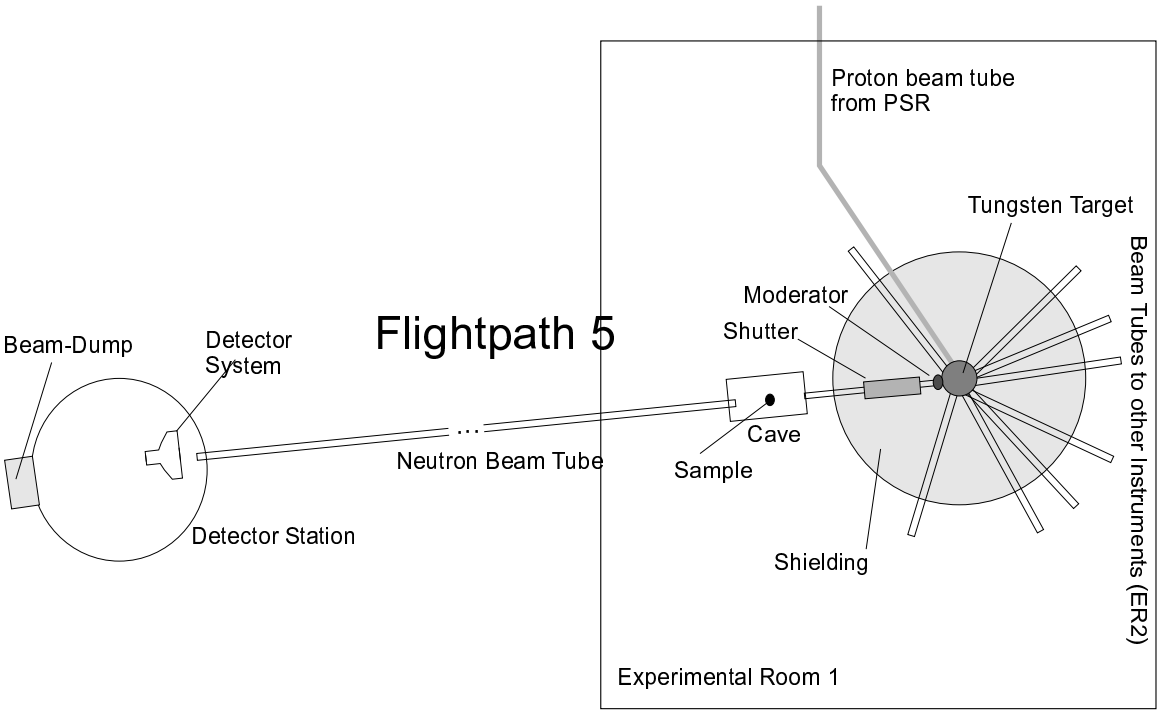

Figure 5.1: Schematic of setup at flightpath 5 of LANSCE. The total distance between moderator and detector is about 58.5 m.

the expected resolution (peak width) of such a setup is given by

$$\frac{\delta\lambda}{\lambda} = \frac{\delta_m}{L} = \frac{0,0336\text{m}}{58.5\text{m}} \approx 6 \cdot 10^{-4} \tag{5.1}$$

where δ_m is the moderator thickness (cf. section 1.3). The contribution of the divergence to the flightpath uncertainty is of second order, as in the worst case of a divergence of 43 cm (detector diameter) the additional flightpath is only $(\sqrt{58.5^2 + 0.43^2} - 58.5)$ m= 1.6 mm.

5.2 Detector and Data Acquisition

The electronics setup is presented in figure 5.2. The efficiency for thermal neutrons of the ^{10}B loaded liquid scintillation detector is virtually 100% (Yen et al., 1993, Knudson et al., 1996). As the neutrons of interest for Bragg-edge transmission experiments are already thermalized, further moderation in the liquid does not happen (as in the case of epithermal neutrons for which the detector system was originally designed). Hence, the additional broadening from the detector system is negligible. The pulses of the 55 photomultiplier tubes viewing the ^{10}B loaded organic liquid scintillators are filtered by a low pass filter. This broadens and reduces the amplitude of the very narrow pulses resulting from γ rays so that they can be better discriminated from pulses of approximately 20 ns FWHM generated by neutrons. The discriminator also shapes the pulses to standard NIM pulses of 7 ns width. As currently only one counting device is available, the signals from the 55 discriminator stages are joined on a single cable using logic fan-in/fan-out stages. This introduces some additional dead-time to the detector system. Over approximately 100 meters distance, the pulses are broadened in transmission and are consequently re-shaped before they are fed into a multi-channel scaler. For each time bin (e.g.

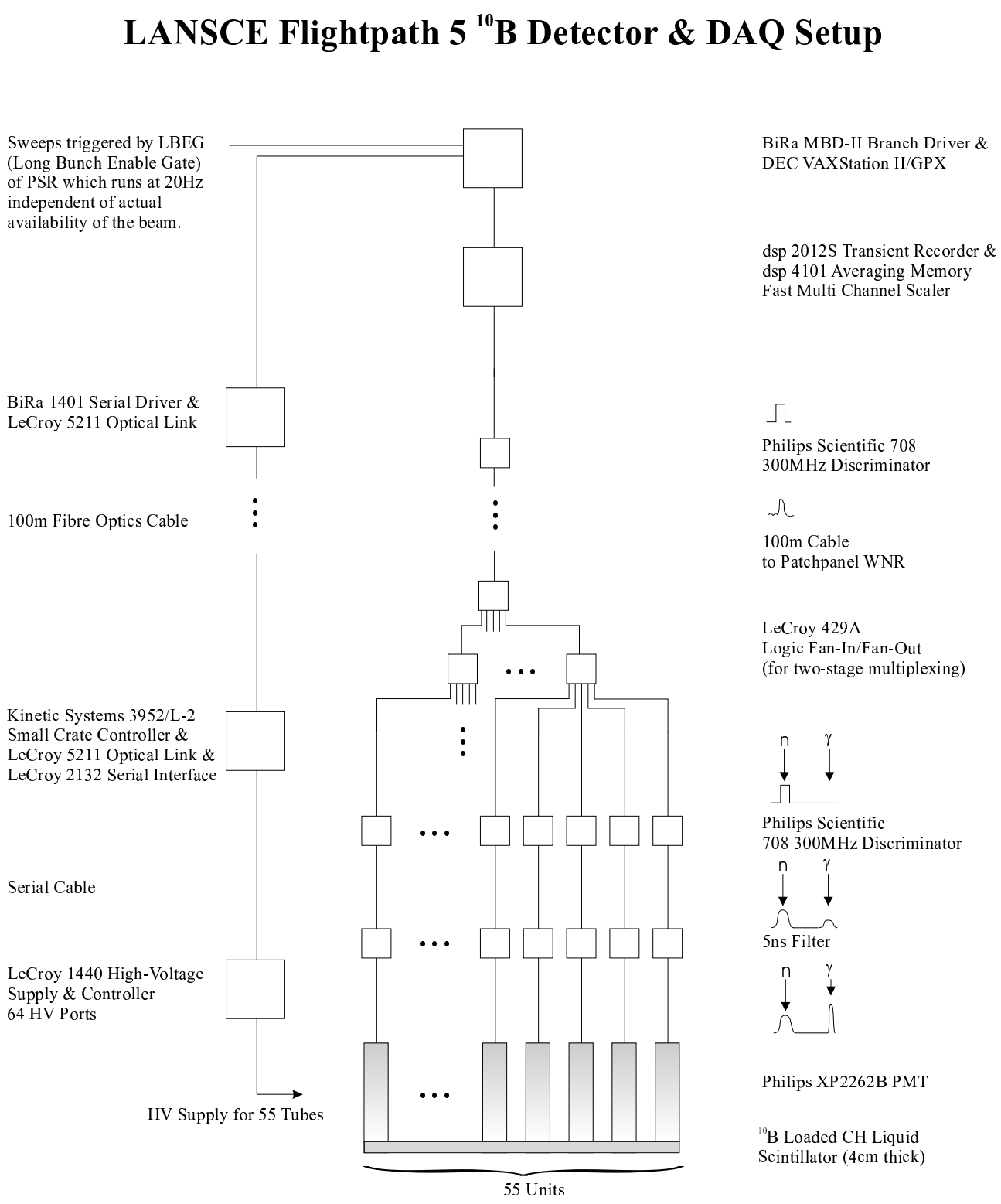

Figure 5.2: Electronics setup at flightpath 5 of LANSCE as used for the Bragg-edge transmission experiments during the 1998 run cycle.

5 μs), the number of counts is digitized and stored within the multiscaler. After each complete scan (8192 time bins) the stored number of counts for each bin is added to a corresponding running sum in an averaging memory module. For static experiments, the data acquisition is triggered via magnetic induction by the proton pulse. Naturally, this trigger is only available when the accelerator produces protons. The data acquisition is optionally triggered by the so-called long bunch enable gate (LBEG), a signal of the proton storage ring (PSR) slightly pre-cursored to the ejection of the proton burst to the spallation target. This signal is also sent when no protons are available from the accelerator, hence, in the case of a beam failure, potentially empty patterns are stored but data continues to be taken at fixed and unvarying real-time intervals - which is important for measurements of reaction kinetics (see section 6.4 for an example of a loss of synchronisation due to beam failure). In most cases the trigger for the data acquisition was further delayed to shift the available wavelength range, defined by the flightpath length/source frequency and the number of available channels of the data acquisition, towards higher d-spacings where the most intense edges are located. After the desired number of neutron pulses/triggers, the content of the averaging memory is read into a DEC VAXStation via the CAMAC bus (Computer Applications to Measurement and Control). At this point, the pattern is stored in a data-area of the XSYS data acquisition software (Setze et al., 1995) running on the VAXStation. When the desired number of data areas is taken (usually 20 patterns), the memory is flushed to hard disk in a single data file.

The VAXStation is also used to control the high voltage of the photomultiplier tubes. Each tube can be controlled individually, allowing the pulse height from each tube to be adjusted equal to that of the other tubes. The high voltage supply at the detector station is remote controlled by a serial controller, connected by fibre optics cable to the data room.

5.3 Calibration Measurements

5.3.1 Background

Due to the high intensity of the transmitted neutrons and the, at least for the 60 m detector, long distance from the source, background is a second-order problem for the Bragg-edge transmission technique. Nevertheless, the background was measured by placing foils of indium, cadmium and gold in the neutron beam. The transmitted intensity was then counted with a single detector at the 60m detector station (see figure 5.3). Indium and gold exhibit strong resonances at 9.07, 3.85, 1.46 eV (^{115}In) and 4.91 eV (^{197}Au), meaning that neutrons of such energies are absorbed with a very high probability. Cadmium absorbs neutrons with energies smaller than 250 eV (approximately from channel 4000 in figure 5.3) over a very broad energy range. All stated resonances are termed 'black' for the thicknesses of the foils used because the transmitted intensity drops to zero at those energies. Thus, any signal at the energy range of the black resonances must be from background. The detector used was a lithium-glass scintillator with photomultiplier-tube of the current-mode setup (i.e. a special wiring of the photomultiplier base). The high voltage was adjusted such that it optimized the tradeoff between dead-time and pulse size when a neutron was detected. These conditions were found to be fulfilled with a voltage of -1520 V. The signal was then passed through a low-pass filter, amplified by 26 db, discriminated, reshaped and fed into a multichannel scaler PC-board made by EG&G Ortec. The background shows a decaying component which drops to zero after about 7 ms. This is most likely some decaying process from the initial high-energy neutron burst or the γ-flash of the spallation. The region of interest for Bragg-edge transmission measurements at 60 meters is from approximately 10 ms to 50 ms. As figure 5.3 clearly shows, the background is negligible in this region because in the

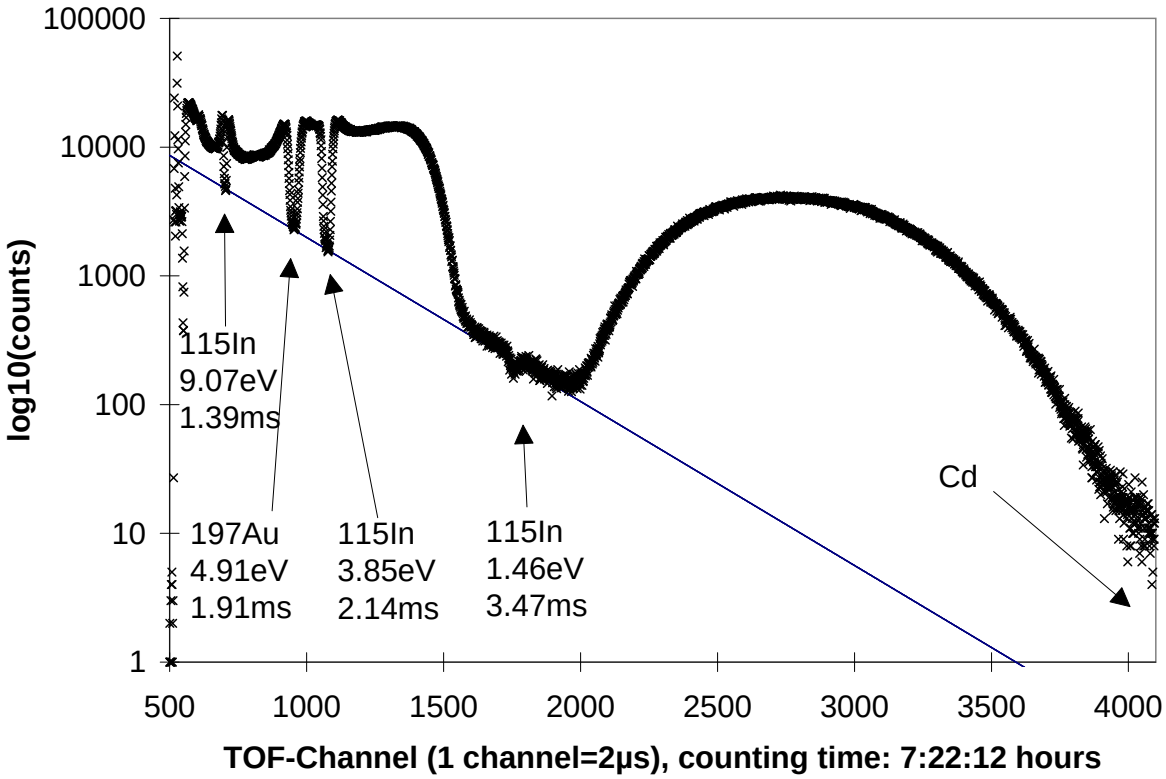

Figure 5.3: Background measurement. The drops in the intensity result from nuclear resonances of the indicated isotopes.

range of the cadmium resonance count-rates in the order of 10 per hour are detected. Consequently, for the 60 m experiments no explicit background correction with the function described in section 3.9.2 was needed. As can be seen in figure 5.4, with a sample absorbing neutrons much less than cadmium, a time- and approximately sample thickness independent background of about 2000 counts per bin of 5μs bin width accumulated during a measurement time of 450 seconds. This is equivalent to about $9 \cdot 10^5$ counts per second of time-independent background at the detector station (a 'neutron gas'). In the measurements described in the following chapters, much thinner samples were used and the relative background is much less.

It is therefore likely, that any fitted background having a non-constant shape, at least in the case of 60m experiments, is completely due to misfits between fit-model and measured data.

5.3.2 Flightpath Length

To calibrate the flightpath for the 1998 run cycle with the at that time new detector system, a Bragg-edge transmission pattern of 99.2% pure Fe powder of 48 mesh was taken. The thickness of the Fe powder layer was about 2.5 cm along the beam direction. Assuming that this powder has a lattice constant of 2.8665 Å, the flightpath and the time offset were determined by fitting these variables to this pattern. The procedure is described in appendix H as part of the **BETMAn** tutorial. As can be seen in figure 5.5, the difference curve is very flat. The flightpath length determined from this fit is 58.60 m, and the time offset was 8.153 ms. It should be noted that these values depend on the profile function used (edge profile derived from Jorgensen et al.) and may vary if, for instance,

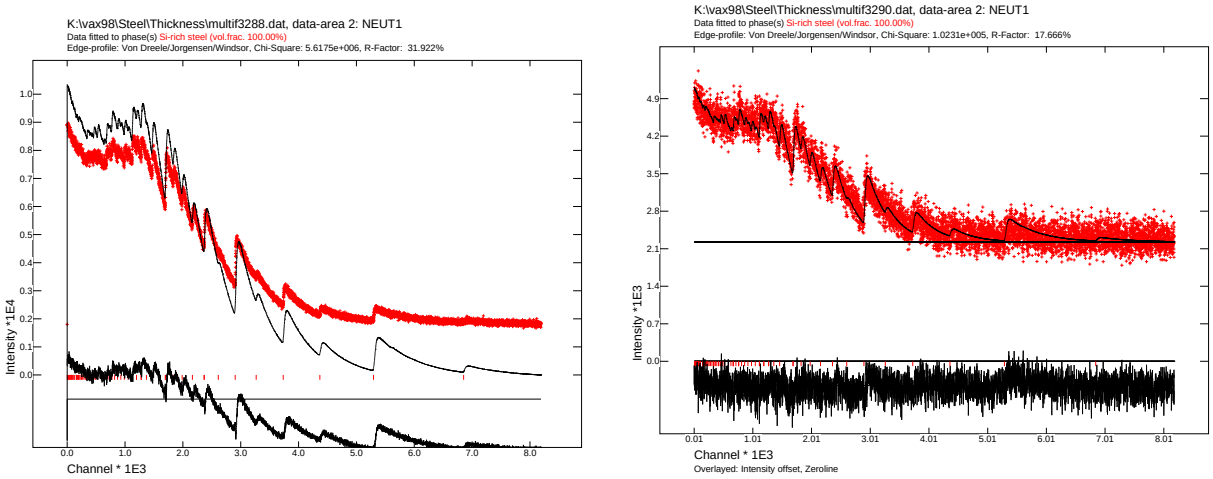

Figure 5.4: Measured transmitted intensity for 50mm (left) and 80mm steel. 9000 neutron pulses were accumulated in both cases. A time-independent background level of about 2000 counts (for accumulation of 9000 pulses) is clearly visible in both plots. In the left plot, a fit without modeling this constant background is shown (sample thickness was held constant at 50mm during the fit, the only variable parameter was the overall scale factor). For the right plot, the overall scale factor and an offset were fitted (thickness set to 80mm). The agreement is much better.

the complementary error function is utilized to describe the edges. Six coefficients of the background function were fit. The estimated sample thickness calculated from the refined number of unit cells per unit area is about 1 cm. This thickness is of the right magnitude for a sample of ideal density rather than an uncompressed powder. The fit coefficient σ_1 (see section 3.3.4) is with $3.4 \cdot 10^{-3}$ about 5 times larger than expected by equation (5.1), indicating additional sources of broadening, e.g. from the sample or the used collimator setup. The former may be excluded by another calibration substance like MgO, known to contribute very little to reflection broadening. Also fit were the profile parameters α_0, β_0 and β_1 as well as $B_{iso,n}$ of the iron atom. The first three also affect the edge broadening coefficient σ_1 and may be a numerical contribution to the discrepancy between the expected and fitted value.

5.3.3 60 Hz Noise

If data has to be taken in current mode, as, for instance, the neutron intensity at a short flightpath length is too high for counting mode or old data is analysed, the measured signal is likely include a contribution of 60 Hz noise pickup from the power supply (see figure 5.6). It is strongly desirable to correct for this noise as it affects the structural parameters especially of phases with small volume fractions.

One way to correct the patterns is a 60 Hz subtraction implemented in hardware as described by Bowman et al. (1990). This assumes that n/60th of a second after the spallation pulse the pattern contains only noise. By measuring this pattern for 1/60th of a second, data is obtained that can be subtracted from the original data which is then corrected for the 60Hz noise. With a 20 Hz beam repetition rate, the value for n can be either 1 or 2 and still allow the taking of the noise data before the next neutron pulse starts at $n = 3$, but in practice only $n = 1$ is used so as to provide enough time to execute the subtraction by the electronics. Another assumption is obviously that the noise does not scale with the measured neutron intensity. This procedure is possible only for short flightpaths or

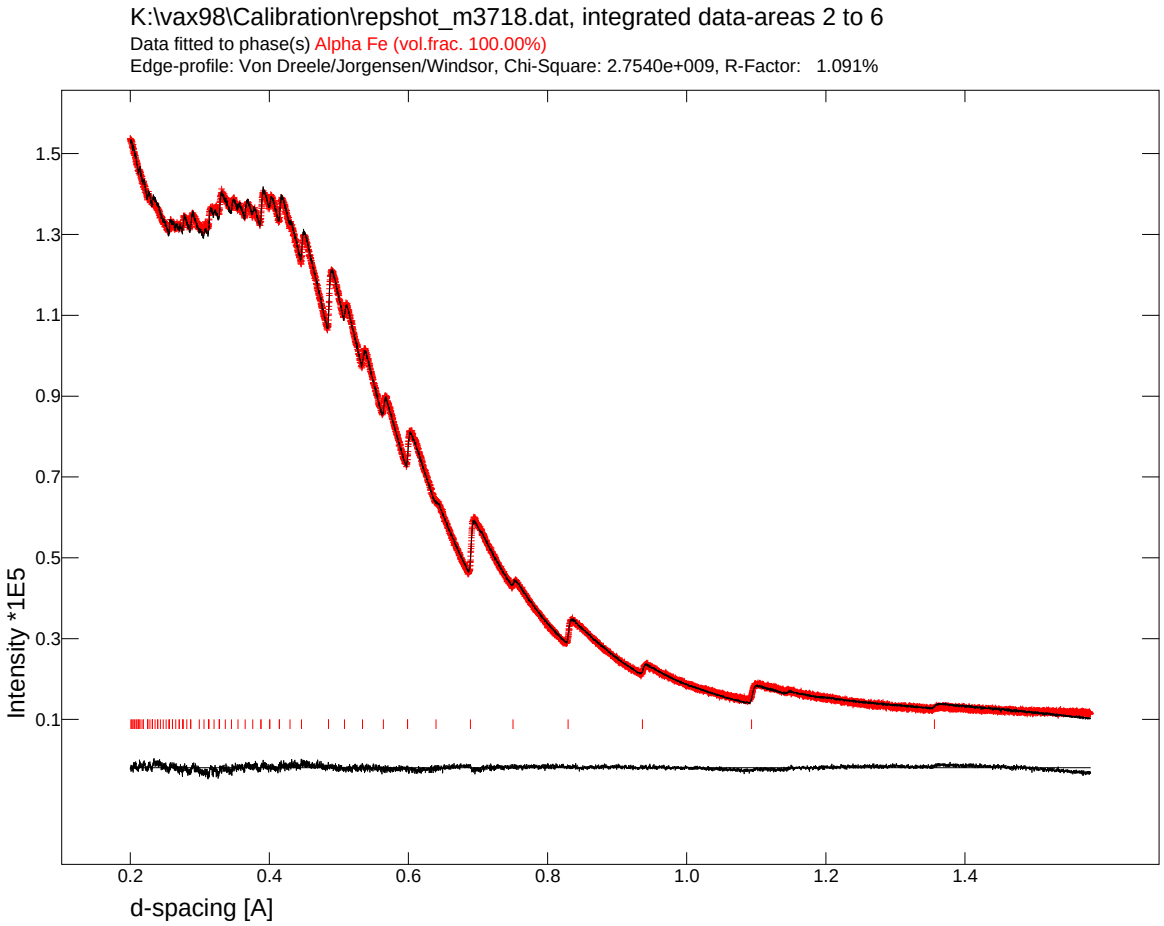

Figure 5.5: Measured data (crosses) and fit through the data of 99.2% pure Fe powder. Edge positions are indicated by tick-marks, the curve below is the difference curve in the same scale as the data. The measurement time was 15 minutes.

highly absorbing materials, transmitting virtually no low energy neutrons as is the case for samples used in nuclear resonance spectroscopy (NRS). Otherwise, the assumption of zero neutron intensity during the 1/60 second taken as 60 Hz noise only is not fulfilled.

Although the shape of this noise can be readily measured by doing a simple closed shutter run (see figure 5.6), an offline correction is not possible as the noise does not remain constant with time.

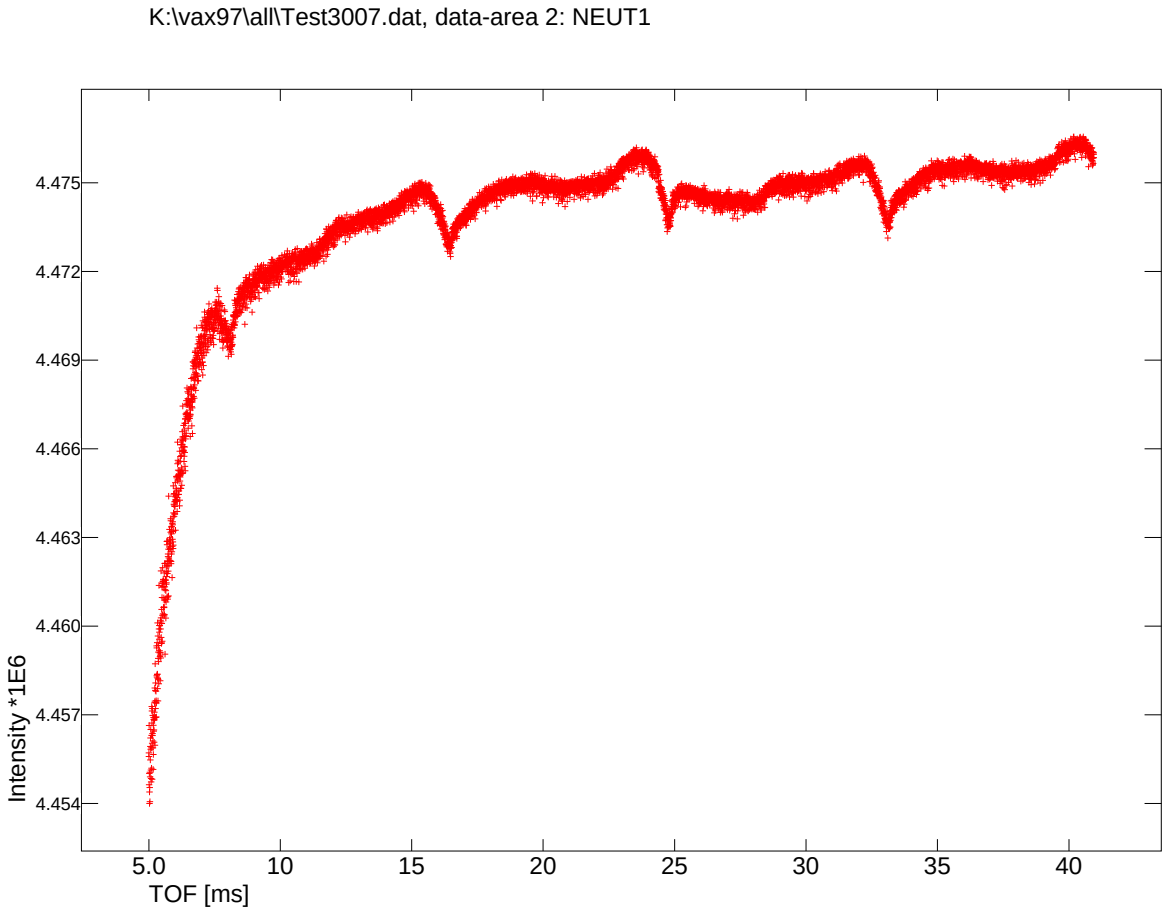

Figure 5.6: Example of 60 Hz noise measured in current mode. The signal voltage is inversely proportional to beam intensity. An arrangement of bricks of 4.5 cm polyethylene, 11.5 cm steel and 5 cm polyethylene was placed in the beam, so that no thermal neutrons reached the detector. It is clearly visible that the structure repeats every 16.6 ms and also contributes to higher intensity (most likely from the γ-flash).

Chapter 6

Validation & Benchmarking

In this chapter experiments validating the results of **BETMAn** are described. The capability to fit an incident intensity spectrum is descibed in section 6.1. A simulated Bragg-edge transmission pattern of cristobalite is compared with the corresponding measurement in section 6.2. In section 6.3, the influence of sample thickness on the refined parameters is investigated. The resolution of the setup at LANSCE is derived from the thermal expansion of steel in section 6.4. Section 6.5 presents an application of **BETMAn** to data acquired at ISIS to study the strain response of a steel sample on external stress.

6.1 Fitting Incident Intensity

Figure 6.1 shows the open beam taken with counting mode detector setup at the 60 m detector station. Clearly, the Maxwellian distribution superimposed on an exponential decay of the spallation neutron intensity is visible. The fit was performed with the incident intensity function (3.73), coefficients P_2 to P_{11} were fitted. The moderator temperature as derived from coefficient P_3 using equation (3.77) is 314 K, in good agreement with the water moderator at room temperature. For clearity, the difference curve is multiplied by 5. From the tick-marks indicating positions of aluminum reflections, the contamination of the incident intensity spectrum by aluminum edges (end-caps of beam tubes) can be clearly seen in the difference curve. In a second step, for the same pattern an additional phase α-Al was fitted. The residual χ^2 is reduced by about 25% by this and the difference curve becomes flatter, although some edge-like structures are still apparent. It is remarkable that even a refinement of the lattice parameter does not result in a divergence of the fit. The layer thickness from the refined number of unit cells per unit area of aluminum is about 1 cm, the moderator temperature is estimated from this fit to 303 K. Both values are in very good agreement with the experimental parameters. The sample thickness for aluminum can be estimated much more reliably as aluminum exhibits virtually no incoherent scattering and therefore the incomplete model of the total cross-section is negligible.

Comparision with figure 6.8 shows that the contamination with aluminum is much more severe at the transmission setup used at the ENGIN instrument at ISIS.

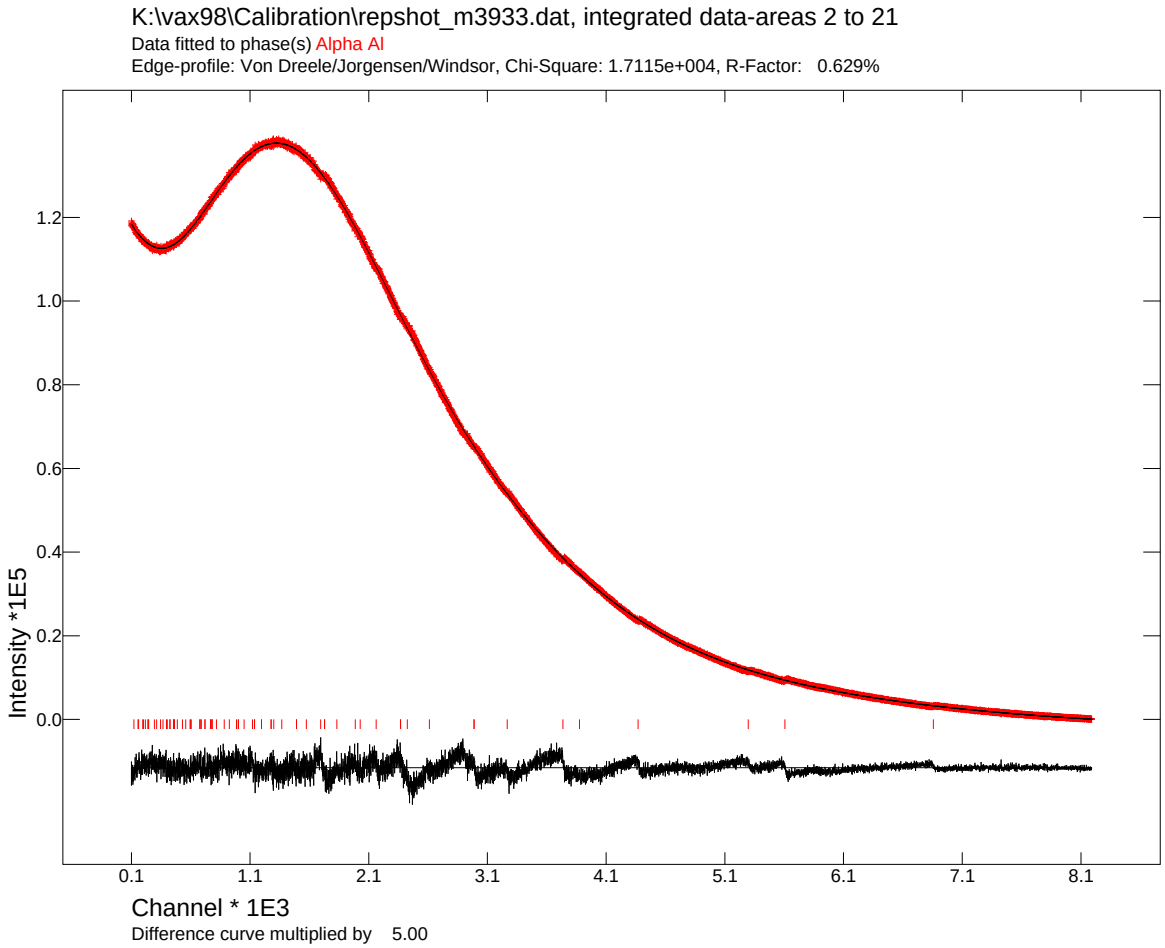

Figure 6.1: Fit of the open beam (incident intensity) at flightpath 5 of LANSCE with the incident intensity function. The difference curve is scaled by 5. The tick-marks indicate the positions of Al reflections, showing that the difference curve exhibits the main deviations between fit and measured data at those positions.

6.2 Simulation of Bragg-Edge Transmission Patterns

To plan experiments, it is desirable to predict Bragg-edge transmission patterns of the material of interest. If it turns out from the simulation, that the material is suitable for Bragg-edge transmission, i.e. the edges are likely to be clearly visible and hence attempting a fit may lead to convergence, calculation of an 'optimal' sample thickness is necessary. Both tasks can be done with **BETMAn**.

Figure 6.2 shows simulated and measured Bragg-edge transmission patterns of cristobalite, a (metastable) high-temperature, low-pressure modification of SiO_2 (e.g. Putnis, 1992, section 6.8.1). The data were taken at room temperature, therefore the tetragonal low-cristobalite rather than the cubic high-cristobalite was used for the simulation. Measurement and simulation were performed to judge whether investigation of kinetics of the high↔low cristobalite transformation is possible by means of Bragg-edge transmission. It was concluded that at the current stage (data analysis, experimental setup) the edges are to weak for a meaningful refinement, although the edges of the cubic high-cristobalite are expected to be more pronounced. The calculated sample thickness for a transmission of $T = 0.1$ (i.e. in average over the accessible wavelength range 10 % of the neutrons reach the

detector) is approximately 10 cm assuming ideal sample density, i.e. x-ray density and no porosity or other powder effects. Therefore, doubling the used powder layer thickness will improve the contrast. Cristobalite leaves much weaker edges in the transmitted intensity than iron due to the fact that silicon and oxygen have much weaker coherent scattering cross-sections (2.16 and 4.23 barn, respectively) than iron (11.22 barn, see also the cross-section plots in the bottom of figure 6.2). Nevertheless, the measurement clearly shows the quality of the simulation: Despite some shift due to different flight-path lengths, the few distinct features of the cristobalite pattern between 1.1 and 1.3 Å were predicted correctly.

In figure 6.2, also the calculated cross-sections for iron and cristobalite are shown. To simplify comparison, the cross-section is given per volume (i.e. the cross-section calculated per unit cell is divided by the unit cell volume). Keeping in mind that the accessible d-spacing range with the 60m setup at LANSCE ends at about 1.7 Å (calculated from the flightpath lengths and the neutron pulse frequency), it is obvious that no good Bragg-edge transmission patterns can be expected from tetragonal cristobalite as the elastic coherent scattering cross-section per volume is in the order of 20 barn per unit volume and exhibits much smaller edges than the cross-section for iron, being additionally three times larger. It can also be seen that cristobalite exhibits more intense edges at d-spacings > 2.5 Å, hence a measurement at 10 m (accessible d-spacing range up to 9 Å given that the moderator releases neutrons of such wavelengths) may make investigations of cristobalite possible. A suggestions for a 'quality-factor' for judgement of the suitability of crystal structures for Bragg-edge transmission measurements is presented in appendix I.

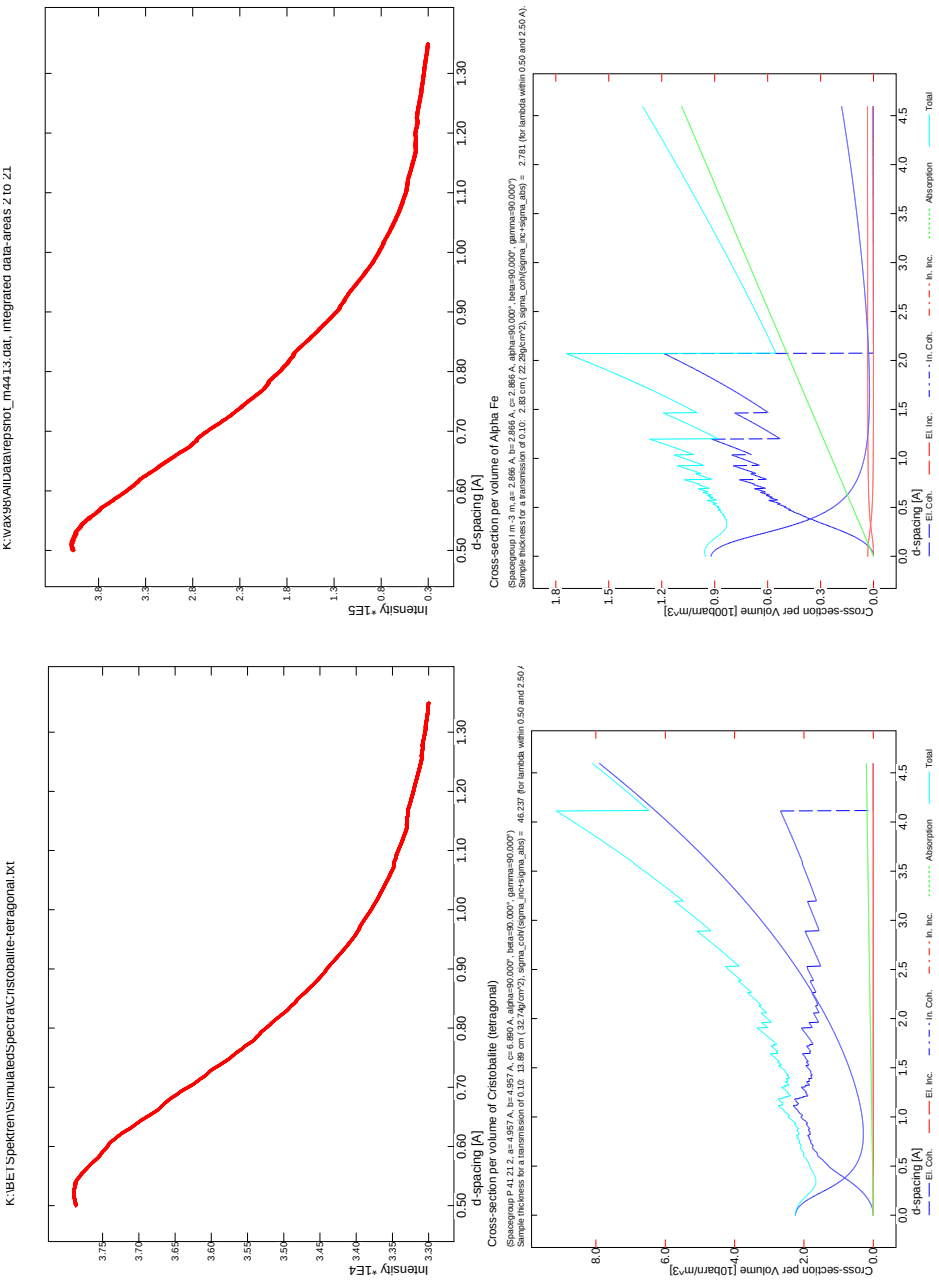

Figure 6.2: Comparision of simulated (top left) and measured (top right) Bragg-edge transmission pattern of low-cristobalite. The measured pattern was taken with a layer of about 7.5 cm cristobalite tablets (3 cm diameter) within 10 minutes of beam time. For comparison, the calculated cross-sections for low-cristobalite (bottom left) and iron (bottom rigth) are shown. Note that the scale is 10 barn per m^3 for cristobalite and 100 barn per m^3 for iron. The inelastic coherent scattering cross-section of cristobality is very likely not realistic due to the fact that no Debye temperature, as necessary for the inelastic cross-sections, for oxygen is given and a default was used.

6.3 Sample Thickness

To determine the influence of sample thickness on refined structural parameters, a series of measurements with steel disks of varying thickness was performed (see section 7.1.2 for a description of the steel). From manual refinement of a pattern taken with 24 mm steel in the beam, starting values for automated refinements were derived. A measured open beam pattern was used as incident intensity. A total of 11 different thicknesses between 2 and 80 mm were measured. Figure 6.3 shows the results

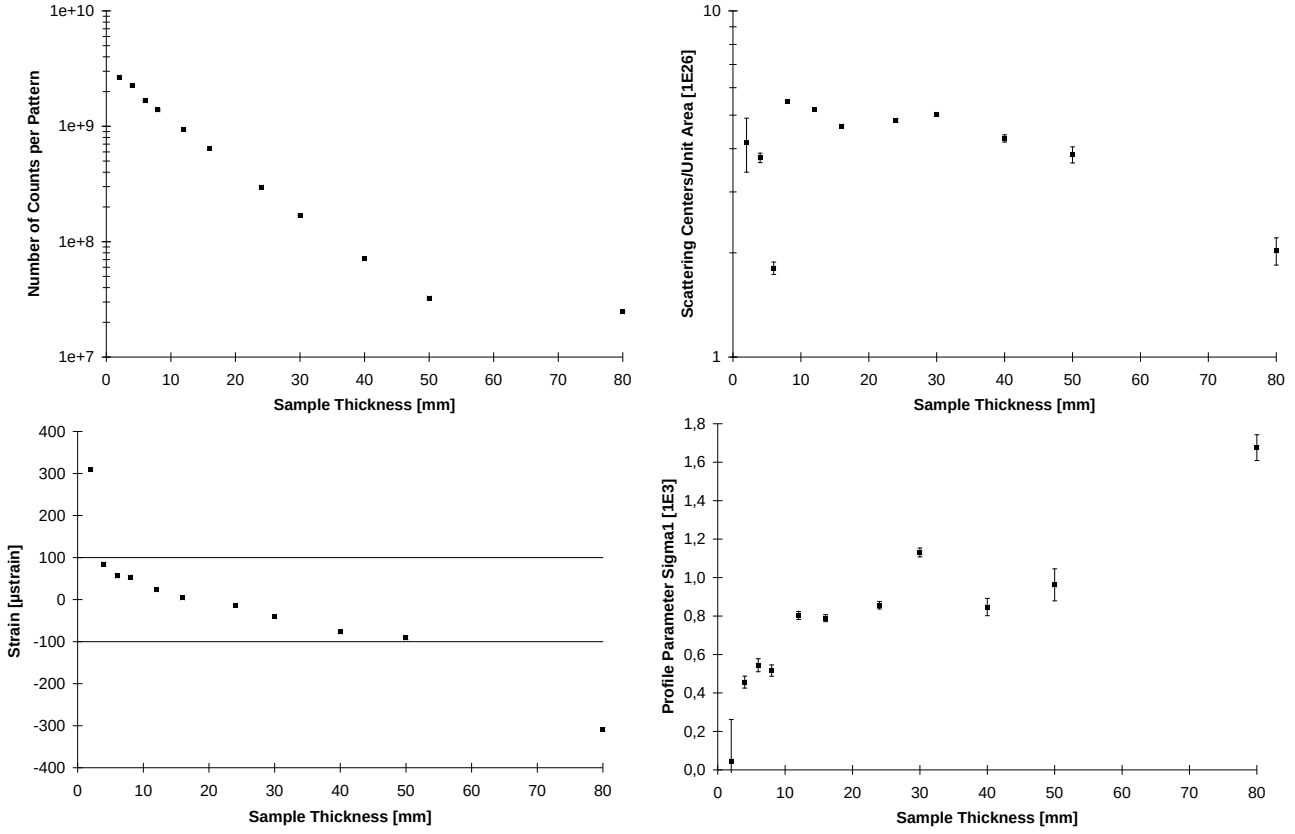

Figure 6.3: Results of refinements of patterns resulting from different layer thicknesses of steel (Fe-0.38C-1.94Si-2.99Mn wt. %). From top left to bottom right, the number of detected neutrons, refined unit cells per unit area, the strain relative to the average refined lattice parameter and the refined profile parameter σ_1 are displayed. All error-bars correspond to the e.s.d. resulting from the fit.

of the refinements. The number of detected neutrons exhibits the expected behaviour of a line with negative slope on a logarithmic scale. This plot also indicates that no major variations of the neutron flux appeared throughout the measurement. Except for thin sample thicknesses, the refined number of scattering centers/unit cells per unit area shows the same behaviour, although the data is much more scattered. This might be due to the not yet complete model used in **BETMAn**. Volume fractions in multi-phase systems are not affected by the incomplete model as they are derived from edge-height ratios.

The lattice parameter, displayed as strain

$$\varepsilon = \frac{a - a_0}{a_0} \tag{6.1}$$

with the average lattice parameter (2.8619 Å) as reference lattice parameter a_0, exhibits a clear decreasing trend with increasing sample thickness. The same effect was found during data-analysis by a single edge fit approach of data from a similar experiment performed at ISIS (Santisteban, 1999). Nevertheless, except for very thin or very thick layers, the results are within 100 microstrain. An effect depending on the sample thickness and hence a possible explanation is multiple scattering. Assuming, that some backscattered neutrons, i.e. traveling towards the source, are backscattered again such that they arrive with some delay at the detector, a potentially thickness dependent shift of the edges is conceivable. Despite the fact that backscattered neutrons are much more likely to be scattered by other lattice planes than the one with the appropriate d-spacing for a second backscattering and hence would never reach the detector, this effect should lead to a shift towards higher d-spacings for thicker samples. This is contrary to the obeserved effect and hence multiple scattering can be clearly excluded as its reason. Further investigations on the reason and potential correction of this systematic change of the lattice parameter are required. The same is the case for the edge width parameter σ_1: Although the values are much closer to the expected value of $0.4 \cdot 10^{-3}$ (see equation (5.1) and section 5.3.2), they exhibit again a systematic dependence on the sample thickness.

The findings may be not applicable to varying volume fractions, i.e. 'layers' consisting of many grains distributed within the sample rather than a single bulk piece as in the present case: As a physical reason for the dependence of structural parameters on the sample thickness is not realistic, a numerical artefact introduced by the data analysis procedure is likely. Clearly affected by the sample thickness is the slope of the falling flank of the Maxwellian: For a thick sample, the Maxwellian becomes flat due to the small number of transmitted neutrons. If the effect depends on the slope of the Maxwellian, on which the analysed Bragg edges are superimposed, in a solid-solid phase transition the effect should not appear as the overall attenuation and hence the slope of the Maxwellian remains constant. This could be examined by using slabs of ferritic and austenitic steel with a constant overall thickness.

6.4 Thermal Expansion/d-Spacing Resolution

To estimate the resolution for lattice parameter changes of the Bragg-edge transmission setup used at LANSCE, the coefficient of thermal expansion (cte) of a silicon rich steel (Fe-0.38C-1.94Si-2.99Mn) was derived from Bragg-edge transmission patterns taken during heatup to austenitisation temperature (1000° C). The steel sample and further experiments on the decomposition of austenite to bainite are described in section 7.1. The disk-shaped sample had a diameter of 5 cm and a thickness in beam direction of 2 cm. The collimation in the first beam tube was 2 cm, making sure that no intensity passed the sample which was centered to the beam. The sample temperature was measured with a thermocouple stuck in the center of the disk into an approximately 5 mm deep hole. The sample temperature was recorded on a PC. Data acquisition was triggered by the proton pulse and thus susceptible to beam failures. Figure 6.4 shows the first and last Bragg-edge transmission pattern used for the refinement. In total, 80 patterns of accumulation time of 1 minute each were refined for this analysis. As can be seen in figure 6.4, the difference curve does not show any significant deviation between measured data and fit. The refinement was done using **BETMAn**'s batch mode and consisted of three steps: First, only the scale factor was refined to avoid compensation of neutron intensity changes by structural parameters. In the second step, additionally an intensity offset, four background parameters, $B_{iso,n}$ and B_n of the Fe atom were refined (only parameters of a single atom refined as the second atom in the bcc structure is equivalent by symmetry and hence has the same parameters). As no phase transition appears in the analysed temperature region, the number of

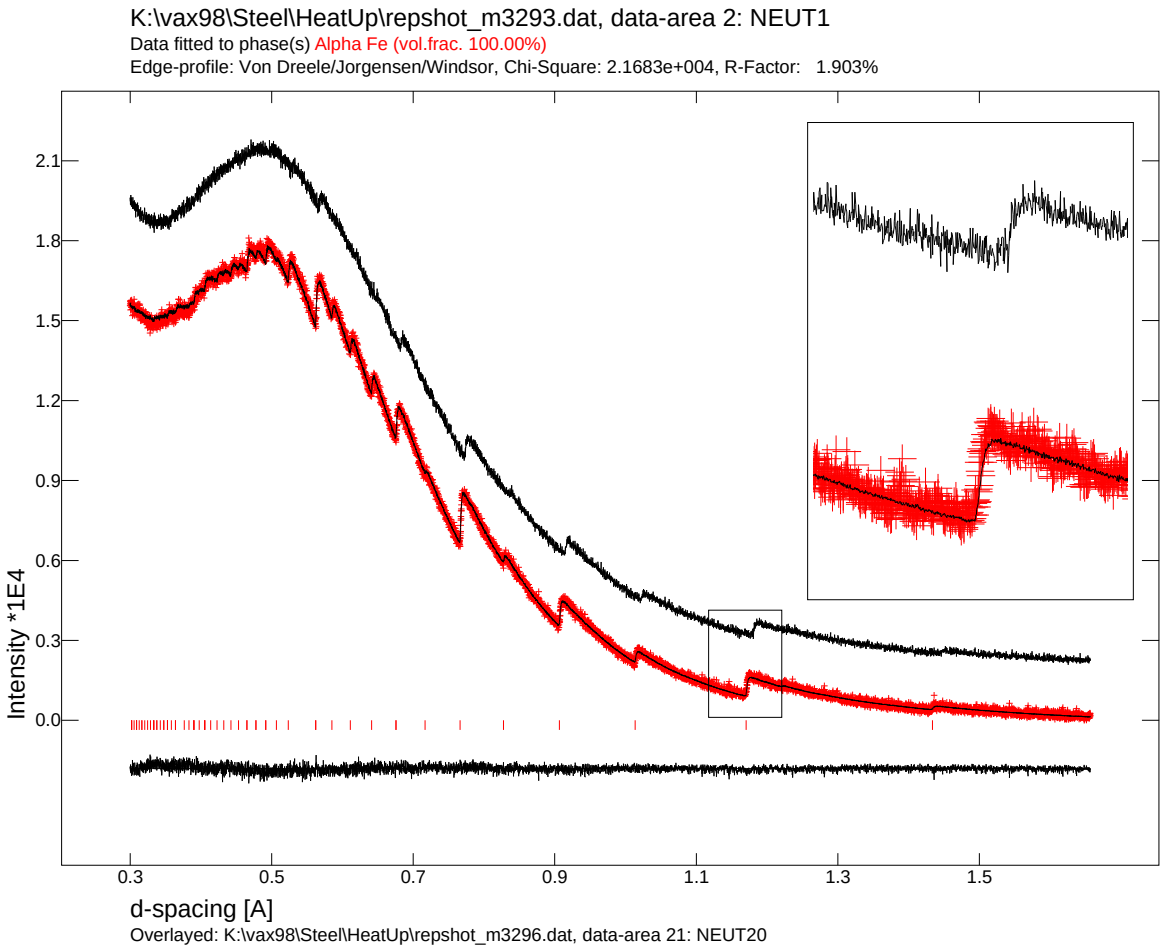

Figure 6.4: Refined first pattern (164° C) of a series of patterns taken during heating of a Si-rich steel sample to austenisation temperature. Overlayed (upper curve) is the last refined pattern (705° C), showing clearly the attenuation of the edge intensity due to the Debye-Waller factor and the edge shift due to thermal expansion. The tick marks indicate calculated positions of α-Fe reflections. The box around 1.15 Å is magnified to show the edge shift.

unit cells is constant during the data analysis and was refined in the last step together with lattice parameter, the edge profile parameter σ_1 and all parameters of the previous steps. It is necessary to continue refining parameters during a Rietveld refinement once they are set variable as fixing of parameters reduces the e.s.d. of others and hence the e.s.d.s are too small (Sivia, 1996, section 3.2). In the plots of figure 6.5 and 6.6 the horizontal spacing of data points is changed in case of instable beam because the data acquisition for this measurement was triggered by the proton beam. One disadvantage of the current data acquisition at flightpath 5 is that only time stamps for start and end time of data files are available, but none for the individual patterns (data areas) contained in the data files. The only possibility to assign timestamps to data areas is to divide the time between start and end of a file into 20 (the number of data areas per file) periods and assign those to the data areas[1].

The present experiment is an example of the hazard of loosing synchronisation between real time

[1] Saving of a data file and clearing the data acquisition afterwards costs about 15 seconds virtually independently of the data volume written. Hence, writing each data area into its own data file would lead to many gaps during the experiment. The use of the LBEG signal rather than the proton pulse as trigger for the data acquisition as described in section 5.2 cures the problem.

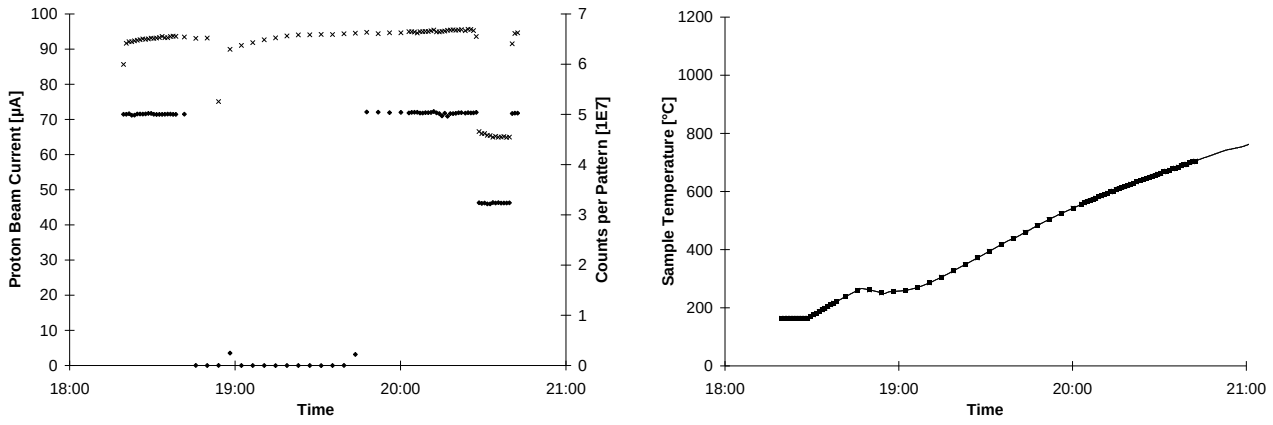

Figure 6.5: Left: Beam current (diamonds) and number of neutrons per pattern (crosses). Right: Temperature versus real time. The solid squares are the values assigned to the corresponding patterns by **BETMAn** during the data-analysis, the line is the direct readout from the thermocouple. The interruption of sample heating due to the announced beam failure around 19:00 is visible.

and experiment time given by the timestamps assigned to the patterns by this procedure. As can be seen from figure 6.5, the beam went off at 18:45. This was announced by the central control room to be the status for an unknown time and heating of the sample was interrupted (figure 6.5, right). After approximately 20 minutes, the beam was announced to be back on and heating was continued, although the proton beam log provided by LANSCE shows that the beam was back not before about 19:45. The timestamps for all 20 data areas of the data file containing the one during which the beam disappeared are incorrect, as only the start time of the first and the end time of the last data area are known and all others have to be interpolated. Therefore, the times of all data points between 18:39 and 20:02 have to be ignored in figure 6.6. The explanation for the missing drop of the neutron counts per pattern during the beam failure in figure 6.5 is similar. No problem occured during the period of beam reduced to 46 μA after 20:30, which is unambigously reflected by a synchronous lower detected neutron intensity. The residual χ^2 exhibits only minor fluctuations except during the weak beam after 18:45 (figure 6.6). Relatively broad scatter exhibits the refined edge width parameter σ_1, while the isotropic displacement factor $B_{iso,n}$ remains approximately constant until 600° C and increases afterwards. The highest temperature in figure 6.6 is close to the transition from ferrite to austenite in this steel, which may explain the strong increase of $B_{iso,n}$ when approaching this temperature. The strange behaviour of the lattice parameter between 250 and 550° C is due to the beam failure explained above.

Excluding the data points resulting from the corrupted data file, a linear regression was performed, leading to a function

$$a\,(T) = m \cdot T + c = (4.21 \pm 0.02) \cdot 10^{-5}\text{Å}/^{\circ}\text{C} \cdot T + (2.8622 \pm 0.0001)\,\text{Å} \tag{6.2}$$

for the lattice parameter a. Figure 6.6, bottom right, shows good agreement with this linear description and justifies neglection of a quadratic term. As the thermal expansion is defined as

$$a\,(T) = a_0\,(1 + \alpha\,(T - T_0)) = \underbrace{a_0\alpha}_{m}\,T + \underbrace{a_0\,(1 - \alpha T_0)}_{c} \tag{6.3}$$

the coefficient of thermal expansion (cte) and the reference lattice parameter are given by

$$\alpha = \frac{m}{c + mT_0}, \qquad a_0 = c + mT_0 \tag{6.4}$$

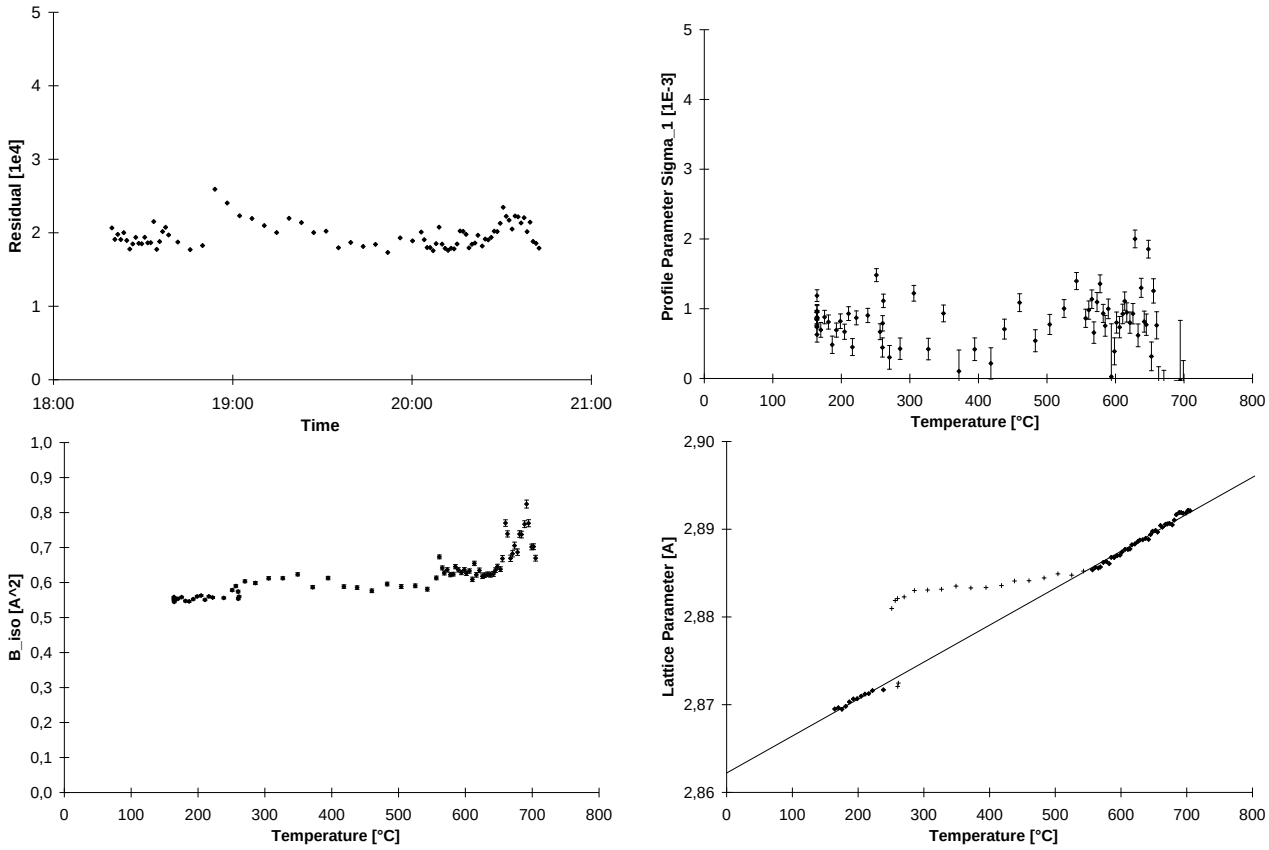

Figure 6.6: Top left: Residual χ^2 of the refinements. Top right: Refined profile parameter σ_1. Bottom left: Refined isotropic displacement factor $B_{iso,n}$. Bottom right: Refined lattice parameters. In the latter, solid diamonds correspond to the data points used for linear regression from which the coefficient of thermal expansion was derived. Crosses result from the corrupted data file, see text. All error-bars correspond to the e.s.d.s resulting from the fit, for lattice parameter the e.s.d.s were too small for display.

Using the above coefficients and a reference temperature of 20° C, this evaluates to $\alpha = (14.72 \pm 0.07) \cdot 10^{-6\circ}$ C^{-1} and $a_0 = 2.8631 \pm 0.0001$Å. The latter depends of course strongly on accurate calibration of the flightpath and therefore is not comparable to literature values. Interpolation of a lattice parameter in the range of the beam failure and application of error propagation may give an estimate of the achievable resolution with BET: For instance, for a temperature of 400°C, the resulting lattice parameter is $a = (2.8791 \pm 0.0002)$Å. The relative error is $7 \cdot 10^{-5}$. Taking into account the short integration time per pattern, the problems with beam stability and uniform heat treatment (see discussion of systematic errors below), this resolution is acceptable. Also, the cte is in reasonable agreement with a value of $\alpha = 13.049 \cdot 10^{-6\circ}$ C^{-1} determined from dilatometric measurements by Bhadeshia (1982) for a comparable steel of composition Fe-0.22C-2.03Si-3.0Mn. As this values is not within the margin of error of the present experiment, systematic errors are likely. One may be a deviation between average temperature of the bulk, which is probed by the lattice parameter averaged over the illuminated sample volume, and thermocouple due to temperature gradients within the sample volume. For a precise determination of the cte by Bragg-edge transmission, at each temperature the sample needs to equilibrate and the integration time should be in the order of 10 minutes rather than 1 minute.

6.5 Stress/Strain

The data for this analysis was collected at the instrument ENGIN at ISIS within the framework of the Ph. D. thesis of D. Wang (1996, chapter 7). The measurement is described there and here only the key features are repeated: Tensile and compressive stress was applied perpendicular to the beam direction to medium carbon steel bars with a thickness in beam direction of 6 mm (tension) and 10 mm (compression). The applied stress was measured with strain gauges while the sample was mounted on a stress-rig. The probed volume, defined by intersection of beam and sample, was equivalent to $6 \cdot 5 \cdot 5$ mm^3 for the tensile and $10 \cdot 5 \cdot 5$ mm^3 for the compressive measurement. Therefore, probably neutron intensity passed the sample, making refined parameters depending on the cross-section, like $B_{iso,n}$, worthless. Nevertheless, such setup is unlikely to affect refined lattice parameters significantly. A (counting) detector of effective area of $5 \cdot 5$ cm^2 was used, the measurement time was 2 hours per pattern. From the moderator thickness and the total flightpath length, a resolution of

$$\frac{\Delta d}{d} = \frac{\delta L}{L} = \frac{28\text{mm}}{16190\text{mm}} = 1.7 \cdot 10^{-3} \tag{6.5}$$

is expected (cf. section 5.1). As quoted in the above work, this resolution is by a factor of 3 better than for the diffraction setup of the same instrument ($5.6 \cdot 10^{-3}$) and comparable to the HRPD instrument at ISIS ($2 \cdot 10^{-3}$)[2]. Uniaxial tensile and compressive stresses resulting in strain gauge values of 0, -1010, $-1840\mu\epsilon$ (microstrain= $10^6 \cdot \Delta l/l_0$) and 1000, $1850\mu\epsilon$, respectively, were applied. The strain was derived by Wang graphically from the average edge-shift of the three most intense Bragg-edges in patterns normalised by the incident intensity.

As in any measurement of lattice parameters in transmission, strain parallel to the neutron beam is probed and therefore the extension or contraction in the direction perpendicular to the applied stress is measured in this experiment. Let x_i be an orthogonal coordinate system with x_1 along the beam direction and x_3 parallel to the applied stress (perpendicular to the beam). From the definition of strain as the variation of the displacement u_i with direction x_j (e.g. Noyan & Cohen, 1987, equation (2.9)),

$$\varepsilon_{ij} = \frac{\partial u_i}{\partial x_j} \tag{6.6}$$

it can be seen that ϵ_{11} is probed in a transmission experiment. With the uniaxial stress written as σ_{33}, the stress/strain relation is given according to Hooke's Law by (e.g. Nye, 1998, chapter VIII)

$$\varepsilon_{11} = s_{1133}\sigma_{33} \tag{6.7}$$

where s_{ijkl} is the fourth-rank tensor describing the compliance of the crystal. For isotropic materials, like steel in this case, the relation

$$\varepsilon_{11} = -\frac{\nu}{E}\sigma_{33} \tag{6.8}$$

holds (Nye, 1998, section VIII.4.2). ν is Poisson's Ratio and E is Young's Modulus. The strain in direction of the applied stress is given by (ibid.)

$$\varepsilon_{33} = s_{3333}\sigma_{33} = \frac{1}{E}\sigma_{33} \tag{6.9}$$

and probed by the strain gauges mounted on the sample. Thence, for the strain probed by Bragg-edge transmission,

$$\varepsilon_{11} = -\nu\varepsilon_{33} \tag{6.10}$$

[2] Meanwhile, the resolution of the High Resolution Neutron Powder Diffractometer HRPD with its flightpath of 100 m is quoted better than 10^{-3} (Ibberson et. al., 1992).

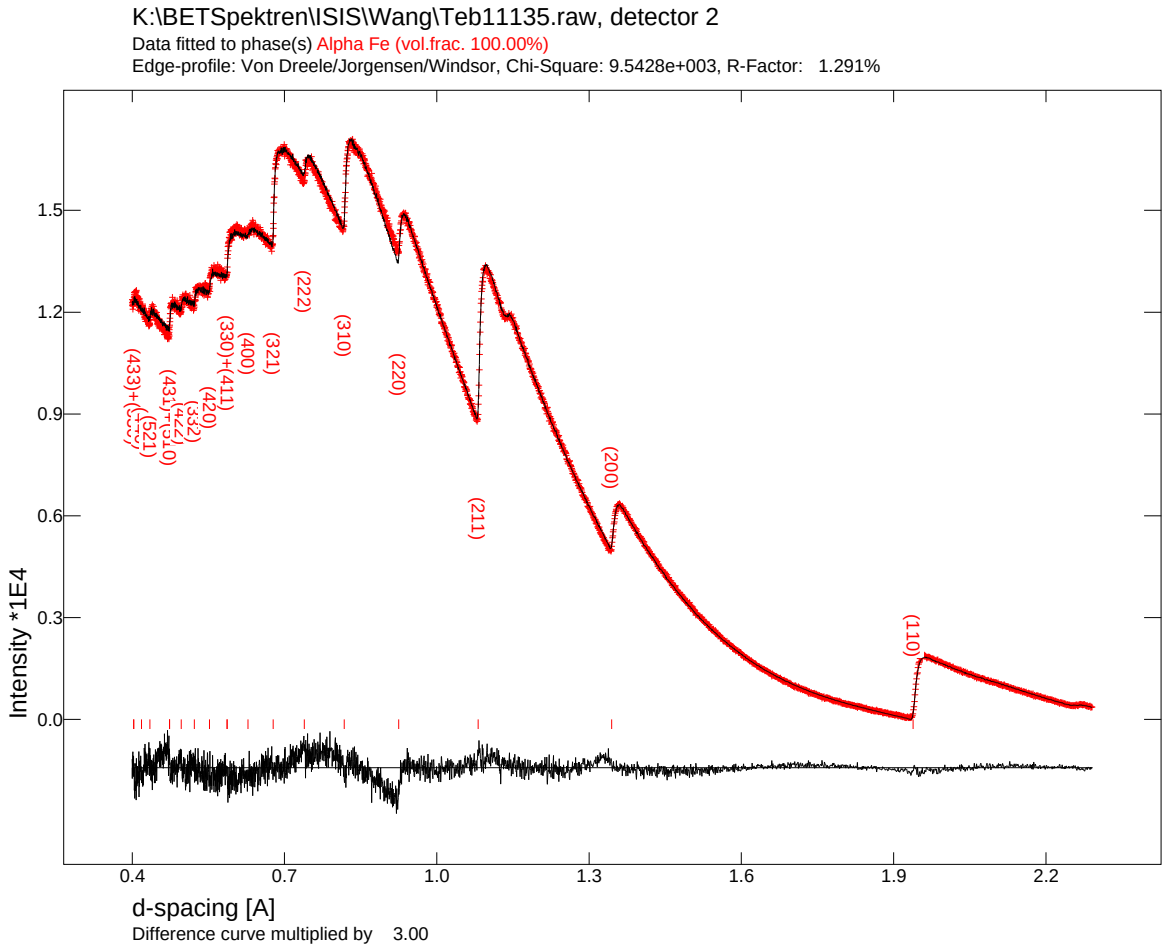

Figure 6.7: Fit of the pattern used to calibrate the instrument at ISIS (zero load). The difference curve is multiplied by 3 and indicates some misfits of edge intensities and/or profiles.

must hold. Poisson's Ratio for iron and steels is typically 0.28-0.30 (e.g. 0.293 for pure iron, Noyan & Cohen, 1987, table 2.1, or 0.29 for 304-type stainless steel).

The Bragg-edge transmission patterns measured in 1995 by Wang were re-analysed using **BETMAn** with a full pattern analysis over the d-spacing range from 0.4 to 2.3 Å (including 16 reflections). As strain-free reference, the run with zero load was used to calibrate flightpath L and profile parameters α_0, β_0 and β_1 (figure 6.7). Incident intensity was modeled by a scaled measured pattern (figure 6.8) and 8 background parameters compensated for incorrect approximations in the fit model and probably also for intensity passing the sample. The parameters contained in the resulting `.irXXX`-file were used as starting values for the other runs for which in a first step the scale, background, $B_{iso,n}$ and B_n, in a second step additionally the lattice parameter and in the last step also the edge width were refined[3]. The results are displayed in figure 6.9. The line fitted through the data points of the

[3] It is important to note that the fit-function incorporated into **BETMAn** currently works on a channel basis rather than time-of-flight. This is due to the fact that XSYS data gathered at LANSCE have this format. As the ISIS data is provided versus time-of-flight, ISIS data sets are converted to pseudo-channels when opened with **BETMAn**. This is done based on time offsets and flightpath lengths. For automated refinements, the values given in the setup-file (see `#setup`-command in section 4.6) are used, for manually opened files the parameters given in the measurement record requested during opening. Care has to be taken that these values are identical for refinements of multiple patterns like in the present case. Using channels as abscissa representation rather than time, the natural variable of a time-of-flight

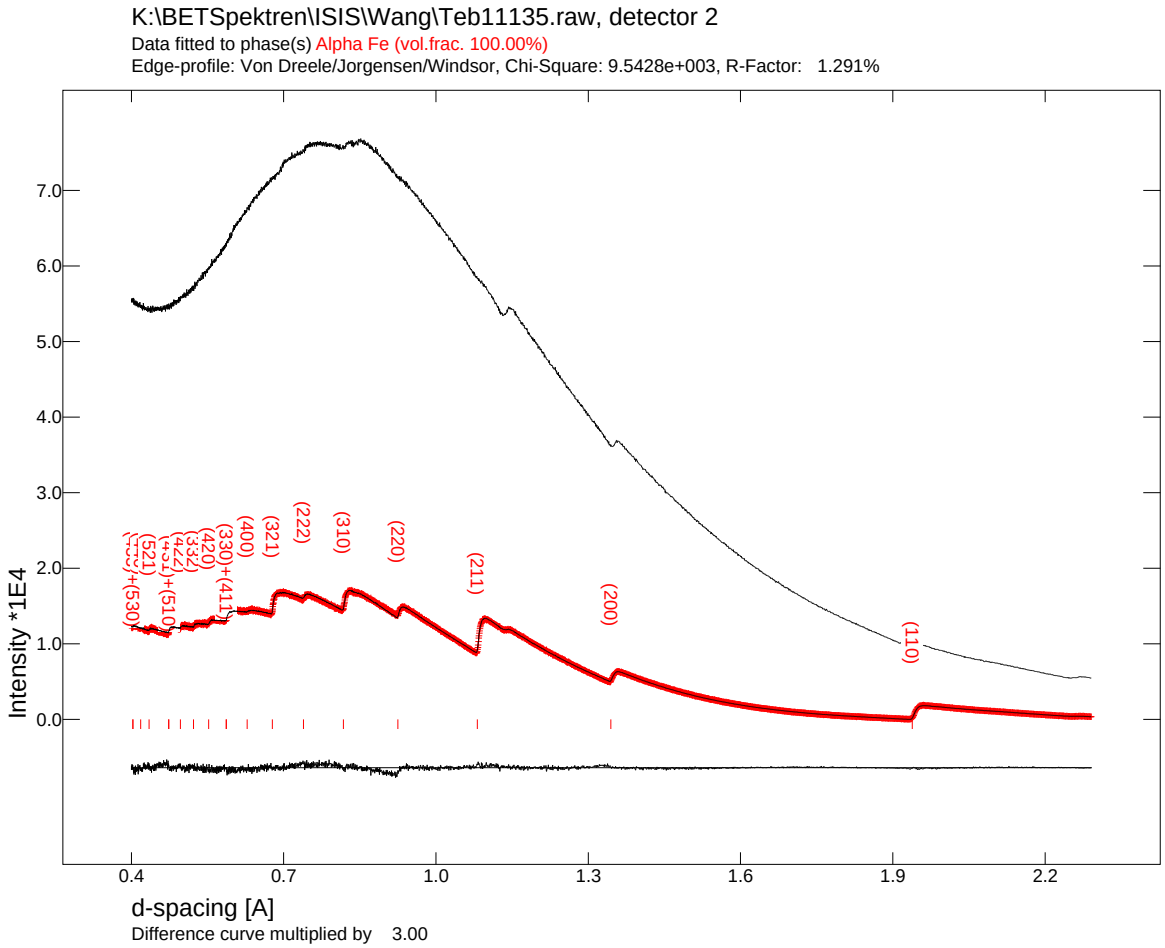

Figure 6.8: Same pattern as before with overlayed incident intensity. The deviation of the incident intensity from a smooth curve due to the contamination with aluminum and therefore the advantage of using a measured rather than a modeled incident intensity is clearly visible. The aluminum edges are at the same positions as iron edges under examination in this experiment, very likely to add some error to the results for iron.

strain according to (6.10) is given by

$$\varepsilon_{11} = (-0.27 \pm 0.02)\,\varepsilon_{33} - (27.9 \pm 22.5) \tag{6.11}$$

The slope reproduces Poisson's Ratio for a steel quite well. Deviations from linear behaviour may be of systematic nature (anisotropy, plasticity, dependence on sample thickness, see section 6.3), more data points would be necessary to examine this. As aluminum edges fall on top of iron edges in all cases (see figure 6.8 and table 6.1), some additional error may be introduced. It is worth noting that probably the only way to correct for this Al contamination of the incident beam for a single edge refinement is to divide the measured pattern by an appropriately scaled measured open beam pattern and directly refine edges in transmission data rather than the measured intensity data.

The values for the edge width parameter are all in the order of the expected resolution given by equation (6.5). Qualitatively, broadening of reflections with increasing tensile strain may be interpreted by a broader variation of the lattice parameter around its mean value, i.e. a broader range of possible

experiment, clearly is a design bug of **BETMAn** and will be fixed in the near future.

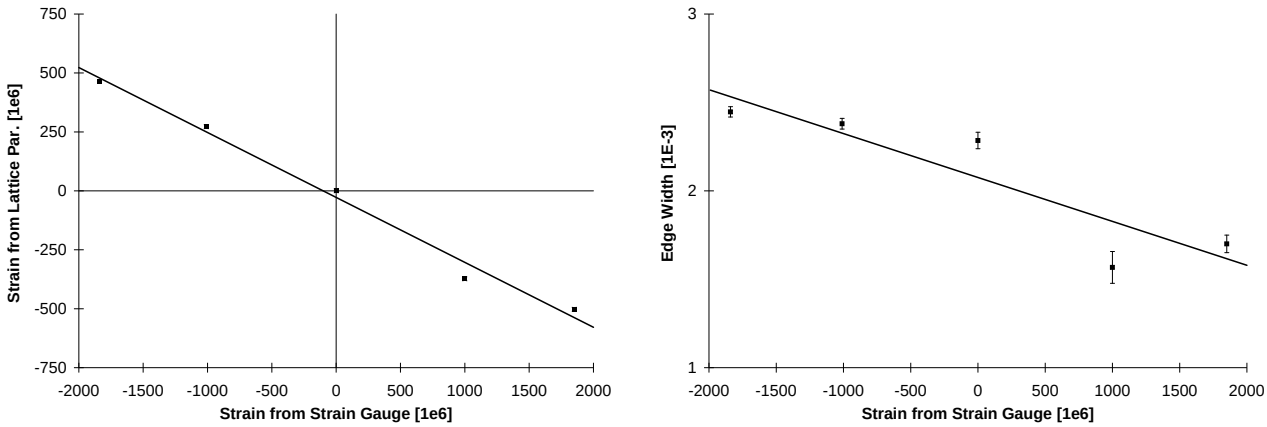

Figure 6.9: Results for strain (left) and edge width parameter(right). The error bars are the e.s.d.s resulting from the fit, for the lattice parameter/strain the e.s.d. is in the order of the extent of the squares. See text for a discussion of the results.

lattice parameters (cf. Todd et al., 1995) due to the overall expansion of the lattice. Similar, a compressed lattice decreases the range of possible lattice parameters probed by neutron diffraction, resulting in a decreased edge width.

Fe	Al	difference
	$d_{111} = 2.3381$	n.a.
$d_{110} = 2.0269$	$d_{200} = 2.0249$	0.0021
$d_{200} = 1.4333$	$d_{220} = 1.4318$	0.0015
	$d_{311} = 1.2210$	n.a.
$d_{211} = 1.1702$	$d_{222} = 1.1690$	0.0012
$d_{220} = 1.0135$	$d_{400} = 1.0124$	0.0010
	$d_{331} = 0.9291$	n.a.
$d_{310} = 0.9065$	$d_{420} = 0.9055$	0.0009
$d_{222} = 0.8275$	$d_{422} = 0.8266$	0.0008
$d_{321} = 0.7661$	$d_{333+511} = 0.7794$	-0.0133
$d_{400} = 0.7166$	$d_{440} = 0.7159$	0.0007
$d_{330+411} = 0.6756$	$d_{531} = 0.6845$	-0.0089

Table 6.1: Comparision of aluminum and iron edge positions calculated for lattice constants of $a_{Al} = 4.0497$ and $a_{Fe} = 2.8665$ (all values given in Å).

Chapter 7

Application Examples

To demonstrate the usefulness of the Bragg-edge transmission technique, two application examples are described in more detail. The first is a study of the isothermal decomposition of austenite (fcc or γ-iron) to bainite (ferrite or bcc/α-iron plus carbides forming a special microstructure). By Bragg-edge transmission, not only volume fractions of the participating steel phases could be observed in real-time and in-situ to investigate transformation kinetics, but also the carbon content in both phases could be derived from the lattice parameter changes. The changes of the carbon concentration during the transformation is very important for the understanding of the transformation mechanism. Investigation of this quantity with similar time resolution as in the present experiment by other techniques is barely possible, hence, Bragg-edge transmission is a unique tool to study such transformations.

The second example describes a study of the kinetics and lattice parameter changes during the reduction of nickeloxide to nickel at temperatures above 1000°C. Again, the availability of volume fraction *and* lattice parameter data proved to be very valuable. Obtaining lattice parameter changes at time resolutions in the order of one minute at temperatures above 1000°C with other diffraction techniques, e.g. synchrotron radiation, is clearly a non-trivial task.

Measurement and understanding of both reaction types is of great interest in order to improve materials properties and processing in the field of metals and alloys as well as ceramics and compound materials.

7.1 Bainite

The transformation of a Fe-0.38C-1.94Si-2.99Mn wt.% steel from austenite to bainite was observed at seven temperatures between 250°C and 450°C [1]. The reaction remains incomplete in the sense that there is no thermodynamic equilibrium between austenite and bainite (so-called incomplete reaction phenomenon). Using the Bragg-edge transmission technique, the crystallographic parameters volume fraction, lattice parameter and reflection width are accessible for both phases in situ with a time resolution of a minute. The latter two observables allow to study the distribution of carbon between the two phases with the same time resolution. Consistent with theory, an increase of the carbon concentration in austenite and a decrease in bainite was found. At lower temperatures a post-transformation change of the carbon concentration at constant volume fractions was observed.

[1] The results of the experiment described here are to be published in Vogel et al. (2000a).

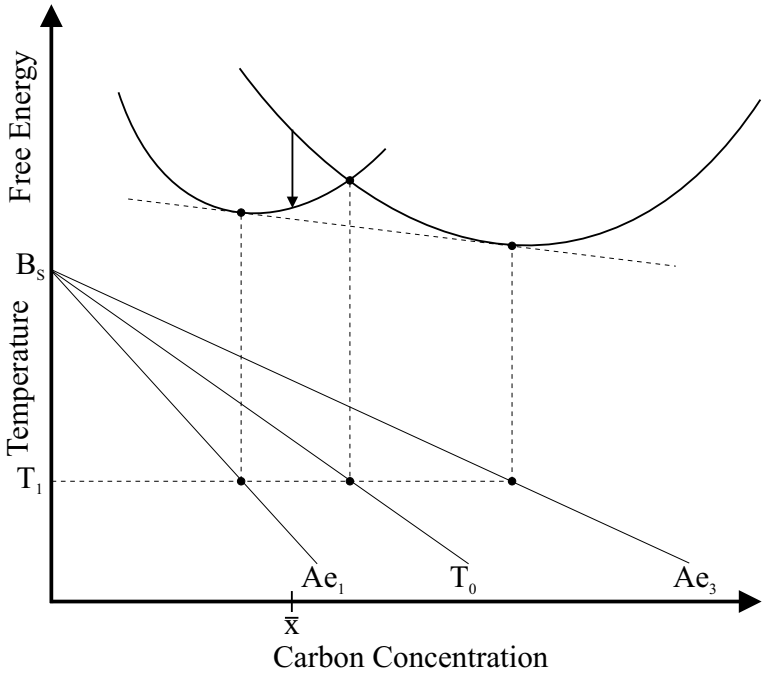

Figure 7.1: Schematic illustrating the change of Gibbs free energy during the reaction from austenite to bainite (after Bhadeshia, 1992, figure 1.4). The incorporation of strain energies does not change the scenario significantly. See text for further explanations.

7.1.1 Introduction

During isothermal decomposition of the high temperature austenitic phase in steel at temperatures between about 550 to 720°C, pearlite (α-iron plus cementite Fe_3C with a specific microstructure) forms by diffusion in a reconstructive transformation. Below about 250°C, carbon diffusion occurs very slowly and the austenite instead undergoes a diffusionless transformation to martensite (bct/α'-iron, with a specific microstructure). In the intermediate range, fine aggregates of ferrite plates (or laths) and cementite particles are formed with a much smaller driving force than in the case of martensite, resulting in a structure termed bainite. Depending on the formation and location of additional carbides, the microstructure is characterized as upper and lower bainite. The aggregates of typical thickness 1-5 μm have a sheaf-like morphology consisting of ferritic subunits of typical thickness of 0.2 μm (bainitic ferrite). The subunits grow fast, but unlike martensite at a speed far below the velocity of sound in the alloy (e.g. Bhadeshia & Christian, 1990).

Two limiting cases for the formation of bainite are conceivable (Honeycomb & Bhadeshia, 1996): The carbon may partition during growth so that there is no supersaturation of bainitic ferrite at any time. Then the transformation would proceed until the carbon concentration in the austenite reaches thermodynamic equilibrium (Bhadeshia, 1992, section 6.1.1, Ae_3 curve in figure 7.1). Alternatively, the growth of bainite could be completely diffusionless. Then the carbon would be trapped in transformed grains of bainitic ferrite and the bainite would remain supersaturated. The transformation should in principle go to completion as there is no diffusion necessary, although in practice kinetic restrictions would hinder completion of the transformation.

Bhadeshia & Edmonds (1979, 1980) showed for a steel of composition Fe-0.43C-2.12Si-3.00Mn that the following mechanism takes place: The bainitic ferrite grows without diffusion and is initially

supersaturated with trapped carbon atoms as it inherits the full carbon content of the parent austenite phase. To reach thermodynamic equilibrium (Ae_1 curve in figure 7.1), the excess carbon is then rejected by diffusion from the bainitic ferrite either to adjacent austenite grains (upper bainite, α_{ub}) or to adjacent austenite grains and growing intragranular carbide nuclei (lower bainite, α_{lb}). In both cases, the next plate of bainite has to grow from carbon enriched austenite. Since the proposed transformation is diffusionless, this process stops at a carbon concentration where the austenite and bainitic ferrite have the same free energy (T_0 in figure 7.1). The locus of this concentration in a temperature versus concentration diagram is called the T_0 curve whereas the equilibrium carbon concentration in austenite lies on the Ae_3 curve. Indeed, Bhadeshia & Edmonds found that the transformation stops when the carbon concentration in austenite reaches the T_0 curve as predicted for the diffusionless transformation followed by carbon rejection to austenite. As this concentration is below the equilibrium concentration Ae_3, the reaction is termed incomplete and the effect of the cessation of the transformation 'incomplete reaction phenomenon'. As x_{T_0} decreases with increasing temperature, an upper temperature limit for bainite formation exists, termed the B_S (bainite start) temperature. An increasing amount of bainite formation with undercooling below B_S down to M_S (martensite start temperature), the temperature at which diffusion is that much hindered that martensite forms by a displacive transformation, is another consequence of this fact.

The transformation mechanisms for the decomposition of austenite to bainite can thus be summarized as follows (Bhadeshia & Christian, 1990): For upper bainite (α_{ub}) the reaction sequence is

$$\begin{aligned} \gamma &\rightarrow \alpha_{ub}^{\text{supersaturated}} + \gamma \\ &\rightarrow \alpha_{ub}^{\text{unsaturated}} + \gamma^{\text{enriched}} \\ &\rightarrow \alpha_{ub}^{\text{unsaturated}} + \alpha + \Theta \end{aligned} \tag{7.1}$$

where the last step describes the decomposition of the retained austenite (γ) to secondary ferrite (α) parallel to a more sluggish formation of cementite (Θ). Each step happens on a different timescale. For lower bainite (α_{lb}), the corresponding reaction sequence would be in the case of a high dislocation density, where sufficient carbon can be tied up at the dislocations to form cementite directly,

$$\begin{aligned} \gamma &\rightarrow \alpha_{lb}^{\text{supersaturated}} + \gamma \\ &\rightarrow \alpha_{lb}^{\text{unsaturated}} + \Theta^{\text{in ferrite}} + \gamma^{\text{enriched}} \\ &\rightarrow \alpha_{lb}^{\text{unsaturated}} + \Theta^{\text{in ferrite}} + \alpha + \Theta^{\text{between ferrite plates}} \end{aligned} \tag{7.2}$$

while in the case of a low dislocation density the excess carbon initially forms hexagonal ϵ-carbide within the bainitic ferrite which is then converted to cementite:

$$\begin{aligned} \gamma &\rightarrow \alpha_{lb}^{\text{supersaturated}} + \gamma \\ &\rightarrow \alpha_{lb}^{\text{unsaturated}} + \varepsilon\text{−carbide}^{\text{in ferrite}} + \gamma^{\text{enriched}} \\ &\rightarrow \alpha_{lb}^{\text{unsaturated}} + \varepsilon\text{−carbide}^{\text{in ferrite}} + \alpha + \Theta^{\text{between ferrite plates}} \\ &\rightarrow \alpha_{lb}^{\text{unsaturated}} + \Theta^{\text{in ferrite}} + \alpha + \Theta^{\text{between ferrite plates}} \end{aligned} \tag{7.3}$$

In contrast to the bainite reactions, the cooperative growth of ferrite and cementite in the (reconstructive) pearlite reaction would be described as

$$\gamma \rightarrow \alpha + \Theta \left[+\gamma'\right] \tag{7.4}$$

where γ' describes austenite possibly stabilized by alloyed elements.

So far, the initial carbon supersaturation of the bainitic ferrite is just a consequence of the mechanism described above, and to the best of the author's knowledge direct experimental evidence of it is

still missing. Potential problems occurring even when the post-transformation carbon concentration in austenite is measured by TEM, X-Ray or atom probe are described by Hall et al. (1982). From calculations based on diffusion constants of carbon in ferrite and austenite, Mujahid & Bhadeshia (1992) found for a steel Fe-0.4C-2Mn wt. % that supersaturated ferrite should decarburize within a few tens of seconds if it is assumed that carbon diffuses into an austenite grain from one side only (absence of so-called soft impingement) and always a sufficient volume of austenite is available to absorb the carbon atoms. As this is very likely to be not the case in reality, the decarburisation might take significantly longer or even a significant amount of bainitic ferrite might remain partially supersaturated. Kang et al. (1990) report from hot stage TEM for a steel Fe-0.4C-1.45Si-0.90Mn-1.44Cr-0.50Mo-0.10V wt. % periods of 20 minutes after completion of the ferrite growth before carbides precipitate, indicating that bainitic ferrite remains supersaturated during that time. After Stark et al. (1990), no segregation of substitutional elements between bainite and austenite has been observed, hence only the interstitial carbon can be considered mobile.

With Bragg-edge transmission it was attempted to provide additional insights into the transformation mechanism. The Bragg-edge transmission monitors in-situ the volume fractions, lattice parameters and reflection widths of both the bainite and austenite. From these, conclusions can be drawn concerning the underlying processes, namely the variation of the carbon concentration, during the transformation.

7.1.2 Sample Preparation

A high strength steel (Bhadeshia, 1992, table 13.2) of composition Fe-0.38C-2.99Mn-1.94Si wt.% was cast at the institute of iron- and steel technology at the Technical University Freiberg, Germany. The composition determined by spark spectrometry is given in table 7.1. The silicon prevents or impedes cementite precipitation in the upper and lower bainite, respectively. Without the silicon, because of the then possible cementite formation, the decomposition of austenite would proceed faster and go to completion as the carbon could be also partitioned into cementite instead of the austenite only. It is remarkable that silicon is therefore responsible for the cessation of the transformation to bainitic ferrite although it is known to favor ferrite rather than austenite (Schumann, 1990, section 4.6.2). In a study of a similar steel of composition Fe-0.43C-3.00Mn-2.12Si, Bhadeshia & Edmonds (1979) found no carbides in upper bainite and some intragranular bainitic carbide in lower bainite, which they identified as cementite. The manganese stabilizes the austenite at lower temperatures than in a pure iron-carbon system and thus retards the formation of pearlite during the quenching.

C	Si	Mn	P	S	Cr	Ni	Ti	Al
0.38	1.94	2.99	0.014	0.012	0.03	0.41	0.041	0.003

Table 7.1: Mass percents of the alloying elements of the cast steel.

After casting, the steel was homogenized at 1200°C for two days to minimize chemical segregation and subsequently rolled to a cylindrical shape without prior cooling. Following rolling, the steel was reheated to 1000°C for another 40 minutes and cooled in air to room temperature. To remove the decarburized layer produced by the homogenization, the steel was heated to 750°C for four hours and cooled in air to establish a ferritic/pearlitic microstructure amenable to machining. After that, the steel was 'reset' to its prior state by heating it to 1000°C for ten minutes followed by cooling in air to room temperature. Finally, disks 20 mm in thickness and 50 mm in diameter were cut from the rod

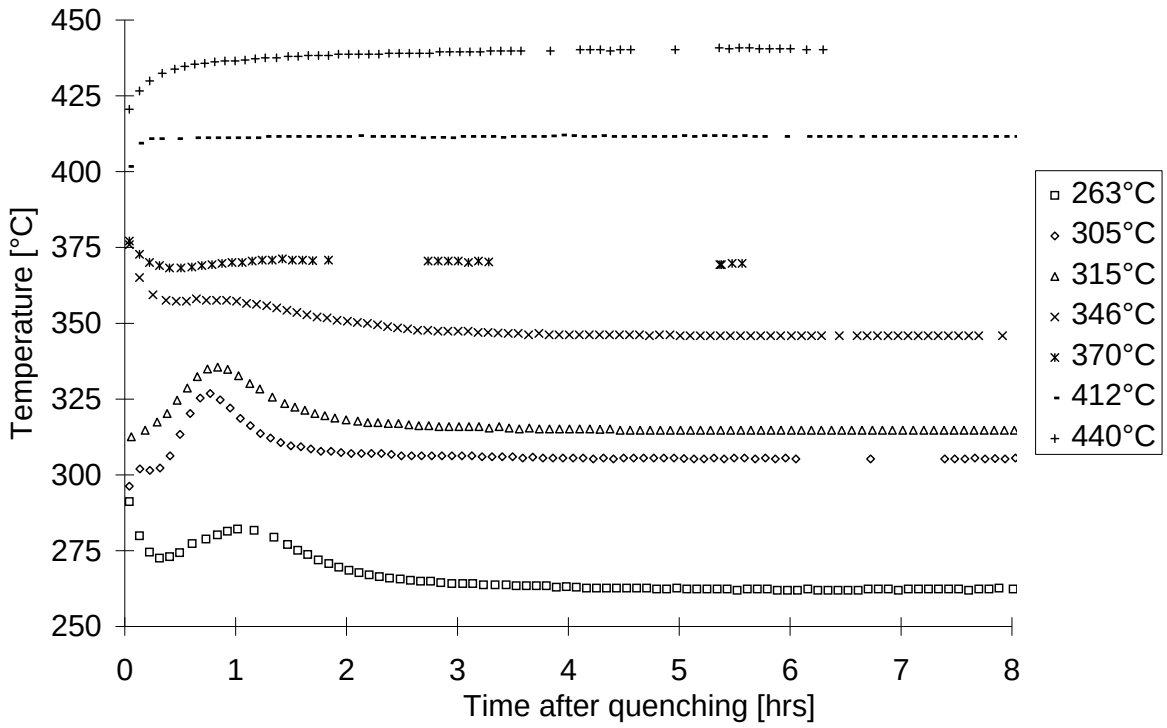

Figure 7.2: Temperature profiles of the samples after quenching and insertion in the furnace at transformation temperature. The data points correspond to analyzed Bragg-edge transmission patterns and gaps indicate intervals during the experiments where the beam was unavailable. In all cases the time to quench from 1000°C was below 0.1 hrs and is not shown here.

by electric discharge machining.

7.1.3 Experiment

The objective was to study the decomposition of austenite into bainite focusing on the carbon distribution between the two phases. Accordingly, the transformation at temperatures of 263, 305, 315, 346, 370, 412 and 440°C were studied. To establish an austenitic microstructure the samples were heated to 1000°C at 4°C/min and held there for at least 30 minutes. They were then quenched to within ±20°C of the desired transformation temperature in water and inserted into a tube furnace preheated to the transformation temperature. The period between removal from the austenitisation furnace and insertion into the transformation furnace was no longer than 0.1 hours. As the neutron shutter had to be closed during this access to the sample, for a period of approximately 150 seconds after the insertion of the sample into the second furnace no data could be taken as the neutron shutter had to be reopened. The sample temperature was recorded by a thermocouple inserted in an approximately 5 mm deep hole drilled into the center of the samples. This suggests that after the quenching process, where the regions in contact with water are expected to be significantly cooler than the regions in the core of the sample, the sample temperature is overestimated until the temperature gradients in the sample are balanced. The temperature profiles after the start of taking Bragg-edge transmission patterns of each run are shown in figure 7.2. In each case where a significant amount of bainite was formed, the heat of transformation is visible in the profile. The final sample temperature is considered as the transformation temperature.

The present experiment was performed at LANSCE and the general experimental setup used is described in chapter 5. The tube furnace at the transformation temperature was aligned such that the tube axis and the steel disk axis were parallel to the incident beam direction and the steel disk was centered to the beam collimation. Bragg-edge transmission spectra were recorded for more than 8 hours except at 370°C and 440°C. In the latter case, no transformation was detectable after 6 hours, in the former case the beam was instable during the first 5:30 hours and then went off completely.

A beam failure occurred also during the quenching of the sample intended for the transformation at 346°C. To avoid the loss of the initial phase of the transformation, the sample being at approximately 500°C was reinserted into the austenitisation furnace. When the beam became stable, the quenching procedure was started again. The results for this sample are inconsistent with the other runs and therefore presented grayed in figures 7.7 to 7.16 but excluded from the discussion.

The samples were cooled in air to room temperature after the experiments. For metallography pieces covering the full thickness parallel to the disk axis were cut from the center of the samples transformed at 305°C, 346 °C, 370 °C and 412°C, respectively. A layer of at least 0.2 mm was removed by grinding before the surface was polished and etched for 6 to 10 seconds in 0.5% nital (0.5 ml HNO_3 in 99.5 ml of 95 % ethanol + 5 % H_2O). For x-ray measurements the same samples as for the metallography were used.

7.1.4 Data Analysis

In fitting a single pattern over the accessible d-spacing range from 0.27Å to 1.66 Å, overall parameters (scale factor, background parameters) and phase dependent structural parameters (number of unit cells, lattice parameters) were fitted in a four step process. In each step, the number of varying parameters was increased.

As the crystallographic description of martensite potentially formed during the quenching (see below) and supersaturated bainitic ferrite is identical except a varying carbon content, both were modeled as a single phase. This requires corrections of the derived parameters in order to obtain the desired information on bainitic ferrite only. Due to the spectrometer resolution of the current setup, no splitting of martensite reflections could be resolved and both phases were treated as ferrite, i.e. only one cubic rather than two tetragonal lattice parameters were refined. A second approximation was to model both phases as pure iron rather than taking into account the chemical composition (see next section, table 7.1) and calculate average cross-sections after (3.3) and (3.4). The error is negligible as the coherent elastic cross-sections of both phases are 'scaled' by the same factor and volume fraction information is derived from the edge-height ratios. Lattice parameter information is virtually not affected at all. The discrepancy in the cross-sections is compensated by background at the cost of a wrong sample thickness estimate from the refined numbers of scattering centers.

To model the change of the edge width (visible in figure 7.3 as a change in slope of the edges) it was assumed that the broadening is only due to a constant instrumental contribution and a variable microstrain contribution. Therefore, only σ_1 was refined (cf. section 3.3.4). This assumption is based on findings of Radcliffe & Rollason (1959) who found in an examination of published electron micrographs of bainite no evidence of particle sizes below 1000 Å. Hence, they concluded that the reflection broadening observed in x-ray measurements can be attributed to microstrain originating for example from variations of the local carbon concentrations or dislocation densities. As explained in section 3.3.4, such strain broadening, same as the instrumental contribution, is proportional to the

Element	Site occupation	Scattering Length [fm]	σ_{inc} [barn]
Fe	0.9139	9.450	0.400
Mn	0.0301	-3.730	0.400
Si	0.0382	4.149	0.004
Cr	0.0003	3.635	1.830
Ni	0.0039	10.300	5.200
Mo	0.0127	6.715	0.040
Ti	0.0005	-3.438	2.870
P	0.0002	5.130	0.005
S	0.0002	2.847	0.007

Table 7.2: Scattering lengths and incoherent scattering cross-sections of elements in a steel as given by the chemical composition of the sample used here. The resulting values for $\bar{\sigma}_{coh}$ and $\bar{\sigma}_{inc}$ are 9.75 and 1.16 barn for the Si-rich steel compared to 11.22 and 0.40 barn for pure iron.

d-spacing $d_{\vec{h}}$ of a reflection while particle size broadening would be proportional to the square of the d-spacing and therefore would be described by σ_2.

In the present experiments typically 2000 sequential patterns of 15 seconds accumulation time each were recorded per transformation run. Even after a reduction of the temporal resolution to 5 minutes by adding 20 patterns offline, the number of patterns is too big for a manual refinement and **BETMAn**'s automated refinement was utilized for data analysis. During this automated analysis, lattice and edge width parameters were varied only conditionally depending on the volume fraction of the corresponding phase. The isotropic displacement factors were fitted for all patterns during execution of a script. It was found that $B_{iso,n}$ varies during the transformation and for small volume fractions the fit increased $B_{iso,n}$ to clearly unphysical values values rather than decreasing the number of scattering centers per unit area of this phase. Consequently, $B_{iso,n}$ was kept constant at the average value taken over a range after the transformation. The resulting values of $B_{iso,n}$ are displayed in figure 7.4 and agree well with values predicted by equation (3.12). Generally, the values for (bainitic) ferrite are below those of austenite, indicating less thermal motion in the ferritic (bcc) than in the austenitic (fcc) lattice. Nevertheless, the agreement is not yet satisfying, most likely due to the inappropriate approximations of the inelastic coherent scattering cross-section as described in section 3.2.5.

For the automated data analysis, patterns with too few neutrons due to beam failure were excluded. Since this automation offers the possibility of bias, e.g. due to the use of results of a refined patterns as starting values for the next pattern, the analysis was performed from the first to the last pattern and vice versa. Additionally, the number of added patterns was varied, i.e. the time resolution was changed from 5 minutes to 1 minute and to 15 seconds, and again the analysis was performed from the first to the last pattern and vice versa. In all cases the results were consistent, although of course the scatter of the parameters with the better temporal resolutions was increased. Another consistency check was performed by calculating the total number of iron atoms from the refined numbers of unit cells of ferrite and austenite (figure 7.5), which remained also constant as would be expected. Automated analysis was performed in three steps: First, the scale factor is fitted to avoid compensation of beam fluctuations by structural parameters. In the seconds step, the number of unit cells of both phases and background were fitted. In the last step, conditional refinements of lattice and edge width parameters were performed depending on the previously refined volume fractions. The resulting script for the forward analysis of one run is presented in appendix F.4.

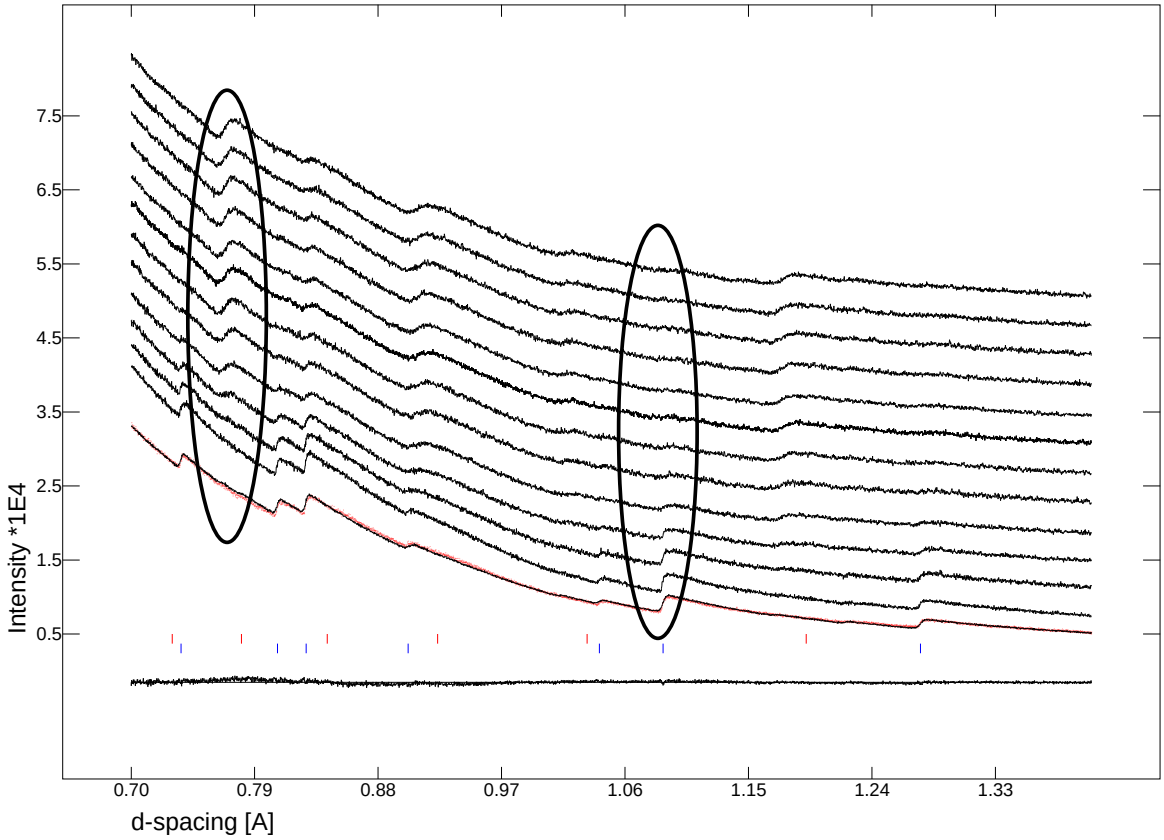

Figure 7.3: Bragg-edge transmission patterns from the run at 305°C in 10 minute steps. The pattern at the bottom is the first pattern taken during that run. Tickmarks indicate the calculated positions of bainite (upper row) and austenite edges (lower row), the difference curve results from the fit of the first pattern and is displayed in the same scale as the data. The increase of the bainite edge intensities (e.g. (321) edge at d=0.78 Å, left ellipse) and the decrease of the austenite edge intensities is visible (e.g. (311) at d=1.08 Å, right ellipse). The change in reflection-width is visible as a change of slope of the edges: The last $(321)_{\alpha_b}$ edge and the first $(311)_{\gamma}$ edge have about the same height, but the slope of the $(321)_{\alpha_b}$ edge is smaller, indicating a broader edge width.

7.1.5 Results

Martensite Formation

The quenching from the austenitisation to the transformation temperature was done in water rather than in air to avoid the formation of pearlite in the slower cooling core of the sample volume. The disadvantages of this treatment are the formation of martensite in the layer in direct contact with water and different quenching profiles for each sample due to the manual execution. Because of the identical crystallographic description of martensite and potentially supersaturated bainitic ferrite, the martensite contributes to any reflection of the bainitic ferrite and it is not possible to distinguish them during the refinements. In all cases except the transformation at 346°C, the volume fraction of the ferrite phase (e.g. the sum of martensite and bainite) did not start at zero vol. % but at values between 3 and 9 vol. % (see table 7.3). To obtain the volume fraction of bainitic ferrite, this initial amount was ascribed to martensite and subtracted from the ferrite volume fractions refined from subsequent patterns. The volume fractions of both bainite and austenite were then re-normalized with respect to

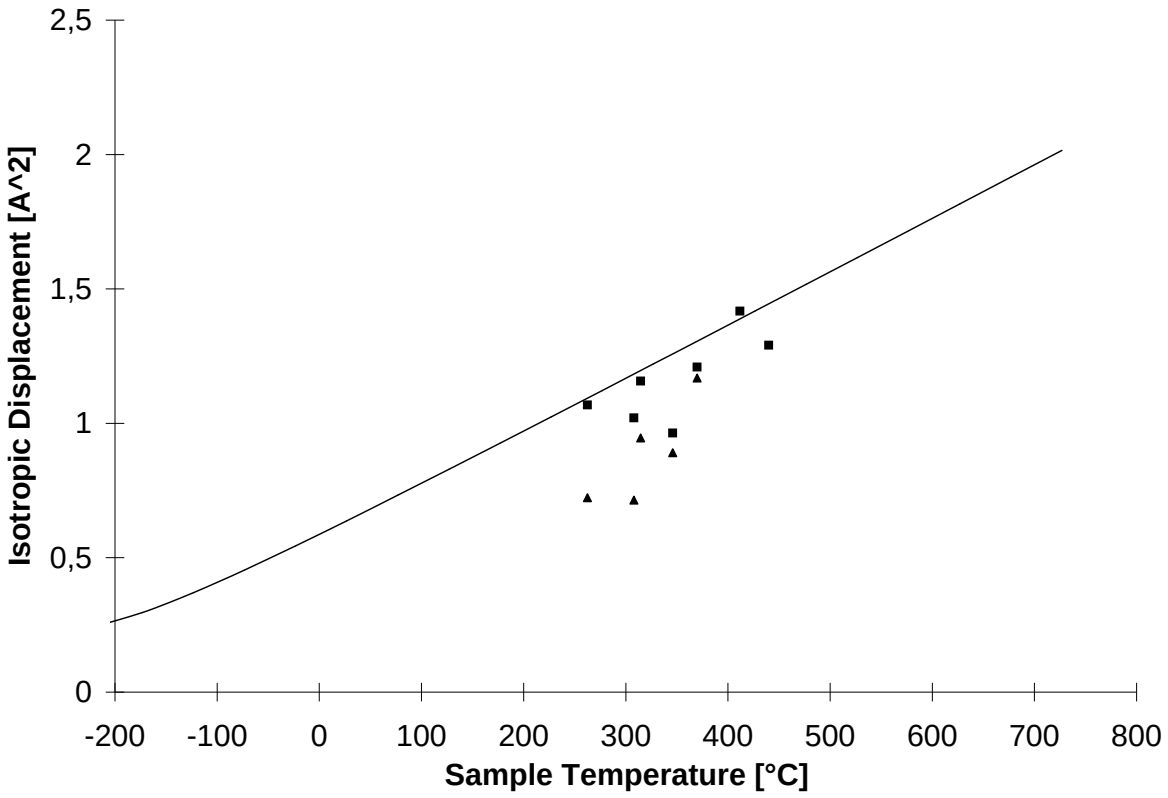

Figure 7.4: Refined isotropic displacement factors($B_{iso,n}$) for the Fe atom in ferrite (triangles) and austenite (squares). The curve results from a theoretical calculation of $B_{iso,n}$ according to equation (3.12) for a Debye-temperature of iron of 453 K.

the system bainite-austenite. The procedure assumes that the amount of martensite remains constant throughout the transformation time. The assumption is supported by the constant value of 3 vol. % ferrite observed in the run at 440° C.

Transformation temperature [°C]	263	305	315	346	370	412	440
Initial volume fraction ferrite[%]	3	4	7	0	5	9	3

Table 7.3: Initial volume fractions of phase 'ferrite' which are ascribed to martensite.

Because of the relatively small amount of ferrite refined from the first pattern and the huge changes taking place during that period, both the initial volume fraction and lattice parameter of ferrite have large errors. During the first minutes of each run the neutron shutter was not yet fully opened, reducing the available neutron intensity and additionally increasing the errors of the refined parameters. In the case of the run at 315°C, during the first 10 minutes the beam was very instable. A calculation of the lattice parameter of bainitic ferrite from the refined lattice parameter of ferrite (measured was the weighted average of martensite and bainitic ferrite lattice parameters) generally would introduce big errors even for those lattice parameters derived from patterns where ferrite occupies a large volume fraction and the error from the original ferrite lattice parameter is very small. The same is true for the edge width parameter. Therefore, the uncorrected values for the lattice and edge width parameters are presented. Nevertheless, for the calculation of the carbon content of bainitic ferrite, the correction

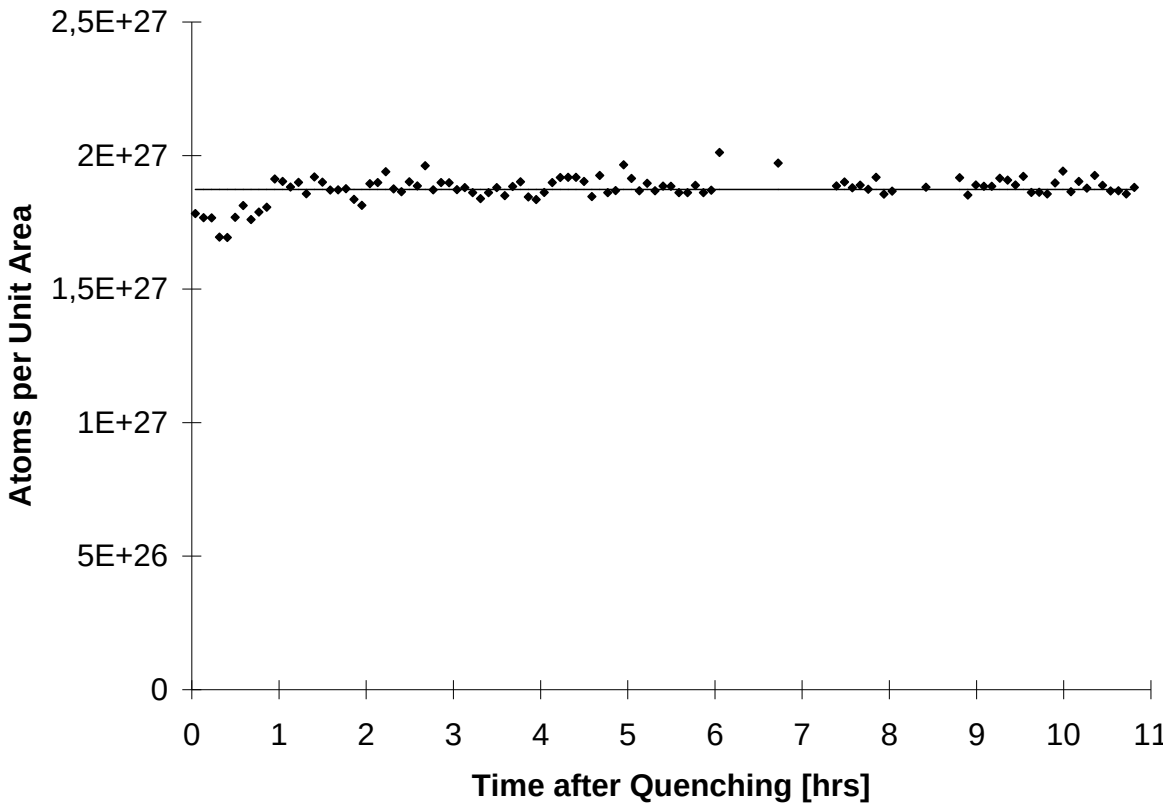

Figure 7.5: Total number of Fe atoms per unit area as calculated from the refined number of unit cells of ferrite and austenite.

was performed at the cost of a systematic error introducing an offset. The term "ferrite" refers in the following sections to the mixture of martensite and bainitic ferrite while "bainite" and "bainitic ferrite" refer to corrected values.

X-Ray

X-Ray measurements were carried out with $Cu_{K\alpha}$-radiation at 50 kV and 200 mA. To validate the homogeneity of the samples, diffraction patterns were taken at different regions corresponding to top, center and bottom of the sample transformed at 305°C. The two other samples were analyzed in the center of the bulk. The patterns were refined with phases ferrite and austenite (see figure 7.6) using GSAS (Larson & Von Dreele, 1994). The obtained results are displayed in table 7.4 and suggest a slightly lower lattice parameter in the near-surface regions of the samples, potentially due to decarburisation. In all cases, relatively broad reflections were observed.

	305°C, center	305°C, top	305°C, bottom	346°C, center	412°C, center
x_α [vol. %]	71	70	74	70	83
a_α [Å]	2.8665(2)	2.8633(3)	2.8634(3)	2.8696(2)	2.8678(3)
a_γ [Å]	3.6121(12)	3.6105(11)	3.6057(16)	3.6056(8)	3.6012(9)

Table 7.4: Results of the post-transformation x-ray analysis.

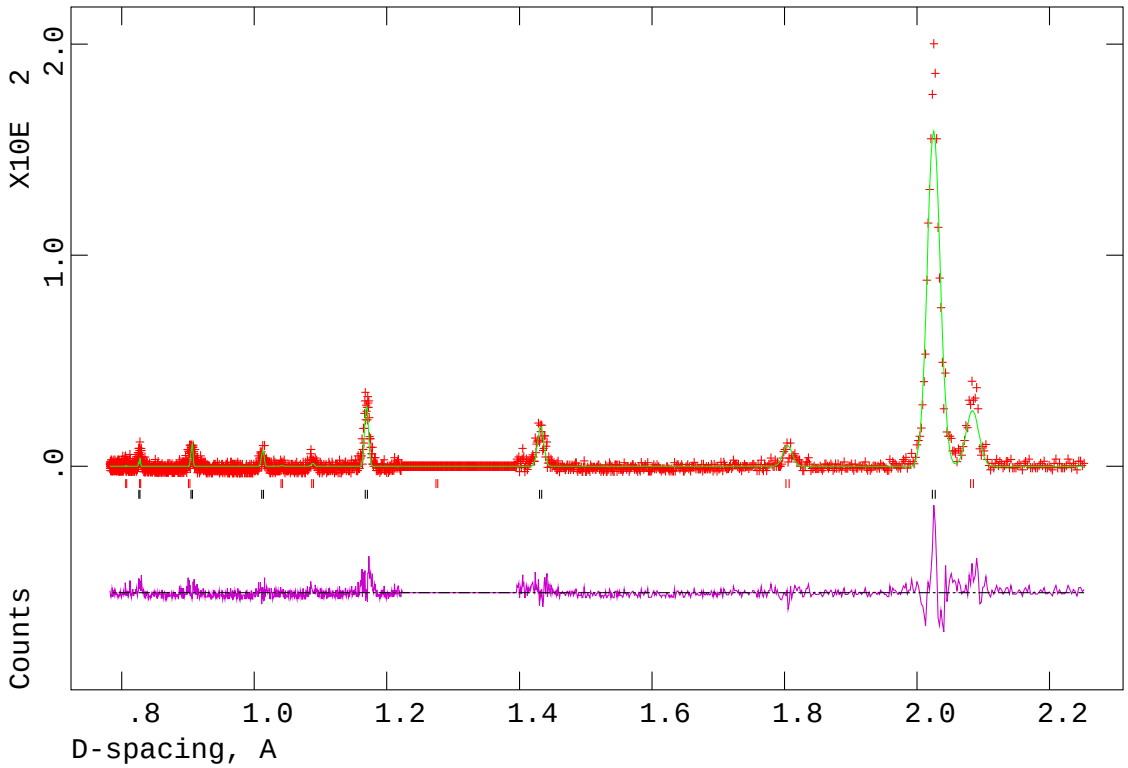

Figure 7.6: X-Ray powder diffraction pattern obtained from the center portion of the sample transformed at 305°C. The measured data are displayed as crosses, the line corresponds to the Rietveld fit. The fitted background is subtracted. The difference curve is displayed below using the same scale as the data. The tick marks indicate austenite (top) and ferrite (bottom) reflections (the calculated splitting is due to $K_{\alpha 1}/K_{\alpha 2}$ lines). The region between 1.25 and 1.4 Å was excluded from the fit due to a large bump, most likely resulting from flourescence of the manganese.

Metallography

During cooling in air after completion of the neutron measurements, the remaining austenite partly transformed to martensite. The visible amount of bainite increases in the sequence of the samples transformed at 412, 370 and 305°C. In all cases, in the regions corresponding to top and bottom of the disk, a homogeneous layer of less than a millimeter martensite was visible in the micrographs. The assignment of martensite and bainite was confirmed by microhardness measurements where in the regions close to the rim an about 30% higher Rockwell hardness was observed. As the illuminated sample volume does not include the circumference of the disks, the corresponding volume fraction of martensite in the Bragg-edge transmission data should therefore be below 10%. This is consistent with the amount of initial martensite listed in table 7.3.

Volume Fraction Results

The evolution of the bainite volume fraction for each run is presented in figure 7.7. At 440°C, no formation of bainite was detected. In all other cases the volume fraction of bainite increased rapidly during the first 10^4 seconds and stayed constant after that. The final volume fraction of bainite

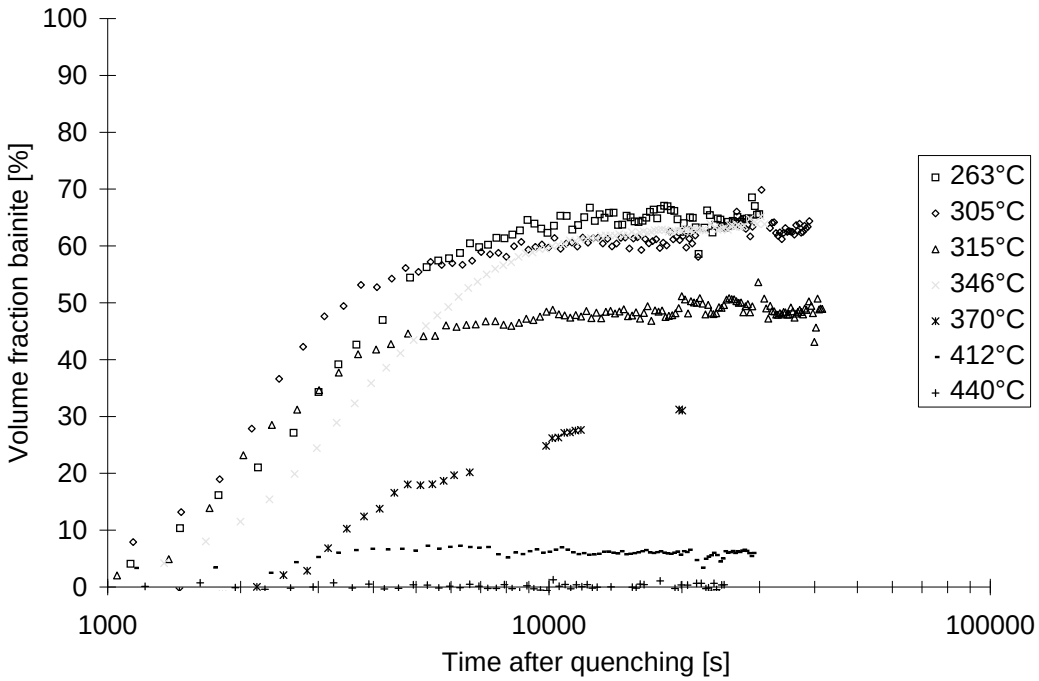

Figure 7.7: Evolution of bainite volume fractions. Each datapoint is derived from a pattern of 5 minutes accumulation time. Gaps indicate beam failures. The run at 346°C received a different heat treatment, see text.

decreased with increasing transformation temperature (figure 7.8). The results for the run at 370°C suffer from the poor beam quality during that run.

Lattice Parameter Results

The lattice parameters versus transformation time for both austenite and ferrite are displayed in figure 7.9. As already stated above, at 440°C only a small, constant amount of ferrite was detected which did not allow to refine a lattice parameter for ferrite. In all other cases, the austenite lattice expanded while the average ferrite lattice parameter decreased during the transformation. In table 7.5, the lattice parameters of austenite derived from the first and last pattern of each run are tabulated with the corresponding average temperatures of those patterns and the differences of the initial and final sample temperatures and lattice parameters. The same information is displayed in figures 7.10 (see discussion for further explanations of the lines in this figure) and 7.11. During the transformations at 263, 305 and 315°C the observed change of the austenite lattice parameter was considerably larger than during the transformations at higher temperatures. The runs at these temperatures also exhibit a change of the ferrite lattice parameter during the first hour of the transformation while in the same runs the austenite lattice parameter expands much slower. At higher temperatures, the change of both lattice parameters lasts for more than one hour. It was observed that during the three runs at lower temperatures the lattice parameter of austenite kept changing even after the volume fractions remained constant (figure 7.12). This was not the case for the transformations at higher temperatures.

Due to the large changes of the ferrite lattice parameters during the initial stage of the transformation and the small ferrite volume fraction at this stage, a reliable determination of an initial lattice parameter of ferrite is not possible. Therefore, only the final lattice parameters of ferrite are tabulated

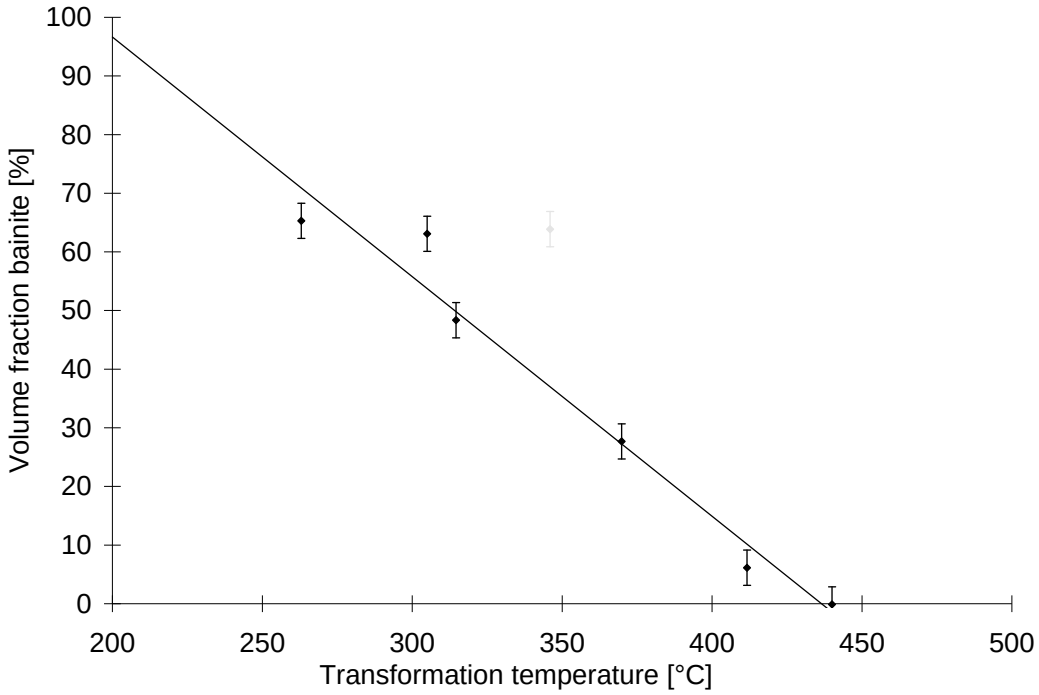

Figure 7.8: Volume fraction of bainite after 8 hours at the transformation temperature. The error bars are assumed to be constantly 3 vol. %. The data point at 346°C is not included in the linear regression, see text.

T_{final} [°C]	$a_{0,\alpha,final}$ [Å]
263	2.879
305	2.879
315	2.881
346	2.879
370	2.886
412	2.901
440	N/A

Table 7.6: Final lattice parameters of ferrite.

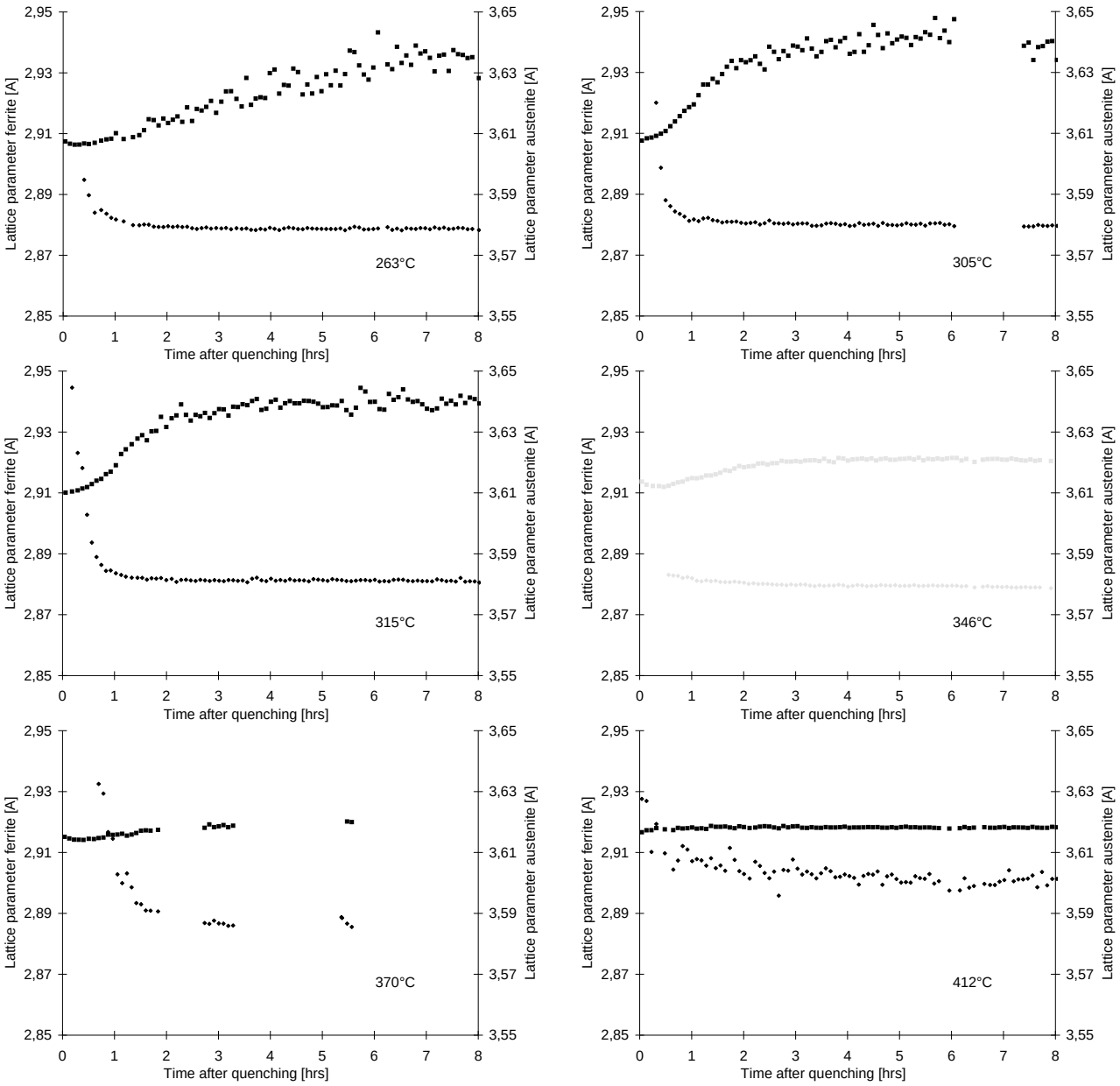

Figure 7.9: Change of lattice parameters of ferrite (diamonds) and austenite (squares). In the case of 440°C, the volume fraction of bainite was never high enough to refine the lattice parameter.

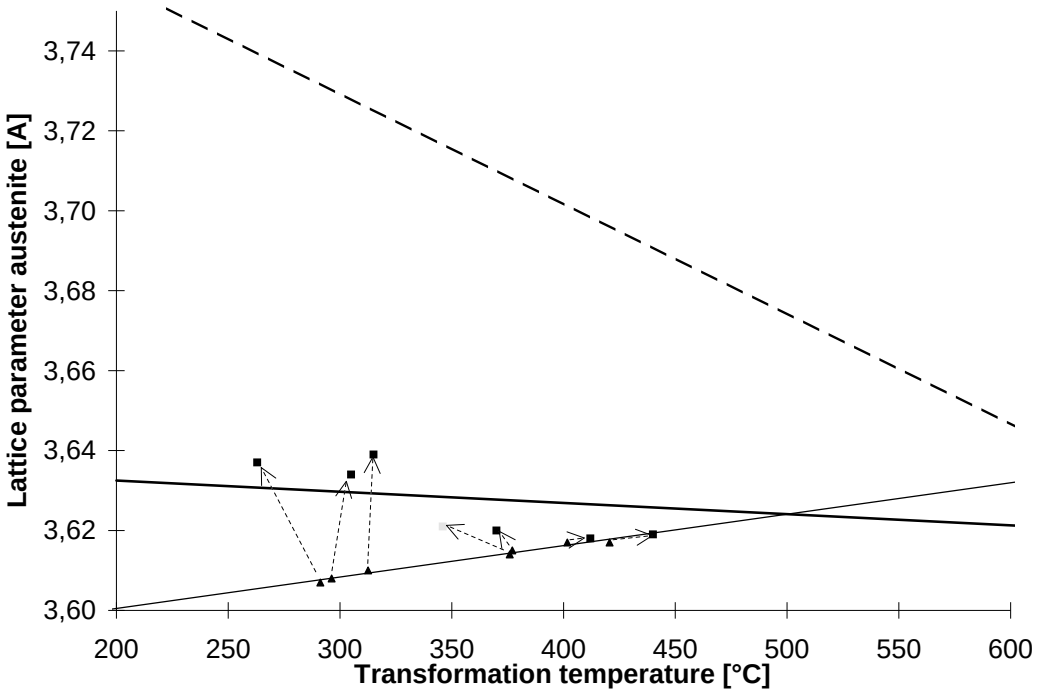

Figure 7.10: Observed initial (triangles) and final (squares) lattice parameters of austenite versus the average temperature of the first and last pattern, respectively. The thin solid line is a fit through the initial lattice parameters while the fat solid and dashed lines are the calculated lattice parameters for the T_0 and the Ae_3 curve, respectively. The arrows connect initial and final lattice parameters.

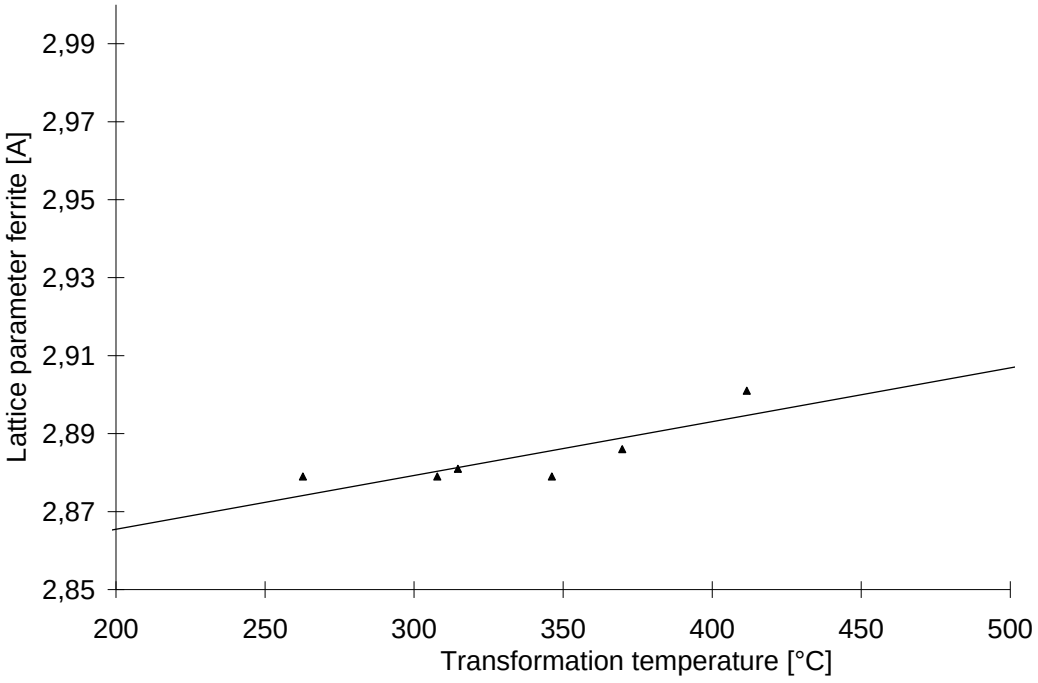

Figure 7.11: Final lattice parameter of bainite versus final sample temperature.

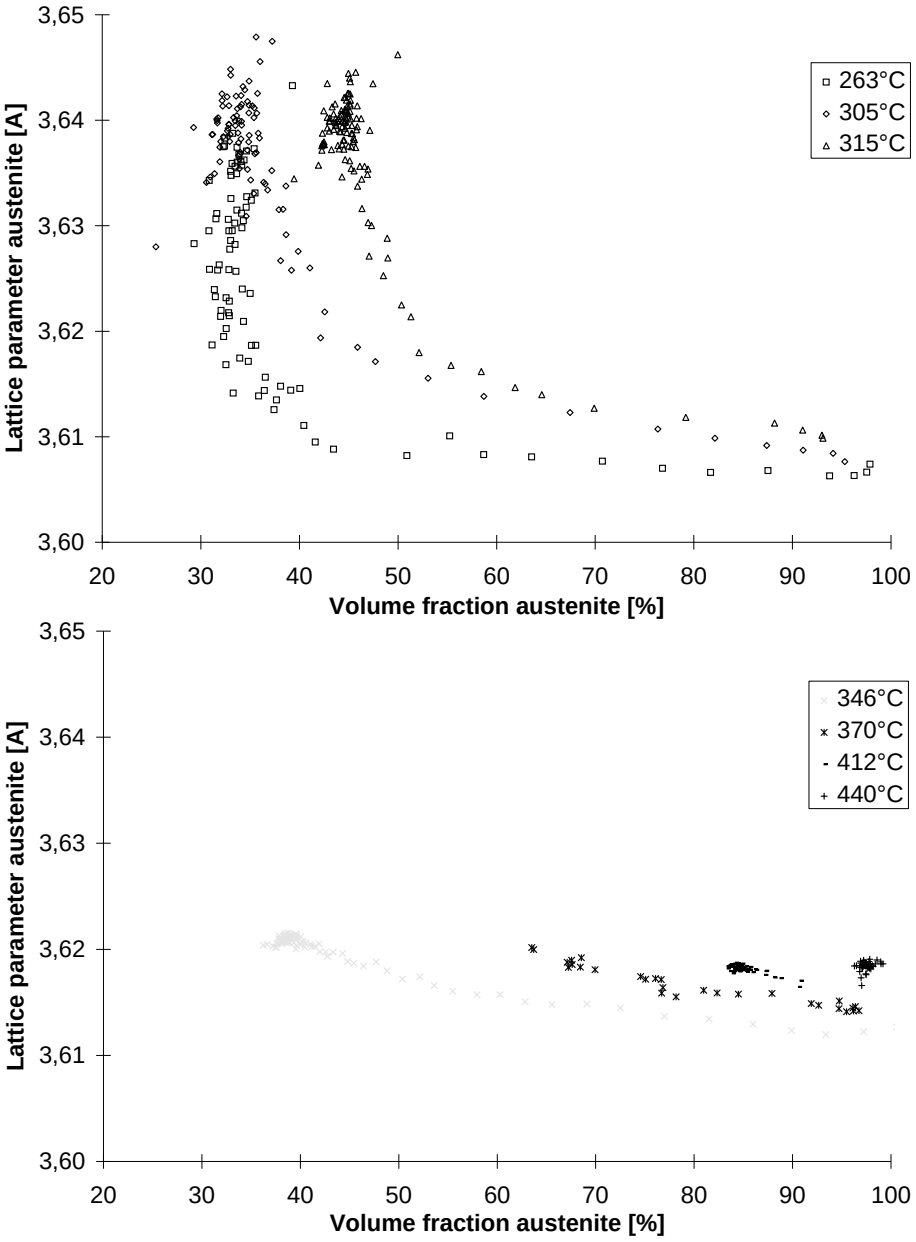

Figure 7.12: Lattice parameter of austenite versus volume fraction of austenite for the runs in the expected regime of lower (top) and upper bainite (bottom).

in table 7.6 and plotted in figure 7.11.

T_{start} [°C]	$a_{0,\gamma,start}$ [Å]	T_{final} [°C]	$a_{0,\gamma,final}$ [Å]	ΔT [°C]	$\Delta a_{0,\gamma}$ [Å]
291	3.607	263	3.637	-28	0.030
296	3.608	305	3.634	9	0.026
313	3.610	315	3.639	2	0.029
376	3.614	346	3.621	-30	0.007
377	3.615	370	3.620	-7	0.005
402	3.617	412	3.618	10	0.001
421	3.617	440	3.619	19	0.002

Table 7.5: Initial and final lattice parameters of austenite.

Edge Width Results

The evolution of the dimensionless edge width parameter σ_1 for ferrite and austenite is shown in figure 7.13. The initial and final values are tabulated in table 7.7 and plotted for ferrite and austenite in figure 7.14. The behavior of the edge width parameters is very similar to that of the lattice parameter, e.g. austenite starts at a small value and increases during the course of the transformation while the edge width of ferrite exhibits its largest value in the beginning and decreases afterwards. Much bigger changes for both the ferrite and the austenite edge width are observed during the transformations at 263, 305 and 315°C. The behavior of this parameter for the transformation at 346°C is clearly different from the other runs. The final edge widths of ferrite are about the same at all temperatures while in the case of austenite all initial values are around 0.003 and the final values for the lower transformation temperatures are about an order of magnitude larger than those of the transformations at 346, 370, 412 and 440°C.

Transformation T [° C]	$\sigma_{1,\alpha,final}$	$\sigma_{1,\gamma,start}$	$\sigma_{1,\gamma,final}$	$\Delta\sigma_{1,\gamma}$
263	0.019	0.003	0.053	0.050
305	0.011	0.003	0.039	0.036
315	0.011	0.003	0.053	0.050
346	0.006	0.002	0.006	0.004
370	0.010	0.004	0.008	0.004
412	0.015	0.003	0.003	0.000
440		0.003	0.002	-0.001

Table 7.7: Variations of the edge width parameters.

7.1.6 Discussion

Volume Fractions Discussion

The transformation is proposed to stop when the carbon concentration in austenite reaches the value given by the T_0-curve (figure 7.1). This curve is essentially linear, consequently, the amount of formed

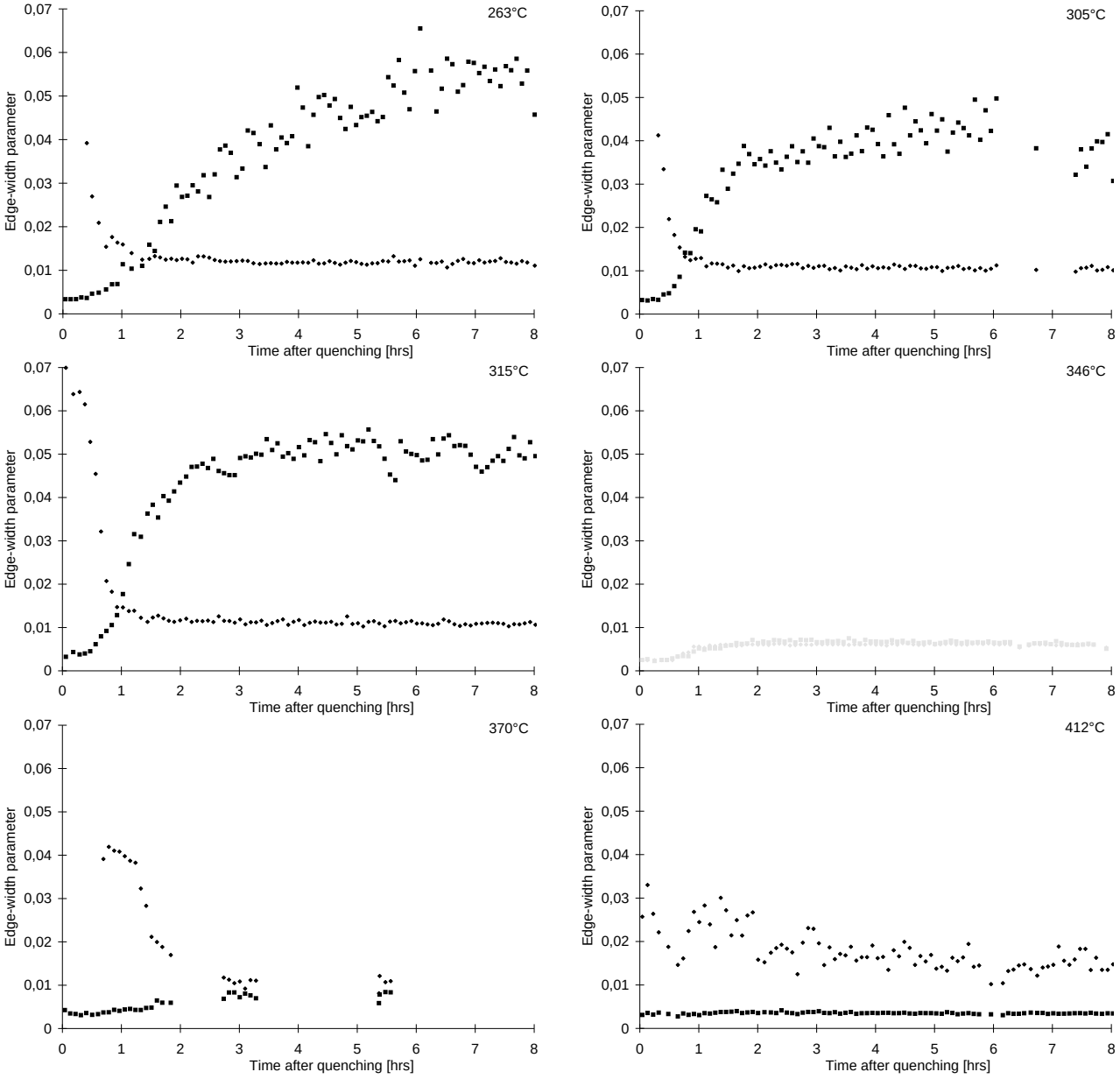

Figure 7.13: Change of edge width (distribution of lattice spacings) of ferrite (diamonds) and austenite (squares). In the case of 440°C, the ferrite never reached a volume fraction allowing a reliable refinement of the edge width parameter.

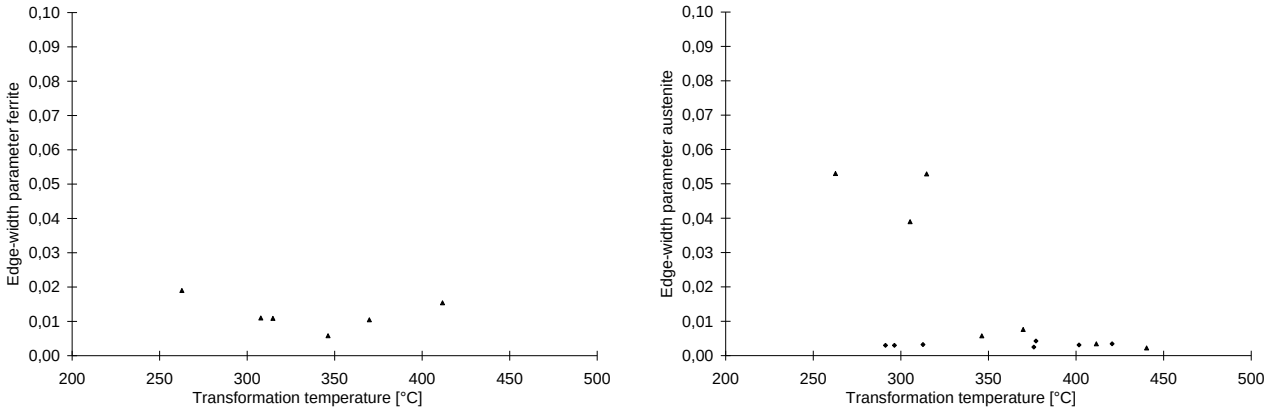

Figure 7.14: Left: Final edge width parameter of ferrite (bainitic ferrite and martensite) against temperature. Right: Initial (diamonds) and final (triangles) edge width parameters of austenite against temperature.

bainite should increase linearly with undercooling below B_S. As can be seen from figure 7.8, the results for the final volume fractions of bainite agree with this and therefore a cessation of the transformation in agreement with the theory was observed.

Above a certain temperature B_S no bainite is formed at all. For B_S Steven & Haynes (1956) propose an empirical equation

$$B_S[^\circ C] = 830 - 270w_C - 90w_{Mn} - 37w_{Ni} - 70w_{Cr} - 83w_{Mo} \tag{7.5}$$

where w_i is the weight per cent of element i. For the given chemical composition, this results in a bainite start temperature of 443°C. Although the chemical composition of the steel samples used in the present work is not within the extent of validity of this equation (for the elements contained in the used sample system the equation is stated to be valid for 0.1-0.55 wt. % carbon, 0.1-0.35 wt. % silicon and 0.2-1.7 wt. % manganese), the agreement with the failure of any detectable formation of ferrite at 440°C and the B_S temperature of 438°C determined from the linear regression in figure 7.7 is good.

Modelling of Kinetic Data

The quality of the volume fraction data derived by Bragg-edge transmission is sufficient for an analysis of the kinetics according to the model of Johnson & Mehl (1939), Avrami (1939, 1940, 1941) and Kolmogorov, however such an analysis has not been performed as the experimental conditions were neither close to isothermal, as assumed for the JMAK model, nor has the heat treatment of the samples been similar enough to allow comparison of the kinetic parameters from different transformation temperatures.

Although in a first order approximation the formation of bainite in austenite is a nucleation and growth process and thus can be described by a JMAK-type of kinetic equation, the modelling of kinetic data by such equations in general is probably more valuable in order to predict the transformation behaviour of a special system rather than obtain insights into processes on an atomic scale (see for example Christian, 1965, section 58, table IX for relations between parameters of the JMAK equation and such processes). As the JMAK model neither includes a dependence on composition nor on the evolving microstructure (e.g. pearlite, bainite or martensite) and its corresponding formation mechanism (for example parameters describing the induction of new martensite embryos due to the formation of martensite plates, so-called autocatalysis, or the diffusionless transformation of austenite to bainite followed by a diffusional decarburisation), it can be only used to interpolate the behaviour of the system for which the temperature dependence of the kinetic coefficients has been performed. This circumstance is also reflected by several corrections of the JMAK model necessary to adapt it to specific systems (e.g. Wert & Zener, 1950, Weinberg, 1992, Erukhimovitch & Baram, 1994, Jones & Bhadeshia, 1997) and several alternative models for isothermal transformations (e.g. Austin & Rickett, 1939, Cahn, 1956, Starink, 1997, Réti et al., 1997).

A more sophisticated model for the particular case of decomposition kinetics of austenite to bainite was developed by Bhadeshia (1982). Nevertheless, the application of such a model has been beyond the scope of the present work.

Lattice Parameter Discussion

Before the implications of the transformation mechanism explained in the introduction to the lattice parameters are addressed, first other mechanisms that will lead to lattice parameter changes shall be considered. During an isothermal first order transformation, changes of the lattice parameter may be due to (mechanical) transformation strain from a density difference between parent phase and transformation product or due to chemical strain from changes of the (local) concentration of substitutional or interstitial elements. For a Fe-Mn-Si-C steel, according to Stark et al. (1990) only carbon has to be considered mobile and chemical strain can be only due to changes of the local carbon concentration. In the present case, the transformation was not truly isothermal due to the latent heat of the transformation. Besides, the large sample volume did not reach the transformation temperature at the same time and instantly with the begin of the transformation which introduces temperature gradients. Additional changes of the lattice parameters are therefore introduced due to thermal expansion. According to an estimation by Hall et al. (1982), the effect of transformation strain on the austenite lattice parameter can be neglected compared to that of carbon concentration changes.

The remaining effects of chemical and thermal strain on the lattice parameter of austenite can be approximated for the present case by

$$a_\gamma\left(\mathrm{T}, x_C^\gamma\right) = \left(3.570 + 0.044 x_C^\gamma\right)\left(1 + 21.9 \cdot 10^{-6}\left(T - 20°C\right)\right) \tag{7.6}$$

The lattice expansion of austenite depending on carbon content given in wt. % for low alloyed steels is described by Roberts (1953). To derive the reference lattice parameter and the coefficient of thermal expansion, the initial lattice parameters of austenite are assumed to be pre-transformation lattice parameters and thus to be only dependent on thermal expansion and a carbon concentration given by the overall chemical composition. This assumption is justified by the good agreement of the measured values with the fit to $\alpha_\gamma = m \cdot T + const$ (thin line in figure 7.10). Via $\alpha = m/(const + m \cdot T_{ref})$, with a reference temperature of T_{ref}=20°C, the coefficient of thermal expansion of $\alpha_\gamma = (21.9 \pm 1.5) \cdot 10^{-6}$°C $^{-1}$ is determined. This value agrees well with $\alpha_\gamma = 21.151 \cdot 10^{-6}$°C $^{-1}$ as reported by Bhadeshia (1982) for a steel of similar composition (Fe-0.22C-2.03Si-3.0Mn) from dilatometry data. The room temperature lattice parameter of austenite resulting from the linear regression is (3.5863 ± 0.0019) Å. With the chemical composition and the constant given in 7.6, the carbon-free room temperature lattice parameter of austenite used as a reference in 7.6 can be estimated as 3.5696 Å. As can be seen from 7.6, a temperature change of 60°C would be necessary to obtain the same effect as a change of 0.1 wt. % of carbon content. Hence, the change of the austenite lattice parameter is governed by the change of carbon content.

Similar considerations for ferrite lead to a dependence of the lattice parameter on temperature and carbon content given by

$$a_\alpha\left(T, x_C^\alpha\right) = \left(2.863 + 0,030 x_C^\alpha\right)\left(1 + 14.7 \cdot 10^{-6}\left(T - 20°C\right)\right) \tag{7.7}$$

where the coefficient of thermal expansion for bainite was derived from analysis of 60 neutron Bragg-edge transmission patterns taken during heating one of the samples to austenitisation temperature before the transformation (see section 6.4 for a description of this analysis). The CTE agrees well with the value of $\alpha_\alpha = 13.049 \cdot 10^{-6}$°C $^{-1}$ given by Bhadeshia (1982) for the steel stated above. The factor relating lattice parameter and carbon content in wt. % is calculated for a single lattice constant from equations given for the lattice constants of martensite by Roberts (1953). Both equations for the lattice constants may be solved for the carbon concentration allowing to measure this quantity with

the same time resolution as the lattice parameter. In the case of bainite, the refined lattice parameter of ferrite has to be corrected for martensite using the first refined values of the volume fraction and the lattice parameter which are ascribed to martensite. The resulting plots are presented in figure 7.15. To have more datapoints in the initial stage of the transformation, a time resolution of 1 minute rather than 5 minutes as for the other plots was used for the analysis. In all cases the carbon concentration in austenite is initially very close to the chemical composition and increases during the transformation. The derived carbon concentration in bainite is initially very high and decreases within approximately one hour to its final value. As already stated above, the carbon concentration in bainite is subject to large errors arising from the poorly defined lattice parameter and volume fraction of martensite. Some additional error for very small volume fractions is likely to be introduced by the tendency of too high refined lattice parameters for small layer thicknesses (see section 6.3). This explains that the weighed average of the carbon concentration is not in all cases consistent with the chemical composition. Due to the weak beam of the initial 10 minutes of the run at 315°C, where the martensite parameters are derived, the systematic error is largest in the case of the transformation at this temperature, explaining the calculated negative carbon concentration. The scatter is largest in the case of the transformation at 412°C as in that case the volume fraction of ferrite was low throughout the whole run, increasing the errors of its structural parameters. From the transformation mechanism explained in the introduction, a reduction of the carbon content of bainitic ferrite and an increase of the amount of carbon absorbed by austenite is expected. If the decomposition of austenite stops before equilibrium, the final carbon content of austenite is anticipated to be close to the T_0 curve rather than the Ae_3 curve. If an initial supersaturation of bainitic ferrite is observed, the lattice parameter of ferrite should be high in the beginning and decrease rapidly. A formation of carbides, as expected in the temperature regime of lower bainite, should lead to a decrease of the carbon concentration in both ferrite and austenite.

In all cases, the lattice parameter and the derived carbon concentration changes are qualitatively consistent with the expected behavior, e.g. the ferrite lattice parameter/carbon content decreases while the austenite lattice parameter/carbon content increases (figure 7.9 and figure 7.15). This means that carbon is partitioned from bainitic ferrite and absorbed by austenite. To quantitatively judge the final austenite lattice parameter, the lattice parameters for carbon concentrations given by the T_0 and the Ae_3 curve where calculated using equation 7.6. They are plotted as thick solid and dashed lines in figure 7.10, respectively. The carbon concentrations were calculated for the chemical composition of the steel studied in the present work using the program `MAP_STEEL_MUCG46` which is part of the Materials Algorithms Project (MAP, 1997). All measured final lattice parameters scatter around the lattice parameters expected for the T_0 curve which confirms findings that the decomposition of austenite to bainite stops at a carbon concentration in austenite close to the T_0 curve rather than the Ae_3 curve. Because of the big difference between those curves, this is a sensitive indication of the failure of the transformation to reach equilibrium. The same is true for the final carbon concentrations derived from the austenite lattice parameters (figure 7.16). As the measured initial carbon concentration in austenite is close to the chemical composition, both initial and final values are consistent with the expected values. Furthermore, the final carbon concentrations of ferrite and austenite are consistent with findings of Bhadeshia and Waugh who determined carbon concentrations by atom probe for a steel Fe-0.43C-2.02Si-3.0Mn transformed at 350°C of approximately 0.5 (α_b) and 4 atom % (γ), corresponding to 0.1 and 0.8 wt. % carbon in bainitic ferrite and austenite, respectively (figure 7.17). It is therefore concluded that the applied conversion of the lattice parameter to carbon content is a valid approximation. Nevertheless, the large errors introduced by the martensite overlaying the bainitic ferrite reflections do not allow to conclude the initial supersaturation of bainitic ferrite unambiguously.

The data clearly indicate that the change of lattice parameter and therefore the carbon con-

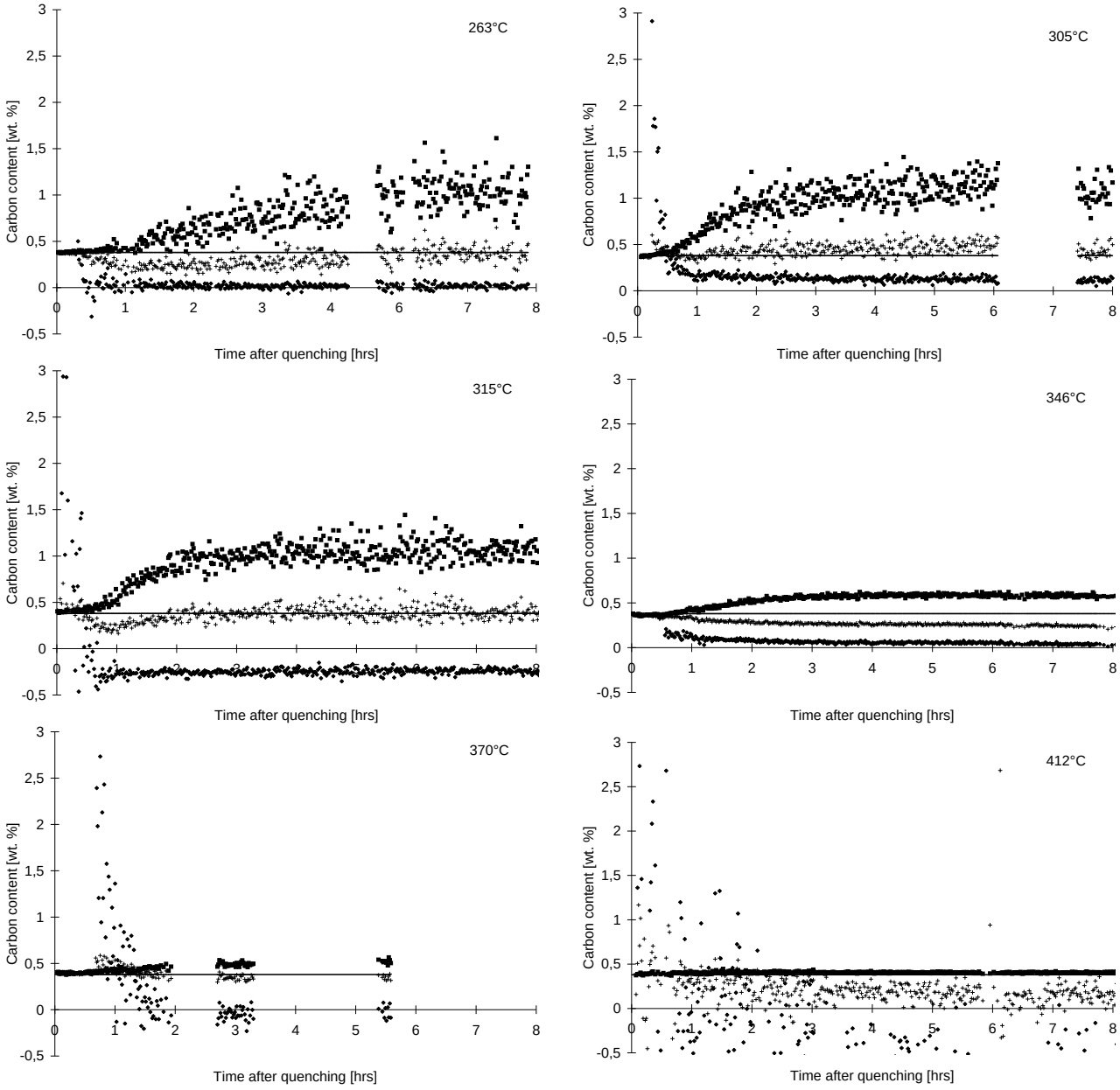

Figure 7.15: Carbon content of bainite (diamonds) and austenite (squares) as calculated from the lattice parameters. The calculated average carbon concentration weighted by the volume fractions is displayed as "+", the solid line corresponds to the carbon concentration according to the chemical composition of the sample (0.38 wt. %). Each datapoint results from a lattice parameter refined from a pattern gathered within one minute.

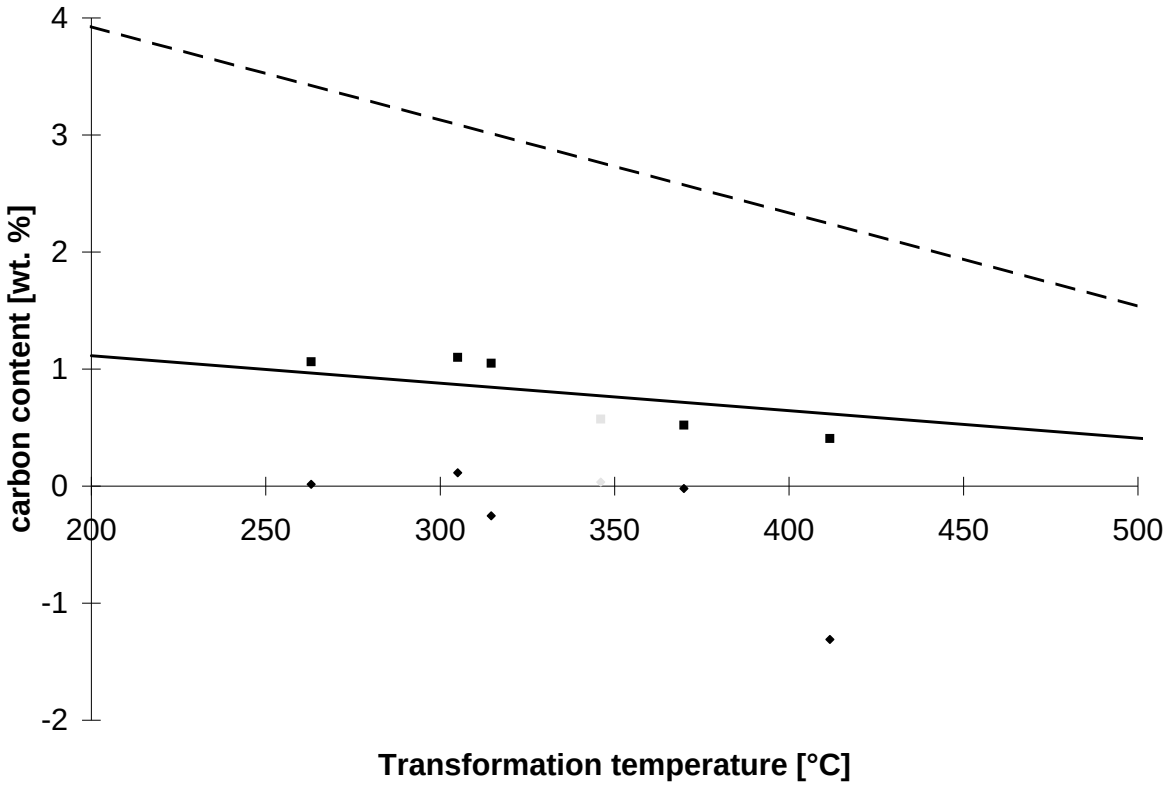

Figure 7.16: Final carbon content of bainite (diamonds) and austenite (squares) as derived from the lattice parameters. The solid and dashed line correspond to the T_0-curve and the Ae_3-curve, respectively. The negative values result from the correction of the bainitic ferrite lattice parameters, see text.

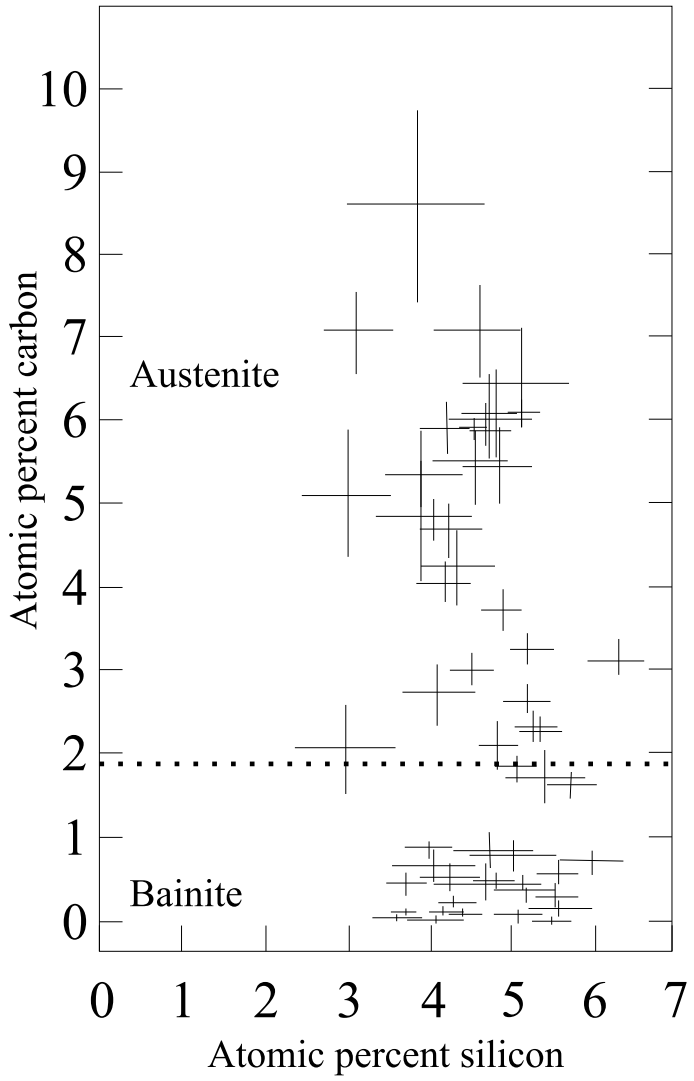

Figure 7.17: Local silicon and carbon concentrations in a similar steel as determined by Bhadeshia & Waugh, 1982 (figure 2) using the atom probe technique. The dotted line represents the overall carbon concentration of 1.93 at. %, data points below this line correspond to bainite. See text for further information.

centration continues for transformation temperatures 263, 305 and 315°C after the cessation of the transformation, e.g. after the volume fractions reached almost their final values. This is best visible in figure 7.12. It is worth mentioning that during a dilatometer measurement this may appear as a macroscopic length change, dividing the derived transformation kinetics into a faster part, where the volume fractions actually change, and a second part of more sluggish kinetics where only the carbon is redistributed (reported for example by Hunkel et al., 1999, for a 100Cr6-type steel Fe-1.0C-0.24Si-0.27Mn-1.42Cr). In this particular case it is beneficial to measure volume fractions and lattice parameters independently, which is uniquely provided by the Bragg-edge transmission technique.

Edge Width Discussion

After Todd et al. (1995), the reflection profile after removing all sources of broadening not caused by strain (e.g. instrumental and particle size broadening) represents the variance of the (Gaussian) probability distribution of the peak shifts corresponding to the strains. As stated above, strain caused by temperature and volume changes can be treated as second order effects, leaving changes of the chemical composition as reason for lattice parameter shifts. Hence, the results indicate a decrease of the width of the distribution of lattice parameters of ferrite during the course of the transformation and thus a decrease of the variation in the local carbon concentration. For the retained austenite, on the other hand, the increase in reflection widths indicates an increase of the variation width of the local carbon concentration. Again, the refined edge width parameter for ferrite contains contributions of martensite and bainitic ferrite. Nevertheless, for both ferrite and austenite, the results are consistent with the findings of Bhadeshia & Waugh (1982) already stated above, who found for the local carbon concentration broad respectively narrow distributions for austenite respectively bainitic ferrite (figure 7.17).

The smaller edge widths at the higher temperatures indicate a more homogeneous distribution of carbon. This is consistent with the higher diffusion at those temperatures, allowing a redistribution of carbon atoms over longer ranges. As both the final carbon content and the edge width exhibit a step between the lower and higher transformation temperatures and the border between the regimes of upper and lower bainite for the given chemical composition is assumed to be around 350°C, a relatively sharp change of the diffusion may be concluded at this temperature. Although, more measurements would be necessary to confirm this.

The behavior of the edge widths for the transformation at 346°C is clearly different from the other runs. The explanation may be the different heat-treatment of this sample, although the processes leading to these observations are not understood. As both the lattice parameter and edge width of ferrite for this run exhibit only a much smaller increase during the initial stage of the transformation, i.e. no supersaturated ferrite was formed, it is speculated that in this case another (ferritic) phase than bainite was formed. Because the transformation in that case started at 100 vol. % austenite, a remaining partial transformation to pearlite from the quenching to 500°C and then re-heating to 1000°C can be excluded. Although, it is likely that pearlite has formed during this period which afterwards was transformed to austenite again when the austenitisation temperature was reached. Because of this, the formation of pearlite might be favored over the formation of bainite as the arrangement of the atoms was already close to that of pearlite.

7.1.7 Conclusions

During the decomposition of austenite to bainite in a steel Fe-0.38C-1.94Si-2.99Mn the volume fractions, lattice and edge width parameters of both phases were monitored using neutron Bragg-edge transmissions. The parameters allow to study the kinetics, average local carbon concentration and variation width of the local carbon concentrations in both phases. In all cases, a good agreement with other work and the formation mechanism of bainite as proposed by Bhadeshia & Edmonds (1979) was found. The transformation at 346°C has to be excluded as the heat-treatment of this sample was significantly different from the other samples, resulting in a different transformation product and hence different behavior of the parameters. The transformation at 370°C suffered from the poor quality of the neutron beam during that transformation.

The cessation of the transformation was clearly observed. From the comparison of the measured carbon concentrations in retained austenite with calculated carbon concentrations for the T_0 and the Ae_3-curve it can be unambiguously concluded that the transformation stops at a carbon content in austenite corresponding to the non-equilibrium T_0 rather than equilibrium Ae_3 concentration. Therefore, the reaction remained incomplete. This is in full agreement with the transformation mechanism explained in the introduction. The observed variation of the austenite lattice parameter and therefore the change of the carbon concentration after the cessation of the transformation, i.e. after the volume fractions reached a virtually constant level, for the case of the lower temperatures only indicates a difference in the formation process for upper and lower bainite. This is also supported by the much broader edges of austenite for those temperatures, suggesting a broader distribution of lattice parameters and therefore a broader variation of local carbon concentrations. The initial supersaturation of bainitic ferrite cannot be concluded unambiguously due to the 'contamination' of the lattice parameter with martensite from the quenching process. Nevertheless, the derived carbon concentrations in bainitic ferrite exhibit high values during the first hour of the transformation.

As for each phase the number of unit cells per unit area, lattice and edge width parameter can be measured independently with Bragg-edge transmission, no ambiguities arise in the determination of quantities derived from these parameters. In contrast, this is not the case for example for volume fractions determined by resistivity or dilatometric measurements where both changes in the volume fractions and internal strains result in a change of the measured quantity (reported for resistance measurements by Radcliffe & Rollason, 1959). Given a stable beam, Bragg-edge transmission is a powerful tool to study phase transitions in systems with a high crystallographic symmetry consisting of good neutron scatterers. The availability of **BETMAn** transferred the power of full-pattern refinements after the Rietveld (1969) method to Bragg-edge transmission patterns and, in conjunction with the new detector system used at flightpath 5, proved to increase the quality of the results compared to Bragg-edge transmission experiments in the past.

Highly desirable for future experiments is a method to automate and control the quenching. As the sample in a transmission experiment does not have to be a single bulk, for example by splitting the sample into thin slabs the surface could be increased allowing to quench the sample volume by a high pressure helium jet or water spray directed to the surfaces. This would take away ambiguities arising due to the manual cooling procedure and also reduce temperature gradients between the bulk and the, due to slabs, much larger sample surface, i.e. the temperature distribution in the sample would be more uniform. Avoiding the formation of martensite could be achieved by this procedure, allowing to improve the determination of the carbon content in bainitic ferrite.

7.2 Nickeloxide

7.2.1 Introduction

The Bragg-edge transmission technique was used to study the kinetics of a model solid-state reaction, the reduction of nickeloxide to nickel according to

$$NiO \rightarrow Ni + \tfrac{1}{2}O_2 \tag{7.8}$$

Two runs were performed, one at 1100°C and the second at 1400°C. The goal of the study described in this section was to obtain insight in the rate controlling process by fitting various models to the kinetic data derived from Bragg-edge transmission patterns. It could be confirmed that the reaction rate is controlled by diffusion at 1100°C, but is somewhat a mixed process for 1400°C. Such problems are conventionally studied by thermogravimetry. Bragg-edge transmission provides additionally to volume fractions of the two phases nickeloxide and nickel information on the crystallographic state, namely the lattice parameter, of both phases.

This study is the first application of Bragg-edge transmission to a solid-state reaction where the reaction layer proceeds uniformly from the sample surface inward. It is also the first application to a ceramic system and to phase transitions at temperatures above 1000°C. Therefore, the objective from the point of view of exploring the technique was also to investigate the applicability of Bragg-edge transmission at high temperatures where the Bragg edges are expected to diminish due to thermal vibration of the atoms. The general interest is a study of the influence of specimen geometry on the kinetics data. The reduction of NiO was chosen from a range of examples as a model system due to quality of the patterns obtained in this system. Other candidates for similar investigations were

- reduction of nickel-spinel, $NiAl_2O_4$, to alumina, Al_2O_3, and nickel,
- reduction of perovskite structure type PZT, $PbZr_{0.9}Ti_{0.1}O_3$, and
- phase transition between high- and low-cristobalite as already mentioned in section 6.2.

For all systems, room temperature patterns of available samples were gathered, but NiO exhibited the most promising ones.

7.2.2 Sample Preparation

The cylindrical samples were prepared at the California Institute of Technology by dry pressing commercial NiO powders into a cylindrical compact. After sintering, the samples had dimensions of about 27 mm diameter and 12 mm thickness. The thickness was chosen to reach about 20% neutron transmission at room temperature averaged over the accessible wavelength range. More details about the specimens can be found in Vogel et al. (2000b).

7.2.3 Experiment

As the general experimental setup used is described in chapter 5, only specific changes and additional setup is described here. The collimation was adjusted to 3 cm by choosing a 4 cm collimation in the

first beam tube and a setup in front of the furnace of ring shaped pieces with 3 cm inner diameter made of steel (7.5 cm, slowing down and removing fast neutrons from the direction of the incident beam), polyethylene (2.5 cm, same for slow neutrons), borated polyethylen (2.5 cm, absorb neutrons over a wide energy range, see equation (1.5)), polyethylen (2.5 cm) and steel (5 cm) again. By adjusting the disk-shaped sample of 2.7 cm diameter such that its center was in line with the center of the collimation, the assumption of the complete sample bathing in the slightly diverging beam was fulfilled. The latter simplifies the calculations necessary to validate the kinetics models.

In order to provide the controlled atmosphere, the tube furnace with its 95 cm long ceramic tube (14 cm inner diameter) was sealed at both ends with aluminum endcaps. A heat resistant silicon-rubber gasket made a tight connection between endcaps and tube. On the endcaps, fittings for hoses were mounted outside the area illuminated by the neutron beam to transport the gas to and from the furnace volume. The endcaps contributed of course to the measured pattern and, contrary to the beam tube endcaps, were subject to thermal expansion. The latter makes it impossible to simply use a measured pattern taken at room temperature as incident intensity spectrum for the data analysis.

For this experiment, the data acquisition was triggered by the LBEG signal of the proton storage ring (cf. sections 5.2 and 6.4) to avoid loss of synchronisation between data acquisition time (i.e. the time stamp of each pattern) and real time (i.e. the timespan the reduction is running). The trigger was delayed by 8 ms to cover the high d-spacing range with the available 8192 channels of 5 μs each.

Samples were heated to the transformation temperature in air and held there for approximately one hour to allow equilibration. Thermocouples were not necessary in this case as the furnace set points were found in a previously performed calibration run. After equilibration, the reducing atmosphere was turned on by running a gas mixture of 0.5 l/min CO and 0.05 l/min CO_2 diluted by 0.5 l/min N_2 through the furnace tube. By offline calibration it was found that the oxygen partial pressure reached its equilibrium value of about $2.3 \cdot 10^{-10}$ Pa (1100°C) and $3.9 \cdot 10^{-6}$ Pa (1400°C) to within two orders of magnitude in less than 5 minutes. Further information on calibration of the gas setup can be found in Vogel et al. (2000b).

7.2.4 Data Analysis

As stated above, the thermal expansion of the aluminum endcaps prevents the use of a measured pattern as incident intensity spectrum to get rid of the unwanted aluminum edges. Therefore, additionally to nickeloxide (NaCl structure, space group F m$\bar{3}$m, a=4.18 Å) and nickel (fcc structure, space group F $\frac{4}{m}\bar{3}\frac{2}{m}$, a=3.52 Å) an aluminum phase (same structure as Ni, a=4.05 Å) was included in the refinement. The aluminum contribution of the beam tube endcaps was accounted for by using a measured open beam pattern. By manually fitting the room temperature pattern of NiO in the controlled atmosphere setup, starting values for an automated refinement of the patterns gathered during heating the sample were obtained. The refined values of the last pattern during heatup were used as starting values of the refinement of patterns collected during the actual reduction. Similar to the analysis of the bainite transformation data, a three step approach was used for the automated refinement, resulting in a script similar to the one described in section 7.1.4 and listed in appendix F.4. The major difference to the case of the bainite transformation are the much weaker edges due to higher transmission T and the strong attenuation of the elastic coherent scattering at the temperatures reached here due to thermal motion of the atoms (see figure 7.18 and discussion in next section). Additionally, a large fraction of the intensity is lost due to incoherent scattering (5.2 barn) and absorption (4.5 barn) by the nickel atoms, although the scattering power of nickel is with 13.3 barn for

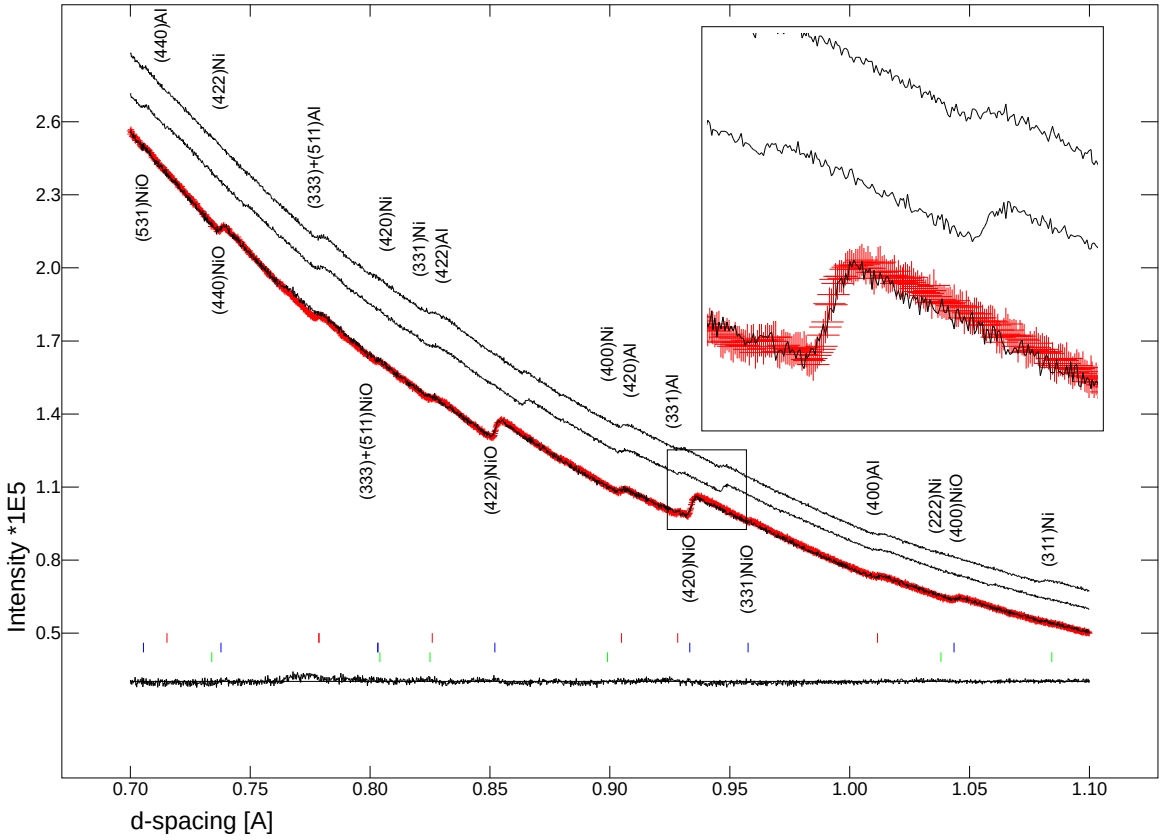

Figure 7.18: Fraction of Bragg-edge transmission patterns of the sample system taken at room temperature (lowest curve), 1100°C before (middle) and after (top) the reduction. The tick marks indicate postions of (top to bottom) aluminum, nickeloxide and nickel, the difference curve results from the refinement of the room temperature pattern. The edges are labeled with their Miller indices and phases. The inset shows the shift and attenuation of the NiO (420) edge due to the increase of the temperature (lowest to middle curve) and the further decrease of the edge height due to the decreasing volume fraction of NiO (middle to upper curve).

coherent scattering very good. The oxygen does not contribute much to the Bragg-edge transmission patterns as the coherent scattering cross-section is only about 4.2 barn with virtually no incoherent scattering and absorption cross-section (for comparison, iron has values of 11.2, 0.4 and 2.6 barn for coherent scattering, incoherent scattering and absorption). Owing to the much weaker edges, it was necessary to carefully set the volume fraction and neutron intensity limits for conditional refinements and exclusion of patterns due to low neutron intensity, respectively.

Again, the analysis was performed in forward and backward direction at different temporal resolutions as a check of consistency. Isotropic displacement factors $B_{iso,n}$ of all contributing atoms, number of unit cells and lattice parameter of aluminum were kept fixed at values averaged over an analysis run of all patterns to reduce the degrees of freedom of the fit and therefore make it more robust. This is justified as these parameters remained constant during the isothermal reaction. From the refined numbers of unit cells of nickeloxide and nickel the volume fractions of the two phases in the system NiO-Ni were derived.

The kinetics analysis is described in Vogel et al. (2000b). Essentially, the volume fraction versus transformation time data points were fitted against models describing a diffusion- and an interface-

reaction-controlled process. By judging the agreement of the data with the fit, conclusions on the underlying process may be drawn.

7.2.5 Results

Fractions of Bragg-edge transmission patterns of the sample system taken at room temperature, 1100°C before and after the reduction are presented in figure 7.18. Shift and attenuation of the nickeloxide edges (e.g. (422) at 0.85 Å) due to heating of the sample are clearly visible. Nickel edges being not visible before the reduction appeared in the pattern during reduction (e.g. (311) at 1.09 Å). Aluminum edges remain virtually constant in the graph (e.g. (333)+(511) at 0.78 Å). From refined lattice parameters of aluminum, the definition of thermal expansion (6.3) and $\alpha_{Al} = 23.1 \cdot 10^{-6} °C^{-1}$, a temperature change of the endcaps by $\approx 170°C$ results.

Figure 7.19, page 113, shows the resulting volume fraction information for nickel at the two reduction temperatures. Clearly, the reduction kinetics are different and a higher Ni volume fraction is reached at the higher temperature. Both time resolutions of the analysis (varied by integrating different numbers of patterns prior to the refinement) result in consistent curves (also performed analysis runs with 5, 2.5 and 1 minute resolution are not shown but yielded also consistent results). Naturally, the scatter is decreased with increasing integration time. For the 30 second time resolution about 1400 Rietveld refinements were performed. The time for each refinement with up to 15 variable parameters is about 30 seconds on a Pentium CPU running at 233 MHz.

Another independent check of consistency of the Bragg-edge transmission analysis is obtained by comparing the results of weight measurements to those from Bragg-edge transmission. Assuming that weight change during reduction is due to loss of oxygen, it was calculated that the weight fraction of Ni in the sample reduced at 1100°C is 43% and that in the sample reduced at 1400°C is 64%. These values are approximately the same ones obtained from Bragg-edge transmission analysis (accounting for the scatter at the end and the fact that the reduction proceeded, although slower, during cooling in the reducing atmosphere).

A principle benefit of the Bragg-edge transmission technique compared to classical methods for studies of reaction kinetics (dilatometry, thermogravimetry) is to provide additional information on lattice and edge width parameters. This was applied in the study of the austenite-bainite reaction described in the first part of this chapter. Unfortunately, at the high temperatures used during processing of ceramics, the attenuation of the reflection intensities (see figure 7.18) due to thermal motion of the atoms makes extraction of such information much tougher than in the region below 500°C like in the case of the transformation of steel. Refinement of lattice parameters for nickel and nickeloxide did not lead to divergence of the fit as was expected when inspecting the observed patterns for the first time due to the, compared to steel, very weak edges. The results are presented in figure 7.20, page 114. The nickeloxide lattice parameter remains virtually constant throughout the reaction at both investigated temperatures. Most striking is the decrease of the nickel lattice parameter during the reaction at 1100°C. This is in agreement with the much more rigid lattice formed by ionic bonded nickel and oxygen atoms compared to the metallic bond of nickel. The fact that the NiO lattice parameter did not change during this process excludes a mechanical source that would lead to elastic strain energy generation. If this were the case, the elastic strain in Ni would have to create an elastic strain of opposite sign in NiO. A chemical source for the change in the Ni lattice constant, however, is possible: Similar to the role of interstitial carbon during the bainite reaction described above, nickel (atomic radius Ni: 1.24Å, Rösler, 1991, table 16.2) initially supersaturated with (substitutional)

oxygen (ionic radius O^{2-}: 1.32 Å) could be formed, resulting in a widened lattice. By diffusion, the excess oxygen could be partitioned from nickel to the atmosphere, reducing the average lattice parameter probed by Bragg-edge transmission. Nevertheless, currently this is speculation and further research is necessary. It is also necessary to re-confirm the finding of a constant lattice parameter at 1400°C, e.g. by additional experiments either using conventional powder diffraction or Bragg-edge transmission.

The speculation above is supported by a broader edge width found for nickel by refinement of the final pattern: σ_1 was refined to about 0.10 for nickel while for nickeloxide only values of 0.01-0.02 were found. The much broader edges of nickel prevent a reliable refinement of σ_1 at least for nickel during an automated analysis. Nevertheless, the finding indicates a broader variation of nickel lattice parameters, for example due to varying local oxygen concentrations.

Results for the kinetics analysis are reported in more detail in Vogel et al. (2000b), here only the principal results are given. For the 1100°C run, a fit to a model function based on a diffusion controlled reaction provided much better agreement with the data than fit to an interface controlled model. Therefore, it is concluded that the reaction at this temperature is actually diffusion controlled. For 1400°C, the interface-controlled model seems to fit the data derived from Bragg-edge transmission better, but neither of the two options fits as good as the diffusion model for 1100°C. Besides the refinements, potential sources of error may be the assumptions of the model, namely a propagation of the reaction interface inward from all surface. Cracks in the sample may significantly violate this assumption.

7.2.6 Conclusions

The experiment presented in this section proves that it is possible to track a high-temperature solid state reaction with 30 sec time resolution, at least by means of volume fractions, by Bragg-edge transmission. With a poorer time resolution, information on the lattice parameter could be obtained. To confirm the findings, additional experiments are necessary, partly repeating the same experiments with thicker samples to improve the contrast, but also vary the density/porosity of the samples to establish the dependence of the kinetics on this parameters. The latter is of direct impact for processing of ceramics. It is also desirable to perform measurements on the reaction in the opposite direction, i.e. investigate the oxidation of nickel by Bragg-edge transmission. To improve the contrast in the Bragg-edge transmission patterns, thicker samples are necessary. This does not need to be a single piece but could consist of two pieces in a certain distance.

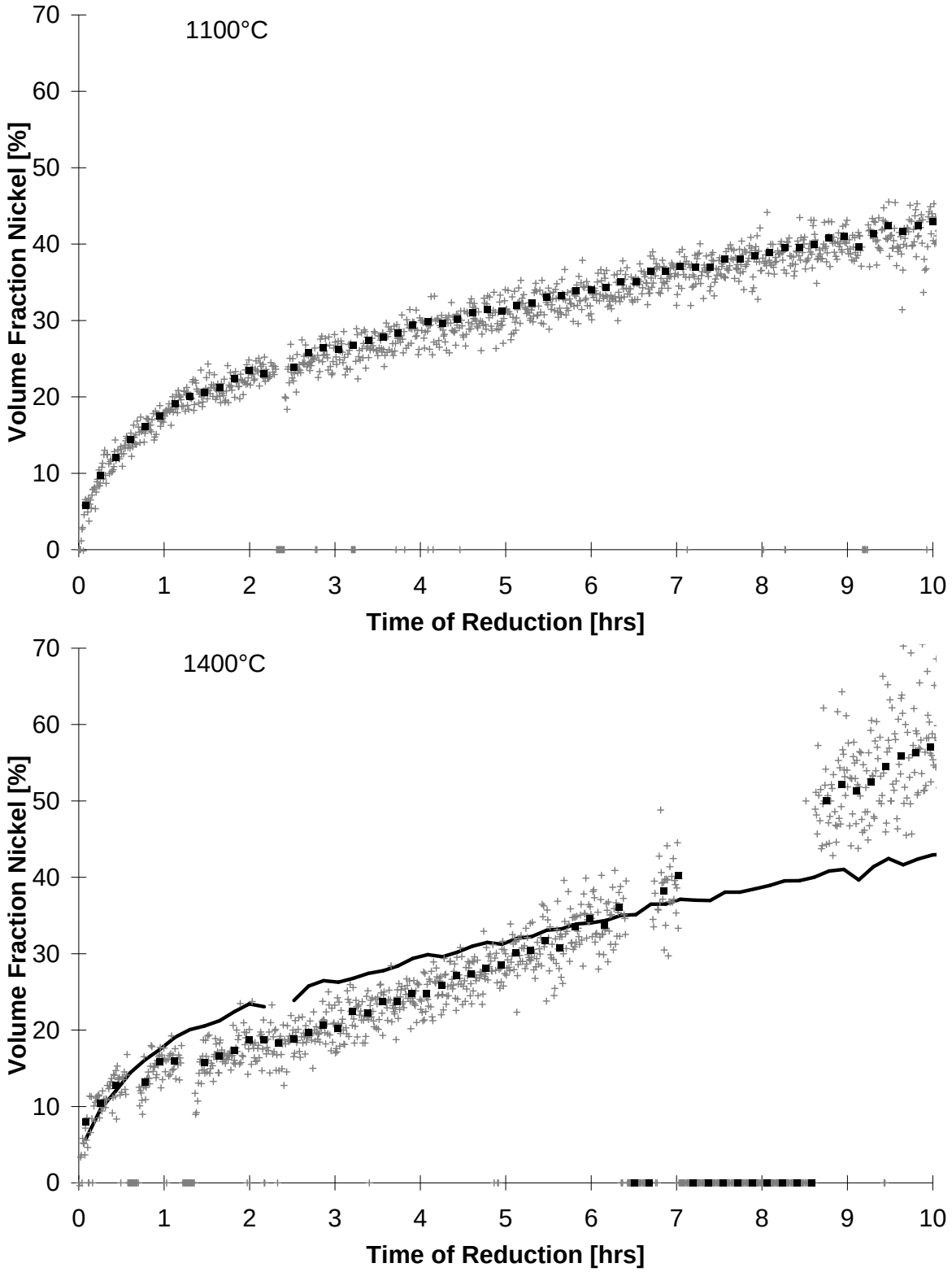

Figure 7.19: Volume fraction of nickel within the system NiO-Ni versus reduction time for the run at 1100°C (top) and 1400° C (bottom). Thick black squares result from an analysis run with 10 minutes time resolution, gray crosses from 30 seconds. In the bottom plot the curve resulting from the 1100°C run is reproduced for comparison. Zero volume fraction means beam failure.

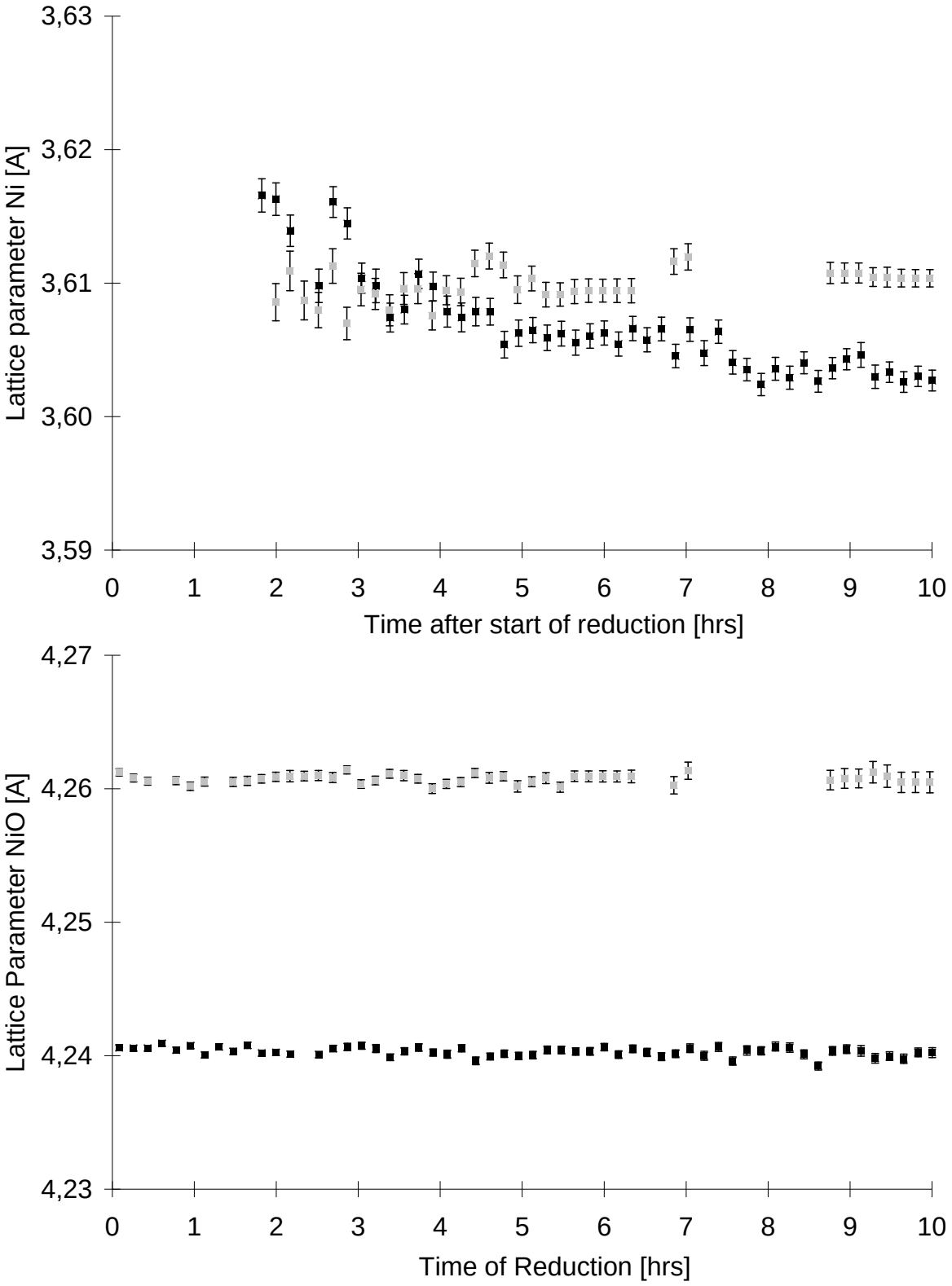

Figure 7.20: Lattice parameter of nickel (top) and nickeloxide (bottom) versus reaction time at 1100°C (black squares) and 1400°C (gray squares). The error bars result from the e.s.d.s of the fit. For nickel, a refinement of the lattice parameter during the first two hours was not possible due to the too low volume fraction of the phase.

Chapter 8

Discussion & Conclusions

A model for the description of Bragg-edge transmission patterns and its implementation into a Rietveld-type refinement program **BETMAn** were described in the present work. The description of the elastic coherent scattering cross-section is complete and allows application of the technique to obtain crystallographic information (lattice and edge width parameters, volume fractions) with a good temporal resolution. An appropriate edge profile function for patterns measured at LANSCE was developed, allowing for the first time a full pattern refinement of Bragg-edge transmission patterns after the Rietveld method. A simple texture model for transmission data was presented, although, experimental verification of this model is still missing. Further work is necessary to complete the approximations used in the epithermal region and understand the behaviour of the parameters used to model the inelastic scattering. Without this, the desired determination of the sample thickness from Bragg-edge transmission patterns, necessary for example for tomography, is impossible.

BETMAn provides an easy-to-use graphical user interface, providing direct feedback to the progress of the refinement. It is capable to support the design of experiments by calculating both the cross-sections of arbitrary phases and, based on this, simulated Bragg-edge transmission patterns and estimates for appropriate sample thicknesses. Direct access to the CIF-format, for example generated by the Inorganic Crystal Structures Database (ICSD), further simplifies experiment design and generation of appropriate phase descriptions for refinements. An efficient script language allows automated refinements, inevitable for the large number of patterns typically gathered during investigations of reactions or phase transformations with Bragg-edge transmission. The software was used to refine more than 10.000 Bragg-edge transmission patterns and proved to be stable. A built-in database allows to store records describing measured patterns and exempts the user from providing nuclear data.

Calibration of the flightpath used at LANSCE was described as well as the validation of features of **BETMAn**. A dependence of the refined lattice parameter on the sample thickness in the order of 100 microstrain was found, calling for further investigations on the understanding and correction of this effect. Data collected during heating and applying stress to a sample yielded good agreement with expected results for the coefficient of thermal expansion and strain/Poisson's Ratio of the sample system. Nevertheless, the promising expected resolution for strain measurements could not yet be achieved.

The possibility of short accumulation times was successfully applied in an investigation of the transformation mechanism of the isothermal decomposition of austenite to bainite in a Si-rich steel.

In this study, the carbon content and its homogenity in both participating phases, crucial for the understanding of the transformation mechanism, could be followed with a time resolution of one minute. The applicability of the Bragg-edge transmission technique to study high-temperature reactions in ceramcis was also demonstrated by an investigation of the reaction kinetics of the isothermal reduction of nickeloxide. Volume fractions could be obtained with a temporal resolution of 30 seconds in this case while lattice parameters were averaged over 10 minutes. In both experiments, a good agreement with theory, validation measurements and prior works was achieved. The inclusion of a large part of the transmission spectrum with many Bragg-edges in the data analysis clearly proved to be superior over the single edge analysis performed in past work. It should be noted, that for such experiments a sufficiently large sample volume must be probed under a special environment (e.g. reducing atmosphere, temperature above 1000°C), a requirement which is not trivially achieved by synchrotron radiation (e.g. Barnes et al., 2000).

Summarizing, it can be stated that **BETMAn** is a big step forward in the application of the Bragg-edge transmission technique, both for the efficiency of the data analysis and especially the qualitiy of the results. The Bragg-edge transmission technique has proven to be very promising in the field of investigations of reaction kinetics.

Chapter 9

Outlook

Potential improvements of the Bragg-edge transmission technique may be separated into desired changes of the experimental setup/data acquisition at LANSCE and extensions of the data analysis. Further experiments are also proposed.

Currently, the signals of each photomultiplier tube are joined on a single transmission cable from the detector silo to the data acquisition electronics and counted in a single electronic counter of constant bin width. Desirable optimisations include more counters and transmission lines to reduce artificial dead time from joining the signals and a variable bin width according to $\Delta t/t = const$ as used for most neutron time-of-flight diffraction instruments. This provides shorter channels in the low d-spacing/high energy region, where reflection density and incident intensity are much higher. Special data acquisition would be also beneficial for the combination of Bragg-edge transmission and nuclear resonance spectroscopy (NRS): In the epithermal energy range, where the resonances are located, a small channelwidth is required to accurately determine the temperature from the resonance broadening (typically 100 ns). Contrary, in the range of thermal neutrons, for the Bragg-edges much longer bin widths are needed (1 to 5 μs). Combination of both techniques requires also extensions of the data analysis software. A detector system capable of counting the very high rates at 10 m from the moderator would increase the available wavelength range and potentially allow to investigate systems like cristobalite, having the most intense edges outside the accessible wavelength range at 60 m. As for such intensities the active detector area should be divided into small elements, the same setup would allow spatially resolved measurements, for example of 2D strain fields.

From the point of view of data analysis, further investigations on approximations for inelastic cross-sections as well as the dependence of the lattice parameter on the layer thickness are most urgent. The former will lead to better estimations of the sample thickness from transmission data, for instance of interest for different porosities of ceramic samples. On a longer time scale, tomography may become a topic and correct estimations of layer thicknesses are prerequisite for such measurements. Addition of a parameter describing detector deadtime in the model function would make this parameter a calibration parameter similar to flightpath-length or time-offset. Fit of this parameter to a series of patterns of known sample thickness would simplify deadtime determination and provide a verification of other methods to determine detector deadtime.

Introduction of restraints/constraints to the fitting algorithm, as for example described by Raymond (1972), are hoped to increase robustness of automated refinements. For the latter, a mechanism to detect divergence, for example by checking absolute parameter values or e.s.d.'s, would be also of

advantage. To make the fitting procedure more robust, the former is also suggested by Izumi (2000) and applied in the Rietveld code RIETAN (Izumi, 1993): If try-values of a parameter leave a physical meaningful range, e.g. a profile width becomes negative, the new vector of try-values should be discarded, the Levenberg-Marquardt parameter λ should be increased, which decreases the step width for the new guess values, and new guess values should be calculated. Again according to Izumi (2000), in RIETAN it proved to be beneficial to apply the conjugate directions or Powell's method to the result vector achieved by convergence of the Levenberg-Marquardt algorithm. As no derivatives are required for Powell's method, the procedure is slower than the Levenberg-Marquardt algorithm, but capable of solving ill-conditioned problems in which very high correlations between parameters exist. Hence, it can be tested whether the Levenberg-Marquardt algorithm was trapped in a local minimum with a lower minimum nearby. Both approaches may result in significant improvements of the robustness of **BETMAn**'s fitting procedure.

Inclusion of tabulated parameters for calculation of Debye-Waller factors depending on temperature after Sears & Shelley (1991) would allow calculation of appropriate starting values for the atomic displacement factors. Further investigation in the field of texture would be advantageous.

Further experiments could include:

- Austenite decomposition to bainite under a controlled atmosphere, at least for the austenization, to avoid decarburization of outer layers. Highly desirable is also avoidance of martensite formation during quenching, for instance by splitting the bulk sample into several slabs to increase the surface and therefore the heat transfer. Splitting into slabs requires a controlled atmosphere at all stages of the experiment to avoid decarburization. Potentially, such experiment allows to provide experimental evidence for the initial supersaturation of bainitic ferrite. For this purpose, also a correction for the observed lattice parameter dependence on the layer thickness is mandatory. Investigation of the transformation using samples from the same batch by dilatometry to validate the hypothesis of a second, more sluggish expansion of the sample due to the observed austenite lattice expansion is also of interest. In the bainite transformation in general, also much work was done in this field since the discovery of bainite, unresolved issues remain (Bhadeshia, 1999): The precipitation of carbides and the formation of bainite from plastically deformed austenite. Potentially, utilizing Bragg-edge transmission some further insight can be contributed.

- Nickeloxide reduction at more temperature points to validate the finding of different mechanisms and potentially establish a transition point. With samples of different porosities, investigations of the relation between reduction kinetics and sample density and, with a very low porosity, minimization of deviations from the assumption of a uniform reaction layer are possible. Contrast of the Bragg-edge transmission patterns should be improved by thicker samples. Further validation with other techniques is also necessary.

- Determination of systematic deviations of Poisson's ration from linearity by measuring the lattice parameter at several applied strains. Using the large detector area and resolution available at LANSCE, such a measurement could be performed with a low amount of beam time.

- Precise determination of structure factors. As in Bragg-edge transmission patterns the reflection intensity and therefore the structure factor is accessible also between edges, the latter can be measured accurately. This, in turn, may allow to investigate the distribution of carbon among interstitial sites in steels as for example performed by Mazzone (1987) for diffraction data.

Chapter 10

Acknowledgements

I would like to express my gratitude to my supervisor, Hans-Georg Priesmeyer for providing me with the task of exploring Bragg-edge transmission and making its application easier. His continuous advice and encouragement helped a lot during the ups and downs while developing and applying **BETMAn**.

To Mark Bourke (LANL) I am indebted for inviting me several times to Los Alamos and providing so much support for this work.

I would like to thank Joyce Roberts for granting funding for stays at LANSCE during which the presented experiments were performed and many useful discussions with the LANSCE-12 staff, lead by Joyce, were possible.

Funding from the Deutsche Akademische Austauschdienst (DAAD) for stays at the Open University, Milton Keynes, UK, are also gratefully acknowledged. The time spent with Lyndon Edwards' group was very valuable for me. I wish to thank Lyndon for allowing me to use David Wang's data for the re-analysis described in section 6.5.

I should also thank the LANSCE-3 group, lead by Steve Wender, for support during use of their flight path 5. I am appreciative to the team managing flightpath 5, the Low Energy Neutron Science Team of P-23, lead by David Bowman, for their support during my work. Special thanks are due to Vincent Yuan for his inexhaustible readiness to assist during electronics and data acquisition setup and Walt Trela for a lot of assistance especially during my first stays at Los Alamos. I am thankful to Werner Abfalterer, Art Bridge, Gregg Chapparo, Lloyd Hunt, Dennis Martinez, Russ Mortensen and Tom Langston for helping to solve technical problems.

I am grateful to H. K. D. H. 'Harry' Bhadeshia (Cambridge) for suggesting and supporting the bainite experiment. I wish to thank Pascal Jacques (Cambridge) for valuable discussions during the data analysis for this experiment, Robert Reiswig (LANL) for preparation of the samples for metallography, W. Schmitz (GKSS) for carrying out the metallography and Partha Rangaswamy (LANL) for assistance doing the x-ray measurements.

I thank Ersan Üstündag and Jay Hanan (both California Institute of Technology) for their cooperation during the nickeloxide experiment.

In the development of **BETMAn**, suggestions and results of discussions with many people were incorporated. I am especially thankful to Robert von Dreele (LANSCE-12) for many discussions and suggestions regarding edge profiles and the Rietveld method in general, Javier Santisteban (Open Uni-

versity) for providing me with the CRIPO program and the reference of Granada with approximations for the total neutron scattering cross-section and Giovanni Bruno (Open University, now HMI, Berlin) for the cooperation during the development of the texture model.

I thank Graham Madin for his efforts to make the english in this thesis more readable.

Last, but not least, I am very thankful to my parents, my girlfriend Merle Fürstenwerth and her parents for their various support during my studies.

References

A. Albinati & B. T. M. Willis, *The Rietveld Method in Neutron and X-ray Powder Diffraction*, J. Appl. Cryst., **15**, 361-374 (1982).

J. B. Austin & R. L. Rickett, *Kinetics of the decomposition of Austenite at Constant Temperature*, Trans. AIME, **135**, 396-415 (1939).

M. Avrami, *Kinetics of Phase Change Part I: General Theory*, Journal of Chemical Physics, **7**, 1103-1112 (1939).

M. Avrami, *Kinetics of Phase Change Part II: Transformation-Time Relations for Random Distribution of Nuclei*, Journal of Chemical Physics, **8**, 212-224 (1940).

M. Avrami, *Kinetics of Phase Change Part III: Granulation, Phase Change, and Microstructure*, Journal of Chemical Physics, **9**, 177-184 (1941).

G. E. Bacon, *Neutron Diffraction*, Monographs on the Physics and Chemistry of Materials, Clarendon Press, Oxford/UK (1955).

D. Balzar, R. B. Von Dreele, K. Bennett & H. Ledbetter, *Elastic-strain tensor by Rietveld refinement of diffraction measurements*, J. Appl. Phys., **84, No. 9**, 4822-4833 (1998).

P. Barnes, S. Colston, B. Craster, C. Hall, A. Jupe, S. Jacques, J. Cockcroft, S. Morgan, M. Johnson, D. O'Connor & M. Bellotto, *Time- and space resolved dynamic studies on ceramic and cementitious materials*, J. Synchrotron Rad., **16**, 167-177 (2000).

J. Baumann, R. Gähler, J. Kalus & W. Mampe, *Experimental limit for the charge of the free neutron*, Physical Review D, **37**, 3107-3112 (1988).

J.-F. Bérar & P. Lelann, *E.S.D.'s and Estimated Probable Error Obtained in Rietveld Refinements with Local Correlations*, J. Appl. Cryst., **24**, 1-5 (1991).

H. K. D. H. Bhadeshia, *Bainite: Overall transformation kinetics*, Journal de Physique IV, Colloque C4, supplément au no 12, Tome 43, decembre 1982, **43**, 443-448 (1982).

H. K. D. H. Bhadeshia, *Bainite in Steels: Transformations, Microstructure and Properties*, The Institute of Materials, London, England (1992).

H. K. D. H. Bhadeshia, *The bainite transformation: unresolved issues*, Materials Science and Engineering A, **273-275**, 58-66 (1999).

H. K. D. H. Bhadeshia & J. W. Christian, *Bainite in Steels*, Metallurgical Transactions, **21A**, 767-798 (1990).

H. K. D. H. Bhadeshia & D. V. Edmonds, *The Bainite Transformation in a Silicon Steels*, Metallurgical Transactions, **10A**, 895-907 (1979).

H. K. D. H. Bhadeshia & D. V. Edmonds, *The Mechanism of Bainite Formation in Steels*, Acta metall., **28**, 1265-1273 (1980).

H. K. D. H. Bhadeshia & A. R. Waugh, *Bainite: An atom-probe study of the incomplete reaction phenomenon*, Acta metall., **30**, 775-784 (1982).

K. Binder, *Total Coherent Cross Sections for the Scattering of Neutrons from Crystals*, Phys. Stat. Sol., **41**, 767-779 (1970).

D. L. Bish & S. A. Howard, *Quantitative Phase Analysis Using the Rietveld Method*, J. Appl. Cryst., **21**, 86-91 (1988).

J. D. Bowman, J. J. Szymanski, V. W. Yuan, C. D. Bowman & A. Silverman, *Current-mode detector for neutron time-of-flight studies*, Nucl. Instrum. Meth., **A 297**, 183-189 (1990).

C. D. Bowman, P. A. Egelstaff, H. G. Priesmeyer, *Experiments Using Single Neutron Pulses*, in M. Misawa, M. Furusaka, H. Ikeda (eds.), Proc. ICANS-XI (*International Collaboration on Advanced Neutron Sources*), October 22-26 1990, KEK Report 90-25 (March 1991), AMRD Vol. II, 840-847 (1991).

I. N. Bronstein & K. A. Semendjajew, *Taschenbuch der Mathematik*, B. G. Teubner Verlagsgesellschaft, Stuttgart/Germany (1991).

B. Buras & A. Holas, *Intensity and Resolution in Neutron Time-of-Fligt powder diffractometry*, Nukleonika - TOM XIII, **6**, 591-619 (1968).

J. W. Cahn, *The kinetics of grain boundary nucleated reactions*, Acta metallurgica, **4**, 449-459 (1956).

J. M. Carpenter, M. H. Mueller, R. A. Beyerlein, T. G. Worlton, J. D. Jorgensen, T. O. Brun, K. Sköld, C. A. Pellizari, S. W. Peterson, N. Watanabe, M. Kimura & J. E. Gunning, *Neutron Diffraction Measurements on Powder Samples Using the ZING-P Pulsed Neutron Source at Argonne*, in Proc. Neutron Diffraction Conf. Petten, The Netherlands, 5-6 August 1975 (Reactor Centrum Nederland, RCN-234), 192-208 (1975).

J. M. Cassels, *The Scattering of Neutrons by Crystals*, in: O. R. Frisch (ed.): *Progress in Nuclear Physics*, Pergamon Press, London, **65**, 185-215 (1950).

E. E. Castellano & P. Main, *On the Classical Interpretation of Thermal Probability Ellipsoids and the Debye-Waller Factor*, Acta Cryst., **A41**, 156-157 (1985).

J. W. Christian, *The Theory of Transformations in Metals and Alloys*, Pergamon Press, Oxford, England (1965).

I. Cole & C. G. Windsor, *The Lineshapes in Pulsed Neutron Powder Diffraction*, Nucl. Instrum. Meth., **171**, 107-113 (1980).

M. J. Cooper, K. D. Rouse, B. T. M. Willis, *Neutron Diffraction Studies of Anharmonic Temperature Factors in BaF_2*, Acta Cryst., **A24**, 484-493 (1968).

M. Dahms & H. J. Bunge, *The Iterative Series-Expansion Method for Quantitative Texture Analysis. I. General Outline*, J. Appl. Cryst., **22**, 439-447 (1989).

M. Dahms, *The Iterative Series-Expansion Method for Quantitative Texture Analysis. II. Applications*, J. Appl. Cryst., **25**, 258-267 (1992).

M. R. Daymond & P. J. Withers, *A New Stroboscopic Neutron Diffraction Method For Monitoring Materials Subjected to Cyclic Loads: Thermal Cycling of Metal Matrix Composites*, Scripta Materialia, **35, No. 6**, 717-720 (1996).

M. R. Daymond, M. A. M. Bourke, R. B. Von Dreele, B. Clausen & T. Lorentzen, *Use of Rietveld refinement for elastic macrostrain determination and for evaluation of plastic strain history from diffraction spectra*, J. Appl. Phys., **82 (4)**, 1554-1562 (1997).

M. R. Daymond & P. J. Withers, *In situ Monitoring of Thermally Cycled Metal Matrix Composites by Neutron Diffraction and Laser Extensometry*, Applied Composite Materials, **4**, 375-392 (1997).

D. L. Decker, R. A. Beyerlein, G. Roult & T. G. Worlton, *Neutron diffraction study of KCN III and KCN IV at high pressure*, Physical Review, **10 (8)**, 3584-3593 (1973).

L. Dobrzynski & K. Blinowski, *Neutrons and Solid State Physics*, Ellis Horwood, Hemel Hempstead (1994).

W. A. Dollase, *Correction of Intensities for Preferred Orientation in Powder Diffractometry: Application of the March Model*, J. Appl. Cryst., **19**, 267-272 (1986).

G. Eckold, M. Hagen & U. Steigenberger, *Non-equilibrium states in ferroelectrics: Time-resolved studies in* Rb_2ZnCl_4, Physica, **B 234-236**, 151-152 (1997).

V. Erukhimovitch & J. Baram, *Crystallization kinetics*, Physical Review, **B 50 (9)**, 5854-5856 (1994).

ESS Website: http://www.kfa-juelich.de/ess/WIE/What_is_ess.html (1999).

E. Fermi, W. J. Sturm, R. G. Sachs, *The Transmission of Slow Neutrons through Microcrystalline Materials*, Physical Review, **71, No. 9**, 589-594 (1947).

K. Geiger, *Inside ODBC*, german translation of *Inside ODBC*, Microsoft Press, Unterschleißheim, Germany (1995).

J. R. Granada, *Total Scattering Cross Section of Solids for Cold and Epithermal Neutrons*, Z. Naturforsch., **39a**, 1160-1167 (1984).

R. W. Grosse-Kunstleve, *Algorithms for deriving crystallographic space-group information*, Acta Cryst., **A55**, 383-395 (1999). See also http://atb.csb.yale.edu/sginfo/.

S. Großmann, *Mathematischer Einführungskurs in die Physik*, Teubner Studienbücher, Stuttgart (1991).

C. Guéneau & C. Servant, *Quantitative Determination of Low Phase Volume Fraction in FerroSilicon Alloys by the Rietveld Profile-Refinement Method. Neutron Diffraction Data Compared with Other Methods*, J. Appl. Cryst., **28**, 707-716 (1995).

D. J. Hall, H. K. D. H. Bhadeshia & W. M. Stobbs, *The incomplete bainite reaction: Possible reasons for the apparent differences in TEM and atom probe determination of austenite carbon content*, Journal de Physique IV, Colloque C4, supplément au no 12, Tome 43, decembre 1982, **C4**, 449-454 (1982).

S. R. Hall, F. H. Allen & I. D. Brown, *The Crystallographic Information File (CIF): a New Standard Archive File for Crystallography*, Acta Cryst., **A47**, 655-685 (1991). See also: http://ndbserver.ebi.ac.uk:5700/NDB/mmcif/software/CIFLIB/.

R. J. Hill & C. J. Howard, *Quantitative Phase Analysis from Neutron Powder Diffraction Data Using the Rietveld Method*, J. Appl. Cryst., **20**, 467-474 (1987).

R. W. K. Honeycomb & H. K. D. H. Bhadeshia, *Steels: microstructure and properties*, Edward Arnold, London (1996).

M. Hunkel, T. Lübben, F. Hoffmann & P. Mayr, *Modellierung der bainitischen und perlitischen Umwandlung bei Stählen*, Härterei Technische Mitteilungen, **6** (1999).

D. K. Hyer (ed.), *Condensed matter research at LANSCE*, LANL document code LALP 90-7, Los Alamos, USA (1990).

R. M. Ibberson, W. I. F. David & K. S. Knight, *The High Resolution Neutron Powder Diffractometer (HRPD) at ISIS - A User Guide*, Rutherford Appleton Laboratory Report RAL-92-031 (1992). Also available online: http://www.isis.rl.ac.uk/Crystallography/HRPDguide.htm.

M. Iizumi, *Real-time neutron diffraction studies of phase transition kinetics*, Physica, **B 136**, 36-41 (1986).

S. Ikeda & J. M. Carpenter, *Wide-Energy-Range, High-Resolution Measurements of Neutron Pulse Shapes of Polyethylene Moderators*, Nucl. Instrum. Meth., **A239**, 536-544 (1985).

F. Izumi, *Rietveld analysis programs RIETAN and PREMOS and special applications*, in: R. A. Young (ed.), *The Rietveld Method*, Oxford University Press, Oxford (1993).

F. Izumi, priv. communication 25th May 2000.

JINR: User guide neutron experimental facilities for condensed matter investigations at FLNP JINR, JINR, Dubna, Russia (1997). Also available online: http://nfdfn.jinr.dubna.su/flnph/userguide-97/ibr-2/.

W. H. Johnson & R. F. Mehl, *Reaction Kinetics in Processes of Nucleation and Growth*, Trans. AIME, **135**, 416-458 (1939).

R. G. Johnson & C. D. Bowman, *High Resolution Powder Diffraction by White Source Neutron Transmission*, AIP Conference Proceedings Number 89, Neutron Scattering 1981, John Faber, Jr. (ed.), American Institute of Physics, 53-55 (1982).

S. J. Jones & H. K. D. H. Bhadeshia, *Kinetics of the simultaneous decomposition of austenite into several transformation products*, Acta mater., **45, No. 7**, 2911-2920 (1997).

J. D. Jorgensen, D. H. Johnson, M. H. Mueller, S. W. Peterson, T. G. Worlton & R. B. Von Dreele, in *Proc. Conf. on Diffraction Profile Analysis*, Cracow, Poland, 14-15. August 1978, 20-22 (1978).

M. K. Kang, J. L. Sun & Q. M. Yang, *High-Temperature Transmission Electron Microscopy In Situ Study of Lower Bainite Carbide Precipitation*, Metallurgical Transactions, **21A**, 853-858 (1990).

J. G. King, *Search for a small charge carried by molecules*, Physical Review Letters (later results quoted in Shull et al. (1967)), **5 (12)**, 562-565 (1960).

C. Kittel, *Einführung in die Festkörperphysik*, (German translation of 'Introduction to Solid State Physics'), Oldenbourg, München (1996).

J. N. Knudson, J. D. Bowman, B. E. Crawford, P. P. J. Delheij, C. M. Frankle, C. R. Gould, D. G. Haase, M. Iinuma, L. Y. Lowie, A. Masaike, Y. Masuda, G. E. Mitchel, S. I. Pentilla, H. Postma, N. R. Roberson, S. J. Seestrom, E. I. Sharapov, H. M. Shimizu, S. L. Stephenson, Y. F. Yen, V. W. Yuan & S. H. Yoo, *A High-Rate Detection System to Study Parity Violation with Polarized Epithermal Neutrons at LANSCE*, J. Neutron Research, **4**, 209-213 (1996).

F. Kropff & J. R. Granada, *CRIPO: A fast computer code for the evaluation of σ_T in polycrystalline materials*, unpublished Report (CAB-1977), Centro Atomico Bariloche, Institute Balseiro, 8400 Bariloche, Argentina (1977).

W. F. Kuhs, *Generalized Atomic Displacements in Crystallographic Structure Analysis*, Acta Cryst., **A48**, 80-98 (1992).

A. C. Larson & R. B. Von Dreele, *GSAS - General Structure Analysis System*, LANL document code LAUR 86-748, Los Alamos, US (1994).

F. Liebau, *Die Systematik der Minerale*, Die Naturwissenschaften, **49**, 481-491 (1962).

P. W. Lisowski, C. D. Bowman, G. J. Russell & S. A. Wender, *The Los Alamos National Laboratory Spallation Neutron Sources*, Nuclear Science and Engineering, **106**, 208-218 (1990).

S. W. Lovesey, *Theory of Neutron Scattering from Condensed Matter, Volume 1: Nuclear Scattering*, Clarendon Press, Oxford (1986).

J. E. Lynn, G. H. Kwei, W. J. Trela, V. W. Yuan, B. Cort, R. J. Martinez & F. A. Vigil, *Vibrational properties of Pu and Ga in a Pu-Ga alloy from neutron-resonance Doppler spectroscopy*, Physical Review B, **58 (17)**, 11408-11415 (1998).

J. E. Lynn, *Analysis of Doppler-Broadened Neutron Resonance Data*, Task Order 13 of Subcontract No 0416JO007-3Y between LANL and Sumner Associates, Summary Report (1999).

W. Mampe, P. Ageron, J. C. Bates, J. M. Pendlebury & A. Steyerl, *Neutron lifetime from a liquid walled bottle*, Nucl. Instrum. Meth., **A284**, 111-115 (1989a).

W. Mampe, P. Ageron, C. Bates, J. M. Pendlebury & A. Steyerl, *Neutron lifetime Measured with Stored Ultracold Neutrons*, Physical Review Letters , **63**, 593-596 (1989b).

MAP Website: http://www.msm.cam.ac.uk/map/steel/programs/mucg46-b.html (after entering the MAP library at http://www.msm.cam.ac.uk/map) (1997).

A. March, *Mathematische Theorie der Regelung nach der Korngestalt bei affiner Deformation*, Zeitschr. f. Kristallographie, **81, Bd. 19**, 285-297 (1932).

S. Matthies, H.-R. Wenk & G. W. Vinel, *Some Basic Concepts of Texture Analysis and Comparision of Three Methods to Calculate Orientation Distributions from Pole Figures*, J. Appl. Cryst., **21**, 285-304 (1988).

J. Mayers, G. Baciocco & A. C. Hannon, *Temperature Measurement by Neutron Resonance Radiography*, Nucl. Instrum. Meth., **A275**, 453-459 (1989).

G. Mazzone, *The Distribution of Carbon Among Interstitial Sites of the F. C. C. Iron-Alloy Lattice*, J. Appl. Cryst., **20**, 187-190 (1987).

L. B. McCusker, R. B. Von Dreele, D. E. Cox, D. Louer & P. Scardi, *Rietveld refinement guidelines*, J. Appl. Cryst., **32**, 36-50 (1999).

K. Meggers, H. G. Priesmeyer, W. J. Trela, C. D. Bowman & M. Dahms, *Real time neutron transmission investigation of the austenite-bainite transformation in grey iron*, Nucl. Instrum. Meth., **B 88**, 423-429 (1994a).

K. Meggers, H. G. Priesmeyer, W. J. Trela & M. Dahms, *Investigation of the austenite-bainite transformation in grey iron using real time neutron transmission*, Materials Science and Engineering A, **188**, 301-304 (1994b).

E. W. J. Mitchell & R. J. Stewart, *The Characterization of Crystal Defects by the Fourier Transform of Long Wavelength Neutron Scattering Data*, Philosophical Magazine, **15**, 617-622 (1967).

S. A. Mujahid & H. K. D. H. Bhadeshia, *Partitioning of Carbon from Supersaturated Ferrite Plates*, Acta metall. mater., **40**, 389-396 (1992).

F. Natterer, *The Mathematics of Computerized Tomography*, John Wiley & Sons, New York (1986).

NIST Web-Site for numerical algorithms: http://gams.cam.nist.gov/cgi-bin/gams-serve/list-package-components/SPECFUN.html (1998).

NIST Web-Site for nuclear data: http://www.ncnr.nist.gov/resources/n-lengths/ (1999), the information published there is based on Neutron News, Vol. 3, No. 3, 1992, pp. 29-37.

I. C. Noyan & J. B. Cohen, *Resiudal Stress: Measurement by Diffraction and Interpretation*, Springer, New York (1987).

J. F. Nye, *Physical Properties of Crystals: Their Representation by Tensors and Matrices*, Oxford University Press, Oxford (1998).

D. Olsen, T. Bhatia, Y. Cho, Y. Lee, T. Mason, T. McManamy & J. Staples, *SNS Parameter List*, SNS document code 100000000PL0001R00, revision July 8, 1999 (1999).

G. S. Pawley, *Unit-Cell Refinement From Powder Diffraction Scans*, J. Appl. Cryst., **14**, 357-361 (1981).

P. U. Pennartz, U. Löchner & H. Fuess, *Powder Diffraction in the Range of Milliseconds*, J. Appl. Cryst., **25**, 571-577 (1992).

G. Placzek, B. R. A. Nijboer & L. V. Hove, *Effect of Short Wavelength Interference on Neutron Scattering by Dense Systems of Heavy Nuclei*, Physical Review, **82 (3)**, 392-403 (1951).

G. Placzek, *The Scattering of Neutrons by Systems of Heavy Nuclei*, Physical Review, **86**, 377-388 (1952).

G. Placzek, *Incoherent Neutron Scattering by Polycrystals*, Physical Review, **93**, 895-896 (1954).

G. Placzek & L. V. Hove, *Interference Effects in the Total Neutron Scattering Cross-Section of Crystals*, Il Nuovo Cimento, **1 (1)**, 233-256 (1955).

N. C. Popa, *Texture in Rietveld Refinement*, J. Appl. Cryst., **25**, 611-616 (1992).

W. H. Press, S. A. Teukolsky, W. T. Vetterling & B. P. Flannery, *Numerical Recipes in C - The Art of Scientific Computing*, Cambridge University Press, Cambridge, UK (1992).

H. G. Priesmeyer, *Reverse Time-Of-Flight Fourier Technique for Strain Measurements*, in: M. T. Hutchings, A. D. Krawitz (eds.), *Measurement of Residual and Applied Stress Using Neutron Diffraction*, Kluwer Academic, 329-334 (1992a).

H. G. Priesmeyer, *Transmission Bragg-Edge Measurements*, in: M. T. Hutchings, A. D. Krawitz (eds.), Measurement of Residual and Applied Stress Using Neutron Diffraction, Kluwer Academic, 389-394 (1992b).

H. G. Priesmeyer, *Residual Stress Characterisation by Fourier-RTOF Neutron Diffractometry*, Schriftenr. f. Geowiss., **6**, 29-37 (1998).

H. G. Priesmeyer, C. D. Bowman, V. W. Yuan, S. J. Seestrom, S. A. Wender, R. Richardson, O. A. Wasson, X. Xzu & P. A. Egelstaff, *Fast Transient Neutron Diffraction at LANSCE*, unpublished memo (1989).

H. G. Priesmeyer, J. Larsen & K. Meggers, *Neutron Diffraction fo Non-Desctructive Strain/Stress Measurements in Industrial Devices*, Journal of Neutron Research, **2 (1)**, 31-52 (1994).

E. Prince, *Mathematical Techniques in Crystallography and Material Science*, Springer, Berlin (1994).

E. Prince, *Mathematical Aspects of Rietveld Refinement*, in: R. A. Young (ed.), *The Rietveld Method*, Oxford University Press, Oxford (1993).

A. Prudnikov, Y. Brychkov & O. Marichev, *Integrals and Series, Volume 2: Special Functions*, Gordon and Breach Science Publishers, New York (1986).

A. Putnis, *Introduction to mineral sciences*, Cambridge University Press (1992).

S. V. Radcliffe & E. C. Rollason, *The kinetics of the formation of bainite in high-purity iron-carbon alloys*, Journal of the Iron and Steel Institute, **191**, 56-65 (1959).

K. N. Raymond, *Application of Constraints to Derivatives in Least-Squares Refinement*, Acta Cryst., **A 28**, 163-166 (1972).

T. Réti, L. Horváth & I. Felde, *A Comparative Study of Methods Used for the Prediction of Non-isothermal Austenite Decomposition*, Journal of Materials Engineering and Performance, **6 (4)**, 433-442 (1997).

J. W. Richardson, *Background Modeling in Rietveld Analysis*, in: R. A. Young (ed.), The Rietveld Method, Oxford University Press, Oxford (1993).

H. M. Rietveld, *Line profiles of neutron powder-diffraction peaks for structure refinement*, Acta Cryst., **22**, 151-152 (1967).

H. M. Rietveld, *A Profile Refinement Method for Nuclear and Magnetic Structures*, J. Appl. Cryst., **2**, 65-71 (1969).

H. M. Rietveld, *The early days: a retrospective view*, in: R. A. Young (ed.), *The Rietveld Method*, Oxford University Press, Oxford, 39-42 (1993).

C. S. Roberts, *Effect of Carbon on the Volume Fractions and Lattice Parameters of Retained Austenite and Martensite*, Trans. AIME, **197**, 203-204 (1953).

J. A. Roberts, *The Los Alamos Neutron Science Center (LANSCE)*, Neutron News, **10, No. 4**, 11-14 (1999).

H. J. Rösler, *Lehrbuch der Mineralogie*, Deutscher Verlag für Grundstoffindustrie, Leipzig, Germany (1991).

M. Sakata & M. J. Cooper, *An Analysis of the Rietveld Profile Refinement Method*, J. Appl. Cryst., **12**, 554-563 (1979).

J. Santisteban, Open University, Milton Keynes, UK, private communication (1999).

H. Schumann, *Metallographie*, Deutscher Verlag für Grundstoffindustrie, Leipzig (1990).

H. G. Scott, *The Estimation of Standard Deviations in Powder Diffraction Rietveld Refinements*, J. Appl. Cryst., **16**, 159-163 (1983).

F. Schwabl, *Quantenmechanik*, Springer, Berlin (1993).

V. F. Sears & S. A. Shelley, *Deybe-Waller Factor for Elemental Crystals*, Acta Cryst., **A47**, 441-446 (1991).

R. Setze, C. Gould, C. Howell & J. Walston, *XSYS Reference Manual*, Triangle Universities Nuclear Laboratory, P. O. Box 90308, Durham, NC 27706-0308 (1995). Also available online: http://www.tunl.duke.edu/ walston/xsysman/manual.html.

C. G. Shull, K. W. Billman & F. A. Wedgwood, *Experimental Limit for the Neutron Charge*, Physical Review, **153 (5)**, 1415-1422 (1967).

D. S. Sivia, *Data Analysis - A Bayesian Tutorial*, Clarendon Press, Oxford (1996).

R. Spagna & M. Camalli, *Analysis of weighting schemes*, J. Appl. Cryst., **32**, 934-942 (1999).

M. Stalder, S. Vogel, M. A. M. Bourke, J. G. Maldonado, D. J. Thoma & V. W. Yuan, *Retransformation (alpha'→gamma) kinetics of strain induced martensite in 304 stainless steel*, Materials Science and Engineering A, **280 (2)**, 270-281 (2000).

M. J. Starink, *Kinetic equations for diffusion-controlled precipitation reactions*, Journal of Materials Science, **32**, 4061-4070 (1997).

I. Stark, G. D. W. Smith & H. K. D. H. Bhadeshia, *The Distribution of Substitutional Alloying Elements during the Bainite Transformation*, Metallurgical Transactions, **21A**, 837-844 (1990).

U. Steigenberger, G. Eckold & M. Hagen, *Time resolved studies on a millisecond time scale by elastic neutron scattering: transient properties of the ferroelectric phase transition in Rb2ZnCl4*, Nucl. Instr. Meth, **B 93**, 316-321 (1994).

W. Steven & A. G. Haynes, *The Temperature of Formation of Martensite and Bainite in Low-alloy Steels: Some Effects of Chemical Composition*, Journal of the Iron and Steel Institute, **183**, 349-359 (1956).

B. Stroustrup, *Die C++ Programmiersprache*, german translation of *The C++ programming language*, Addison-Wesley, Bonn (1992).

R. I. Todd, C. Borsa, B. Derby & M. A. M. Bourke, *Analysis of neutron diffraction peak broadening caused by internal stresses in composite materials*, Nucl. Instrum. Meth., **A 354**, 139-144 (1995).

H. Toraya, *Position-constrained and unconstrained powder-pattern-decomposition methods*, in: R. A. Young (ed.), The Rietveld Method, Oxford University Press, Oxford (1993).

P. Van Der Linden, *Expert-C-Programming*, German translation of *Expert C Programming - Deep C Secrets*, Heise, Hannover (1995).

S. Vogel, *Neutronendiffraktometrie in Transmissionsgeometrie mit einem Transientenrekorder*, Diplomarbeit an der Mathematisch-Naturwissenschaftlichen Fakultät der Christian-Albrechts-Universität, Kiel, Germany (1996).

S. Vogel, M. A. M. Bourke, A. Franke, H. Priesmeyer & V. Yuan, *Study of the Incomplete Reaction Phenomenon in the Austenite → Bainite Transformation in a Si-rich Steel with Neutron Real-Time Transmission*, to be submitted to Metallurgical Transactions A (2000a).

S. Vogel, M. A. M. Bourke, J. C. Hanan, E. Üstündag & V. W. Yuan, *In-situ Investigation of the Reduction of NiO by a Neutron Transmission Method*, to be submitted to Physical Review Letters (2000b).

R. B. Von Dreele, J. D. Jorgensen, C. G. Windsor, *Rietveld Refinement with Spallation Neutron Powder Diffraction Data*, J. Appl. Cryst., **15**, 581 (1982).

R. B. Von Dreele, *Neutron Powder Diffraction*, in: D. L. Bish, J. E. Post (eds.), *Modern Powder Diffraction*, Reviews in Mineralogy, vol. 20, Mineral Society of America, Washington (1989).

R. B. Von Dreele, *Quantitative Texture Analysis by Rietveld Refinement*, J. Appl. Cryst., **30**, 517 (1997).

R. B. V. Dreele, *Combined Rietveld and stereochemical restraint refinement of a protein crystal structure*, J. Appl. Cryst., **32**, 1084-1089 (1999).

D. Q. Wang, *Strain Measurement Using Neutron Diffraction*, Ph. D. Thesis, Materials Discipline, Open University, Milton Keynes, UK (1996).

D. Q. Wang, L. Edwards, *Pulsed neutron strain scanning*, Technical Report FRG/97/3/1, Materials Discipline, Faculty of Technology, The Open University, Milton Keynes/UK (1997).

M. C. Weinberg, *Transformation kinetics of particles with surface and bulk nucleation*, Journal of Non-Crystalline Solids, **142**, 126-132 (1992).

R. Weinstock, *Inelastic Scattering of Slow Neutrons*, Physical Review, **65**, 1-20 (1944).

R. J. Weiss & J. R. Clark, *Neutron Diffraction Studies of Cold-Worked Brass*, J. Appl. Phys., **23 (12)**, 1379-1382 (1952).

H. Wenk (ed.), *Preferred Orientation in Deformed Metals and Rocks: An Introduction to Modern Texture Analysis*, Academic Press, London, (1985).

C. Wert & C. Zener, *Interference of Growing Spherical Precipitate Particles*, Journal of Applied Physics, **21**, 5-8 (1950).

A. Williams, G. K. Kwei, R. B. Von Dreele, A. C. Larson, I. D. Raistrick & D. L. Bish, *Joint x-ray amd neutron refinement of the structure of superconducting* $YBa_2Cu_3O_{7-x}$*: Precision structure, anisotropic thermal parameters, strain and cation disorder*, Physical Review, **B37 (13)**, 7960-7962 (1988).

C. C. Wilson & R. I. Smith, *Pulsed neutron diffraction: new opportunities in time-resolved crystallography*, in J. R. Helliwell, P. M. Rentzepis (ed.), *Time-resolved Diffraction*, Oxford Series on Synchrotron Radiation, Clarendon Press, Oxford, 401-435 (1997).

C. G. Windsor, *Pulsed neutron scattering*, Taylor & Francis, London (1981).

C. G. Windsor, N. Copeman, G. S. Faulkner, A. Allen & M. T. Hutchings, *Neutron Transmission Measurements on Bragg Edges and their Application to the Determination of Internal Strains* (unpublished), private communication (1986).

L. Winsberg, D. Meneghetti, S. S. Sidhu, *Total Neutron Cross Sections of Compounds with Different Crystalline Structures*, Physical Review, **75, No. 6**, 975-979 (1949).

T. G. Worlton, J. D. Jorgensen, R. A. Beyerlein & D. L. Decker, *Multicomponent Profile Refinement of Time-Of-Flight Neutron Diffraction Data*, Nucl. Instrum. Meth., **137**, 331-337 (1976).

Y. Yen, J. D. Bowman, Y. Matsuda, S. I. Penttilä, S. Seestrom, H. M. Shimizu, R. W. Strickland, S. Takahashi, S. H. Yoo & V. W. Yuan, *500-MHz Neutron Detector*, Proc. of 2nd Int. Workshop on Time Reversal Invariance and Parity Violations in Neutron Reactions, Dubna, Russia, 4.-7. May 1993, Published by World Scientific , 210-219 (1993).

R. A. Young & E. Prince, *Suggested guidelines for the publication of Rietveld analyses and pattern decomposition studies*, J. Appl. Cryst., **15**, 357-359 (1982).

R. A. Young, *The Rietveld Method*, Oxford University Press, Oxford (1993).

V. W. Yuan, B. W. Asay, R. Boat, J. D. Bowman, D. J. Funk, R. Hixson, L. Hull, G. Laabs, R. London, G. L. Morgan, R. Rabie & C. E. Ragan, *Dynamic Temperature and Velocity Measurements using Neutron Resonance Spectroscopy*, in G. Reffo, A. Ventura, C. Grandi, Conference Proceedings Nuclear Data for Science and Technology, Trieste, Italy, **59**, 1723-1727 (1997).

Appendix A

Evaluation of Functions φ_1 and φ_3

The functions φ_m as introduced in sections 3.2.1 and 3.2.4 are defined as

$$\varphi_m(\Theta) = \int_{-1}^{1} \frac{\varepsilon^m}{e^{-\varepsilon/\Theta} - 1} d\varepsilon \tag{A.1}$$

They can be accurately evaluated in terms of (Granada, 1984)

$$\varphi_m(\Theta) = \frac{(-1)^{m+1}}{m+1} + I_m \left[(-1)^{m+1} + 1\right] \tag{A.2}$$

where I_m is given by

$$I_m = \Theta \log\left(1 - e^{-1/\Theta}\right) + \Theta^{m+1} m! \xi(m+1) - \sum_{n=1}^{\infty} a_{n,m} \tag{A.3}$$

with the Riemann Zeta-function

$$\xi(m) = \sum_{n=1}^{\infty} \frac{1}{n^m} \tag{A.4}$$

and

$$a_{n,m} = e^{-n/\Theta} \sum_{k=1}^{m} \Theta^{k+1} m(m-1)\ldots(m-k+1) n^{-(k+1)} \tag{A.5}$$

Of interest for calculations of cross-sections are φ_1 and φ_3. The former, φ_1, evaluates to

$$\varphi_1(\Theta) = \frac{(-1)^{1+1}}{1+1} + I_1 \left[(-1)^{1+1} + 1\right] = \frac{1}{2} + 2I_1 \tag{A.6}$$

where

$$\begin{aligned} I_1 &= \Theta \log\left(1 - e^{-1/\Theta}\right) + \Theta^{1+1} 1! \xi(1+1) - \sum_{n=1}^{\infty} a_{n,1} \\ &= \Theta \log\left(1 - e^{-1/\Theta}\right) + \Theta^2 \xi(2) - \sum_{n=1}^{\infty} a_{n,1} \end{aligned} \tag{A.7}$$

For odd m, the Zeta-function $\xi(m+1)$ is given directly in terms of the Bernoulli numbers B_k by (Bronstein & Semendjajew, 1991, eq. 1.1.3.1.19., p. 30)

$$\xi(2k) = \sum_{n=1}^{\infty} \frac{1}{n^{2k}} = \frac{2^{2k-1}\pi^{2k}}{(2k)!} B_k \qquad (k = 1, 2, 3....) \tag{A.8}$$

For the present purpose, i.e. finding expressions for $m = 1$ and $m = 3$, the Bernoulli numbers B_1 and B_2 are required (Bronstein & Semendjajew, 1991, table 1.1.3.1.1., p. 31):

$$B_1 = \frac{1}{6} \qquad B_2 = \frac{1}{30} \tag{A.9}$$

Hence, $\xi(2)$ and $\xi(4)$ are given by

$$\xi(2) = \frac{2^{2-1}\pi^2}{(2)!}B_1 = \frac{\pi^2}{6}, \qquad \xi(4) = \frac{2^{4-1}\pi^4}{(4)!}B_2 = \frac{8\pi^4}{24}\frac{1}{30} = \frac{\pi^4}{90} \tag{A.10}$$

Back to the case of $m = 1$, the coefficients $a_{n,1}$ are given by

$$a_{n,1} = e^{-n/\Theta}\Theta^2 n^{-2} \tag{A.11}$$

With this, the full expression for $m = 1$ is given by

$$\varphi_1(\Theta) = \frac{1}{2} + 2\left(\Theta\log\left(1 - e^{-1/\Theta}\right) + \Theta^2\left(\frac{\pi^2}{6} - \sum_{n=1}^{\infty}\frac{1}{e^{n/\Theta}n^2}\right)\right) \tag{A.12}$$

For $m = 3$, the coefficients $a_{n,3}$ are given by

$$\begin{aligned} a_{n,3} &= e^{-n/\Theta}\sum_{k=1}^{3}\Theta^{k+1}m(m-1)\ldots(m-k+1)n^{-(k+1)} \\ &= e^{-n/\Theta}\left(\underbrace{3\Theta^2 n^{-2}}_{k=1} + \underbrace{6\Theta^3 n^{-3}}_{k=2} + \underbrace{6\Theta^4 n^{-4}}_{k=3}\right) \\ &= \frac{6\Theta^2 e^{-n/\Theta}}{n^2}\left(\frac{1}{2} + \frac{\Theta}{n} + \left(\frac{\Theta}{n}\right)^2\right) \end{aligned} \tag{A.13}$$

and the full expression for φ_3 reads

$$\begin{aligned} \varphi_3(\Theta) &= \frac{1}{4} + 2\left(\Theta\log\left(1 - e^{-1/\Theta}\right) + \Theta^4 3!\xi(4) - \sum_{n=1}^{\infty}a_{n,3}\right) \\ &= \frac{1}{4} + 2\left(\Theta\log\left(1 - e^{-1/\Theta}\right) + \frac{6(\Theta\pi)^4}{90} - 6\Theta^2\sum_{n=1}^{\infty}\frac{1}{e^{n/\Theta}n^2}\left(\frac{1}{2} + \frac{\Theta}{n} + \left(\frac{\Theta}{n}\right)^2\right)\right) \\ &= \frac{1}{4} + 2\left(\Theta\log\left(1 - e^{-1/\Theta}\right) + 6\Theta^2\left(\frac{\pi^4}{90}\Theta^2 - \sum_{n=1}^{\infty}\frac{1}{e^{n/\Theta}n^2}\left(\frac{1}{2} + \frac{\Theta}{n} + \left(\frac{\Theta}{n}\right)^2\right)\right)\right) \end{aligned} \tag{A.14}$$

The summations in the two expressions for φ_1 and φ_3 are executed until the difference between two subsequent iterations is less than 10^{-6} which is usually reached after less than 10 steps.

Appendix B

Integration of Edge-Profile Function from Peak-Profile after Jorgensen et al.

The theory predicts an abrupt cut-off of the cross-section at the wavelength where a certain set of lattice planes is excluded from the elastic coherent scattering. In practice, instrumental and sample uncertainties contribute to form a more smooth, broad edge. These edges need to be described accurately for a successful refinement of a spectrum. The principles are described in section 3.3 and in this section the derivation of an asymmetric edge-profile from the diffraction peak profile function proposed by Jorgensen et al. (1978) is described. Applying (3.35) to the peak profile function (3.40) and its parameters (3.41) and (3.42) yields

$$k\left(\lambda, d_{\vec{h}}, \alpha, \beta, \sigma\right) = 1 - \int_{-\infty}^{\lambda} \frac{\alpha\beta}{2(\alpha+\beta)} \left\{ e^{\frac{\alpha^2\sigma^2}{2}+\alpha\left(\lambda'-2d_{\vec{h}}\right)} \operatorname{erfc}\left(\frac{\alpha\sigma^2+\lambda'-2d_{\vec{h}}}{\sqrt{2}\sigma}\right) + e^{\frac{\beta^2\sigma^2}{2}-\beta\left(\lambda'-2d_{\vec{h}}\right)} \operatorname{erfc}\left(\frac{\beta\sigma^2-\lambda'+2d_{\vec{h}}}{\sqrt{2}\sigma}\right) \right\} d\lambda' \tag{B.1}$$

The subtraction from 1 will be omitted from now on as it does not contribute to the following algebra. The integral can be split into two parts with the factors not depending on the integration variable in front of the integrals:

$$\begin{aligned} k\left(\lambda, d_{\vec{h}}, \alpha, \beta, \sigma\right) &= \frac{\alpha\beta}{2(\alpha+\beta)} e^{\frac{\alpha^2\sigma^2}{2}-2\alpha d_{\vec{h}}} \int_{-\infty}^{\lambda} e^{\alpha\lambda'} \operatorname{erfc}\left(\frac{\alpha\sigma^2+\lambda'-2d_{\vec{h}}}{\sqrt{2}\sigma}\right) d\lambda' + \frac{\alpha\beta}{2(\alpha+\beta)} e^{\frac{\beta^2\sigma^2}{2}+2\beta d_{\vec{h}}} \int_{-\infty}^{\lambda} e^{-\beta\lambda'} \operatorname{erfc}\left(\frac{\beta\sigma^2-\lambda'+2d_{\vec{h}}}{\sqrt{2}\sigma}\right) d\lambda' \\ &= N_\alpha \int_{-\infty}^{\lambda} e^{\alpha\lambda'} \operatorname{erfc}\left(\frac{\alpha\sigma^2+\lambda'-2d_{\vec{h}}}{\sqrt{2}\sigma}\right) d\lambda' + N_\beta \int_{-\infty}^{\lambda} e^{-\beta\lambda'} \operatorname{erfc}\left(\frac{\beta\sigma^2-\lambda'+2d_{\vec{h}}}{\sqrt{2}\sigma}\right) d\lambda' \end{aligned} \tag{B.2}$$

where new constants

$$N_\alpha = \frac{\alpha\beta}{2(\alpha+\beta)} e^{\frac{\alpha^2\sigma^2}{2} - 2\alpha d_{\vec{h}}}, \qquad N_\beta = \frac{\alpha\beta}{2(\alpha+\beta)} e^{\frac{\beta^2\sigma^2}{2} + 2\beta d_{\vec{h}}} \tag{B.3}$$

are defined. With the subsitution

$$l = \frac{\alpha\sigma^2+\lambda'-2d_{\vec{h}}}{\sqrt{2}\sigma} \Leftrightarrow \lambda' = \sqrt{2}\sigma l + 2d_{\vec{h}} - \alpha\sigma^2 \rightarrow \frac{d\lambda'}{dl} = \sqrt{2}\sigma, \qquad l\left(\lambda' = -\infty\right) = -\infty, \qquad l\left(\lambda' = \lambda\right) = \frac{\alpha\sigma^2 + \lambda - 2d_{\vec{h}}}{\sqrt{2}\sigma} \tag{B.4}$$

for the first and

$$l' = \frac{\beta\sigma^2-\lambda'+2d_{\vec{h}}}{\sqrt{2}\sigma} \Leftrightarrow \lambda' = -\sqrt{2}\sigma l' + 2d_{\vec{h}} + \beta\sigma^2 \rightarrow \frac{d\lambda'}{dl'} = -\sqrt{2}\sigma, \qquad l'\left(\lambda' = -\infty\right) = \infty, \qquad l'\left(\lambda' = \lambda\right) = \frac{\beta\sigma^2 - \lambda + 2d_{\vec{h}}}{\sqrt{2}\sigma} \tag{B.5}$$

for the second integral, the function becomes

$$\begin{aligned} k\left(\lambda, d_{\vec{h}}, \alpha, \beta, \sigma\right) &= N_\alpha \int_{-\infty}^{\frac{\alpha\sigma^2+\lambda-2d_{\vec{h}}}{\sqrt{2}\sigma}} e^{\alpha\left(\sqrt{2}\sigma l + 2d_{\vec{h}} - \alpha\sigma^2\right)} \operatorname{erfc}\left(\frac{\alpha\sigma^2+\sqrt{2}\sigma l+2d_{\vec{h}}-\alpha\sigma^2-2d_{\vec{h}}}{\sqrt{2}\sigma}\right)\sqrt{2}\sigma dl \\ &\quad -N_\beta \int_{\infty}^{\frac{\beta\sigma^2-\lambda+2d_{\vec{h}}}{\sqrt{2}\sigma}} e^{-\beta\left(-\sqrt{2}\sigma l' + 2d_{\vec{h}} + \beta\sigma^2\right)} \operatorname{erfc}\left(\frac{\beta\sigma^2+\sqrt{2}\sigma l'-2d_{\vec{h}}-\beta\sigma^2+2d_{\vec{h}}}{\sqrt{2}\sigma}\right)\sqrt{2}\sigma dl' \\ &= N'_\alpha \int_{-\infty}^{\frac{\alpha\sigma^2+\lambda-2d_{\vec{h}}}{\sqrt{2}\sigma}} e^{\sqrt{2}\alpha\sigma l} \operatorname{erfc}\left(l\right) dl - N'_\beta \int_{\infty}^{\frac{\beta\sigma^2-\lambda+2d_{\vec{h}}}{\sqrt{2}\sigma}} e^{\sqrt{2}\beta\sigma l'} \operatorname{erfc}\left(l'\right) dl' \end{aligned} \tag{B.6}$$

where new constants collecting the variables independent of the integration variables are defined as

$$\begin{aligned} N'_\alpha &= \sqrt{2}\sigma e^{\alpha\left(2d_{\vec{h}} - \alpha\sigma^2\right)} N_\alpha = \sqrt{2}\frac{\alpha\beta}{2(\alpha+\beta)}\sigma e^{\frac{\alpha^2\sigma^2}{2} - 2\alpha d_{\vec{h}} - \alpha^2\sigma^2 + 2\alpha d_{\vec{h}}} = \sqrt{2}\frac{\alpha\beta}{2(\alpha+\beta)}\sigma e^{-\frac{\alpha^2\sigma^2}{2}} \\ N'_\beta &= \sqrt{2}\sigma e^{-\beta\left(2d_{\vec{h}} + \beta\sigma^2\right)} N_\beta = \sqrt{2}\frac{\alpha\beta}{2(\alpha+\beta)}\sigma e^{\frac{\beta^2\sigma^2}{2} + 2\beta d_{\vec{h}} - \beta^2\sigma^2 - 2\beta d_{\vec{h}}} = \sqrt{2}\frac{\alpha\beta}{2(\alpha+\beta)}\sigma e^{-\frac{\beta^2\sigma^2}{2}} \end{aligned} \tag{B.7}$$

which are renamed immediately to N_α and N_β, respectively. The integrals are now of the type (Prudnikov et al., 1986, eq. 1.5.2.3)

$$\int e^{bx} \operatorname{erfc}\left(ax\right) dx = \frac{1}{b}\exp\left(bx\right)\operatorname{erfc}\left(ax\right) - \frac{1}{b}\exp\left(\frac{b^2}{4a^2}\right)\operatorname{erfc}\left(ax - \frac{b}{2a}\right) \tag{B.8}$$

As the integral is given in the cited source erroneously with a positive sign in front of the second term, the derivative for the required case of $a = 1$ shall be validated here:

$$\begin{aligned}\frac{d}{dx}\left(\frac{1}{b}\exp\left(bx\right)\operatorname{erfc}\left(x\right)-\frac{1}{b}\exp\left(\frac{b^2}{4}\right)\operatorname{erfc}\left(x-\frac{b}{2}\right)\right)&=\frac{1}{b}\left(\frac{d}{dx}\exp\left(bx\right)\operatorname{erfc}\left(x\right)-\frac{d}{dx}\exp\left(\frac{b^2}{4}\right)\operatorname{erfc}\left(x-\frac{b}{2}\right)\right)\\&=\frac{1}{b}\left(\operatorname{erfc}\left(x\right)\frac{d}{dx}\exp\left(bx\right)+\exp\left(bx\right)\frac{d}{dx}\operatorname{erfc}\left(x\right)-\exp\left(\frac{b^2}{4}\right)\frac{d}{dx}\operatorname{erfc}\left(x-\frac{b}{2}\right)\right)\end{aligned} \tag{B.9}$$

The derivative of the complementary error-function is with (see for example Großmann, 1991)

$$\frac{\partial}{\partial\alpha}\int_{a(\alpha)}^{b(\alpha)}f\left(\alpha,x\right)dx=\int_{a(\alpha)}^{b(\alpha)}\frac{\partial}{\partial\alpha}f\left(\alpha,x\right)dx+f\left(\alpha,b\left(\alpha\right)\right)\frac{\partial b}{\partial\alpha}-f\left(\alpha,a\left(\alpha\right)\right)\frac{\partial a}{\partial\alpha} \tag{B.10}$$

given by

$$\frac{d}{dx}\operatorname{erfc}\left(x\right)=\frac{d}{dx}\left(1-\operatorname{erf}\left(x\right)\right)=-\frac{d}{dx}\frac{2}{\sqrt{\pi}}\int_0^x e^{-t^2}dt=-\frac{2}{\sqrt{\pi}}e^{-x^2} \tag{B.11}$$

yielding the desired result

$$\begin{aligned}&\frac{1}{b}\left(\operatorname{erfc}\left(x\right)\frac{d}{dx}\exp\left(bx\right)+\exp\left(bx\right)\frac{d}{dx}\operatorname{erfc}\left(x\right)-\exp\left(\frac{b^2}{4}\right)\frac{d}{dx}\operatorname{erfc}\left(x-\frac{b}{2}\right)\right)\\&\quad=\frac{1}{b}\left(b\operatorname{erfc}\left(x\right)\exp\left(bx\right)-\exp\left(bx\right)\exp\left(-x^2\right)+\exp\left(\frac{b^2}{4}\right)\exp\left(-x^2+bx-\frac{b^2}{4}\right)\right)\\&\quad=\frac{1}{b}\left(b\operatorname{erfc}\left(x\right)\exp\left(bx\right)-\exp\left(bx-x^2\right)+\exp\left(bx-x^2\right)\right)\\&\quad=\operatorname{erfc}\left(x\right)\exp\left(bx\right)\end{aligned} \tag{B.12}$$

Applying (B.8) for the special case of $a = 1$ and $b = \sqrt{2}\alpha\sigma$ to (B.6), the edge-function reads

$$\begin{aligned}k\left(\lambda,d_{\vec{h}},\alpha,\beta,\sigma\right)&=\frac{N_\alpha}{\sqrt{2}\alpha\sigma}\left(e^{\sqrt{2}\alpha\sigma l}\operatorname{erfc}\left(l\right)-e^{\frac{\left(\sqrt{2}\alpha\sigma\right)^2}{4}}\operatorname{erfc}\left(l-\frac{\sqrt{2}\alpha\sigma}{2}\right)\right)\Bigg|_{-\infty}^{\frac{\alpha\sigma^2+\lambda-2d_{\vec{h}}}{\sqrt{2}\sigma}}\\&\quad-\frac{N_\beta}{\sqrt{2}\alpha\sigma}\left(e^{\sqrt{2}\beta\sigma l'}\operatorname{erfc}\left(l'\right)-e^{\frac{\left(\sqrt{2}\beta\sigma\right)^2}{4}}\operatorname{erfc}\left(l'-\frac{\sqrt{2}\beta\sigma}{2}\right)\right)\Bigg|_{\infty}^{\frac{\beta\sigma^2-\lambda+2d_{\vec{h}}}{\sqrt{2}\sigma}}\\&=\frac{N_\alpha}{\sqrt{2}\alpha\sigma}\left(e^{\sqrt{2}\alpha\sigma\frac{\alpha\sigma^2+\lambda-2d_{\vec{h}}}{\sqrt{2}\sigma}}\operatorname{erfc}\left(\frac{\alpha\sigma^2+\lambda-2d_{\vec{h}}}{\sqrt{2}\sigma}\right)-e^{\frac{\left(\sqrt{2}\alpha\sigma\right)^2}{4}}\operatorname{erfc}\left(\frac{\alpha\sigma^2+\lambda-2d_{\vec{h}}}{\sqrt{2}\sigma}-\frac{\sqrt{2}\alpha\sigma}{2}\right)\right)\end{aligned} \tag{B.13}$$

$$
\begin{aligned}
&-\tfrac{N_\alpha}{\sqrt{2}\alpha\sigma}\left(e^{-\sqrt{2}\alpha\sigma'\infty'}\mathrm{erfc}\left(-'\infty'\right)+e^{\frac{\left(\sqrt{2}\alpha\sigma\right)^2}{4}}\mathrm{erfc}\left(-'\infty'-\tfrac{\sqrt{2}\alpha\sigma}{2}\right)\right)\\
&-\tfrac{N_\beta}{\sqrt{2}\alpha\sigma}\left(e^{\sqrt{2}\beta\sigma\frac{\beta\sigma^2-\lambda+2d_{\vec{h}}}{\sqrt{2}\sigma}}\mathrm{erfc}\left(\tfrac{\beta\sigma^2-\lambda+2d_{\vec{h}}}{\sqrt{2}\sigma}\right)-e^{\frac{\left(\sqrt{2}\beta\sigma\right)^2}{4}}\mathrm{erfc}\left(\tfrac{\beta\sigma^2-\lambda+2d_{\vec{h}}}{\sqrt{2}\sigma}-\tfrac{\sqrt{2}\beta\sigma}{2}\right)\right)\\
&+\tfrac{N_\beta}{\sqrt{2}\alpha\sigma}\left(e^{\sqrt{2}\beta\sigma'\infty'}\mathrm{erfc}\left('\infty'\right)+e^{\frac{\left(\sqrt{2}\beta\sigma\right)^2}{4}}\mathrm{erfc}\left('\infty'-\tfrac{\sqrt{2}\beta\sigma}{2}\right)\right)
\end{aligned}
$$

The expressions with infinity in the argument are given by

$$
\begin{aligned}
&\mathrm{erfc}\left('\infty'\right)=0, \qquad \mathrm{erfc}\left(-'\infty'\right)=2-\mathrm{erfc}\left('\infty'\right)=2\\
&\lim_{x\to\infty}e^x\mathrm{erfc}\left(x\right)=\lim_{x\to\infty}\tfrac{\mathrm{erfc}(x)}{e^{-x}}=\lim_{x\to\infty}\tfrac{\frac{2}{\sqrt{\pi}}e^{-x^2}}{-e^{-x}}=-\tfrac{2}{\sqrt{\pi}}\lim_{x\to\infty}e^{-x^2+x}\overset{(*)}{=}0
\end{aligned}
\tag{B.14}
$$

where in the latter case l'Hospital's rule was applied and at $(*)$ $\lim_{x\to\infty}x-x^2\cong\lim_{x\to\infty}-x^2=-\infty$ was used. The edge profile function is hence

$$
\begin{aligned}
k\left(\lambda,d_{\vec{h}},\alpha,\beta,\sigma\right) &= \tfrac{N_\alpha}{\sqrt{2}\alpha\sigma}\left(e^{\alpha\left(\alpha\sigma^2+\lambda-2d_{\vec{h}}\right)}\mathrm{erfc}\left(\tfrac{\alpha\sigma^2+\lambda-2d_{\vec{h}}}{\sqrt{2}\sigma}\right)-e^{\frac{\alpha^2\sigma^2}{2}}\mathrm{erfc}\left(\tfrac{\lambda-2d_{\vec{h}}}{\sqrt{2}\sigma}\right)-0\cdot 2+e^{\frac{\alpha^2\sigma^2}{2}}\cdot 2\right)\\
&\quad -\tfrac{N_\beta}{\sqrt{2}\alpha\sigma}\left(e^{\beta\left(\beta\sigma^2-\lambda+2d_{\vec{h}}\right)}\mathrm{erfc}\left(\tfrac{\beta\sigma^2-\lambda+2d_{\vec{h}}}{\sqrt{2}\sigma}\right)-e^{\frac{\beta^2\sigma^2}{2}}\mathrm{erfc}\left(-\tfrac{\lambda-2d_{\vec{h}}}{\sqrt{2}\sigma}\right)-0+e^{\frac{\beta^2\sigma^2}{2}}\cdot 0\right)\\
&= \tfrac{N_\alpha}{\sqrt{2}\alpha\sigma}\left(e^{\alpha\left(\alpha\sigma^2+\lambda-2d_{\vec{h}}\right)}\mathrm{erfc}\left(\tfrac{\alpha\sigma^2+\lambda-2d_{\vec{h}}}{\sqrt{2}\sigma}\right)+e^{\frac{\alpha^2\sigma^2}{2}}\left(2-\mathrm{erfc}\left(\tfrac{\lambda-2d_{\vec{h}}}{\sqrt{2}\sigma}\right)\right)\right)\\
&\quad -\tfrac{N_\beta}{\sqrt{2}\alpha\sigma}\left(e^{\beta\left(\beta\sigma^2-\lambda+2d_{\vec{h}}\right)}\mathrm{erfc}\left(\tfrac{\beta\sigma^2-\lambda+2d_{\vec{h}}}{\sqrt{2}\sigma}\right)-e^{\frac{\beta^2\sigma^2}{2}}\mathrm{erfc}\left(-\tfrac{\lambda-2d_{\vec{h}}}{\sqrt{2}\sigma}\right)\right)
\end{aligned}
\tag{B.15}
$$

With $\Delta\lambda_{\vec{h}}=\lambda-2d_{\vec{h}}$, the definitions of N_α and N_β and applying

$$
2-\mathrm{erfc}\left(x\right)=1+\frac{2}{\sqrt{\pi}}\int_0^x e^{-t^2}dt=1-\frac{2}{\sqrt{\pi}}\int_0^{-x}e^{-t^2}dt=\mathrm{erfc}\left(-x\right),
\tag{B.16}
$$

this can be rearranged to

$$
k\left(\lambda,d_{\vec{h}},\alpha,\beta,\sigma\right) = \tfrac{\sqrt{2}\alpha\beta\sigma e^{-\frac{\alpha^2\sigma^2}{2}}}{\sqrt{2}\alpha\sigma 2(\alpha+\beta)}\left(e^{\alpha\left(\alpha\sigma^2+\lambda-2d_{\vec{h}}\right)}\mathrm{erfc}\left(\tfrac{\alpha\sigma^2+\lambda-2d_{\vec{h}}}{\sqrt{2}\sigma}\right)+e^{\frac{\alpha^2\sigma^2}{2}}\left(2-\mathrm{erfc}\left(\tfrac{\lambda-2d_{\vec{h}}}{\sqrt{2}\sigma}\right)\right)\right)
\tag{B.17}
$$

$$
\begin{aligned}
& -\frac{\sqrt{2}\alpha\beta\sigma e^{-\frac{\beta^2\sigma^2}{2}}}{\sqrt{2}\beta\sigma 2(\alpha+\beta)}\left(e^{\beta\left(\beta\sigma^2-\lambda+2d_{\vec{h}}\right)}\operatorname{erfc}\left(\frac{\beta\sigma^2-\lambda+2d_{\vec{h}}}{\sqrt{2}\sigma}\right)-e^{\frac{\beta^2\sigma^2}{2}}\operatorname{erfc}\left(-\frac{\lambda-2d_{\vec{h}}}{\sqrt{2}\sigma}\right)\right) \\
= \quad & \frac{\beta}{2(\alpha+\beta)}\left(e^{\frac{\alpha}{2}\left(\alpha\sigma^2+2\Delta\lambda_{\vec{h}}\right)}\operatorname{erfc}\left(\frac{\alpha\sigma^2+\Delta\lambda_{\vec{h}}}{\sqrt{2}\sigma}\right)+\operatorname{erfc}\left(-\frac{\Delta\lambda_{\vec{h}}}{\sqrt{2}\sigma}\right)\right) \\
& -\frac{\alpha}{2(\alpha+\beta)}\left(e^{\frac{\beta}{2}\left(\beta\sigma^2-2\Delta\lambda_{\vec{h}}\right)}\operatorname{erfc}\left(\frac{\beta\sigma^2-\Delta\lambda_{\vec{h}}}{\sqrt{2}\sigma}\right)-\operatorname{erfc}\left(-\frac{\Delta\lambda_{\vec{h}}}{\sqrt{2}\sigma}\right)\right)
\end{aligned}
$$

Re-inserting the omitted subtraction from 1, the edge profile function becomes

$$
\begin{aligned}
k\left(\lambda, d_{\vec{h}}, \alpha, \beta, \sigma\right) &= 1+\frac{\alpha e^{\frac{\beta}{2}\left(\beta\sigma^2-2\Delta\lambda_{\vec{h}}\right)}\operatorname{erfc}\left(\frac{\beta\sigma^2-\Delta\lambda_{\vec{h}}}{\sqrt{2}\sigma}\right)-\beta e^{\frac{\alpha}{2}\left(\alpha\sigma^2+2\Delta\lambda_{\vec{h}}\right)}\operatorname{erfc}\left(\frac{\alpha\sigma^2+\Delta\lambda_{\vec{h}}}{\sqrt{2}\sigma}\right)}{2(\alpha+\beta)}-\operatorname{erfc}\left(-\frac{\Delta\lambda_{\vec{h}}}{\sqrt{2}\sigma}\right)\frac{(\alpha+\beta)}{2(\alpha+\beta)} \\
&= \frac{1}{2}\left(\operatorname{erfc}\left(-\frac{\Delta\lambda_{\vec{h}}}{\sqrt{2}\sigma}\right)+\frac{\alpha e^{\frac{\beta}{2}\left(\beta\sigma^2-2\Delta\lambda_{\vec{h}}\right)}\operatorname{erfc}\left(\frac{\beta\sigma^2-\Delta\lambda_{\vec{h}}}{\sqrt{2}\sigma}\right)-\beta e^{\frac{\alpha}{2}\left(\alpha\sigma^2+2\Delta\lambda_{\vec{h}}\right)}\operatorname{erfc}\left(\frac{\alpha\sigma^2+\Delta\lambda_{\vec{h}}}{\sqrt{2}\sigma}\right)}{\alpha+\beta}\right)
\end{aligned}
\tag{B.18}
$$

With the so-called scaled complementary error-function

$$
erfcx\left(x\right)=e^{x^2}erfc\left(x\right) \tag{B.19}
$$

the edge-profile could be further simplified to

$$
K\left(\lambda, d_{\vec{h}}, \alpha, \beta, \sigma\right)=\frac{1}{2}\left(erfc\left(\frac{\Delta\lambda_{\vec{h}}}{\sqrt{2}\sigma}\right)+e^{-\frac{\Delta\lambda_{\vec{h}}^2}{2\sigma^2}}\frac{\alpha erfcx\left(\frac{\beta\sigma}{\sqrt{2}}-\frac{\Delta\lambda_{\vec{h}}}{\sqrt{2}\sigma}\right)-\beta erfcx\left(\frac{\alpha\sigma}{\sqrt{2}}+\frac{\Delta\lambda_{\vec{h}}}{\sqrt{2}\sigma}\right)}{\alpha+\beta}\right) \tag{B.20}
$$

Algorithms exist for efficient evaluation of the scaled complementary error-function (for example at NIST, 1998), but it turned out that the calculation of the derivatives was approximated to zero too soon, resulting in diverging refinements of lattice parameters and other parameters depending on the profile functions. Consequently, the edge-profile and its derivatives are evaluated using the built-in `exp()` function of the library of the C-compiler and `erfc` as given by Press et al. (1992, p. 220-221) in their second implementation. The first implementation of `erfc` showed inacceptable spikes.

Appendix C

D-Spacing Calculation

The following equations are used to calculate reflection d-spacings for the crystal systems:

- Monoclinic system: $\alpha = \gamma = 90°$

$$d_{\vec{h}} = \frac{abc\sqrt{1-\cos^2\beta}}{\sqrt{b^2c^2h^2 + a^2c^2k^2\sin^2\beta + a^2b^2l^2 - 2ab^2chl\cos\beta}} \tag{C.1}$$

- Orthorhombic system: $\alpha = \beta = \gamma = 90°$

$$d_{\vec{h}} = \frac{1}{\sqrt{\frac{h^2}{a^2} + \frac{k^2}{b^2} + \frac{l^2}{c^2}}} \tag{C.2}$$

- Trigonal system: $\alpha = \beta = 90°$, $\gamma = 120°$, $a = b$

$$d_{\vec{h}} = \frac{\sqrt{3}ac}{\sqrt{4\left(h^2 + k^2 + hk\right)c^2 + 3l^2a^2}} \tag{C.3}$$

- Hexagonal system: $\alpha = \beta = 90°$, $\gamma = 60°$, $a = b$

$$d_{\vec{h}} = \frac{\sqrt{3}ac}{\sqrt{4\left(h^2 + k^2 - hk\right)c^2 + 3l^2a^2}} \tag{C.4}$$

- Tetragonal system: $\alpha = \beta = \gamma = 90°, a = b$

$$d_{\vec{h}} = \frac{1}{\sqrt{\frac{h^2+k^2}{a^2} + \frac{l^2}{c^2}}} \tag{C.5}$$

- Cubic system: $\alpha = \beta = \gamma = 90°, a = b = c$

$$d_{\vec{h}} = \frac{a}{\sqrt{h^2 + k^2 + l^2}} \tag{C.6}$$

Appendix D

Integration Path for the March-Dollase Model

As depicted in figure D.1, the intersection of the cone described by $\vec{H}$ around $\vec{h}$ with the unit-sphere is a circle of radius $\sin\beta_{\vec{h}}$. A circle with unit radius around the direction of the incident beam $(1,0,0)$ is given by

$$\vec{r}\,(\phi) = \begin{pmatrix} 0 \\ \cos\phi \\ \sin\phi \end{pmatrix} \tag{D.1}$$

The circle has to be rotated around $(0,1,0)$ by $-\alpha_{\vec{h}}$, the angle between $(1,0,0)$ and $\vec{h}$ (negative sign because $(0,1,0)$ points away from the reader in figure D.1 and rotation around an axis is defined positive if the rotation is anti-clockwise looking in the opposite direction of the axis):

$$\vec{r}\,(\phi) = \begin{pmatrix} \cos\left(-\alpha_{\vec{h}}\right) & 0 & \sin\left(-\alpha_{\vec{h}}\right) \\ 0 & 1 & 0 \\ -\sin\left(-\alpha_{\vec{h}}\right) & 0 & \cos\left(-\alpha_{\vec{h}}\right) \end{pmatrix} \begin{pmatrix} 0 \\ \cos\phi \\ \sin\phi \end{pmatrix} = \begin{pmatrix} -\sin\alpha_{\vec{h}}\sin\phi \\ \cos\phi \\ \cos\alpha_{\vec{h}}\sin\phi \end{pmatrix} \tag{D.2}$$

Scaling the circle to radius $\sin\beta_{\vec{h}}$ yields

$$\vec{r}\,(\phi) = \begin{pmatrix} -\sin\beta_{\vec{h}}\sin\alpha_{\vec{h}}\sin\phi \\ \sin\beta_{\vec{h}}\cos\phi \\ \sin\beta_{\vec{h}}\cos\alpha_{\vec{h}}\sin\phi \end{pmatrix} \tag{D.3}$$

The circle still has its center at the origin and needs to be shifted along $\vec{h}$ such that the circumference lies on the unit sphere:

$$\begin{aligned} \vec{r}\,(\phi) &= \begin{pmatrix} -\sin\beta_{\vec{h}}\sin\alpha_{\vec{h}}\sin\phi \\ \sin\beta_{\vec{h}}\cos\phi \\ \sin\beta_{\vec{h}}\cos\alpha_{\vec{h}}\sin\phi \end{pmatrix} + \vec{h}\cos\beta_{\vec{h}} = \begin{pmatrix} -\sin\beta_{\vec{h}}\sin\alpha_{\vec{h}}\sin\phi \\ \sin\beta_{\vec{h}}\cos\phi \\ \sin\beta_{\vec{h}}\cos\alpha_{\vec{h}}\sin\phi \end{pmatrix} + \cos\beta_{\vec{h}} \begin{pmatrix} \cos\alpha_{\vec{h}} \\ 0 \\ \sin\alpha_{\vec{h}} \end{pmatrix} \\ &= \begin{pmatrix} \cos\beta_{\vec{h}}\cos\alpha_{\vec{h}} - \sin\beta_{\vec{h}}\sin\alpha_{\vec{h}}\sin\phi \\ \sin\beta_{\vec{h}}\cos\phi \\ \cos\beta_{\vec{h}}\sin\alpha_{\vec{h}} + \sin\beta_{\vec{h}}\cos\alpha_{\vec{h}}\sin\phi \end{pmatrix} \\ &= \vec{H}\,(\phi) \end{aligned} \tag{D.4}$$

This function yields the coordinates of $\vec{H}$ for any point on the path with angular distance $\beta_{\vec{h}}$ around $\vec{h}$. Projection on $(1,0,0)$ provides the cosine of the angle $\alpha_{\vec{H}}$ between $\vec{H}(\phi)$ and the preferred orientation

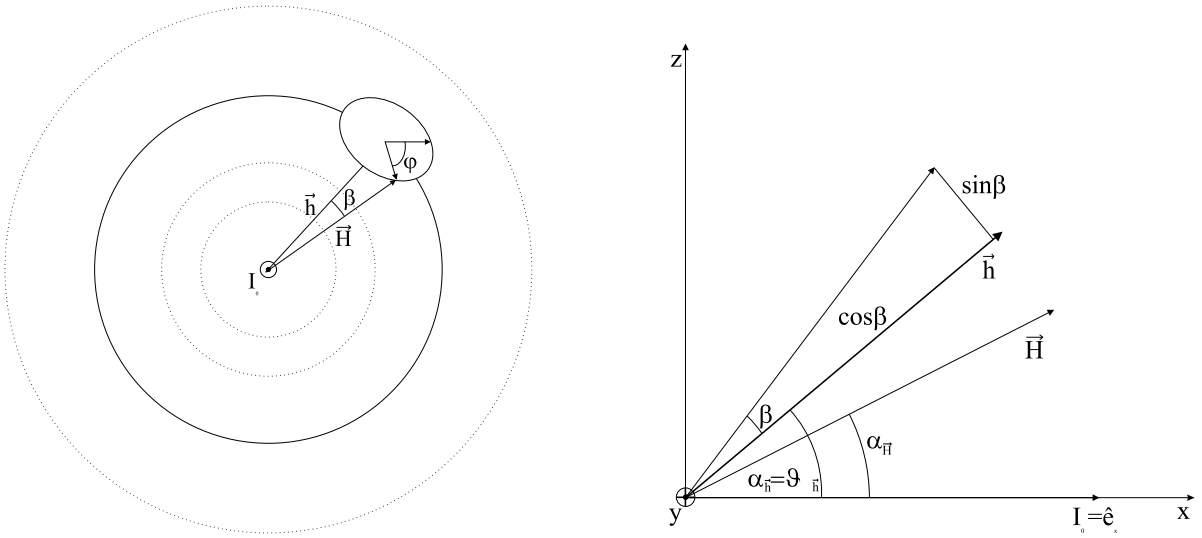

Figure D.1: Schematic of the integration path of $\vec{H}$ around the normal $\vec{h}$ of the diffracting lattice plane. Left: The cylindrical prabability distribution around I_0 (pointing towards the reader) with the path of $\vec{H}$ around $\vec{h}$. The dotted circles mean constant probability, the solid circle corresponds to all possible positions of $\vec{h}$ with constant angle $\alpha_{\vec{h}} = \vartheta_{\vec{h}}$ to the preferred orientation (incident beam) direction. Right: View along y pointing away from the reader (x parallel to I_0 and z perpendicular to I_0).

axis (which is parallel to the incident beam direction):

$$\cos\alpha_{\vec{H}} = \begin{pmatrix} 1 \\ 0 \\ 0 \end{pmatrix} \cdot \vec{H}\,(\phi) = \cos\beta_{\vec{h}} \cos\alpha_{\vec{h}} - \sin\beta_{\vec{h}} \sin\alpha_{\vec{h}} \sin\phi \tag{D.5}$$

This equation can be used in the March-Dollase equation for the case of a preferred orientation around $\vec{I_0}$.

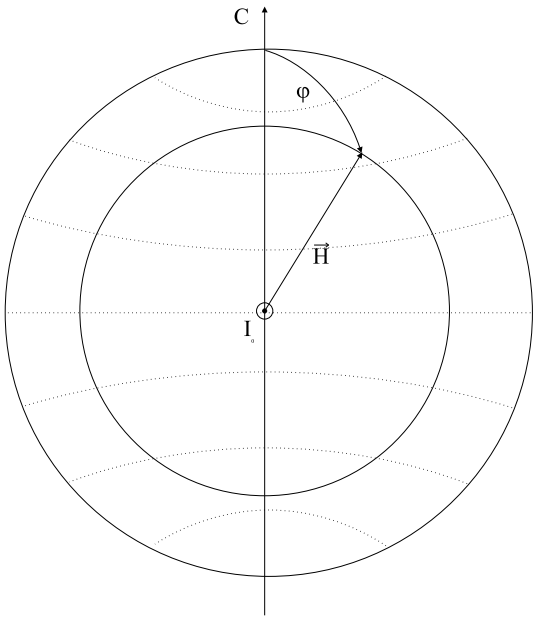

Figure D.2: Schematic of the integration path of $\vec{H}$ around I_0 to obtain the probability of finding $\vec{H}$ at an angle $\alpha_{\vec{h}}$ to I_0 for the case of a preferred orientation distribution with cylindrical symmetry around C. C is perpendicular to I_0 and points in an arbitrary direction. The dotted lines are lines of constant probability.

Appendix E

Calculation of Derivatives

The overall model for the refinement of Bragg-edge transmission patterns is given by equation (3.1). To fit variables to this model efficiently, the partial derivatives of this function with respect to its parameters are necessary. The analytical expressions for the partial derivatives are part of the code for the fit function. All derivatives can be checked numerically with a method of the fit-class. This test is accessible from the fit-control property-page of **BETMAn**'s fit-dialog. It evaluates the derivatives of all parameters refined in the preceding refinement cycle. The results may be written to a file `BETMAN_Derivatives.txt` in the `TEMP`-path of the system and can be used to compare the numerical and analytical (e.g. the coded derivative) values graphically. For example, sign-errors can be detected very easily using this approach.

During refinement cycles, the evaluation of the model function and its derivatives are executed many times. Consequently, optimisations in the code will be most fruitful here. The main goals followed were

- Pre-calculate as many values as possible, even if much more memory is allocated. Hence, parts of many terms being constant during a fit-cycle (i.e. independent of wavelength) are calculated in advance of each cycle and re-calculated when new guess-values are available.
- Re-use intermediate results, especially of calls to time-consuming functions like `exp`, `sqrt` or `erfc`.
- If some value is used more than once as a divisor, store its reciprocal value and multiply as each division (`FDIV`-instruction) takes about 39 clock cycles on an Intel Pentium CPU while a multiplication (`FMUL`-instruction) takes only 3 cycles.

As an example, the partial derivative of the overall fit-function I in the thermal neutron energy range at channel i with respect to the

isotropic displacement factor of an atom, $B_{iso,n}$, belonging to phase φ is derived[1]:

$$\begin{aligned}\frac{\partial I_i}{\partial B_{iso,n}} &= \left(\frac{\partial I_i}{\partial \sigma_{tot,\varphi}}\right)\left(\left(\frac{\partial \sigma_{tot,\varphi}}{\partial \sigma^{el}_{coh,\varphi}}\right)\sum_{\vec{h}}\left(\frac{\partial \sigma^{el}_{coh,\varphi}}{\partial \left|F_{\vec{h}}\right|^2}\right)\left(\frac{\partial \left|F_{\vec{h}}\right|^2}{\partial B_{iso,n}}\right)+\left(\frac{\partial \sigma_{tot,\varphi}}{\partial \sigma^{el}_{inc,\varphi}}\right)\left(\frac{\partial \sigma^{el}_{inc,\varphi}}{\partial B_{iso,n}}\right)\right) \\ &= \left(-\underbrace{N_\varphi A I_0\left(t\right)\left(1-p\right)e^{-\sum_{\varphi'}N_{\varphi'}\sigma_{tot,\varphi'}}}_{ATP}\right)\left(\sum_{\vec{h}}\left(\frac{\partial \sigma^{el}_{coh,\varphi}}{\partial \left|F_{\vec{h}}\right|^2}\right)\left(\frac{\partial \left|F_{\vec{h}}\right|^2}{\partial B_{iso,n}}\right)+\left(\frac{\partial \sigma^{el}_{inc,\varphi}}{\partial B_{iso,n}}\right)\right)\end{aligned} \tag{E.1}$$

The partial derivative of the model function with respect to the total scattering cross-section of a phase is used frequently and hence a variable ATP is defined as shown above. The squared structure factor contributes only to the elastic coherent scattering cross-section and this part of the derivative is given by

$$\frac{\partial \sigma^{el}_{coh,\varphi}}{\partial \left|F_{\vec{h}}\right|^2} = \frac{\partial}{\partial \left|F_{\vec{h}}\right|^2}\frac{\lambda^2}{2V_0}\sum_{\vec{h}'}\left|F_{\vec{h}'}\right|^2 d_{\vec{h}'}k\left(\Delta\right) = \frac{\lambda^2}{2V_0}d_{\vec{h}}k\left(\Delta\right) \tag{E.2}$$

The partial derivative of the squared absolute value of the structure factor with respect to the atomic displacement factor $B_{iso,n}$ of the n-th atom of the asymmetric unit is with $|a+ib|^2 = a^2+b^2$ given by

$$\begin{aligned}\frac{\partial \left|F_{\vec{h}}\right|^2}{\partial B_{iso,n}} &= \frac{\partial}{\partial B_{iso,n}}M_{\vec{h}}\left|\sum_k o_k b_k e^{-\frac{B_{iso,k}}{4d^2_{\vec{h}}}}\left(\cos 2\pi\vec{h}\cdot\vec{x}_k + i\sin 2\pi\vec{h}\cdot\vec{x}_k\right)\right|^2 \\ &= \frac{\partial}{\partial B_{iso,n}}M_{\vec{h}}\left|\sum_k o_k b_k e^{-\frac{B_{iso,k}}{4d^2_{\vec{h}}}}\cos 2\pi\vec{h}\cdot\vec{x}_k + i\sum_k o_k b_k e^{-\frac{B_{iso,k}}{4d^2_{\vec{h}}}}\sin 2\pi\vec{h}\cdot\vec{x}_k\right|^2 \\ &= \frac{\partial}{\partial B_{iso,n}}M_{\vec{h}}\left(\left(\sum_k o_k b_k e^{-\frac{B_{iso,k}}{4d^2_{\vec{h}}}}\cos 2\pi\vec{h}\cdot\vec{x}_k\right)^2+\left(\sum_k o_k b_k e^{-\frac{B_{iso,k}}{4d^2_{\vec{h}}}}\sin 2\pi\vec{h}\cdot\vec{x}_k\right)^2\right) \\ &= 2M_{\vec{h}}\left(\sum_k o_k b_k e^{-\frac{B_{iso,k}}{4d^2_{\vec{h}}}}\cos 2\pi\vec{h}\cdot\vec{x}_k\right)o_n b_n e^{-\frac{B_{iso,n}}{4d^2_{\vec{h}}}}\cos 2\pi\vec{h}\cdot\vec{x}_n\left(-\frac{1}{4d^2_{\vec{h}}}\right) \\ &\quad +2M_{\vec{h}}\left(\sum_k o_k b_k e^{-\frac{B_{iso,k}}{4d^2_{\vec{h}}}}\sin 2\pi\vec{h}\cdot\vec{x}_k\right)o_n b_n e^{-\frac{B_{iso,n}}{4d^2_{\vec{h}}}}\sin 2\pi\vec{h}\cdot\vec{x}_n\left(-\frac{1}{4d^2_{\vec{h}}}\right)\end{aligned} \tag{E.3}$$

[1] Modeling of inelastic contributions is still under development, therefore the contributions of these cross-sections are omitted here.

$$= -\frac{M_{\vec{h}}}{2d_{\vec{h}}^2} o_n b_n e^{-\frac{B_{iso,n}}{4d_{\vec{h}}^2}} \left(\left(\sum_k o_k b_k e^{-\frac{B_{iso,k}}{4d_{\vec{h}}^2}} \cos 2\pi \vec{h} \cdot \vec{x}_k \right) \cos 2\pi \vec{h} \cdot \vec{x}_n + \left(\sum_k o_k b_k e^{-\frac{B_{iso,k}}{4d_{\vec{h}}^2}} \sin 2\pi \vec{h} \cdot \vec{x}_k \right) \sin 2\pi \vec{h} \cdot \vec{x}_n \right)$$

$M_{\vec{h}}$ is the multiplicity of the reflection $\vec{h}$, o_k is the site occupation factor of the k-th atom and b_k its scattering length. The sum runs over all atoms in the unit cell. Grouping the factors independent of the isotropic displacement factor $B_{iso,n}$, which are constant during the whole refinement (as long as occupation factors o_n and positional parameter $\vec{x}_n$ are not refinable), allows to define constants

$$f_n^{\vec{h},re} = M_{\vec{h}} o_n b_n \cos 2\pi \vec{h} \cdot \vec{x}_n \tag{E.4}$$

$$f_n^{\vec{h},im} = M_{\vec{h}} o_n b_n \sin 2\pi \vec{h} \cdot \vec{x}_n \tag{E.5}$$

With this, (E.3) can be simplified to

$$\frac{\partial \left| F_{\vec{h}} \right|^2}{\partial B_{iso,n}} = -\frac{e^{-\frac{B_{iso,n}}{4d_{\vec{h}}^2}}}{2M_{\vec{h}} d_{\vec{h}}^2} \left(f_n^{\vec{h},re} \left(\sum_k f_k^{\vec{h},re} e^{-\frac{B_{iso,k}}{4d_{\vec{h}}^2}} \right) + f_n^{\vec{h},im} \left(\sum_k f_k^{\vec{h},im} e^{-\frac{B_{iso,k}}{4d_{\vec{h}}^2}} \right) \right) \tag{E.6}$$

The second part of the derivative of the total cross-section of phase ϕ with respect to $B_{iso,n}$ is given by the contribution of the elastic incoherent scattering cross-section:

$$\begin{aligned} \frac{\partial \sigma_{inc}^{el}}{\partial B_{iso,n}} &= \frac{\partial}{\partial B_{iso,n}} \bar{\sigma}_{inc} \lambda^2 \sum_k \frac{1}{2B_{iso,k}} \left(1 - e^{-\frac{2B_{iso,k}}{\lambda^2}} \right) \\ &= \frac{\bar{\sigma}_{inc} \lambda^2}{B_{iso,n}} \left(-\frac{1}{2B_{iso,n}} \left(1 - e^{-\frac{2B_{iso,n}}{\lambda^2}} \right) + \frac{e^{-\frac{2B_{iso,n}}{\lambda^2}}}{\lambda^2} \right) \end{aligned} \tag{E.7}$$

The complete derivative of the measured intensity with respect to $B_{iso,n}$ is thus

$$\begin{aligned} \frac{\partial I_i}{\partial B_{iso,n}} = {} & ATP \frac{\lambda^2}{2V_0} \sum_{\vec{h}} \frac{e^{-\frac{B_{iso,n}}{4d_{\vec{h}}^2}}}{2M_{\vec{h}} d_{\vec{h}}^2} \left(f_n^{\vec{h},re} \left(\sum_k f_k^{\vec{h},re} e^{-\frac{B_{iso,k}}{4d_{\vec{h}}^2}} \right) + f_n^{\vec{h},im} \left(\sum_k f_k^{\vec{h},im} e^{-\frac{B_{iso,k}}{4d_{\vec{h}}^2}} \right) \right) d_{\vec{h}} k(\Delta) + \\ & ATP \frac{\bar{\sigma}_{inc} \lambda^2}{B_{iso,n}} \left(-\frac{1}{2B_{iso,n}} \left(1 - e^{-\frac{2B_{iso,n}}{\lambda^2}} \right) + \frac{e^{-\frac{2B_{iso,n}}{\lambda^2}}}{\lambda^2} \right) \end{aligned} \tag{E.8}$$

For optimisation purpose, a factor calculated once per fit cycle is defined for each reflection $\vec{h}$ and each atom n:

$$F'_{\vec{h},n} = \frac{e^{-\frac{B_{iso,n}}{4d^2_{\vec{h}}}}}{4V_0 M_{\vec{h}} d_{\vec{h}}} \left(f_n^{\vec{h},re} \left(\sum_k f_k^{\vec{h},re} e^{-\frac{B_{iso,k}}{4d^2_{\vec{h}}}} \right) + f_n^{\vec{h},im} \left(\sum_k f_k^{\vec{h},im} e^{-\frac{B_{iso,k}}{4d^2_{\vec{h}}}} \right) \right) \tag{E.9}$$

Applying it to the derivative, the latter becomes the following much more compact expression

$$\frac{\partial I_i}{\partial B_{iso,n}} = ATP \cdot \lambda^2 \left(\sum_{\vec{h}} F'_{\vec{h},n} k\left(\Delta\right) + \frac{\bar{\sigma}_{inc}}{B_{iso,n}} \left(\frac{1}{2B_{iso,n}} \left(e^{-\frac{2B_{iso,n}}{\lambda^2}} - 1 \right) + \frac{e^{-\frac{2B_{iso,n}}{\lambda^2}}}{\lambda^2} \right) \right) \tag{E.10}$$

Using the constants defined above, the structure-factor becomes

$$\begin{aligned} \left| F_{\vec{h}} \right|^2 &= M_{\vec{h}} \left(\left(\sum_k o_k b_k e^{-\frac{B_{iso,k}}{4d^2_{\vec{h}}}} \cos 2\pi \vec{h} \cdot \vec{x}_k \right)^2 + \left(\sum_k o_k b_k e^{-\frac{B_{iso,k}}{4d^2_{\vec{h}}}} \sin 2\pi \vec{h} \cdot \vec{x}_k \right)^2 \right) \\ &= M_{\vec{h}} \left(\left(\sum_k \frac{f_k^{\vec{h},re} e^{-\frac{B_{iso,k}}{4d^2_{\vec{h}}}}}{M_{\vec{h}}} \right)^2 + \left(\sum_k \frac{f_k^{\vec{h},im} e^{-\frac{B_{iso,k}}{4d^2_{\vec{h}}}}}{M_{\vec{h}}} \right)^2 \right) \\ &= \frac{\left(\sum_k f_k^{\vec{h},re} e^{-\frac{B_{iso,k}}{4d^2_{\vec{h}}}} \right)^2 + \left(\sum_k f_k^{\vec{h},im} e^{-\frac{B_{iso,k}}{4d^2_{\vec{h}}}} \right)^2}{M_{\vec{h}}} \end{aligned} \tag{E.11}$$

Appendix F

Listings

F.1 Application Example of Fit-Class

The following C++ listing presents an application example of the fit class developed for **BETMAn**. The purpose of this program is to fit an Avrami-type of function to a given dataset. The actual fit function `AvramiFunction` is omitted here. See 4.3 for further explanations.

```
//////////////////////////////////////////////////////////////////////
// Construction
// Derive class for Avrami fit from general fit-class
//////////////////////////////////////////////////////////////////////
AvramiFit::AvramiFit(spectrum *s) : fit()       // spectrum with measured data and space for fit
{
        set_fit_function(AvramiFunction);       // Declare fit function
        set_number_of_parameters(5);            // Total of 5 parameters

        set_spectrum(s);                        // Declare spectrum object
        set_fit_range(0,s->get_channels());     // Declare fit-range

        // name parameters
        set_parameter_name(OFFSET,"initial volume fraction");
        set_parameter_name(TOTAL,"transformed volume fraction");
        set_parameter_name(TAU,"Avrami time constant tau");
        set_parameter_name(N,"Avrami coefficient n");
        set_parameter_name(TIMEOFFSET,"time offset");
}

//////////////////////////////////////////////////////////////////////
// Main program
//////////////////////////////////////////////////////////////////////
int main( int argc, char *argv[ ], char *envp[ ] )

{
        spectrum                s;

        // load the data points
        if(!s.read_spectrum(argv[1],0,0,0,NULL,NULL,0,0)) return -1;
        s.set_poisson_statistics(1);

        AvramiFit               f(&s);          // Initialize AvramiFit-object

        f.read_controls("Avrami.ctr");

        f.set_parameter(OFFSET,0);              // set starting values
        f.set_parameter(TOTAL,50);
        f.set_parameter(TAU,1000);
        f.set_parameter(N,3);
```

```
        f.set_parameter(TIMEOFFSET,0);

        f.variation_allowed(OFFSET,0);          // set variation flags
        f.variation_allowed(TOTAL,1);
        f.variation_allowed(TAU,1);
        f.variation_allowed(N,1);
        f.variation_allowed(TIMEOFFSET,0);

        f.do_fit(1,5);                          // Perform fit with full output and terminate after
                                                // 5 consecutive steps with no residual reduction
        return 1;
}
```

F.2 Intermediate Result File

The following listing is an example of an intermediate result file (`.irXXX`-file) as created by **BETMAn** after each refinement cycle. See section 4.3 for further explanations. For layout purpose, the number of decimals was reduced from 9 to 6.

```
BETMAn result file
Do not change!

Control parameters:
                  72    // Number of parameters
                   1    // Number of involved phases
                   1    // Background model
                   4    // Reflection profile type
                   0    // Incident intensity model
Parameter lines contain absolute value, e.s.d., rel. error, refinement flag and name of the paramter.
Overall parameters:
    0.000000e+000        0.000000e+000        0.000000e+000    0       // P1
    6.020932e-013        4.114235e-018        6.833220e-006    1       // P2
    1.779084e-005        4.130752e-011        2.321841e-006    1       // P3
    1.677787e-001        7.890403e-006        4.702861e-005    1       // P4
    1.684794e+005        1.331725e+001        7.904381e-005    1       // P5
   -3.781926e-001        5.647778e-006       -1.493359e-005    1       // P6
    2.461252e+007        1.119068e+002        4.546744e-006    1       // P7
    0.000000e+000        0.000000e+000        0.000000e+000    0       // P8
    1.539840e+008        0.000000e+000        0.000000e+000    0       // P9
    0.000000e+000        0.000000e+000        0.000000e+000    0       // P10
    1.879920e+010        0.000000e+000        0.000000e+000    0       // P11
   -1.813100e+005        0.000000e+000        0.000000e+000    0       // scale
    1.216136e+004        1.175564e-002        9.666385e-007    1       // intensity offset
    0.000000e+000        0.000000e+000        0.000000e+000    0       // passing neutrons
    1.014247e+001        1.105441e-007        1.089912e-008    1       // flightpath length
    2.000000e-006        0.000000e+000        0.000000e+000    0       // channelwidth
    0.000000e+000        0.000000e+000        0.000000e+000    0       // time offset
    0.000000e+000        0.000000e+000        0.000000e+000    0       // Background scale
    1.500000e+002        0.000000e+000        0.000000e+000    0       // Background decay
    6.283185e+001        0.000000e+000        0.000000e+000    0       // Source frequency (for Fourier background)
    5.224387e-002        6.627082e-004        1.268489e-002    1       // Background parameter 1
    9.992421e-003        8.905232e-004        8.911986e-002    1       // Background parameter 2
   -1.286478e-001        2.309990e-004       -1.795591e-003    1       // Background parameter 3
    0.000000e+000        0.000000e+000        0.000000e+000    0       // Background parameter 4

...

    0.000000e+000        0.000000e+000        0.000000e+000    0       // Background parameter 31

Parameters of Phase 1 (G:\WATCOM\rietveld\phases\Alpha_fe.pha)
    4.163459e+026        6.485012e+021        1.557601e-005    1       // Number of scattering centers per unit area (Al
    2.866500e-010        0.000000e+000        0.000000e+000    0       // Lattice parameter a (Alpha Fe)
    2.866500e-010        0.000000e+000        0.000000e+000    0       // Lattice parameter b (Alpha Fe)
    2.866500e-010        0.000000e+000        0.000000e+000    0       // Lattice parameter c (Alpha Fe)
    1.570796e+000        0.000000e+000        0.000000e+000    0       // Lattice parameter alpha (Alpha Fe)
```

```
    1.570796e+000        0.000000e+000        0.000000e+000    0       // Lattice parameter beta (Alpha Fe)
    1.570796e+000        0.000000e+000        0.000000e+000    0       // Lattice parameter gamma (Alpha Fe)
    0.000000e+000        0.000000e+000        0.000000e+000    0       // Edge profile parameter sigma0 (Alpha Fe)
    1.412574e-002        3.489746e-008        2.470487e-006    1       // Edge profile parameter sigma1 (Alpha Fe)
    0.000000e+000        0.000000e+000        0.000000e+000    0       // Edge profile parameter sigma2 (Alpha Fe)
    0.000000e+000        0.000000e+000        0.000000e+000    0       // Edge profile parameter sigma0e (Alpha Fe)
    0.000000e+000        0.000000e+000        0.000000e+000    0       // Edge profile parameter sigma1e (Alpha Fe)
    0.000000e+000        0.000000e+000        0.000000e+000    0       // Edge profile parameter sigma2e (Alpha Fe)
    1.000000e+014        0.000000e+000        0.000000e+000    0       // Edge profile parameter alpha0 (Alpha Fe)
    0.000000e+000        0.000000e+000        0.000000e+000    0       // Edge profile parameter alpha1 (Alpha Fe)
    1.500000e+012        0.000000e+000        0.000000e+000    0       // Edge profile parameter beta0 (Alpha Fe)
    4.000000e-030        0.000000e+000        0.000000e+000    0       // Edge profile parameter beta1 (Alpha Fe)
    0.000000e+000        0.000000e+000        0.000000e+000    0       // Edge profile parameter epsilon_i (Alpha Fe)
    0.000000e+000        0.000000e+000        0.000000e+000    0       // Edge profile parameter epsilon_a (Alpha Fe)
    3.670998e-022        7.865530e-027        2.142613e-005    1       // B_iso for atom Fe (Alpha Fe)
    6.270184e-001        0.000000e+000        0.000000e+000    0       // B for atom Fe (Alpha Fe)
                  0            // Number of textures

The fit-range was d=  0.47 A to d=  2.15 A


The overall R-value was           4.58479e-002
Chi-square was                    5.90555e+007
Goodness-of-fit was               1.37819e+004
Parameters varied                           14
Datapoints                                4299
```

F.3 Example of CIF-file

Example of a CIF-file (Crystallographic Information File) for the structure of ortho-enstatite. See section 4.5 for further explanations.

```
data_64629-ICSD

_audit_creation_date              97-12-08
_audit_creation_method            'generated by RETRIEVE 2.0'

_database_code_ICSD               64629

_chemical_name_systematic         'Magnesium catena-silicate'
_chemical_name_mineral            'Enstatite'
_chemical_compound_source         'synthetic'
_chemical_formula_structural      'Mg (Si O3)'
_chemical_formula_sum             'Mg O3 Si'

_publ_section_title
;
Enstatite, Mg~2~ Si~2~ O~6~: A neutron diffraction refinement of the
crystal structure and a rigid-body analysis of the thermal
vibration.
;
loop_
_publ_author_name
  'Ghose, S'
  'Schomaker, V'
  'McMullan, R K'
_journal_name_full
;
Zeitschrift fuer Kristallographie (149,1979-)
;
_journal_coden_ASTM               ZEKRDZ
_journal_volume                   176
_journal_year                     1986
_journal_page_first               159
_journal_page_last                175
```

```
_cell_length_a                    18.235(3)
_cell_length_b                    8.818(1)
_cell_length_c                    5.179(1)
_cell_angle_alpha                 90
_cell_angle_beta                  90
_cell_angle_gamma                 90
_cell_volume                      832.8
_cell_formula_units_Z             16

_symmetry_space_group_name_H-M    'P b c a'
_symmetry_Int_Tables_number       61
_symmetry_cell_setting            orthorhombic

loop_
_symmetry_equiv_pos_as_xyz
  'x,y,z'
  '1/2+x,1/2-y,-z'
  '-x,1/2+y,1/2-z'
  '1/2-x,-y,1/2+z'
  '-x,-y,-z'
  '1/2-x,1/2+y,z'
  'x,1/2-y,1/2+z'
  '1/2+x,y,1/2-z'

loop_
_atom_type_symbol
_atom_type_oxidation_number
  Mg2+   2.000
  Si4+   4.000
  O2-   -2.000

loop_
_atom_site_label
_atom_site_type_symbol
_atom_site_symmetry_multiplicity
_atom_site_Wyckoff_symbol
_atom_site_fract_x
_atom_site_fract_y
_atom_site_fract_z
_atom_site_occupancy
_atom_site_attached_hydrogens
_atom_site_calc_flag
  Mg1   Mg2+   8 c 0.37584(3) 0.65393(5) 0.8658(1) 1.  0 d
  Mg2   Mg2+   8 c 0.37681(3) 0.48693(6) 0.35882(10) 1.  0 d
  Si1   Si4+   8 c 0.27167(3) 0.34166(7) 0.05031(12) 1.  0 d
  Si2   Si4+   8 c 0.47357(3) 0.33732(7) 0.79827(12) 1.  0 d
  O1    O2-    8 c 0.18346(2) 0.34009(5) 0.03471(9) 1.  0 d
  O2    O2-    8 c 0.56231(2) 0.34034(5) 0.80017(9) 1.  0 d
  O3    O2-    8 c 0.31091(3) 0.50255(5) 0.04319(9) 1.  0 d
  O4    O2-    8 c 0.43277(3) 0.48289(5) 0.68909(10) 1.  0 d
  O5    O2-    8 c 0.30318(3) 0.22259(5) -0.16799(9) 1.  0 d
  O6    O2-    8 c 0.44762(3) 0.19506(5) 0.60361(9) 1.  0 d

loop_
_atom_site_aniso_label
_atom_site_aniso_U_11
_atom_site_aniso_U_12
_atom_site_aniso_U_13
_atom_site_aniso_U_22
_atom_site_aniso_U_23
_atom_site_aniso_U_33
  Mg1   0.00609(17) -0.00032(15) -0.00057(14) 0.00454(17) 0.00011(15) 0.00371(19)
  Mg2   0.00817(19) -0.00069(16) -0.00186(16) 0.00664(19) 0.00049(16) 0.00526(20)
  Si1   0.00378(21) -0.00054(18) 0.00034(18) 0.00373(23) -0.00013(20) 0.00271(23)
  Si2   0.00385(22) 0.00034(18) -0.00022(18) 0.00321(21) 0.00023(19) 0.00301(22)
  O1    0.00377(16) -0.00018(13) 0.00012(13) 0.00551(17) 0.00019(14) 0.00488(18)
  O2    0.00424(16) 0.00006(13) -0.00021(14) 0.00563(16) 0.00029(14) 0.00451(17)
  O3    0.00732(18) -0.00207(14) -0.00106(15) 0.00480(17) 0.00064(14) 0.00563(19)
  O4    0.00737(17) 0.00235(13) -0.00112(15) 0.00514(16) 0.00028(15) 0.00490(18)
  O5    0.00560(16) 0.00055(14) -0.00040(15) 0.00746(18) -0.00197(14) 0.00426(18)
  O6    0.00579(16) -0.00074(14) 0.00052(14) 0.00623(17) -0.00144(13) 0.00431(16)
```

```
_refine_ls_R_factor_all          0.032
```

F.4 Script File Example

A script used to process data of one transformation run acquired during the investigation of the austenite decomposition to bainite (see section 7.1.4 and appendix G):

```
Initialisation
Initialize some variables

Define the fit-setup
#setup g:\watcom\rietveld\setup\58m500With8msDelay.set

Define the control file
#control g:\watcom\rietveld\betfit.ctr

Define the common part of the result files
#resultname k:\vax98\steel\SampleE\SampleE

Define the fit range
#range 200 8192

Define the start values for the very first pattern
#start k:\vax98\Steel\SampleE\STARTVALUES

Define the log file for the XSYS DAQ, containing start and stop times of each run
#xsyslog k:\vax98\AllData\xsort1998.log

Define the log file from CCR providing information on the beam current
#ccrlog k:\vax98\AllData\beamcurrent.txt

Define file with temperature profile
#temperature k:\vax98\temperatures\steel7.txt

Define minimum number of total counts of a pattern to filter no-beam runs
little more than 1E7 counts per data area (300 sweeps)
#min_counts 4e7

add xsys data areas
#xsys_areas 4

exclude data areas having not the name NEUTxxx
#xsys_name NEUT

Define parameters to be included in the overall time series file
#extract Lattice parameter a (Alpha Fe)
#extract Lattice parameter a (Gamma Fe)
#extract Number of scattering centers per unit area (Alpha Fe)
#extract Number of scattering centers per unit area (Gamma Fe)
#extract Edge profile parameter sigma1 (Alpha Fe)
#extract Edge profile parameter sigma1 (Gamma Fe)
#extract B_iso for atom Fe (Alpha Fe)
#extract B_iso for atom Fe (Gamma Fe)
#extract VOLFRACTIONS
#extract TOTALCOUNTS
#extract CHISQ
#extract GOF
#extract RVALUE

Kill previous intermediate result files
#shell del k:\vax98\steel\SampleE\*.ir*

Kill previous result files
#shell del k:\vax98\steel\SampleE\*.brf
```

```
Process file list
#fileloop k:\vax98\steel\SampleE\files.txt


------------------------------------------------------------------------
From here on, the actual refinement is controlled.
All commands are executed for each pattern in the file list.
If a file contains more than one data area, then every command is
executed for each pattern in the file.

Refine scale-factor
#cycles 5
#variable k:\vax98\steel\step1_ADFConst.var
#refine

refine volume fractions and background
#variable k:\vax98\steel\step2_ADFConst.var
#cycles 5
#refine

conditional refinements:
#if VOLFRAC Alpha Fe < 10
        refine N_scatt, edge width and lattice parameter of Austenite and N_scatt of Bainite
        #variable k:\vax98\steel\step3_ADFConst.var
        #cycles 5
        #refine
#endif

#if VOLFRAC Alpha Fe between 10 and 25
        refine N_scatt, edge width and lattice parameter of Austenite plus N_scatt Bainite
        #variable k:\vax98\steel\step4_ADFConst.var
        #cycles 5
        #refine

        refine N_scatt, edge width and lattice parameter of Austenite plus edge width and lattice parameter
        of Bainite with constant number of scattering centers of Bainite
        #variable k:\vax98\steel\step5_ADFConst.var
        #cycles 5
        #refine
#endif

#if VOLFRAC Alpha Fe between 25 and 75
        refine N_scatt, edge width and lattice parameter of both Austenite and Bainite
        #variable k:\vax98\steel\step6_ADFConst.var
        #cycles 5
        #refine
#endif

#if VOLFRAC Alpha Fe between 75 and 90
        refine N_scatt, edge width and lattice parameter of Bainite plus N_scatt of Austenite
        #variable k:\vax98\steel\step7_ADFConst.var
        #cycles 5
        #refine

        refine N_scatt, edge width and lattice parameter of Bainite plus edge width and lattice parameter
        of Austenite with constant number of scattering centers of Austenite
        #variable k:\vax98\steel\step8_ADFConst.var
        #cycles 5
        #refine
#endif


#if VOLFRAC Alpha Fe > 90
        refine N_scatt, edge width and lattice parameter of Bainite and N_scatt of Austenite
        #variable k:\vax98\steel\step9_ADFConst.var
        #cycles 5
        #refine
#endif

write result file
#writeresult
```

```
#endfileloop

------------------------------------------------------------------------
End of the script.
```

Appendix G

BETMAn Script Language

In this appendix, all commands of the script language implemented in **BETMAn** for automated processing of Bragg-edge transmission patterns are explained. All script commands are preceeded by a '#'-symbol, any line not having this symbol as first non-whitespace character (i.e. space or tab) is treated as comment. The input is not case-sensitive. In the following sections the commands are grouped by function and listed alphabetically within these sections. See appendix F.4 for an example of a script file.

G.1 General Commands

G.1.1 `#DoNotUsePoisson`

For each data file loaded, the weight of each measured intensity is set to 1. If this command is not used, the data is assumed to have Poisson statistics, therefore the weight of each intensity value is set to the square root of the intensity. This option is necessary for data measured in current mode.

G.1.2 `#Extract`

The extract command instructs **BETMAn** to add a column with the value of the parameter following the `#Extract` command to the time-series file (see `#ResultName`) after each `#WriteResult` command. The parameter names expected here are the same names given in the comment of each parameter in an intermediate result file (see F.2). Each parameter of interest needs one line with the extract command in the script-file. The most convenient way to create an `#Extract` entry is to cut and paste the parameter names from the comments of an intermediate result file. For refinable parameters, an additional column with the e.s.d. is added to the time-series file. There are some special values defined which are not actual refinable parameters. Those are:

- VOLFRACTIONS: Extracts the volume fractions of each participating phase, calculated from the unit cell volume and the number of unit cells per unit area.
- TOTALCOUNTS: Extracts the total number of counts in the refined pattern. This is an important parameter to judge the data quality of a pattern and set limits for the minimum number

of counts in a pattern using the `#MinCounts` command.

- CHISQ, GOF or RVALUE: Extracts the residual χ^2, goodness of fit and r-value, respectively, of the final refinement of a pattern. Used also to judge the quality of the data and the refined parameters.

The sequence of parameters appearing in the columns of a time series file is given by the sequence of the corresponding `#Extract` commands. A typical example of an extract section of a script file is

```
Parameters to appear in the time-series file:
#extract Lattice parameter a (Alpha Fe)
#extract Number of scattering centers per unit area (Alpha Fe)
#extract Edge profile parameter sigma1 (Alpha Fe)
#extract B_iso for atom Fe (Alpha Fe)
#extract TOTALCOUNTS
#extract CHISQ
#extract GOF
#extract RVALUE
```

G.1.3 `#Load`

Load a pattern for refinement. The data type is identified by the file extension: `.dat` for XSYS binaries, `.raw` for ISIS binaries and `.txt` for ASCII-formats. For the latter, several formats are attempted to identify automatically from the first lines of the file. This command is usually not used as in most cases files are loaded by `#FileLoop`.

G.1.4 `#ResultName`

Provides the common part of the result files (`brf`-files, **B**ETMAn **R**esult **F**iles, generated after the refinement of each file) and the time-series file. In the latter, for each pattern of the analysis run one line with information and results of the pattern as controlled by `#Extract`, `#CCRLog`, `#XSYSLog` and `#Temperature` is generated. This file is in ASCII format and can be easily used for post-processing in graphics or spreadsheet software.

G.1.5 `#Setup`

Provides a setup file used to define flightpath etc.

G.1.6 `#Shell`

Issues a shell command, for example used to delete intermediate result files of previous analysis runs:

```
Kill previous intermediate result files
#shell del k:\vax98\steel\HeatUp\*.ir*

Kill previous result files
#shell del k:\vax98\steel\HeatUp\*.brf
```

G.1.7 #WriteResult

Creates a line in the time-series file (see #ResultName-command). As standard value only the filename of the pattern is recorded. Additional parameters may be parameters requested by a previous #Extract command. Providing #XSYSLog, #CCRLog or #Temperature commands adds the corresponding information (time of the pattern, proton current and sample temperature).

G.1.8 #XSYS_Areas

As data files taken with the XSYS system at flightpath 5 of LANSCE contain multiple data areas, with this parameter a number of data areas can be provided that is added prior to refinement and the resulting pattern is then refined. If this parameter is not used in the **BETMAn** script file, each single data area contained in an XSYS-file is refined. Currently, only dividers of the total number of data areas contained in a file can be used, e.g. if the standard of 20 data areas are contained in each XSYS file, possible values for this parameter are 1, 2, 4, 5, 10 and 20. This allows an offline variation of the time resolution of the experiment. It turned out to be useful to decrease the number of added patterns step by step and compare the resulting parameter curves (e.g. lattice parameter versus time etc.). If these curves are not congruent within the margin of error, the refinement is clearly inconsistent.

G.1.9 #XSYS_Name

As not only data areas containing Bragg-edge transmission patterns may be contained in a XSYS-file, this command allows to provide a constant part of the data-area names as parameter. In most XSYS files analysed so far, the data areas containing the Bragg-edge transmission patterns were named NEUTRONxx, while data areas used in other applications of the system but stored in the same data files had different names. Consequently, by providing #XSYS_Name Neutron those data areas being of no interest for the automated analyses were filtered out.

G.2 Fit Control

G.2.1 #Control

Provides the control file containing flags and defaults for the fit. In virtually all cases this command uses the full path to betfit.ctr as a parameter.

G.2.2 #Cycles

Parameter is the number of consecutive cycles required to terminate fitting. Used for example to refine within $2+n$ cycles the scale factor and within $5+n$ cycles the lattice parameters and numbers of scattering centers per unit area. n may get relatively large as the fit might go through local minima where the Levenberg-Marquardt algorithm reduces its λ, before it moves towards a lower local minimum. It has been observed that this happens occasionally.

G.2.3 #Range

Provides the first and last channel used by the fit.

G.2.4 #Refine

Starts the refinement.

G.2.5 #Start

Parameter is a filename pointing to a file with starting values for all parameters. This may be any intermediate result file (the extension `.irXXX` is not necessary, hence the `.irXXX`-file might be renamed to a more meaningful name, also avoiding deletion as provided by the example of the `#Shell`-command). The phases contained in this file define the phases used during the subsequent refinements. The corresponding `.pha` or `.cif`-files are identified by the comments of the `.irXXX`-file (see section 4.3), hence the referenced phase-files (`.pha` or `.cif`) must be available. The variation flags are initialized by the flags in this file.

G.2.6 #Variable

Defines the variation scheme by providing a filename. This might be again an `.irXXX`-file, but at this time only the flags are read. Again, the extension does not have to be `.irXXX`.

G.3 Conditional Refinements and Loops

G.3.1 #FileLoop

Parameter is an ASCII file with one filename per line. The files are processed in the order in this file (unless the `#Reverse` command is issued). The refined parameter values of a pattern are used as starting values for the next pattern, the starting values for the very first pattern must be provided with a `#Start` command. Full pathnames are not required, if the filenames are given without path, the files are assumed to be in the same path as the file provided as parameter to `#FileLoop`. Such a list of filenames can be easily generated at the command line/shell by

```
dir *.dat /on /b>files.txt
```

which creates a file 'files.txt' with all filenames of `.dat`-files sorted alphabetically. See `#XSYS_Areas` on how to integrate multiple XSYS data-areas stored in the same file.

G.3.2 #EndFileLoop

All commands between `#FileLoop` and `#EndFileLoop` are executed for each file in the file list provided as parameter for `#FileLoop`.

G.3.3 #If

The tendency of divergence in case of parameters refined for too small volumes fractions of the corresponding phase calls for conditional refinement. For example, the refinement of lattice and edge profile parameters is, as a rule of thumb, only possible when the edges are 'visible by eye'. This, in turn, is the case when the volume fraction of, for example, a steel is greater than approximately 5%. Each command between an `#If` and the corresponding `#EndIf` is executed only when the `#If`-condition is true. The syntax is

```
#If <parameter-name> < <value>
```

or

```
#if <parameter-name> > <value>
```

or

```
#if <parameter-name> between <value1> and <value2>
```

Parameter names are the same as in the case of the `#Extract` command. Logical and- or or-conditions have to be modeled by nested or subsequent `#If`-commands. If an `#If`-condition does not evaluate to true, all script lines until the next `#EndIf` are skipped.

G.3.4 #EndIf

Terminates a branch of conditional execution. See `#If`-command for more information.

G.3.5 #MinCounts

Parameter is a minimum number of counts in a pattern above which a refinement of this pattern is performed. This is used to skip patterns with too low intensity due to beam failure. Without such a condition, the fit would be performed in worst case on a pattern with no intensity at all, leading to a divergence of the parameters. If those parameters are used as starting values for the following pattern, the whole analysis run is very likely to be lost. See `#Extract`-command for a possibility to obtain the number of counts per pattern. If it is found that a time series diverges at a certain pattern, either the conditions for minimum values of parameters (e.g. volume fraction) were set too low or that pattern does not contain enough counts. In the latter case, the cure is to change the parameter for `#MinCounts` and re-run the analysis.

G.3.6 #Reverse

Initiates a processing of files in a `#FileLoop` in reverse order. This is used to perform consistency checks: If the results of a forward and reverse analysis, i.e. from the chronologically last to the first pattern, are not identical within the margin of error, the fit followed different paths of minima and the refinement was not consistent. This might be for example due to a bias introduced by 'wrong' starting values for one of the two directions.

G.4 Merging of Data from other Sources

In most cases where a phase transition is followed, one ore more external variables are recorded. Both the Bragg-edge transmission patterns and external variables typically have a timestamp and hence it is convenient to merge the information gained from the Bragg-edge transmission pattern and the external variable into a single result file for further analysis. Currently supported variables are the proton beam current and a temperature. To obtain the timestamp of the patterns, an `#XSYSLog` command has to be issued, providing **BETMAn** with the log-file of the data acquisition.

G.4.1 `#CCRLog`

After this command, the name of a CCR-log file has to be provided. These files are obtainable from the LANSCE CCR (Central Control Room) and contain the beam current and status versus time in a 10 second resolution. If this command is issued in a **BETMAn** script file, in the `#Result` file automatically a column with the beam current averaged over the period of the current pattern is added.

G.4.2 `#Temperature`

The parameter of this command is the name of an ASCII file containing a pair of time and temperature per line separated by spaces or tabs. If this command is issued in a **BETMAn** script file, in the result file automatically a column with the temperature at the middle of the current data file is added. As the value read is not used as a temperature during the script, in principle any other variable can be merged to the time-series file, given that it is provided in the appropriate file format.

G.4.3 `#XSYSLog`

Parameter is the filename of the XSYS log file. In this log file, the start and stop time of each file are recorded. This information is the basis to calculate the time of each pattern and synchronize it with the CCR-log (beam current) and temperature logs. It is beneficial to synchronize at least the clocks of the computer recording the temperature with the microVAX recording the Bragg-edge transmission patterns.

Appendix H

BETMAn Tutorial

In the following section, the application of **BETMAn** is explained. The description is meant to provide potential users with an idea of working with **BETMAn** and guide new users during a first application of **BETMAn**. The file tpyes required for and created during a refinement are also explained. A working installation of **BETMAn** is assumed. The necessary data and phase files are distributed with **BETMAn**.

With `File - New - Measured spectrum binary format` or `File - Open` open the XSYS data file `repshot_m3718.dat`. The data of this file was taken at LANSCE with the counting mode setup, a flightpath of about 58 meters and the file contains five XSYS data areas of 3600 neutron pulses each. The channelwidth of the data acquisition system was set to 5 μs and the t_0-pulse of the accelerator was delayed by about 8ms (time offset 8 ms). This information should be typed in the measurement record appearing after the file is opened. The numerical information is used to convert the x-axis data from channels to other representations (energy, time-of-flight, wavelength, d-spacing) until better values from the refinement are available. Nevertheless, they are not used as starting values for the fit. Make sure that 'Data has Poisson statistics' is checked, else the data is assumed to be current mode data and all data points are weighted by 1 rather than $\sqrt{N}$ (where N is the number of counts of a channel). If the file is not opened for the first time, the information in this dialog may be changed or simply confirmed. As **BETMAn** determined the file to be an XSYS datafile, in the following dialog the desired data area can be chosen. If integration of data areas is demanded, check `Sum data areas`. For a calibration, the latter is chosen and **BETMAn** asks for the first and last data area to be added, the first and last available are the default. By hitting Enter or pressing the OK button loading of the data is initiated. The subsequent messages are for informational purpose only. If the file has been already refined before, **BETMAn** has stored the involved phase description file(s) in the database and asks whether to re-load them. If the file is refined for the first time, use `Phase - Add Phase` to add the phase α-iron to the refinement. The description is given in the file `ALPHA_FE.PHA` and simply looks like (see section 4.5 for a full description of those files)

```
#phase Alpha Fe

#space I m -3 m

#a   2.8665

#atom         Fe   0.0000   0.0000   0.0000
```

In **BETMAn**'s protocol window the output during loading of the data and the phase description

can be viewed. With `Fit - Start the BET-Fit` the fitting of the pattern is initiated. As no setup-file (containing flightpath-length, time offset etc.) is given yet, **BETMAn** prompts for such a file (extension `.set`). Some setup-files are copied to the system during **BETMAn**'s installation, any of those can be used here as the crucial parameters flightpath length and time offset can be changed in the fit-dialog.

In cases where no measured open beam pattern is available, such a setup file may be generated before by using `Fit - Generate starting values`. In the following dialog, starting values for the flightpath, a typical time-of-flight somewhere in the middle of the pattern, the numerical scaling and an intensity offset are requested. For the latter two parameters, in the case of current mode a negative scaling and a positive offset should be given. The fit of these parameters is pretty robust, hence the correct order of magnitude is sufficient. From these values, starting values for the incident intensity parameters are generated. **BETMAn** prompts for a filename of this setup and suggest a name based on the flightpath length and channelwidth. In `Fit - Select Fit-Setup (xxx)`, 'xxx' should now be the name of the generated setup.

After the fit-setup is provided, **BETMAn** request a fit control file (extension `.ctr`). This file contains some default flags for the fitting algorithm and usually the file `betfit.ctr` is chosen here. As in most cases, **BETMAn** stores the paths given for this type of files and suggests it the next time this file-type is loaded again. The fit dialog should now appear. It consists of several pages where fit control and fit parameters are grouped. The fit control page appears first and allows to change the number of consecutive iterations of the fit without change of the resiudal that terminate the fit, turn on and off the logging of the fit's try values in the protocol window and the repainting of the screen after each iteration, and set the profile type for the edges (default is the edge-profile after Jorgensen et al., see section 3.3). There are also buttons to

- view the correlation matrix (stored after each refinement cycle in an ASCII file with the same name as the data file and the extension `.cor`),
- set all parameters constant (i.e. nothing is refined),
- view the last intermediate result file (stored after each refinement in an ASCII file with the same name as the data file and the extension `.irXXX` where `XXX` is a number increased after each refinement cycle),
- generate a setup file from the current parameters (extension `.set`),
- generate an ASCII file with the weighted difference curve $(y_{i,obs} - y_{i,calc})/\sigma_i$ and a second ASCII file with the probability plot[1] of the current refinement,
- generate an ASCII file with the analytical (as coded in the fit function) and numerical derivative (as calculated after Ridders' method, Press et al., 1992) as well as the difference of both for each channel and each parameter that was varied during the last refinement cycle. This is extensively used during debugging of the fit function but might be for instance of interest to study how strong the fit function varies with a certain parameter.

All other pages contain fit parameters in the sequence parameter name, variation flag, current value. If a parameter is checked as refinable, its value will be fitted in the next cycle. Parameter values may

[1] See for example `http://www.minitab.com/resources/whitepapers/normprob.htm` for further explanations of probability plots.

be changed as desired. Leaving all parameters constant, it can be studied how manual changes of a certain parameter affect the fit function.

For the current problem of calibrating the LANSCE flightpath 5 setup as used in 1998, one should start the fit with the following values and refinement flags:

- Overall scaling (overall parameters page): Refine and set to 1 as a measured pattern will be used as incident intensity. In case of a modeled incident intensity, this value should be in the range of the maximum value in the pattern.

- Flightpath and timeoffset (overall parameters page) should be set as given in the measurement record, i.e. 58 m and 8 ms. It should be not refined for now.

- In the incident intensity page, choose 'Measured data' and click the 'Incident intensity file' button. This opens a dialog requesting the file name. In this file, the same number of channels as the current pattern must be contained and the data in this file should correspond to the 'open beam', e.g. only the Al endcaps of the beam tubes or additional endcaps of a furnace or controlled atmosphere setup but no sample. For the given pattern, choose `repshot_m3933.dat` which contains the open beam taken with a 1 cm collimation at a proton current of 50μA (the iron powder was taken at 100μA).

- For now, don't use any background.

- On the main page of the α-iron phase, delete the refinement flag of the phase to vary only the scale.

- On the last page containing profile parameters of α-iron, leave everything at its default values and not refinable.

Start the refinement by hitting the `OK` button or simply press Enter. Refining the scale factor only in the first step avoids that other parameters, namely structural parameters, are 'used' by the fit to decrease differences between measured and calculated data points that are simply due to wrong scaling. A divergence of the refinement would be most likely the case. After the refinement terminated, in the second step set also the number of scattering centers and the isotropic displacement factor $B_{iso,n}$ of α-iron refinable. The latter is accessible via the `Edit atoms` button in the main dialog of α-iron. As only one atom is contained in the structure, only Fe is choosable and by double-clicking this atom, value and refinement flag of the isotropic displacement factor B_{iso} can be changed. To account for deviations between model and measured data, set the first four background parameters refinable. After starting the fit again, it should terminate at a residual about an order of magnitude lower than the previous step with spikes in the difference curve at the edge positions. If the spikes point downwards up to a certain point and upwards then or vice versa, a wrong value of the time offset is most likely to be the reason. In case of a wrong flightpath length or lattice parameter, the spikes are likely to point all in the same direction. Depending on the shape of the difference curve, flightpath length and/or time offset should be set to refinable now and the fit started again.

If the difference curve is still not flat, more background parameters may be released. If the background curve is flat and shows only some deviations at the edge positions, the refinement of the profile parameters may be started. It is suggested, that first σ_1 is refined while β_0, β_1 and α_0 are refined in this sequence in subsequent steps. After checking the final values, they may be used as

starting values for other patterns using the identical setup by saving them to a fit-setup file (use button on fit control page)[2].

By default, the file name of the refined pattern, the used phases with their volume fractions (the color of the phase-name corresponds to the color of reflection indices and tick-marks), the used edge profile function, residual χ^2 and R-factor are given. From the `View` menu, several additional information for presentation or to judge the quality of the refined parameters may be retrieved:

- The edges may be labeled with their Miller indices.
- Reflection markers allow for example to readily test wether spikes in the difference curve appear at edges of the present phase(s) or are due to phases not yet included in the refinement.
- The modeled or (scaled) measured incident intensity may be displayed.
- In case of current mode data, the offset and therefore the zero intensity line may be turned on.
- Plotting the background allows to study potential differences between model and measuered data.
- Plotting the measured data as crosses rather than dots make it easier in monochrome plots to distinguish fit and measured data.
- A timestamp may be added to the right of the plot.
- The difference curve may be scaled in order to look at details.

Most settings are stored in the Windows registry and retrieved the next time **BETMAn** is used.

[2] Note that currently only the overall parameters and, if a modeled incident intensity is used, the parameters of the incident intensity are saved in a setup file. The file with the incident intensity pattern in case of a measuered pattern as incident intensity and the profile parameters currently have to be re-entered in subsequent refinements.

Appendix I

BET Factors

Bragg-edge transmission patterns suitable for refinements require, at least with the currently available resolution, intense edges. The edge intensity depends on the coherent scattering cross-section of the contributing nuclei and the reflection multiplicity, in other words the symmetry of the crystal lattice. A high symmetry provides few but intense reflections while a low symmetry yields many but very weak reflections. Based on this, a factor

$$\eta = \frac{\bar{\sigma}_{coh}^{el}(\lambda)}{NV_o} \tag{I.1}$$

is suggested to allow to estimate the quality of a Bragg-edge transmission pattern of a certain system. The coherent elastic scattering cross-section $\bar{\sigma}_{coh}^{el}$ is averaged over the accessible wavelength range at a given instrument (i.e. 0.5 to 3.3 Å with the 60 m setup at flightpath 5 of LANSCE), N is the number of reflections in this range and normalisation by the unit cell volume V_0 assures that for instance α (bcc) and γ (fcc) iron result in approximately the same quality factor. η is automatically computed by **BETMAn** whenever a phase file is opened in a cross-section window. Additionally, an estimate of the sample thickness for a certain transmission is given. Both, accessible wavelength range and desired transmission can be set in `File - Settings` within **BETMAn**. Following is a table of several systems sorted by ascending η.

System	Space Group	Crystal System	BET-Factor	Reflections	Thickness
Enstatite $MgSiO_3$ (monoclinic)	P $\frac{2_1}{c}$	monocl.	0,010	2225	10,25
ZrO_2 monoclinic	P $\frac{2_1}{c}$	monocl.	0,013	2288	7,84
Enstatite $MgSiO_3$ (orthorhombic)	P b c a	orth.	0,016	1068	12,81
Brookite (orth. TiO_2)	P b c a	orth.	0,020	1136	5,51
γ-TiAl	P $\frac{4}{m}$ m m	tetr.	0,019	361	7,22
low-cristobalite SiO_2	P 4_1 21 2	tetr.	0,026	641	13,20
Quartz SiO_2	P 3_2 2 1	trig.	0,028	665	11,83
Rutile (tetrag. TiO_2)	P $\frac{4_2}{m}$ n m	tetr.	0,037	588	4,83
SiC hexagonal	P 6_3 m c	hexag.	0,051	438	9,76
Cementite Fe_3C	P n m a	orth.	0,055	1194	2,65
Calcite $CaCO_3$	R $\bar{3}$ c	trig.	0,058	330	11,64
ZrO_2 tetragonale	P $\frac{4_2}{n}$ m c	tetr.	0,062	462	7,83
Corundum Al_2O_3	R $\bar{3}$ c	trig.	0,067	327	9,96
σ-Fe_3Cr_2	P $\frac{4_2}{m}$ n m	tetr.	0,068	592	3,49
PZT $PbZr_{0.9}Ti_{0.1}O_3$	R 3 c	trig.	0,073	330	8,96
Anatase (tetrag. TiO_2)	I $\frac{4_1}{a}$ m d	tetr.	0,085	229	5,65
α-Al	F m $\bar{3}$ m	cub.	0,091	66	30,88
Hematite Fe_2O_3	R $\bar{3}$ c	trig.	0,128	334	4,29
Si	F d $\bar{3}$ m	cub.	0,162	47	27,03
Graphite	P 6_3 m c	hex.	0,163	284	4,97
high-cristobalite SiO_2	F d $\bar{3}$ m	cub.	0,301	53	14,04
SiC cubic	F $\bar{4}$ 3 m	cub.	0,363	68	8,93
α-Pb	F m $\bar{3}$ m	cub.	0,384	67	8,75
Magnesiowuestite MgO	F m $\bar{3}$ m	cub.	0,407	67	8,32
ZrO_2 cubic	F m $\bar{3}$ m	cub.	0,410	67	8,20
Nickelspinel $NiAl_2O_4$	F d $\bar{3}$ m	cub.	0,463	60	6,38
α-Cu	F m $\bar{3}$ m	cub.	0,687	61	3,00
Magnetite Fe_3O_4	F d $\bar{3}$ m	cub.	0,730	59	4,25
Wuestite FeO	F m $\bar{3}$ m	cub.	0,738	68	3,58
Si rich steel	I m $\bar{3}$ m	cub.	0,920	59	2,73
NiO	F m $\bar{3}$ m	cub.	0,931	67	2,48
α-Fe	I m $\bar{3}$ m	cub.	1,058	59	2,64
γ-Fe	F m $\bar{3}$ m	cub.	1,062	61	2,58
Diamond	F d $\bar{3}$ m	cub.	1,287	44	4,06
α-Ni	F m $\bar{3}$ m	cub.	1,372	59	1,69

Table I.1: BET quality factor η for several systems. The thickness is given in cm and estimated for a transmission of T =0.1.